Saikat Biswas Supriya Das Sanjay Kumar Ghosh *Editors*

Advanced Detectors for Nuclear, High Energy and Astroparticle Physics

Proceedings of ADNHEAP 2017



Springer Proceedings in Physics

Volume 201

The series Springer Proceedings in Physics, founded in 1984, is devoted to timely reports of state-of-the-art developments in physics and related sciences. Typically based on material presented at conferences, workshops and similar scientific meetings, volumes published in this series will constitute a comprehensive up-to-date source of reference on a field or subfield of relevance in contemporary physics. Proposals must include the following:

- name, place and date of the scientific meeting
- a link to the committees (local organization, international advisors etc.)
- scientific description of the meeting
- list of invited/plenary speakers
- an estimate of the planned proceedings book parameters (number of pages/ articles, requested number of bulk copies, submission deadline).

More information about this series at http://www.springer.com/series/361

Saikat Biswas · Supriya Das Sanjay Kumar Ghosh Editors

Advanced Detectors for Nuclear, High Energy and Astroparticle Physics

Proceedings of ADNHEAP 2017



Editors
Saikat Biswas
Center for Astroparticle Physics and Space
Science, Department of Physics
Bose Institute
Kolkata, West Bengal
India

Supriya Das
Center for Astroparticle Physics and Space
Science, Department of Physics
Bose Institute
Kolkata, West Bengal
India

Sanjay Kumar Ghosh
Center for Astroparticle Physics and Space
Science, Department of Physics
Bose Institute
Kolkata, West Bengal
India

ISSN 0930-8989 ISSN 1867-4941 (electronic) Springer Proceedings in Physics ISBN 978-981-10-7664-0 ISBN 978-981-10-7665-7 (eBook) https://doi.org/10.1007/978-981-10-7665-7

Library of Congress Control Number: 2017962415

© Springer Nature Singapore Pte Ltd. 2018

This work is subject to copyright. All rights are reserved by the Publisher, whether the whole or part of the material is concerned, specifically the rights of translation, reprinting, reuse of illustrations, recitation, broadcasting, reproduction on microfilms or in any other physical way, and transmission or information storage and retrieval, electronic adaptation, computer software, or by similar or dissimilar methodology now known or hereafter developed.

The use of general descriptive names, registered names, trademarks, service marks, etc. in this publication does not imply, even in the absence of a specific statement, that such names are exempt from the relevant protective laws and regulations and therefore free for general use.

The publisher, the authors and the editors are safe to assume that the advice and information in this book are believed to be true and accurate at the date of publication. Neither the publisher nor the authors or the editors give a warranty, express or implied, with respect to the material contained herein or for any errors or omissions that may have been made. The publisher remains neutral with regard to jurisdictional claims in published maps and institutional affiliations.

Printed on acid-free paper

This Springer imprint is published by Springer Nature
The registered company is Springer Nature Singapore Pte Ltd.
The registered company address is: 152 Beach Road, #21-01/04 Gateway East, Singapore 189721, Singapore



Preface

The national conference on "Advanced Detectors for Nuclear, High Energy and Astroparticle Physics" was organized during February 15–17, 2017, as a part of the centenary celebration of Bose Institute. The main aim of this conference was to provide an exceptional venue to showcase outstanding developments and contributions in detector research for the experimental studies in nuclear, high-energy, and astroparticle physics in India.

Experiments in nuclear, high-energy, and astroparticle physics depend on the detection of primary radiation or particles and that of the product particles if any. In general, the detection of radiation/particle is based on its interaction with the detector material. But depending on the area of study and specific observable, the detector itself as well as the detection methodology may be different. For example, in high-energy physics large particle yield necessitates a detector with very high position sensitivity, whereas low flux of particles and requirement of directionality may be a decisive factor in astroparticle physics. On the other hand, a detector used to determine the energy of a particle precisely in an event may furnish only a moderately accurate timing information or may not have any ability for particle identification. Here we have tried our best to cover studies on various detectors as used in the above-mentioned areas of physics.

Different institutes in India provide facilities for nuclear physics experiments, focused at energies around Coulomb barrier, using different accelerator systems. The heavy-ion-induced fusion and fusion–fission reactions are characterized by various quantities, such as fission mass and angular distributions, fusion cross section and barrier distributions, multi-nucleon transfer, neutron and charged particle multiplicity. In order to perform experimental measurements, detector systems based on position sensitive and fast timing proportional counters, particle identification telescopes based on gas ionization chambers and semiconductor detectors, and scintillators for light charged particle and neutron detection have been developed. The detectors are routinely used in experiments involving facilities of mass spectrometers, scattering chamber, gamma and neutron array.

For more than last two decades, India has contributed significantly in the field of research on gaseous detectors for high-energy physics. The gaseous photon

viii Preface

multiplicity detector (PMD) developed in India is being successfully used at the STAR experiment at Relativistic Heavy Ion Collider (RHIC) in BNL and A Large Ion Collider Experiment (ALICE) at CERN in LHC. Various studies on resistive plate chamber (RPC) are being carried out using both glass and bakelite for the future India-based Neutrino Observatory (INO). RPC is one of the most widely used large-area gas-filled detectors in experimental high-energy physics with a potential to be used in PET imaging. Till now, RPCs have found their applications in HEP experiments like STAR, ALICE, ATLAS, CMS, BELLE, BaBar, BESIII and neutrino experiments, e.g., OPERA. Indian researchers are working on the use of gas-filled detector such as multigap resistive plate chamber (MRPC) for medical imaging in place of expensive scintillator detectors. Presently, extremely high-level R&D is in progress on gas electron multiplier (GEM)-based detectors for the CBM muon chamber detector at Facility for Antiproton and Ion Research (FAIR) and for the upgrade of ALICE time projection chamber (TPC).

In India, several institutes such as TIFR, North Bengal University, Gauhati University, BARC, SINP are involved in experiments on astroparticle physics. These institutes are building large detector systems for particle and radiation detection. For example at present, GRAPES-3 array in CRL, TIFR, Ooty, is the highest density conventional EAS array in the world.

Bose Institute is actively involved in the detector development program for ALICE at CERN and future experiment CBM at FAIR. In addition to our ongoing works on the detection of strangelets in cosmic ray air shower using passive detectors, we are also in the process of developing a large active detector array for cosmic ray detection in our Darjeeling campus.

Bose Institute was founded in 1917. Inspired by lofty nationalistic ideals, Acharya Sir Jagadish Chandra Bose, the father of modern science in the Indian subcontinent, founded Bose Institute and dedicated it to the service of the nation on November 30, 1917. He pioneered breakthroughs in radio communication, semi-conductor devices, and plant electrophysiology. His demonstration of wireless millimeter wave propagation in Calcutta in 1895, a first in the world, was a major achievement that led to the foundation for the development of modern wireless communication from radio to satellite communication. The demonstration was possible only because of his ingenious fabrication of a number of novel devices associated with wave generation, propagation, and detection.

After J. C. Bose, Debendra Mohan Bose became the director of Bose Institute in 1937. D. M. Bose and his co-workers were the initiators of experimental high-energy and cosmic ray physics in India using cloud chamber and photographic emulsions. In 1941, his associates R. L. Sengupta and M. S. Sinha built a large cloud chamber of 30 cm diameter triggered by a counter telescope. D. M. Bose and Biva Choudhury made globally recognized contributions in cosmic rays studies including the first recording of pi-meson tracks. Later, he made further pioneering contributions on the susceptibility measurement of paramagnetic compounds. This conference, organized on the occasion of centenary celebration of Bose Institute, is also a tribute to these pioneering researches at Bose Institute.

Preface

The proceedings of the conference include manuscripts from invited review talks, contributory orals, and also the posters from most of the active areas of research in detector physics, namely detectors for accelerator-based high-energy physics, nuclear physics, astroparticle physics, non-accelerator particle physics along with detector simulation, instrumentation, and electronics. In this volume, Parts I, II, and III contain articles corresponding to the review talks, contributory oral presentations, and posters, respectively.

This conference brought together 73 scientists from around the nation and 2 experts from abroad including Head of the GSI detector laboratory, Darmstadt, Germany, to share their knowledge. There were several excellent review talks, a few contributory oral presentations, and posters in the conference. Professor Siddhartha Roy, Director Bose Institute, inaugurated the conference, and Prof. Sibaji Raha, Senior Professor, Bose Institute, delivered the welcome address. Professor Y. P. Viyogi of VECC, Kolkata, delivered the summary talk. Ten students were supported by the "Young Researcher Grant" providing them with registration fee waiver and cost of accommodation.

All the details of the conference including all the presentations are available in the Web site https://indico.cern.ch/event/586317/.

We, the organizers, are immensely grateful to the Springer-Verlag GmbH for agreeing to publish these proceedings. We are extremely thankful to Mr. Aninda Bose, Senior Editor—Hard Sciences, Springer (India) Private Limited, for his constant help and encouragement.

Kolkata, India

Saikat Biswas Supriya Das Sanjay Kumar Ghosh

Acknowledgements

We have been extremely fortunate to have the support and encouragement of many individuals as well as various organizations at every stage of this conference along with the publication of the proceedings. We would like to convey our gratitude to each and every one of them.

We are thankful to centenary celebration committee, Bose Institute, for accepting our proposal to organize the "Advanced Detectors for Nuclear, High Energy and Astroparticle Physics" conference and Department of Science and Technology, Government of India, for providing the required financial support.

We would like to thank advisory committee members, Dr. R. K. Bhandari, Prof. Sunil K. Gupta, Prof. Ajit Kumar Mohanty, Dr. Tapan Kumar Nayak, Prof. Sibaji Raha, Prof. Amit Roy, Prof. Amitava Roy, Prof. Dinesh Kumar Srivastava, and Prof. Y. P. Viyogi, who have guided us throughout the conference with their valuable suggestions.

We would like to acknowledge our fellow organizing committee members, Dr. Subhasis Chattopadhyay, Dr. Sidharth Kumar Prasad, Dr. Rajarshi Ray, and Mr. Ashim Kr. Biswas, for their active participation and help.

We would like to express our gratitude to Prof. Siddhartha Roy, Director, Bose Institute; Prof. Samir Ranjan Sikdar, In Charge Registrar Office; and Prof. Tripurari Prasad Sinha, Chairman, Physics Department, Bose Institute, for their support.

We thank Bose Institute administration and accounts section for their generous assistance in all aspects.

We would like to show our appreciation to CAEN S.P.A and Parsram and Company Pvt Ltd. for their partial financial support. CAEN has sponsored the "Young Researcher Grant."

Thanks to the Director, S. N. Bose National Centre for Basic Sciences, for giving permission to accommodate the outstation participants.

Special thanks to Mr. Arun Kumar Das Gupta for helping us almost in all the arrangement. Thanks to Mr. Kanak Baran Hazra, Ms. Shrabani Sen, Mr. Bholanath Acharya, Mr. Manoj Shee, Mr. Sumanta Ghosh, and Mr. S. Das for their help.

Thanks to Mr. Raju C. Paul for the transport arrangement.

xii Acknowledgements

We would like to thank all the chairman of the session, speakers, and poster presenter for coming and presenting their work in the conference.

Last but not least, we would like to thank our students, Mr. Rama Prasad Adak, Mr. Rathijit Biswas, Mr. Dipanjan Nag, Ms. Shreya Roy, and postdoctoral fellows, Dr. Subikash Choudhury and Dr. Maitreyee Mukherjee, for helping us in all arrangements.

We, the organizers, are immensely grateful to the Springer-Verlag GmbH for agreeing to publish these proceedings. We are extremely thankful to Mr. Aninda Bose, Senior Editor—Hard Sciences, Springer (India) Private Limited, for his constant help and encouragement.

We have included most of the presentations of the conference in these proceedings. We have also included a group photograph of conference participants at the end. We thank all the authors for their cooperation. We sincerely hope that this issue will be useful to the community.

Kolkata, India

Saikat Biswas Supriya Das Sanjay Kumar Ghosh

Contents

| Part I Review | |
|--|----|
| Silicon Sensors in Experimental High Energy Physics Experiments Ashutosh Bhardwaj, Geetika Jain and Kirti Ranjan | 3 |
| Detectors for Nuclear Physics | 15 |
| Detector Development Activities at IUAC | 29 |
| PET: A High Threshold Nuclear Track Detector (NTD) for Rare Event Search | 49 |
| Detectors for Non-accelerator Particle Physics | 59 |
| Device Physics Simulation of Gaseous Ionization Detectors Supratik Mukhopadhyay | 67 |
| Part II Contributory Oral | |
| Experimental Studies of Ion Backflow for a Bulk Micromegas Detector Using Various Argon-Based Gas Mixtures Prasant Kumar Rout, Deb Sankar Bhattacharya, Purba Bhattacharya, Supratik Mukhopadhyay, Sudeb Bhattacharya, Nayana Majumdar, Sandip Sarkar, Paul Colas, David Attie, Serguei Ganjour and Aparajita Bhattacharya | 81 |
| Study of Characteristics of Quadruple GEM Detector with Different Gas Flow Rates | 91 |

xiv Contents

| Comparison of Si, Ge, and Diamond Sensors for Using It in HEP Experiments | 97 |
|--|-----|
| Shyam Kumar, Raghava Varma, K. Das Gupta, Pradeep Sarin and S. K. Deb | 71 |
| An Efficient Approach to Manage DMA Descriptors and Evaluate PCIe-Based DMA Performance for ALICE Common Readout Unit | |
| (CRU) | 107 |
| Sensitivity of ICAL to TeV Gamma Rays at INO | 119 |
| Qualification of Eco-Friendly Gas Mixture for Avalanche Mode Operation of RPC Jaydeep Datta, Abhik Jash, Nayana Majumdar and Supratik Mukhopadhyay | 129 |
| Analysis of Ultra-High-Energy Muons at INO-ICAL Using Pair-Meter Technique | 137 |
| Characteristic Simulations of Stack of Four Gas Electron Multipliers (GEMs) | 147 |
| Performance Study of Muon Detector with CBM Experiment at FAIR | 157 |
| Effect of Electric Field and Gas Mixture on RPC Time Resolution Abhik Jash, Sridhar Tripathy, Nayana Majumdar, Supratik Mukhopadhyay, Satyajit Saha and Subhasis Chattopadhyay | 167 |
| GEANT4 Simulation for Imaging of High-Z Materials Using Cosmic Ray Muons | 175 |
| Part III Poster | |
| Neutron Response of PARIS Phoswich Detector Balaram Dey, C. Ghosh, S. Pal, V. Nanal, R. G. Pillay, K. V. Anoop and M. S. Pose | 187 |
| Simulation of Gamma Detection Using GEANT4 | 193 |

Contents xv

| Measurement of Angular Variation of Cosmic Ray Intensity with Plastic Scintillator Detector | |
|--|-----|
| Some Aspects of Characterization of GEM Detector | 205 |
| A TTL Fast Pulse Counter for Detector Signals | 211 |
| Implementation and Evaluation of Glue Logic for Various Configuration Schemes Based on I2C and HDLC Protocol for ALICE Common Readout Unit (CRU) | 217 |
| A Simulation Model for Triple GEM Detector | 223 |
| Author Index | 231 |

About the Editors

Saikat Biswas is Assistant Professor in the Center for Astroparticle Physics and Space Science (CAPSS), Department of Physics, Bose Institute, Kolkata, India. At Bose Institute, he is mainly involved in TPC upgrade for ALICE at CERN and CBM muon chamber. He did his Ph.D. from the University of Calcutta in 2011. He initiated his career by joining Variable Energy Cyclotron Centre, Kolkata, as a Junior Research Fellow (JRF) in September 2005 and completed his Ph.D. work on development of bakelite based Resistive Plate Chambers in India-based Neutrino Observatory (INO) ICAL experiment. He has got 29 journal publications, 29 conference papers, 1 chapter, and 30 talks to his credit. He received the DST-SERB Ramanujan Fellowship award in 2012. He worked as Scientific Officer in National Institute of Science Education and Research (NISER), Bhubaneswar, from 2013 to 2015. At Bose Institute, he is involved in the stability study of the GEM detector and development of other gaseous and scintillator detectors. His research interests are instrumentation for experimental high-energy physics, detection of cosmic ray, and medical imaging.

Supriya Das is currently an Associate Professor in the Department of Physics, Bose Institute, Kolkata, India. He started his scientific career as a doctoral student at Variable Energy Cyclotron Centre, Kolkata, working in the STAR experiment at the Relativistic Heavy Ion Collider. He received his Ph.D. from Jadavpur University, Kolkata, in 2007. His current research areas are relativistic heavy-ion collision, quark–hadron phase transition, signatures of QGP, detection of cosmic ray air showers, and R&D with nuclear detectors.

Sanjay Kumar Ghosh is Senior Professor in the Department of Physics, Bose Institute, Kolkata, India. He did his Ph.D. from Institute of Physics in 1996. His research interest areas are quark—hadron phase transition, relativistic heavy-ion collision, early universe phase transition, neutron star/quark star, effective models, cosmic ray, atmospheric physics. He has several publications to his credit.

Part I Review

Silicon Sensors in Experimental High Energy Physics Experiments

Ashutosh Bhardwaj, Geetika Jain and Kirti Ranjan

Abstract Si detectors are now being widely used in experimental high energy physics (HEP). This detector technology is more popularly used as particle tracking detectors. Its application is diverse, viz. from the track reconstruction, various parameters of the incident particle like the flight of path, the momentum in the presence of a magnetic field, secondary or a decay vertex, interaction vertex, etc., can be deduced. Si detectors are also used as active layers in sampling calorimeters in some of the experiments.

1 Historical Perspective

1.1 Semiconductor Detectors

The semiconductor detectors have been popular for energy measurements since the 1950s, with germanium (Ge) p-n junctions to be the first detectors used for alpha particle detection [1, 2]. For over a decade, the evolution of the Ge detectors continued, until it was found that unlike Ge, which required substantial cooling, silicon (Si) could be operated at room temperatures. Hence, a significant surge was seen in the use of the Si detectors for spectroscopy, owing to their excellent energy resolution [3–5] in the next few years of the 1960s. However, it was only in the early 1980s that the Si detectors were used for particle tracking and vertexing. It was realized that a small leakage current combined with a high electric field at low operating voltage provides excellent charge collection in these detectors, making them suitable for particle detection. This characteristic, along with the easy availability of the crystalline Si and the planar technology [6] for the fabrication of the sensors (and other advantages described in detail in Sect. 2), led to a rapid development of the Si detector technology in the experimental HEP. This paper covers the various aspects of the developments of Si detectors in the HEP experiments.

A. Bhardwaj (⋈) · G. Jain · K. Ranjan Department of Physics and Astrophysics, Centre for Detector and Related Software Technology, University of Delhi, New Delhi, India e-mail: ashutosh.bhardwaj@cern.ch

[©] Springer Nature Singapore Pte Ltd. 2018

4 A. Bhardwaj et al.

1.2 First Use of Silicon Detectors in HEP

In the late 1970s, several groups of the NA11 and NA32 experiments at SPS, CERN, were interested in the identification and measurement of particles with a lifetime of the order of 10^{-13} s (decay length $\sim 30 \,\mu$ m). This required a detector with a spatial resolution better than 10 µm, with a rate-handling capability of MHz. Si detectors with 1200 diode strips on 2436 mm² active area, fabricated with the planar technology, were installed in the experiments. With a resolution of 4.5 µm achieved by the detectors, the charm meson (D) was successfully identified. This remarkable achievement marked the progress of the use of silicon technology as tracking detectors. Several interesting developments by CERN and Fermilab were reported at the 3rd European Symposium on Semiconductor Detectors and at the 1984 IEEE Nuclear Science Symposium [7–9], which led to construction of a series of unparallel tracking detector system composed of entirely Si, e.g. CDFII and $D\Phi$ at TEVATRON [10]; DELPHI at LEP [11]; ATLAS, ALICE, CMS and LHCb at LHC [12-17] and many more. From a small active tracking area of 0.2 m² in BELLE experiment, the present CMS experiment active tracking area has increased to $\sim 210 \,\mathrm{m}^2$, with 10 million readout channels. The maturity of our understanding of the Si technology and the desire for more ambitious candidates for future experiments challenges have incredibly increased the efforts and prospects for the blooming of the Si detector industry.

2 Basics of Si Detectors and the Principle of Operation

2.1 Basic Properties of Silicon

This section describes the basic silicon properties and technical application to develop a better understanding of silicon sensors.

Si is an element in the periodic table with atomic number 14 and is the second-most abundant material in the earth's crust after oxygen. It is a crystalline, dark grey, solid material at room temperature with a bluish tinge. It does not occur free in nature but is found in the form of silicon dioxide and complex silicates. It is a semiconductor material with electrical resistivity $(2.3 \times 10^3 \ \Omega m)$ which lies somewhere in between metals and insulators.

The forbidden energy gap of silicon is 1.12 eV at room temperature. A particle crossing the material medium needs, on an average, only about 3.6 eV of energy to create one electron–hole pair which is quite low as compared to 30 eV required to ionize a gas molecule in gaseous detectors. Because of its high atomic density $(5 \times 10^{22} \text{ cm}^{-3})$, the average energy loss per unit length ($\sim 390 \text{ eV}/\mu\text{m}$) and ionized number of particles ($\sim 108 \text{ e}$ -hole pairs/ μm) are effectively high.

Si is tetravalent material with intrinsic carrier density of 1.45×10^{10} cm⁻³ (at room temperature), and when it is selectively doped with small amounts of impurities, its electrical properties can be controlled. It can be made to n-type and p-type by

| Parameter | Value |
|--------------------------|---|
| Relative atomic weight | 28.0855 |
| Structure | Diamond |
| Lattice constant | 5.4307 Å |
| Electronic configuration | $1s^2 2s^2 2p^6 3s^2 3p^2$ |
| Mass density | 2.328 gcm^{-3} |
| Dielectric constant | 11.7 |
| Electron mobility | $1350 \text{ cm}^2 \text{ V}^{-1} \text{ s}^{-1}$ |
| Hole mobility | $450 \text{ cm}^2 \text{ V}^{-1} \text{ s}^{-1}$ |
| Max. electric field | 30 V/μm |
| Intrinsic resistivity | 235 kΩ cm |

Table 1 Physical properties of Si

adding small amounts of trivalent (e.g. boron) or acceptor impurities and pentavalent (e.g. phosphorus) or donor impurities, respectively.

With enormous number of applications in semiconductor technology, Si dominates today's entire electronic world. It is extensively used in the solid-state devices in the computer and micro-electronics industries as well. Because of its exclusive properties, Si is an ideal choice to be used as particle detectors. Some of the Si properties are listed in Table 1 [18].

2.2 Fabrication of a Si Detector

Fabrication of Si detectors includes the following steps: single-crystal production; slicing into wafers; processing—oxidation, photolithography, doping, annealing, metallization, etching, and dicing (cutting).

First, SiO_2 is produced from sand which is then reduced by carbon in an arc furnace equipped with graphite electrode. In this process, CO_2 is released and we get low-purity Si which is called metallurgical-quality Si. This Si is then made to react with HCl to produce trichlorosilane which is then filtered and purified by distillation and is finally decomposed at high temperature into HCl and pure silicon. Then, this pure Si is converted to single-crystal Si by using a technique called Czochralski growth (CZ growth). This single-crystal Si ingot can be further refined by using a technique called Float-zone (FZ) technique.

The introduction of doping impurities can be carried out by a number of techniques: doping of molten silicon before CZ growth, thermal diffusion, ion implantation, growth of doped Si layer on an existing substrate (epitaxy) and neutron doping. Few of commonly used techniques are briefly described below.

Ion implantation: This is done by an ion implanter which is basically a particle accelerator, consisting of different stages, in which ions of desired impurities are accelerated by an electric field up to energies usually ranging from 5 to 200 KeV

A. Bhardwaj et al.

and get uniformly distributed across the Si wafer in the target chamber. These can be made to penetrate up to a given depth in the crystal depending upon the implant energy.

Thermal Diffusion: Impurity diffusion is generally carried out at very high temperature (800–1100 °C). At such high temperatures, the impurity atoms can diffuse throughout the Si crystal volume through the interactions with interstitials and vacancies. Gas-phase diffusion doping can also be done in a high-temperature furnace in which the gas containing the doping impurities (BBr_3 for boron or $POCl_3$ for phosphorus) is introduced.

Si can be oxidized either by dry oxidation, in which solid Si is made to react chemically with oxygen at high temperature, or by wet oxidation, in which it is made to react with steam at high temperature. The growth rate of SiO_2 layer is limited initially only by the rate of chemical reaction involved, and after the growth of some oxide, it is limited by the diffusion rate of the oxidizing agent (oxygen or steam).

To grow a thick layer of oxide, wet oxidation is preferred over dry oxidation as the H_2O molecules are smaller than O_2 molecules and these can diffuse through the already-grown oxide layer relatively easily and give rise to higher rate of oxidation. Photolithography is a process which is used at various stages during fabrication of the Si detector, for example, when performing the ion implantation or during the etching of a material in selected areas on the wafer by transfer of a pattern to the Si surface. In this process, the oxidized wafer is covered with photoresist. Parts of resist are then masked and subjected to UV-light, and after the final development, the sensor is etched. As a final step, the resist is etched away, leaving defined windows in the oxide layer.

Etching usually follows the photolithography steps in which we place the wafer in a chemical bath (wet etch) or in a plasma (dry etch). The items are listed in Table 2. Wet etching is very easy to use, but it is not recommended to etch features of sizes smaller than 1 or 2 μm because it is usually isotropic and may lead to overetching problems. So for etching of small patterns, dry etching in plasma is generally used. After ion implantation, a high temperature step is necessary to anneal structural damages. In rapid thermal annealing, Si wafer is rapidly heated up to a high temperature (about 1100 $^{\circ} C$) for a few seconds and is quickly cooled down for the placement of the doping atoms into substitutional sites. It helps in the diffusion of the dopant impurities and to smoothen the edges.

| Table 2 Etchants used for different material | S |
|---|---|
|---|---|

| Materials etched | Chemical etchant | Gas used in plasma |
|--------------------------------|--|-------------------------------------|
| Si, poly-Si | HF + HNO ₃ , hot KOH | $CF_4 + O_2$, $SF_6 + O_2$, HBr |
| SiO ₂ | HF | $CF_4 + H_2, C_2F_6$ |
| Si ₃ N ₄ | hot H ₃ PO ₄ | Same as above |
| Aluminium | HCl, H ₃ PO ₄ | CCl ₄ , Cl ₂ |
| Photoresist | $H_2SO_4 + H_2O_2$, fuming HNO ₃ , Acetone | O ₂ |

Finally, the metallization process occurs in which the back side of the detector is fully metallized for simple electrical contact, while the front side is patterned by photolithography. In this process, the metal is evaporated from a source and redeposited onto Si wafers. The deposition of metal layer is usually carried out in vacuum. Sometimes, chemical vapour deposition (CVD) or sputtering process is also used for metallization. Most widely used metal for the fabrication of detectors is aluminium because of its good electrical conductivity, good connectivity to Si and easy shaping by photolithography. Metallization is used to interconnect devices, supply electrical power, etc.

The last step before characterizing the sensor is the precision cutting of the sensor out of the processed wafer which is usually done by a diamond saw and continuous wafer flushing.

The details of Si detector processing can be found in [19–23].

2.3 Operational Principle of Si Detectors

To keep the signal-to-noise ratio (S/N) high, we need to fully deplete the detector and for that the detector must be configured in reverse bias configuration. Once the detector is fully depleted, an ionizing particle is made to penetrate through the volume of the detector which creates a number of electron—hole pairs along its path. The generated holes drifting along the direction of electric field and electrons drifting in the opposite direction are collected by the respective electrodes which are capacitively coupled to aluminium readout strips. The electrodes are further connected to the readout electronics where the signal is shaped and amplified.

2.4 Types of Si Detectors

Si detectors are used in the HEP experiment in various configurations, depending on their usage. Few more commonly used configurations are described below.

Micro-Strip detector: A single-sided micro-strip detector is a Si sensor segmented in long, narrow elements where each strip is an independent p-n reverse-biased junction and provides the measurement of one coordinate of the particles crossing point with high precision. When a charge particle passes through it, it creates electron—hole pairs which, under the influence of electric field, move to the respective electrodes. When the holes reach the p-type strips, they are collected and induce a measurable charge on the associated aluminium strips which are further connected to sensitive electronic readout channels. By recording which electronic channel is fired, it is possible to determine the position of the charged particle passing through the detector.

Pixel detector: It is a two-dimensional array of sensors monolithically integrated on a single silicon wafer and has the same working principle as the silicon strip sensors.

8 A. Bhardwaj et al.

It is able to track the path of the penetrating particles with desired accuracy and provides two-dimensional information about the position of the particle.

Low gain avalanche detector (LGAD): The strip and pixel detectors suffer from the loss of signal with irradiation. A novel design, LGAD, based on the principle of controlled avalanche multiplication was introduced, as it provides the possibility of an internal gain. In this detector, a deep p-type multiplication layer is doped onto the n-implant of the n-on-p detector. Under the effect of bias, the increase in the electric field at the junction of the implant and the multiplication layer causes an avalanche to occur, thereby increasing the particle signal.

Avalanche photodiode detector (APD): The APDs are based on a similar internal gain mechanism as that of LGADs. Instead of the generation of avalanche locally like in LGADs, in APDs, the avalanche occurs in a larger detector volume. A p-type implant is deep diffused into a low-resistivity n-type substrate. The resultant gain by the APD is 3 orders greater than that by the LGAD. However, the APDs have to be operated at a much higher voltage.

3D detector: In these detectors instead of having n- and p-type electrodes on the front and back surfaces, there are grids of n- and p-type electrode columns passing through the thickness of a silicon substrate. As the spacing between the electrodes is reduced significantly in these 3D Si detectors, the depletion voltage and collection time of these detectors are relatively very small without affecting the charge generated in the device by an ionizing particle.

Ultra-thin 3D detector: The device is a novel ultra-thin silicon detector with only 10-µm-thick active volume, fabricated on a Si wafer. The collecting electrodes are columns etched through the Si instead of being implanted on the surface like in the standard planar technology, allowing lower capacitance.

3 Radiation Damage

Tracking detectors are situated as close to the interaction point as possible, thereby exposed to a high particle flux environment of charged (protons, pions, etc.) and neutral (neutron and photons) radiation. This can lead to the formation of crystal defects, causing damage to the bulk and surface properties of the Si. The properties further degrade with a long-term operation of the detector in the radiation environment, ultimately making it unfit for particle detection [24]. The bulk and the surface damage in Si are briefly described below.

3.1 Bulk Damage

Incident particles, apart from ionizing the Si lattice, also interact with the Si atom via the non-ionizing energy loss (NIEL) [25]. If the particle transfers an energy greater than the threshold energy, the atom (primary knock-on atom, PKA) gets displaced,

creating a vacancy (V) and an interstitial (I) elsewhere. The PKA can further cause ionization and displacements (Frenkel defects—V, I) along its track in the lattice. These V, Is migrate into the Si bulk and form stable defect complexes with other V, Is or impurities (like carbon, oxygen). The point and cluster defects thus formed induce electrically active acceptor and donor type of traps. Depending on the trap energy level in the Si energy band gap, cross section, introduction rate, etc., the traps act as recombination-generation centres (increasing the leakage current with irradiation), deep trap centres (affect the bulk space charge), or trap centres for electron or hole charge carriers (reducing the charge collection efficiency).

The comparison of radiation damage for different incident particles with energies is done through the non-ionizing energy loss (NIEL) hypotheses, which state that damage due to the Si atom displacement can be scaled linearly with the amount of energy imparted in the displacement collisions irrespective of the interaction mechanisms of the particles, with the bulk damage caused by the mono-energetic 1 MeV neutrons considered as calibration reference. Thus, 1 MeV neutron equivalent fluence (ϕ_{eq}) is defined as particle fluence (ϕ) multiplied with an appropriate hardness factor (κ), where κ depends on the particle type and its energy.

3.2 Surface Damage

Unlike the bulk damage, the surface damage is caused by ionization (electron–hole pair generation) of SiO_2 rather than atomic displacement. A complete recombination does not take place in the SiO_2 because the electrons with higher mobility drift quickly to the metal electrode, but the holes drift via the hopping mechanism. The defect concentration is high at the $Si-SiO_2$ interface due to the lattice distortion and the dangling bonds. Therefore, holes get trapped in these defects and form positive fixed charge traps (N_{ox}). Further, the deep traps along the interface act as recombination-generation centres, contributing to surface leakage current or as trap centres known as interface traps (N_{it}).

The presence of N_{ox} attracts electrons towards the surface, leading to formation of an electron accumulation layer. Such an accumulation of electrons at the p^+ strip implants creates a region of high electric field which may lead to decrease in the breakdown voltage. It may also lead to non-depleted regions which may result in loss of signal. Additionally, it leads to an increase in interstrip capacitance (noise increase) and decrease in interstrip resistance (crosstalk increase). A spread in the signal leads to a loss of the position resolution of the detector.

3.3 Radiation Damage Modelling

Measurements are limited by experimental problems, environmental conditions, financial constraints, manpower and resources, etc., which are required for a

10 A. Bhardwaj et al.

comprehensive R&D. For this reason, technology computer-aided design (TCAD) device simulations are useful. They can be tuned and modelled to mimic the known measurement data and then further be used for optimizing the various design parameters. Thus, simulations are not only economically viable, they also save a lot of efforts in the investigation of a new detector technology.

The most popular TCAD device simulators in the HEP community are Silvaco [26], Sentaurus [27] and Cogenda [28]. In all of these simulators, a physical structure of interest is first designed, which requires a knowledge of following parameters: the dimensions of the structure; the front, back, and bulk-doping profiles and type of doping (whether uniform, Gaussian, plane-parallel, etc.); the DC and the AC aluminium contacts; the thickness and choice of the coupling and the passivation layers (SiO₂ or/and Si₃N₄), etc. Next, an intelligent selection of the grid points known as the mesh is built on the structure, on which the physical equations are computed. The physical equations include the Poisson equation, the current density equation and the continuity equation. The choice and application of the physical models for the mobility, impact ionization, generation and recombination, etc., is different in different simulators. Also, the various default parameters are different in these simulators. Further, the bulk and the surface traps (interface and positive fixed oxide) with option for choosing their types (acceptor or donor), energy levels, cross section, introduction rate, etc., is also available. Finally, the bias conditions are defined and the numerical method (like Newton, Gummel, Block) for calculation is chosen.

For a comparison of the measurements of irradiated detectors with TCAD simulations, a radiation damage model was developed using the Silvaco simulator. Due to computational and software constraints, the model is based on five most effective traps only, even when there are plenty of traps seen in measurements. However, these traps are tuned such that the simulated results satisfactorily describe the measurement results (characteristics like current-voltage, capacitance-voltage, charge collection, interstrip resistance, interstrip capacitance). The five-trap model is a combination of two bulk traps, one positive fixed oxide charge density and two interface traps, forming a combined bulk and surface radiation damage model. The detailed modelling and refine tuning of the model and its parameters are described in [29–31]. The model is based on the original work by [32].

4 CMS HPK Campaign for Phase II Strip Tracker Upgrade

The instantaneous luminosity at the Large Hadron Collider (LHC) located at CERN, Switzerland, is anticipated to increase by a factor of ten times higher in the high-luminosity LHC phase (scheduled for the year 2022) than the present 300 fb^{-1} [33–35]. This phase, also known as the phase II upgrade, requires an R&D effort to build a detector technology that can survive during the high luminosity radiation environment, over a period of ten years of detector operation. Hence, the R&D effort aimed at testing and establishing the radiation tolerant abilities of the Si strip detectors was initiated. This is popularly known as the HPK campaign, since the detectors were

fabricated at the Hamamatsu Photonics K. K. [36]. Along with measurement R&D, simulation R&D was also carried out within the campaign. Some of the important simulation results of the campaign are described in the sections below.

4.1 Polarity of the Substrate

Charge collection and noise measurements were carried out for both n-type and p-type Si substrates. It was found that the charge collection is a bit higher for n-type substrates than their p-type counterparts; the collecting charge carrier at the electrode is electron (high mobility for n-type) and holes (low mobility for p-type) [37]. However, the n-type substrates also displayed an undesirable feature of local discharge, leading to an early breakdown [38]. It was through TCAD simulations that further insight into this crucial difference was developed. It was noticed that the electric field increases faster at the implant corners for the n-type (over the p-type) substrates. Further investigations yielded that it was the acceptor polarity of the surface traps that decreases the electric field growth in p-type substrates. This is explained in detail in [39].

4.2 Geometry of Detector

The choice of strip width (w) and strip pitch (p) is also critical when fabricating a detector as these parameters affect the breakdown voltage (V_{bd}), the electric field, the interstrip capacitance (C_{int}), etc. This was also established through an extensive study of the above-mentioned parameters on different configurations of w and p. Following observations were established: decrease in p, for a constant w/p ratio, increases V_{bd} ; increase in w, for a constant p (i.e. increasing w/p ratio), increases V_{bd} ; increase in p increases the electric field at the implant edges; increase in w decreases the electric field at the implant edges; increase in w, for a constant p, increases C_{int} , etc. These observations in simulations are of high importance and were used as an input before fabricating the detectors. The selection of the different parameter values is described in [40].

4.3 Choice of Isolation Technique

The surface damage of the p-type substrates leads to a formation of a positive fixed oxide at the interface of Si-SiO₂. This attracts electrons towards it, which forms an accumulation layer, thereby shorting the n-implants. This calls for a need of a technique to isolate the n-implants. Therefore, the isolation techniques mentioned in [41] were also tested for detector performance in the HPK campaign. Some of the important results developed during the campaign are: for a constant w and p, V_{bd} is higher for p-stop isolation; electric field increases with increase in

12 A. Bhardwaj et al.

p-stop/p-spray doping concentration; the interstrip resistance increases with increase in p-stop/p-spray doping concentration, etc. Various studies have been shown in [42].

4.4 Detector Fabrication at DU

With some knowledge from detector designs used at D0 at the Fermilab, an optimization for low leakage current, high breakdown voltage, etc., was done in the TCAD simulator by University of Delhi (DU) [43]. This design was then fabricated at BEL, Bangalore. These detectors are AC-coupled, poly-Si-biased, p-on-n Si strip detectors and have been indigenously developed for the first time in India. The characterization of these detectors was carried out at DU and Karlsruhe Institute of Technology (KIT), Karlsruhe. Some of the basic results are shown in [44, 45].

Acknowledgements Author is thankful to University of Delhi R&D grant and DST for research and financial support.

References

- 1. K.G. McKay, A germanium counter. Phys. Rev. **76**, 1537 (1949)
- K.G. McKay, Electron-hole production in germanium by alpha-particles. Phys. Rev. 84, 829– 832 (1951)
- 3. J.M. McKenzie, D.A. Bromley, Gold surface barrier (Si) diode. Phys. Soc. 4, 422 (1959)
- 4. E.M. Pell, Ion drift in an n-p junction. J. Appl. Phys. 31, 291 (1960)
- 5. J.H. Elliott, Development of Lithium "drifted" thick detectors. NIM 12, 60 (1961)
- J. Kemmer, Fabrication of low noise silicon radiation detectors by the planar process. NIM 169, 499–502 (1980)
- 7. E. Engels, A silicon strip detector system for Fermilab. NIM A 226, 59 (1984)
- 8. H. Bottcher, Performance of silicon strip detectors with 50-micrometer and 100-micrometer strip distance. NIM A **226**, 72 (1984)
- 9. P.E. Karchin, Test beam studies of a silicon microstrip vertex detector. IEEE Trans. Nucl. Sci. 32(1), 612 (1985)
- 10. F. Bedeschi, A silicon vertex detector for CDF. CDF Note **362**, 123 (1985)
- 11. N. Bingefors, The DELPHI microvertex detector. NIM A 328, 447–471 (1993)
- 12. M. Sitta, The silicon drift detector of the ALICE experiment. NIM A 617, 591–592 (2010)
- C. Kuo, The commissioning and results on the performance of the CMS Preshower detector.
 J. Phys.: Conf. Sers 293, 012058 (2011)
- 14. C. Parkes, First results from the LHCb Vertex Locator. NIM A 628, 81–83 (2011)
- 15. F. Meier, First alignment of the complete CMS tracker. NIM A 636, 177–181 (2011)
- F. Dajma, Commissioning & operation of the ATLAS pixel detector at the CERN LHC collider. JINST 6 C01082
- 17. J.A. Gray, The CMS Phase-I pixel detector. JINST 8 C12047
- 18. J.P. Colinge, C.A. Colinge, *Physics of Semiconductor Devices* (Springer, New York, 2006)
- 19. G.F. Knoll, Radiation Detection and Measurement, 4th edn. (Wiley, Hoboken, 2010)
- D.A. Neaman, Semiconductor Physics and Devices, Basic Principles (McGraw Hill, Avenue of the Americas, New York, 2003). 10020
- 21. W.R. Leo, Techniques for Nuclear and Particle Physics Experiments (Springer, Berlin, 1994)
- 22. S.M. Sze, *Physics of Semiconductor Devices* (Wiley, New York, 1985), p. 2

- 23. G. Lutz, Semiconductor Radiation Detectors (Springer, Berlin, 1999). 16, 65, 85, 86
- F. Hartmann, Evolution of Sensor Technology in Particle Physics (Springer, STMP 231, 2009)
 ISSN 0081-3869
- 25. M. Moll, Radiation damage in silicon particle detectors. DESY-THESIS-1999-040
- ATLAS Silvaco, Version 5.15.32.R Nov 2009, Users manual, Silvaco webpage. http://www.silvaco.com
- Sentaurus TCAD, Industry–Standard process and device simulators, synopsys documentation. http://www.synopsys.com
- 28. Cogenda, Genius device simulator, *User's guides*, Cogenda webpage. http://www.cogenda.com
- CMS Detector Note, Simulation of Silicon Devices for the CMS Phase II Tracker Upgrade. CMS DN-2014/016
- 30. R. Dalal, G. Jain, A. Bhardwaj, K. Ranjan, Simulation of irradiated Si detectors. Proc. Sci. (Vertex) **030** (2014)
- 31. R. Dalal, Performance Characteristics of Si Sensors at Collider Experiments. Ph.D. Thesis, University of Delhi (2015)
- 32. V. Eremin, E. Verbitskaya, Z. Li, The origin of double peak electric field distribution in heavily irradiated silicon detectors. NIM A 476, 556–564 (2002)
- 33. CMS Tracker Technical Design Report. CERN/LHCC 98–6, CMS TDR 5 (1998). CERN/LHCC 2000-016, CMS TDR 5 Addendum (2000)
- S. Mallows, BRIL webpage https://twiki.cern.ch/twiki/bin/viewauth/CMSPublic/BRILR SelbaHGC
- 35. M. Guthoff, BRIL webpage. https://twiki.cern.ch/twiki/bin/view/CMSPublic/BRILRS1D1MeVneqAtTracker
- 36. Hamamatsu K. Photonics, Hamamatsu webpage. http://www.hamamatsu.com/us/en/index. html
- G. Kramberger, V. Cindro, I. Dolenc, I. Mandic, M. Mikuz, M. Zavrtanik, Comparison of pad detectors produced on different silicon materials after irradiation with neutrons, protons and pions. NIM A 612, 288–295 (2010)
- 38. R. Eber, Investigations of new Sensor Designs and Development of an effective Radiation Damage Model for the Simulation of highly irradiated Silicon Particle Detectors. Dissertation Thesis. Karlsruhe Institute of Technology, IEKP-KA/2013-27
- 39. R. Dalal, G. Jain, A. Bhardwaj, K. Ranjan, Comparison of radiation hardness properties of p+n- and n+p- Si strip sensors using simulation approach, in *23rd RD50 Workshop* (CERN, Switzerland, 2013)
- 40. T. Peltola, Numerical simulations of semiconductor radiation detectors for high-energy physics and spectroscopy applications. Ph.D. thesis, University of Helsinki (2016)
- 41. C. Piemonte, Device simulations of isolation techniques for silicon microstrip detectors made on p-type substrates. IEEE Trans. Nucl. Sci. **53**(3), 1694 (2006)
- 42. M. Printz, Analysis of n-in-p type silicon detectors for high radiation environment with fast analogue and binary readout systems. Ph.D. Thesis, Karlsruhe Institute of Technology (2016). IEKP-KA/2016-1
- P. Saxena, K. Ranjan, A. Bhardwaj, R.K. Shivpuri, S. Bhattacharya, Development of multiguard ring-equipped p+–n Si microstrip detectors for the SiD detector at the ILC. Semicond. Sci. Technol. 25, 105012 (2010)
- 44. K. Lalwani, G. Jain et al., Design, fabrication and characterization of multi-guard-ring furnished p+n-n+ silicon strip detectors for future HEP experiments. Nucl. Instrum. Methods A **824**, 428–431 (2015). (13th Elba Conference)
- 45. G. Jain, et al., Development and characterization of ac-coupled Si strip detectors for nuclear & high energy physics applications, in *DAE Symposium on Nuclear Physics*, vol. 59. (Dec. 08 12, 2014) pp. 954–955

Detectors for Nuclear Physics

Tilak Kumar Ghosh

Abstract Progress in nuclear physics is driven by the experimental observation that requires state-of-the-art detectors to measure various kinematic properties, such as energy, momentum, position, of the particles produced in a nuclear reaction. Advances in detector technology have enabled nuclear physicists to measure these quantities with better precision, and the reduced cost of the detection system has helped to have larger detection systems (array of detectors) to measure the rare processes with greater sensitivity. Several detection systems have been designed, developed and built in India over last few decades and are being used by the physicists. In this article, I will focus on such developments of detection systems at Variable Energy Cyclotron Centre (VECC), Kolkata.

1 Introduction

It is a privilege to present this review on the detector developments for nuclear physics research at Variable Energy Cyclotron Centre (VECC), in this particular conference, that celebrates the centenary year of Bose Institute which happens to be the first interdisciplinary research institute in India, founded by Sir Jagadish Chandra Bose. He was one of the legendry Indian experimentalists who used to build his own instruments from the scratch for his research. The components of the instruments that he built (e.g. 60 GHz microwave apparatus) [1] were quite innovative but remained pretty simple that really attract and inspire us when we try to build our detectors in our laboratory.

Variable Energy Cyclotron Centre, 1/AF, Bidhannagar, Kolkata 700064, India e-mail: tilak@vecc.gov.in

T. K. Ghosh

Homi Bhabha National Institute, Training School Complex, Anushaktinagar, Mumbai 400094, India

T. K. Ghosh (⋈)

16 T. K. Ghosh

2 Scope of Detection in Fundamental Nuclear Physics

One of the fundamental questions that we deal in Nuclear Physics is, how do the nucleons work together to form complex nuclei. This branch of Nuclear Physics is often referred as *Nuclear Structure*. On the other hand, many of these nuclei are needed to make them react with target nuclei in order to understand the rearrangement of the nucleons inside nuclei that helps us to know the macroscopic or bulk properties of the nuclei. The interaction between two complex nuclei is broadly studied under the section called *Nuclear Reaction*. In general, the study of nuclear structure and nuclear reaction constitutes the low-energy nuclear physics research. However there is another branch; the study of the constituents of nucleons, i.e. quarks and gluons and their interactions. This study requires very high energy to break the nucleons and this constitutes the high-energy nuclear physics.

Let us have a look at the evolution of nuclear physics with energy (as shown in Fig. 1). The change over from one zone to other is not sharp, rather having considerable overlap. However the classification is indeed helpful for designing experiments and relevant detector systems. The typical binding energy of a nucleon is $\sim 8 \, \text{MeV/u}$; so around that energy (below $\sim 10 \, \text{MeV/u}$) one can basically study the mean field dominated normal nuclear matter and the equilibrium reactions. Mean field gradually breaks down with increase in energy. Typically, around the Fermi energy ($\sim 38 \, \text{MeV/nucleon}$) one may expect transition from mean filed to nucleonic degrees of freedom which is indicated in the change of reaction mechanism. Low-energy binary process is gradually replaced by multi-fragmentation process [2]. One may even expect exotic phenomena like nuclear liquid—gas phase transition [3]. Beyond $\sim 100 \, \text{MeV/u}$, compressed nuclear matter may be produced where the main

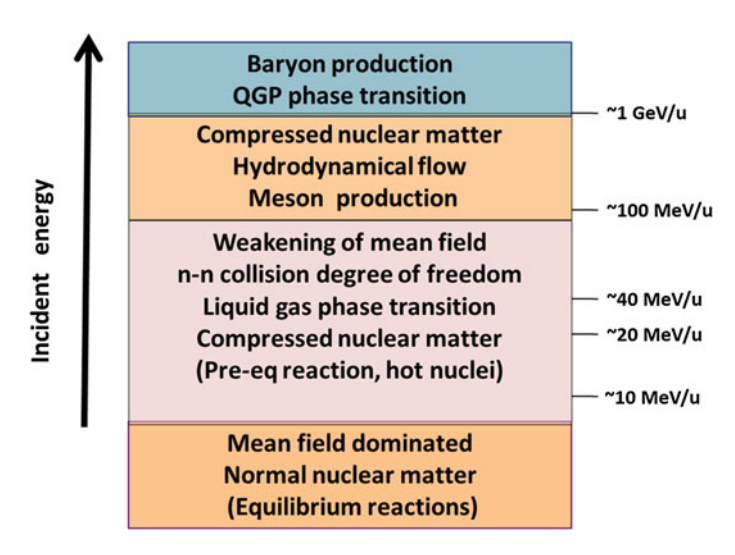


Fig. 1 Evolution of nuclear reaction scenario with incident energy

physics interest is to study the hydrodynamical flow and the dynamics of meson production. Beyond \sim 1 GeV/u, it is possible to study the baryon production and at higher energy one can study physics of quark gluon plasma (QGP).

With the increase in beam energy, the particle multiplicity, as well as the velocity of reaction products and variety of particles increase. Therefore from the detection point of view, at higher beam energy one would require detector system of large granularity and count rate handling capacity.

Usually four fundamental quantities are measured in an experiment, and these are enough to extract the physics information about the nuclei and reaction process. These quantities are: energy (E), time of arrival (t), position (x, y, z) and multiplicity/counts (N) of a detected particle. For example, to know the atomic (Z) and mass number (A) of a particle produced in a nuclear reaction, measurement of particle energy loss (dE/dx) and time flight information are sufficient. So, a detector with good time (t) and energy (E) resolution is required. The excitation energies of the residual nuclei and shapes of angular distributions can tell us about the reaction mechanism and properties of the residual nuclei. By measurement of energy (E) and angle (x, y, z) of the emitted fragments one can achieve that. By counting the number of particles (N) produced in a nuclear reaction, it is possible to calculate the cross section of the nuclear reaction that can inform us about a variety of properties of the nuclei as well as the reaction process.

In India, we have three major accelerator facilities: K130 Cyclotron at Variable Energy Cyclotron Centre in Kolkata, a 14UD pelletron machine at BARC-TIFR pelletron facility in Mumbai and a 15UD pelletron machine at Inter University Accelerator Centre (IUAC), New Delhi. Mumbai and Delhi machines are recently been upgraded with LINAC that provides beam up to sulphur, typically less than 10 MeV/u. A K500 superconducting Cyclotron is under development at VECC.

At present different types of sophisticated detector systems are being developed at the various Indian accelerator centres. Since the list is extensive, it is not possible to describe all of them in this article. I shall concentrate on those detectors, which are more commonly used by experimental nuclear physics community and being developed by us. At our centre (VECC), the detector development activities are aimed at the effective utilisation of the existing and upcoming accelerator facilities in the country.

3 Development of Gas Detectors

Several types of gas detectors are being developed at VECC. One of the major physics research programs at our centre is the investigation of heavy ion-induced fission reactions that has gained momentum in recent times. Apart from fundamental interest to study the dynamics of heavy ion nuclear reactions, these studies may guide us to find out the right kind of target and projectile combination for the synthesis of super heavy elements [4].

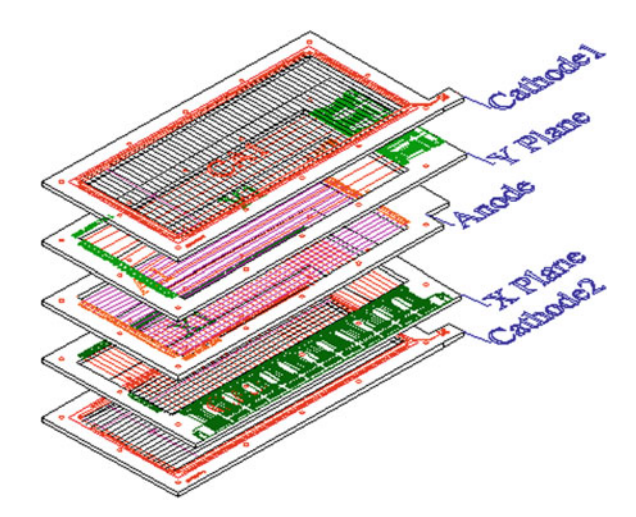
18 T. K. Ghosh

The detection of fission fragments is particularly suitable with gas detectors. Conventionally, segmented silicon detectors were used in past for detecting fission fragments but they have disadvantages like high costs, limited rate handling capacities, vulnerability to radiation damage and generally their smaller size. Multi-wire proportional counter (MWPC), first developed by Georges Charpak [5], are more favourable in such experiments to detect fission fragments because of the flexibility it offers. Apart from being inexpensive, these detectors provide good timing and position resolution and are insensitive to radiation damage. Their ease of fabrication into any shape and size is an added advantage. They have good rate handling capacities and parameters like operating voltages and gas pressures can be fully customised to detect or reject light particles.

The detector we have developed is a low-pressure MWPC. The active area of the detector is 20 cm × 6 cm. It consists of five wire planes: one anode (A), two sense wire planes (X, Y), two cathode (C) planes and in front of the detector there is an window frame which is basically a polypropylene foil (thickness $\sim 0.5 \,\mu\text{m}$). The wires of X and Y planes are of diameter 50 µm and fixed perpendicular to each other. The separation between two wires is kept 2 mm. The anode plane consists of wires with diameter 12.5 µm and separation between two wires is 1 mm, whereas in case of the cathode planes the separation is kept same but the diameter of the wire used is 20 µm. The orientations of the cathode wires are also perpendicular to one another. Thin wires were taken, as smaller the diameter larger the field produced near the wire, and hence, the avalanches are localised. So the timing is faster and the dependence on the position of interaction in the detector becomes negligible. The gold-coated tungsten wires are soldered on to the conducting strips. The two cathode wire planes are shorted outside and connected to a power supply through a charge sensitive preamplifier. This gives us the provision to get the energy loss signal from the cathode. In the X and Y planes, the wires are connected to the individual pads which are connected to successive pads of delay line chips. These delay line chips (each of 20 ns, 2 ns per tap) of the X position have a total delay of 200 ns with 10 chips. In case of Y position, there is a total delay of 150 ns with 3 chips, each having a delay of 50 ns. The anode, cathode, X and Y are printed circuit broads (PCB) and spacers, made of a material called glass epoxy, are used to maintain the desired spacing of the detector. While the separation between anode and X(Y) sensitive planes are 1.6 mm, the separation between cathode and X(Y) sensitive planes are 3.2 mm. A 1 cm \times 1 cm wire mesh of stainless steel wires of diameter 0.4 mm was used as a support to the polypropylene film. Two gas feed-throughs were connected to the back support frame which is made of stainless steel. Isobutane gas is continuously sent through the detector at a constant pressure flow mode with baratron feedback closed-loop flow control system (make MKS, USA). A schematic of the detector wire planes is shown in Fig. 2.

In order to achieve the multi-step avalanche of electrons, the detectors are operated with a high electric field for substantial gas multiplication. Typical voltages applied on anode and cathode planes are +300 V and -200 V, respectively. The operating gas pressure is about two torr. The reduced electric field E/p, where E is the electric field between the cathode and sense wire plane and p is the gas pressure, is high

Fig. 2 Three dimensional view of the wire planes of a MWPC



enough to produce secondary multiplication of the primary electrons produced in the region between cathode and sense wires. However, the electric field in the cathode to anode region is a constant accelerating field. The constant filed in this region is not qualitatively changed by the introduction of the grounded X, Y sense wire planes at 1.6 mm distance. The intense field region around the central anode wire extends roughly 20 times the diameter, i.e. in this case about 0.25 mm.

The detectors were tested with a ²⁵²Cf source in the laboratory for uniformity of the position read outs and correspondence between the timing (anode pulse) and position (X-Y delay line signals). The position resolution (FWHM), measured by illuminating the detector with mask, was found to be 1.2 mm for X-direction and 1.5 mm for Y-direction. The anode signal for the fission fragments with a fast current sensitive preamplifier (ORTEC, VT120) is found to be 0.5 V with rise time better than 5 ns. The typical time resolution of the detector measured with ²⁴¹Am source at a gas pressure of 5 torr is found to be 700 ps. The time resolution was measured by using one detector as a start and the 2nd one as a stop.

These detectors are routinely used for measurement of fission fragment mass distributions using the Indian accelerator facilities (K130 Cyclotron, BARC-TIFR and IUAC Pelletron) to study the fusion–fission and quasi-fission dynamics [4]. Figure 3 shows a typical experimental set up where two gas detectors are placed at folding angle to detect the fission fragments. Pulsed beam from the accelerator are used as start signal and these detectors provide the stop signal in the time-of-flight setup to measure the mass distribution. The typical mass resolution achieved is four *amu*.

MWPCs of several dimensions were made in our laboratory as per the requirement of the experiment [6]. The MWPCs described above can provide the mass of the detected fission fragments from measured time-of-flight information for binary reactions using set of equations m1/m2 = t1/t2 and m1 + m2 = M, where m, t are the mass, time of flight of the binary fission fragments, respectively, and M is the compound nuclear mass. However, at higher beam energies typically in the Fermi

20 T. K. Ghosh



Fig. 3 Experimental setup inside VECC scattering chamber with the MWPCs to measure the fragment mass distributions in heavy ion-induced fission reactions

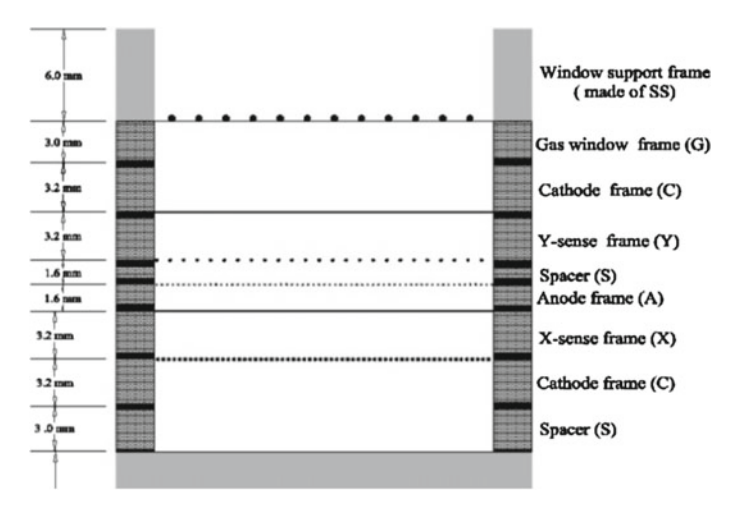


Fig. 4 Vertical cross-sectional view of the hybrid gas detectors

energy domain, the reactions may not be binary in nature. Thus, one would require both energy (E) and time-of-flight (velocity, v) information of the fragment in order to deduce the mass. This necessitates a detector that can simultaneously measure the energy and time of flight of the particle produced in a nuclear reaction.

As a spinoff of MWPC development, we have developed a hybrid gas detector for simultaneous measurement of energy and time. The detector is conceptually a combination of low-pressure MWPC and an assembly of segmented silicon detector. The cross-sectional view of the detector is shown in Fig.4. The active area of the detector is $20\,\mathrm{cm} \times 6\,\mathrm{cm}$. A $300\,\mu\mathrm{m}$ thick segmented silicon detector assembled at

the back of the MWPC has 16 strips each with dimension $30\,\mathrm{mm} \times 96.8\,\mathrm{mm}$. While the timing and position information are achieved from MWPC, the total energy of the particle is taken from the silicon detector.

Figure 5 shows the photograph of the segmented silicon detector made by Micron Semiconductor Ltd, UK, as per our design. The window thickness of the silicon detector is $0.3\,\mu m$ and measured energy resolution (alpha from ^{241}Am source) was found to be 2.5%.

We have also developed few parallel plate avalanche counter (PPAC) with active area $5 \, \text{cm} \times 3 \, \text{cm}$ with three electrode geometry. These are used as start detector in a time flight set up. This is particularly required in an accelerator like K130 Cyclotron where time resolution of the beam is poor (>5 ns).

The central anode wire plane of the detector consists of 10 µm diameter goldplated tungsten wires soldered 1 mm apart. The cathode wire planes were made of 20 µm diameter gold-coated tungsten wire, placed 2 mm apart. The separation between anode and a cathode plane was 3.2 mm. All the wire planes were made of G – 10 quality single-sided glass epoxy, copper-plated boards (PCB) as shown in Fig. 6. The anode wires were soldered on to conducting strips. The cathode wires were similarly soldered to a conducting pad. The two cathode wire planes were shorted outside and connected to a power supply through a charge sensitive preamplifier. Stretched polypropylene films of thickness 0.5 µm were used as the entrance windows of the detector. A 1 cm × 1 cm wire mesh of stainless steel wires of diameter 0.4 mm was used as a support to the polypropylene film. Two gas feed-through were connected to the back support frame which is made of stainless steel. In order to keep the distance (3.2 mm) between anode and cathode, we had to use spacers (made of G10 board) of thickness 1.6 mm. The detectors are operated at +280 V (anode) and -180 V (cathode) with isobutene gas at 3 torr. The detectors provide time resolution better that 500 ps. The detectors are found to be more than 99 % efficient for detection of fission fragments from a ²⁵²Cf source.

At VECC, we have also developed an axial field ionisation chamber [7]. The detector is used as a Δ E-detector of a charged-particle telescope with silicon strip as

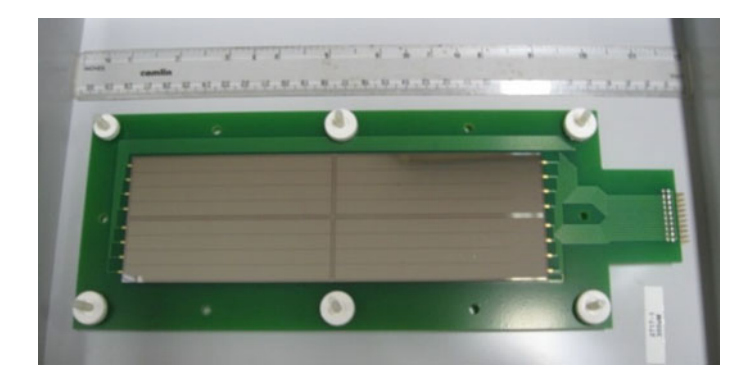


Fig. 5 Segmented silicon detector, assembled at the back of the MWPC

T. K. Ghosh

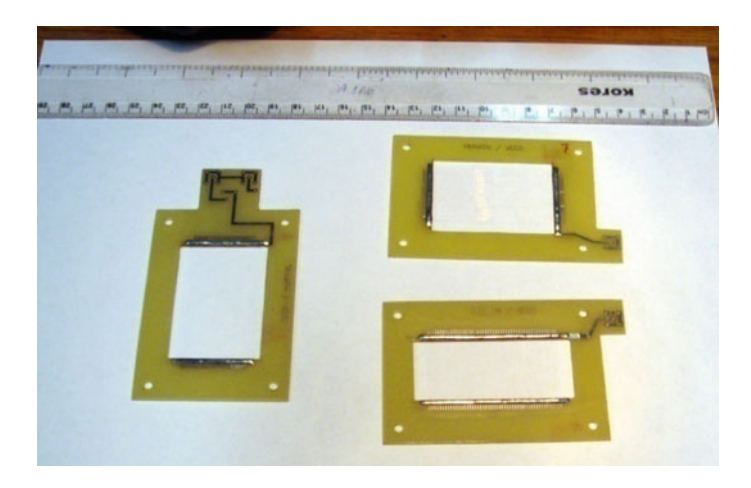
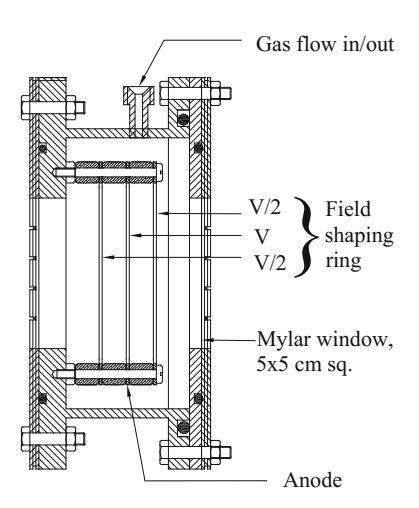


Fig. 6 PCBs of the parallel plate avalanche counters

Fig. 7 Vertical cross-sectional view of the axial ionisation chamber



E-detector (stop) to study the particle-particle, particle-fragment correlation in heavy ion-induced reactions. For detection of heavy fragments, employment of this kind of detector is inevitable because of the non-availability of large area silicon detector of sufficiently smaller thickness (Fig. 7).

The active area of the detector is $5\,\mathrm{cm} \times 5\,\mathrm{cm}$. The detector consisted of three square-shaped field-shaping rings separated by 10 mm. A nichrome wire mesh of 98% transparency was attached with the middle field-shaping ring that acts as an anode. Using a voltage divider resistance chain, a voltage of V is given to anode while V/2 to the other rings. The front and the back of the detector were covered by 2-mm-thick mylar foils, glued on stainless steel (SS) frame. The SS plates were

grounded. The window foils were supported by thin SS wire of diameter $0.3 \,\text{mm}$. The detector is operated with P-10 gas at typical E/p = 1 V/cm/torr.

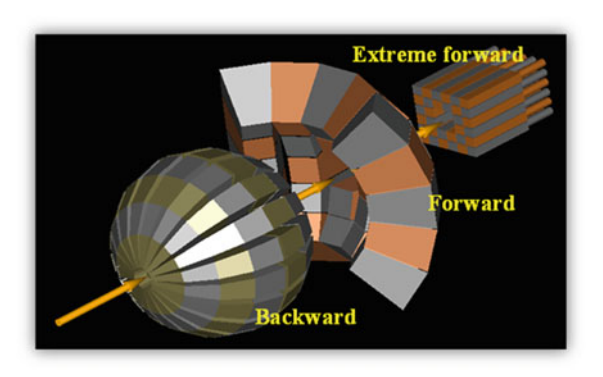
4 Development of a Charged-Particle Detector Array (CPDA)

At VECC, we are developing a high resolution, high-granularity 4-pi array for complete charged-particle spectroscopy. This is a unique tool for the study of multiparticle correlation, resonance spectroscopy, complete calorimetry, etc. One of the main motivations behind the development of this array is to study the decay of highly excited nuclear system and the search for the density dependence of the symmetry energy part of the nuclear equation of state [8]. The density dependence of the symmetry energy is expected to affect several observables (e.g. the ratio, between the isotopic yields of a given fragment in two different reactions) which can be measured in heavy ion collisions. The charged-particle detector array is designed to satisfy the needs of the scientific motivations discussed above, as the array will have excellent angular, energy and isotopic resolutions and large ($\sim 4\pi$) solid angle coverage with high granularity.

The array consists of three parts: the extreme forward array (angular coverage ± 3 to $\pm 7^{\circ}$), forward array (± 7 to $\pm 45^{\circ}$) and backward array (± 45 to $\pm 170^{\circ}$). A schematic view of the charged-particle detector array is shown in Fig. 8.

The extreme forward part of the array consists of 32 plastic slow (10 cm, BC444 crystal) - fast (100/200 μ m, BC408 crystals) phoswich detectors, mostly for the detection of light charged particle, elastic scattering and direct reactions products. These detectors are capable of handling high count rate. They are mounted at 40 cm away from the target that offers angular resolution better than a degree. Typical threshold for these detectors are $\sim\!\!2$ MeV/nucleon for proton and alpha, $\sim\!\!5$ MeV/nucleon for $^{16}{\rm O}$ and $\sim\!\!8$ MeV/nucleon for $^{40}{\rm Ca}$.

Fig. 8 Design of the Charged-Particle Detector Array (CPDA)



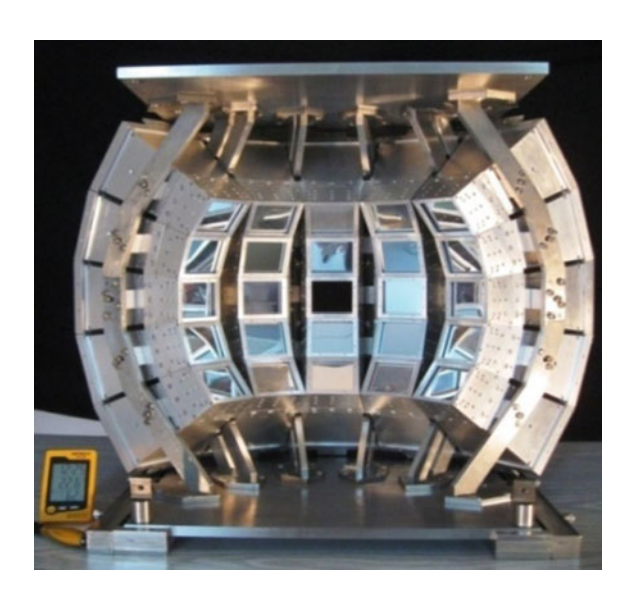
24 T. K. Ghosh

The forward part of the CPDA consists of 24 telescopes, each with silicon strip (50 μ m thick) + silicon strip (500 /1000 μ m) + 4 CsI(Tl) (6 cm) detectors. The centre of each telescope is mounted 20 cm away from the target position. The silicon detectors (*make Micron semiconductor Ltd, UK*) have dimension of 50 mm × 50 mm, the front one is single-sided with 16 strips of 3 mm pitch and the back detector is double-sided (each with 16 strips, orthogonal to each other) with same pitch. The measured thickness variation in 50 μ m thick silicon detector was found to be better than 3%. Each of the CsI crystal has truncated pyramid shape with front face area 25 mm × 25 mm and back face area 35 × 35 mm. Photodiodes are attached to the back side of each crystal to take out the signals. The measured energy resolutions of the crystal were found to be ~5% with ²⁴¹Am alpha source. The maximum non-uniformity of the crystal was less than 0.5% (Fig. 9).

The backward part of the array is to detect only light charged particles (LCP) (Z = 1, 2). LCP will be identified using single CsI(Tl) crystal by pulse shape discrimination (PSD) technique. 114 CsI(Tl) detectors will be mounted in six rings. Geometry of this part of array is such that front face of the detectors forms a part of sphere of radius 15 cm and it does not clash with the other part of the array. The extreme forward and the forward part of the CPDA are ready with analogue electronics ($Mesytec\ GmbH$). The backward part of the array is currently under development.

The development of CPDA at VECC helped us to carry out several experiments. Part of the CPDA (few telescopes), was used in an experiment to extract the direct component of the decay of the famous Hoyle state [9]. The granularity and required energy resolution allowed to carry out a high statistics, high resolution, complete kinematical measurement to estimate the quantitative contributions of various direct 3α decay mechanisms in the decay of the 0_2^+ resonant excited state of 12 C at an

Fig. 9 Photograph of the forward part of the CPDA



excitation energy of 7.654 MeV, using inelastic scattering of 60-MeV α particles on 12 C. Spectroscopic information about different excited states of 26 Al and 26 Mg populated through the 27 Al(d, t) and 27 Al(d, 3 He) reactions [10] and the role of α clustering in the binary complex fragment decay of fully energy-relaxed composites 24,25 Mg*, formed in 12,13 C + 12 C reactions, has also been studied using CPDA telescopes [11].

5 Development of Neutron Detectors

An array of neutron detectors is being developed at VECC for the spectroscopic measurement of fast neutrons produced in accelerator-based experiments. The array will be used for the measurement of energy and angular distribution of neutrons produced in the nuclear collision. This array is planned particularly to study nuclear-level density and fusion–fission dynamics near and above the Coulomb barrier energies.

The detector array will consist of 50 liquid scintillator (BC501A)-based detectors, each of the cell having $5" \times 5"$ cylindrical size and is coupled to 5" photomultiplier tube (XP4512B). The centre of each detector will be at a distance of 2 m from the target position. The target is placed in a 3-mm-thin-walled spherical scattering chamber of 100 cm diameter. Target chamber also has provision to put large area position sensitive multi-wire proportional counters (MWPC) to detect fission fragments in coincidence with neutrons.

For such measurements, the TOF neutron detector array is required to have good pulse shape discrimination, intrinsic time resolution and efficiency over the range of neutron energies from about 1 MeV to few tens of MeV. This developmental activity was guided by several R&D activities which includes development of detectors of several size (7, 5, 3 and 1.5 in. length with 5 in. diameter) and exploration of their detection properties (figure of merit, time resolution and efficiency) to select the optimum detector that suits our requirement. With increase in detector volume, figure of merit (1.26 for 1.5 in, to 1.07 for 7 in.) and time resolution (1.44 ns for 1.5 in, to 1.56 ns for 7 in.) worsen as expected, which is due to higher dimension associated with larger light loss and larger time spread of the arrival of photon at PMT [12]. However, the efficiency of the detector increases with the increase in detector volume. Considering all aspects, for our array, 5 in. × 5 in. detector was chosen that offers time resolution (FWHM) \sim 1.53 ns, figure of merit (with threshold 350 keVee) 1.08 and efficiency (at 2 MeV, threshold 100 keVee) ~64%. A photograph of the detector array around the thin wall scattering chamber at K500 superconducting beam hall at VECC is shown in Fig. 10.

The detectors can easily be transported to different experimental area. Few such detectors are routinely used in in-beam experiments performed at K130 Cyclotron in VECC. Angular momentum dependence of nuclear-level density [13] out of collectivity in nuclear-level density [14], shell effect in nuclear-level density in ²⁰⁸Pb region [15] were extensively studied using these detectors.



 $\textbf{Fig. 10} \ \ \text{Photograph of the detector array around the thin wall scattering chamber at K500 superconducting beam hall at VECC }$

6 Summary

In summary, several state-of-the-art detectors are being developed at VECC. The detectors are being effectively utilised to study fundamental Nuclear Physics such as the study of multi-particle correlations, fragment emission mechanism, study of nuclear-level density and fusion fission—dynamics.

Acknowledgements The major part of this work was carried out under the Superconducting Utilisation Project. The author is thankful to S. Bhattacharya, C. Bhattacharya, K. Banerjee, S. Kundu, T. K. Rana, J. K. Meena, A. Chaudhuri, G. Mukherjee, P. Roy, R. Pandey, S. Manna, A. Sen, J. K. Sahoo, A. Saha, R. Saha Mondal, Trinath Banik, Arnab Ghosh who have contributed in this work. Sincere thanks to Prof. S. Bhattacharya for his suggestions to prepare of the manuscripts.

References

- 1. J.C. Bose, Collected Physical Papers (Longmans, Green and Co., New York, 1927)
- 2. C.B. Das et al., Phys. Rep. 406, 1 (2005)
- 3. J. Mabiala et al., J. Phys.: Conf. Ser. 420(1) (2013)
- T.K. Ghosh, Pramana J. Phys. 85, 291 (2015); A. Chaudhuri et al., Phys. Rev. C 92, 041601 (2015) (R)
- 5. C. Charpak, F. Sauli, Nucl. Instrum. Methods **162**, 405 (1979)
- 6. T.K. Ghosh et al., Nucl. Instrum. Methods Phys. Res. A **540**, 285 (2005)
- 7. S.K. Bandopadhyay et al., Nucl. Instrum. Methods Phys. Res. A 278, 467 (1989)
- 8. P. Danielewicz, J. Lee, Int. J. Mod. Phys. E 18, 892 (2009)
- 9. T.K. Rana et al., Phys. Rev. C 88, 021601 (2013) (R)
- 10. V. Srivastava et al., Phys. Rev. C **93**, 044601 (2016). Phys. Rev. C **91**, 054611 (2015)
- 11. S. Manna et al., Phys. Rev. C 94, 051601 (2016) (R)
- 12. K. Banerjee et al., Nucl. Instrum. Methods Phys. Res. A 608, 440 (2009)
- 13. K. Banerjee et al., Phys. Rev. C 85, 064310 (2012)
- 14. P. Roy et al., Phys. Rev. C 88, 031601 (2013) (R)
- 15. P. Roy et al., Phys. Rev. C 94, 064607 (2016)

Detector Development Activities at IUAC

Akhil Jhingan

Abstract Inter University Accelerator Centre (IUAC), New Delhi provides facilities for nuclear physics experiments, focused at energies around Coulomb barrier, using the Pelletron-LINAC accelerator system. The heavy ion-induced fusion and fusion-fission reactions are characterized by performing measurements such as fission mass and angular distributions, fusion cross section and barrier distributions, multi-nucleon transfer, neutron and charged particle multiplicity, Coulex etc. To execute these experiments, detector systems (Jhingan in Pramana J. Phys. 85:483, 2015 [1]) based on position sensitive and fast timing proportional counters, particle identification telescopes based on gas ionization chambers and gas-silicon detectors, and scintillators for light-charged particle and neutron detection have been developed. The detectors are routinely used in experiments involving facilities of mass spectrometers (Madhavan et al. in Pramana J. Phys. 75:317, 2010 [2]), scattering chamber and neutron array (Sugathan et al. in Pramana J. Phys. 83:807, 2014 [3]) at IUAC. New detector systems are being planned and developed for these facilities as well as for the future facilities such as NUSTAR and SPIRAL2. This article presents an overview of developments in detector instrumentation at IUAC.

1 Introduction

The study of heavy ion-induced reactions around Coulomb barrier is a forefront area of nuclear research at IUAC [4]. For better understanding of reaction mechanisms, the detector systems need to provide information on important parameters of the reaction products such as its energy, timing, position and identity in terms of mass (A) and nuclear charge (Z). In view of these experimental demands, detector systems based on multiwire proportional counters, gas ionization chambers and gas-silicon detectors for Z identification, liquid organic scintillators for neutron detection and CsI scintillators for light-charged particle detection have been developed. Associated

nuclear instrumentation, and pulse shape discrimination techniques for scintillators, have also been developed. Several nuclear reaction experiments have been performed using these detector systems. New detectors with enhanced capabilities in terms of higher count rates, better timing resolutions and particle identification capabilities are being planned for future experiments.

2 Multiwire Proportional Counters (MWPCs)

Position sensitive gas detectors based on MWPC have been the most important detector used in nuclear physics experiments. They provide good timing and position resolutions, are insensitive to radiation damage and have high count rate handling capability. They can be operated with a 2/3/4/5 electrode geometry depending upon the experimental requirement. Generally, a two-dimensional position sensitive counter is operated with a three-electrode geometry [5]: a central cathode sandwiched between two position sensing anodes. Figure 1 shows the general schematic of a five-electrode MWPC, also called a multi-step geometry [6]. All electrodes are wire frames. The detector has two cathodes (one each at entrance and exit), one anode sandwiched between two position electrodes (X and Y). The wires in X and Y are oriented orthogonal to each other. The region between cathode and position electrodes (also called pre-amplification region) is made to operate in drift region whereas that between positions and anode in avalanche region. Last electrode can be removed to provide a four-electrode configuration. This design provides much higher gains as compared to the three-electrode design. A three-electrode MWPC with central aluminized mylar cathode provides better timing. MWPCs at IUAC are operated with iso-butane gas. Positions are extracted using delay line technique. Rhombus delay chip model TZB12-5 (2 ns/tap, $Z = 50 \Omega$) are used for the same. Wire frames are made using stretched gold-plated tungsten wires (diameter: 20 μm/10 μm) soldered on commercial printed circuit boards (PCB).

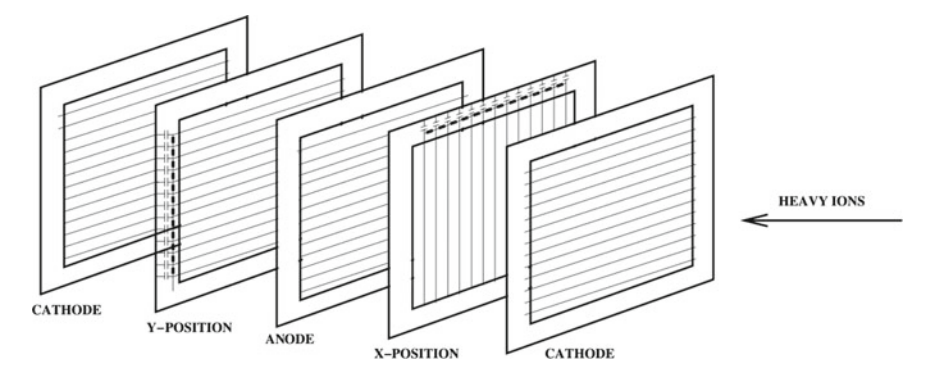


Fig. 1 Multi-step MWPC schematic showing arrangement of electrodes

3 Gas Ionization Chambers (ICs)

IC has been used for nuclear charge (Z) identification of the reaction products. The detector can be operated only as a gas detector or as hybrid detector in combination with a silicon detector. They are operated in transverse field or in axial field geometry mode. Figure 2 shows the schematic of an IC operated in transverse field geometry mode. It has an anode which is segmented to provide differential energy loss (ΔE) information by charge-sensitive preamps (CSPAs). The other two electrodes are cathode and Frisch grid. Guard electrodes (G) with field shaping gradient provide optimum signal collection at the edges. The length of the IC can be reduced using

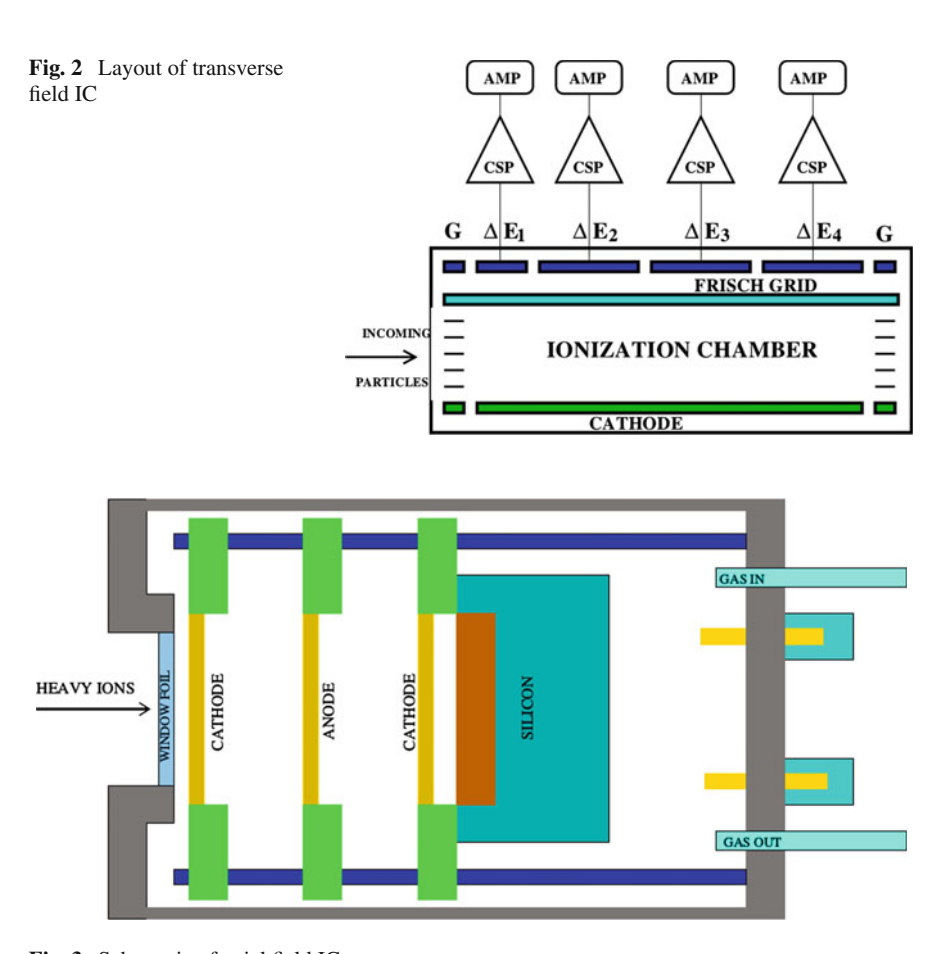


Fig. 3 Schematic of axial field IC

hybrid configuration, where there is only one anode segment as ΔE detector, and E information is provided by silicon detector. More compactness is achieved using axial field geometry shown in Fig. 3. Axial field IC is fabricated using three-electrode configuration of anode sandwiched between two cathodes. They are operated with silicon forming a hybrid telescope. Hybrid telescopes with both transverse and axial field geometry have been developed at IUAC. In former case, silicon detector of area 5×5 cm² with resistive anode (for position sensitivity) [7] was used. In later case, an annular silicon strip detector [8] was used. The detectors were installed at HIRA focal plane and used to perform measurements with $^7\text{Be RIB}$ [9].

4 Detector System for Fission Mass Distribution Experiments

Three pairs (six MWPCs) have been fabricated to perform fission mass distribution and fission fragment-gated neutron multiplicity measurements. Each pair has different area and different design parameters. All the detectors are position sensitive (in two dimension) providing horizontal (X) and vertical (Y) position information. The detectors are placed at folding angles for detecting complementary fission fragments. A small MWPC [1] acting as a start detector for TOF measurements is also used for absolute timing.

The first pair of MWPC [10] has a five-electrode geometry. All electrodes are wire frames (20 μm diameter) with an active area of $20 \times 10 \, \rm cm^2$ and provide, along with position signals, timing signal for time of flight (TOF) measurements and energy signal for the differential energy loss (ΔE) in the active volume. The distance between adjacent wire frames is 3.2 mm and wire pitch is 1.27 mm. The electrode assembly is mounted inside a rectangular aluminium housing (Fig. 4). Entrance window is 1 μm mylar foil. Start MWPC has a four-electrode geometry, all wire frames, with 0.63 mm wire pitch, and 0.5 μm entrance and exit mylar windows. Figure 5 shows the picture of the detection system inside GPSC.

Fig. 4 Assembled MWPC



The timing signals are amplified from in-house fabricated fast timing amplifiers [1], having a gain of 150. The delay line signals are further amplified by an octal fast

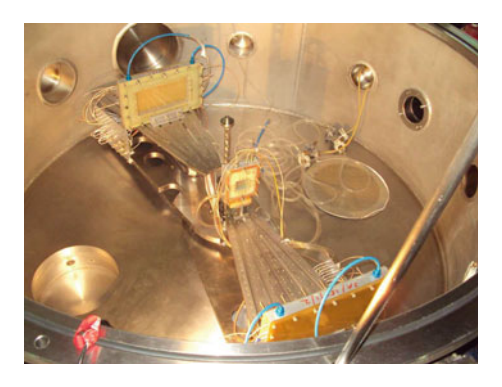


Fig. 5 Detector set-up inside GPSC

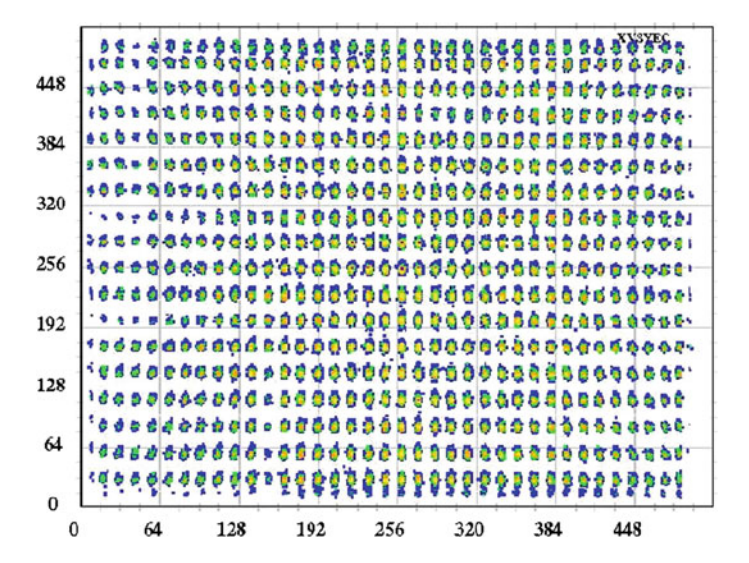


Fig. 6 Masked position plot

NIM amplifier (Phillips 777). Anode pulses are sent to Ortec935/Phillips715 CFD. This signal serves as a start for various time measurements and is used to define the master trigger of data acquisition. A coincidence between signal from anodes of the both MWPCs and the RF (from accelerator) is generated. This logic signal serves as the master trigger. All timing signals such as position signals of both MWPC and their TOF are recorded with respect to this signal. Position signals are fed to Ortec CF8000 unit. The cathode signals are processed using a CSPA developed at IUAC. It has a sensitivity of about 7 mV/MeV (Si equivalent). The output of CSPA is fed to the Ortec 572 shaping amplifier. The MWPC detector was tested with 241 Am α -source for determining its position and timing resolution, as well as its detection efficiency. MWPC was operated with a gas pressure of 5 mbar with +540 and -180 V on anode and cathode, respectively. Rise times were about 10 ns. To

determine the position resolution, a thin mask, with holes of 1 mm diameter and spacing 5.08 mm, was placed between the source and the detector. As shown in Fig. 6, the projection of the mask on the detector is reproduced hole by hole in the X–Y plot. Resolution is \sim 1.1 mm FWHM. The detection efficiency for α 's is \sim 98% with respect to silicon.

Fission mass distribution and mass-gated neutron multiplicity experiments were performed for several systems. Some of the experiments can be found in [3, 11, 12]. To extract TOF information, pulsed beams were used from IUAC tandem with a bunch width of \sim 1.1 ns. The detectors in all these experiments were operated at 3 mbar iso-butane, and +420 and – 180 V on anode and cathode, respectively. Typical anode pulse height signals are >500 mV for fission fragments. Figure 7 shows the correlation between TOF and energy loss with a clean separation between the projectile-like particles, fission fragments and the target recoils for $^{19}\text{F+}$ ^{208}Pb system. For beam-like elastics, a timing resolution of 2.5 ns FWHM is observed. For fission fragments, time resolutions are expected to be better (\sim 1 ns FWHM) because of higher amplitude pulses. The start–stop detector system was used to study the mass distribution of $^{6.7}\text{Li} + ^{238}\text{U}$ system. Rise times were \sim 4 ns and time resolution \sim 400 ps FWHM.

The other two pairs of MWPC [1, 13] have been fabricated using three-electrode geometry. The three electrodes are: an anode wire plane made from $10~\mu m$ diameter wires (X-position), a central cathode foil and strip plane (Y-position). Wire pitch is 0.63 mm in all cases. Thinner wires and reduced pitch give higher avalanche gains. Inter-electrode separation is 3.2 mm. Active area of second pair is $12.5 \times 7.5 \, \mathrm{cm^2}$, and that for third pair is $16 \times 11 \, \mathrm{cm^2}$. The cathode is a 2 μm thick mylar foil aluminized on both surfaces. For 2^{nd} pair, the X-plane is made of 200 wires, and the Y-plane consists of 30 tin-plated copper strips, 2.2 mm wide with a pitch of 2.54 mm, made on a PCB. In X-plane, four wires are grouped together and connected to

Fig. 7 Plot of TOF versus energy loss

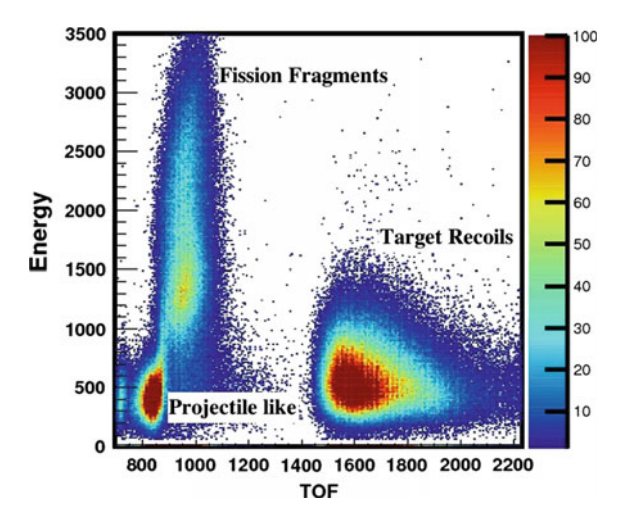


Fig. 8 MWPC with three-electrode geometry

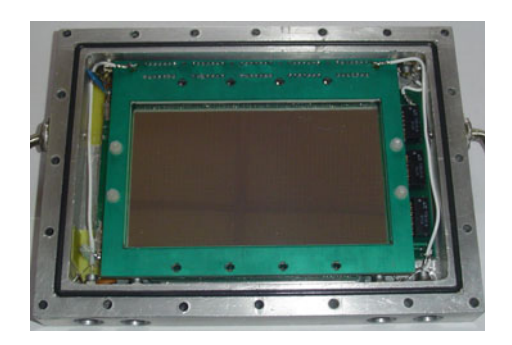
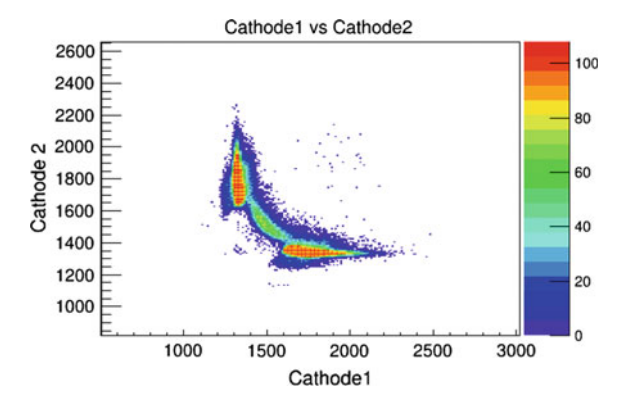


Fig. 9 Mass distribution plot with TOF of one fragment against the other



one tap of delay chip. This design gave a position resolution of \sim 2.5 mm. For third pair of MWPC [13], discrete LC elements [5] or chip capacitor (C) and inductor (L) were used to construct the delay line of 1 ns/tap with an impedance of 50 Ω . This design improved the position resolution by a factor of two (\sim 1.2 mm). The X-plane has a total of 256 wires, and total delay is 128 ns. For Y-plane, there are 88 strips with total delay of 88 ns. Entrance window is 0.9 μ m thick mylar foil. Figure 8 shows an assembled MWPC. Front-end electronics is same as that for first pair of MWPC. They were tested with 241 Am α -source at 7 mbar iso-butane. A negative bias of 600 V was applied on the cathode. Cathode signals, after preamplifier, had an amplitude of \sim 300 mV with rise times \sim 3.5 ns. The detectors were operated at 4 mbar iso-butane and cathode bias of –450 V for fission experiments. Fission- induced neutron multiplicity experiments have been performed for various projectile-target combination [3]. A time resolution of \sim 300 ps was observed for the position-gated elastic events in 28 Si beam. Figure 9 shows the time correlation of both MWPCs for the system 48 Ti + 154 Sm.

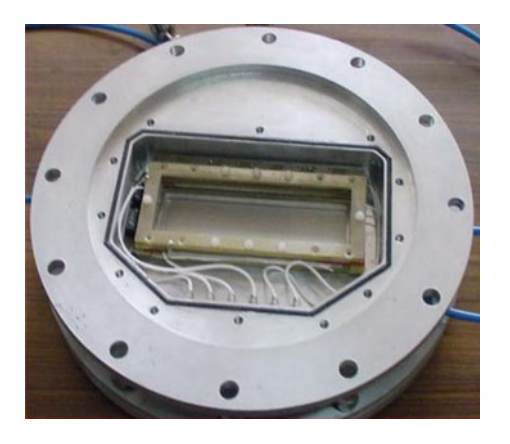
5 Focal Plane Detector Systems for Mass Spectrometers

The first MWPC [14] at HIRA [15] focal plane had a three-electrode geometry. Wire pitch is 1 mm with inter-electrode separation 3.2 mm and wire diameter of 20 μm. This design performed well with heavy ions such as ER, heavy projectiles (silicon and above) but gave very inferior signals for lighter particles such as α 's, Li, Be. With the development of ⁷Be RIB facility of HIRA, it was required to develop MWPC with higher gains in order to detect lighter particles. MWPC [7] with a five-electrode configuration and active area 57 mm × 57 mm was developed for the same. This design provided a factor of 10 higher gains as compared to the earlier design. For mass identification at focal plane of spectrometer with higher detection efficiency/solid angle, the small MWPC was replaced by a larger area MWPC [1] with active area $150 \,\mathrm{mm} \times 50 \,\mathrm{mm}$ (Fig. 10). The detector has been used for the detection of ER and target-like transfer products. Figure 11 shows the position against TOF spectrum for ⁴⁰Ca + ⁷⁰Zn fusion reaction with resolved mass peaks. For HYRA, the focal plane MWPC [1] uses a four-electrode configuration. Design features are identical to that of HIRA focal plane detector except that anode and cathode wires have 0.63 mm pitch, and for the anode 10 µm diameter wires are used for higher gains.

6 Detector System for Multi-nucleon Transfer

A detector system [16] has been developed to carry out experiments such as multinucleon transfer reactions using the GPSC facility at IUAC. The detector system consists of a pair of two-dimensional position sensitive MWPC (with a four-electrode geometry) and a ΔE -E gas IC. Both MWPC have an active area of $5 \times 5 \,\mathrm{cm}^2$.

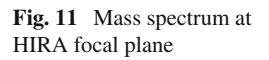
Fig. 10 Assembled MWPC

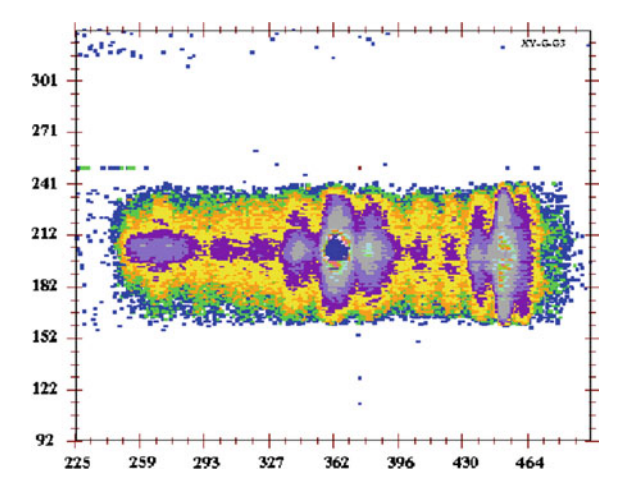


The main design feature of MWPC is the reduced wire pitch of 0.63 mm for all electrodes, giving uniform field and faster charge collection. The usage of 10 μm diameter wire in anode frame results in higher gains. The position resolution of the detectors was determined to be 0.45 mm FWHM, and time resolution was estimated to be 400 ps FWHM. The timing and position signals of the detectors are used for kinematic coincidence measurements and subsequent extraction of their mass and angular distributions. The ionization chamber has a transverse field geometry with segmented anode providing multiple ΔE signals for nuclear charge (Z) identification. The MWPC is placed at kinematically coincident angles. One of the MWPCs (used for detecting projectile-like particles) is followed by an IC. Inter-electrode separation in MWPC is 1.6 mm. Cathode and position wire frames have 20 μm diameter wire. In position electrodes, wires are shorted in pair and connected to one tap of delay chip. Figure 12 shows an assembled MWPC. Entrance window is 0.5 μm mylar. The MWPC is operated at pressures 2–3 Torr.

The gas IC operates in a transverse field mode (Fig. 2). The anode is segmented into four parts with a length of 3 cm for the first part and remaining three having a length of 6 cm each along the beam direction. The active area of IC is 8 cm (horizontal direction) by 4.5 cm (vertical direction/cathode-Frisch grid distance). A reduced field of 2 and 5 V cm $^{-1}$ Torr $^{-1}$ is achieved in cathode-Frisch grid and anode-Frisch grid regions, respectively. The detector is operated with iso-butane gas at pressures 20–70 Torr. Entrance window is 0.5 μm mylar.

Figure 13 shows the experimental set-up inside the GPSC. The front-end electronics for MWPC is same as discussed in Sect. 4. The signals from each anode of the IC are processed using CSPA with a gain of 90 mV/MeV (Si equivalent) followed by Ortec 572 amplifiers. Figure 14 shows a masked position spectrum from MWPC. FWHM of the peaks is \sim 0.5 mm. The detector system was used to study the multi-nucleon transfer process for the ^{28}Si + $^{90,94}\text{Zr}$ system at 120 MeV [17]. Figure 15 shows the $\Delta\text{E-E}$ plot from IC. Here the differential energy loss signal ΔE





from second anode segment is plotted against the total energy. The various reaction products of projectile-like particles (Si in this case) are well separated according to their Z.

7 Hybrid Telescope Array for Reaction Dynamics

This array [18] has been developed at IUAC for the study of reaction mechanisms around Coulomb barrier. The hybrid detector module is a combination of gas (ΔE) and silicon detector (stopping). They have been developed for heavy ion detection in fission angular distribution [19] and quasi-elastic scattering experiments. Currently, the array consists of 16 such telescopes.

Fig. 12 Assembled MWPC

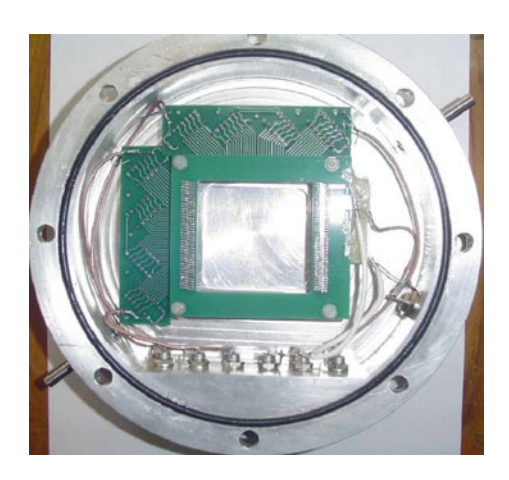


Fig. 13 Detector set-up inside GPSC



Figure 3 shows the cross section of the hybrid telescope. It consists of a gas ionization chamber (IC), operating in axial field geometry mode, followed by a silicon detector. The IC is composed of three wire frames of active diameter 20 mm. The wire frames are a central anode sandwiched between two cathodes. Inter-electrode separation is 9 mm, and wire pitch (20 μ m diam.) is 1 mm. The two cathodes are grounded, and signals are from anode by applying positive voltage with a reduced field of about 2 V cm⁻¹ Torr⁻¹. The electrodes are housed inside a cylindrical stainless steel tube. The detector is operated with iso-butane gas at pressures 20–75 Torr. The entrance window is 0.9 μ m mylar. Figure 16 shows the detector set-up inside the GSPC. Thirteen telescopes are used in this set-up. One group with four telescopes was mounted in a ring at 170° with respect to beam direction. They detect the back-scattered projectile-like particles for quasi-elastic barrier distribution. Remaining detectors are at forward angles (160° to 30°).

Custom-designed CSPA was developed for the telescopes. Two versions were developed: one for gas detector with a gain of 90 mV/MeV (Si equivalent) and other for silicon detectors with a gain of 3.5 mV/MeV. The CSPA output is fed to Mesytec STM16+ amplifier followed by Phillips 7164H ADC for digitization. Figure 17 shows a Δ E-E plot for the 19 F + 194 Pt system. Fission fragments are well separated from projectile-like particles. The detector system has been used to study quasi-elastic barrier distribution for system 28 Si + 154 Sm [20].

8 CsI based Charged Particle Array

A detector system using CsI scintillators [21] has been developed for the detection of light-charged particles to investigate fusion–fission dynamics. The CsI scintillators

Fig. 14 X-position distribution

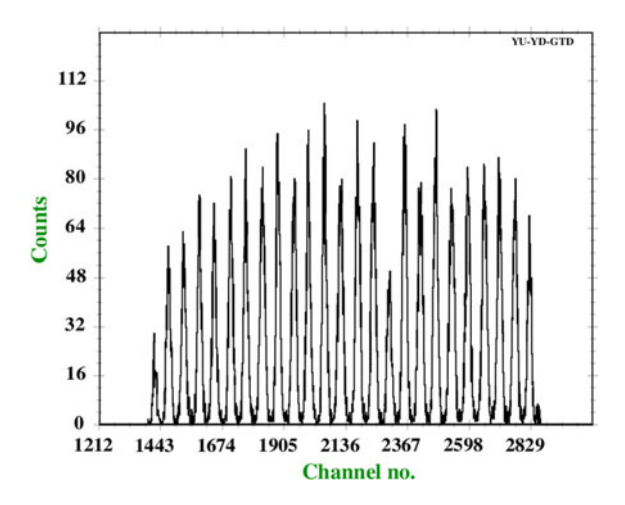


Fig. 15 ΔE -E plot of IC

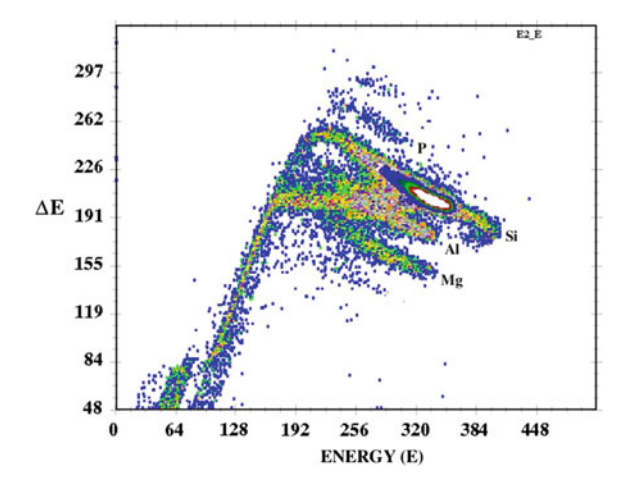




Fig. 16 Telescope array in GPSC

are read by photodiodes. They are used to measure the emission energy of light-charged particles such as protons and α -particles. The main feature of the array is its compact and simple high-density front-end electronics which includes custom-developed low noise CSPA, NIM differential drivers and Mesytec amplifiers with two different time constants for particle identification using ballistic deficit technique. The crystals ($20 \times 20 \times 3 \text{ mm}^3$) are read out by $10 \times 10 \text{ mm}^2$ photodiode. The assembled units, model no. V 20 PM 3/10-Cs, have been supplied by Scionix.

CSPA has a gain of 90 mV/MeV (Si equivalent). The output of CSPA, through a differential driver unit, is fed to two 16 channel STM-16+ unit from Mesytec, one with a shaping time constant of 3 μs (for energy) and the other with 0.5 μs (for particle identification). Using the two different shaping times, ballistic deficit technique was implemented for pulse shape discrimination (PSD). The detector was tested with γ -ray and α source. A resolution of 9.5 and 5.8% is observed for 662

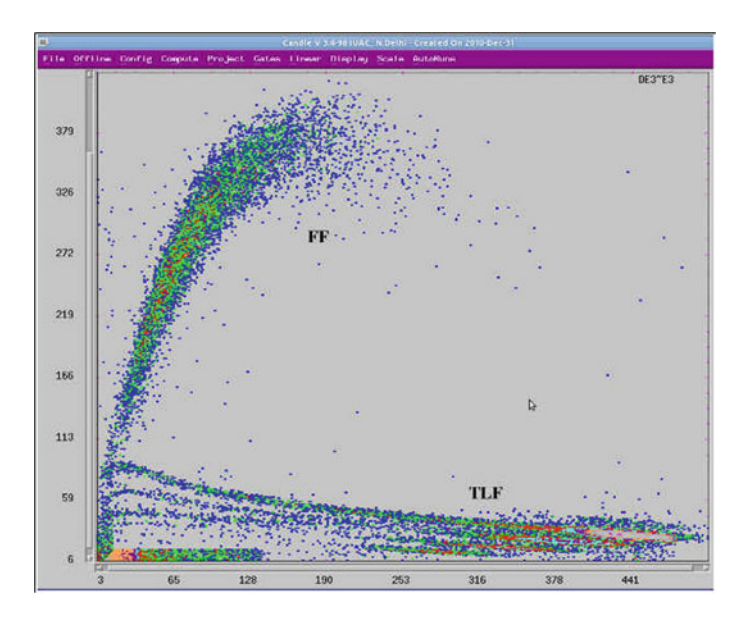


Fig. 17 ΔE -E plot from telescope

keV and 1.33 MeV γ -ray lines, respectively. The resolution for an 8.37 MeV α -line (229 Th) is about 250 keV. The detector system was used to study pre- and post-scission-charged particle multiplicity for the system 16 O + 194 Pt at 100 MeV. The CsI detectors were assembled as quads in 2 \times 2 configuration (Fig. 18). The four detectors were mounted on a common PCB motherboard with CSPA mounted on its back. Figure 19 shows the scatter plot displaying correlation between energy and PSD.

Fig. 18 Assembled CsI units with integrated CSPA



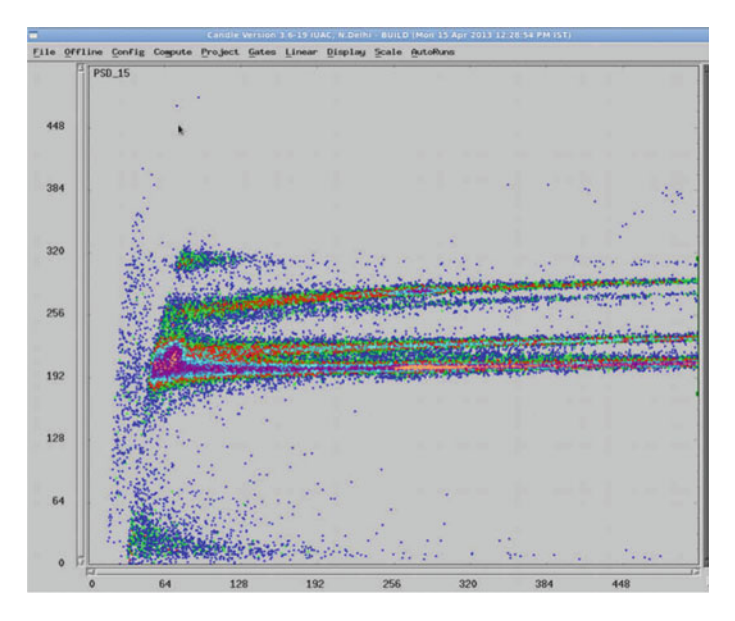


Fig. 19 Plot of PSD against energy

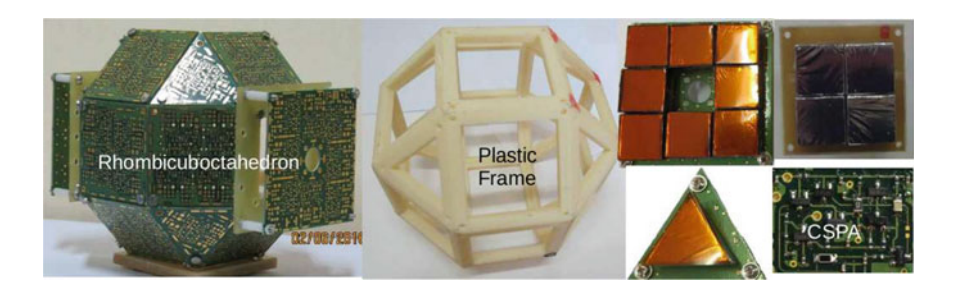


Fig. 20 Structure of the CsI ball for nuclear reactions

Efforts are on to have CsI array as an ancillary detector for NAND and γ -spectroscopy. Figure 20 shows the prototype rhombicuboctahedron structure. The CSPA boards integrated with CsI crystals will be mounted on a plastic frame. Each face of the structure will have four crystals. Front and back face will have eight crystals. The eight corners will have triangular-shaped crystals. A total of 80 detectors will be there having a solid angle coverage of 85% of 4π .

9 Annular Parallel Plate Proportional Counter (APPPC)

The main motive of developing this detector system [22] is to perform Coulomb excitation (Coulex) experiments using particle- ν coincidence technique. The detector system has been integrated with the existing GDA facility at IUAC to perform Coulex measurements with germanium detectors. APPPC provides information about the scattering angles of the reaction products which along with TOF (velocity) information is used for correcting Doppler energy shift of events coming from in-flight decay of reaction products. The detector has a two-electrode geometry: a cathode and an anode. Cathode is segmented to provide azimuthal angle (ϕ) , whereas the anode is segmented to provide polar angles (θ) of the reaction products. The inner and outer active radius is 2.5 and 12.5 cm, respectively, with angular coverage 12° to 45°. Cathode is fabricated using a 1.5 μm aluminized mylar foil stretched on a 3.2 mm thick PCB. Figure 21 shows the schematic layout of the detector system. The foil is segmented into a cake-like structure with 16 sectors so as to provide ϕ information with an angular pitch of 22.5°. The anode is made on PCB, segmented into two halves with each half having tracks etched in the form of concentric rings as shown in Fig. 21. Each ring has a width of 1 mm. These rings are interconnected by delay line. Each half of the anode segment is perfectly aligned to cover eight cathode sectors each, dividing the detector into equal right and left halves. Inter-electrode separation is 3.2 mm. The entire electrode assembly is housed inside an aluminium chamber (Fig. 22). The detector is isolated from vacuum with a 2 µm mylar foil. The detector has central through hole of 2 cm for beam passage. APPPC provides 20 timing signals: four for delay line anode and 16 for the cathode. The timing signals are extracted using in-house fabricated fast timing amplifiers (FTAs) [1] followed by Ortec CF8000 CFD units. The logic outputs are fed to Phillips 7186 TDC. The individual CFD outputs in TDC provides hit pattern to identify the cathode segment. The detector is operated at 10 mbar iso-butane with -500 V on cathode. The detector has been used to perform Coulex measurements, using 175 MeV ⁵⁸Ni on various isotopes of Sn,Te [23] and Ba. Four clover germanium detectors were used for γ detection.

Fig. 21 Schematic of the detector system for Coulex studies

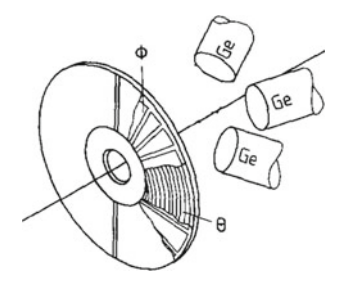


Fig. 22 Assembled APPPC



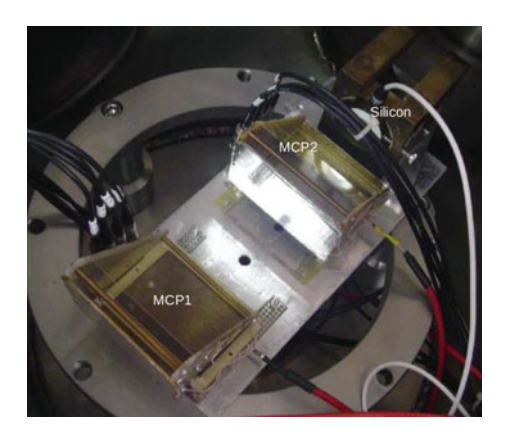
10 Charged Particle Detectors for NUSTAR LEB

In the scope of future slowed down beam campaign of low energy branch (LEB) in NUSTAR, major developments have been initiated for a charged particle detector setup for the slowed down beam studies. The detection system [24] will consist of beam tracking detectors preceding the secondary target and a particle identification system for identifying the beam/secondary reaction products. The high-energy beam from super fragment separator (SFRS) will be slowed down in a degrader to Coulomb energies. The resultant beam is poor in quality in terms of energy spread (3–10 MeV/u), angular spread and spot size (\sim 5 cm FWHM).

The beam tracking detectors will determine trajectory, mass and energy of all species using position information and time of flight (TOF) technique. This can be achieved by employing thin transmission type, position sensitive fast timing detectors. It is desirable to have detectors which can provide timing resolutions $\sim\!100$ ps, position resolution $\sim\!1$ mm, and have count rate handling capabilities $\sim\!10^6$ pps. TOF systems based on micro-channel plates (MCPs) and/or MWPC are the best solution. Feasibility studies were carried out by performing measurements with MCP detectors. They [25] are based on secondary emission of electrons knocked out by the detected particle from the conversion foil. Two MCP detectors were tested with active area 60×40 mm². Figure 23 shows the picture of the set-up with the MCP detectors. Their timing characteristics were evaluated by setting a TOF between them backed by a silicon detector for energy measurement. The flight path was set at 12 cm. The system was exposed to 229 Th α -emitter. Figure 24 shows the plot between TOF and energy from silicon detector. A timing resolution of $\sim\!160$ ps was observed for the 8.38 MeV transition.

The secondary target will be surrounded by array of charged particle detectors for identifying the secondary reaction products. The particle identification system requires double-sided silicon strip detectors (DSSD) based TOF and ΔE -E telescopes. TOF in combination with energy is a very powerful tool for mass identification. Totally depleted thin silicon detectors (40 μ m) can give time resolutions as good as 100 ps and energy resolution \sim 100 keV. A major constraint with SSDs is

Fig. 23 MCP-TOF set-up



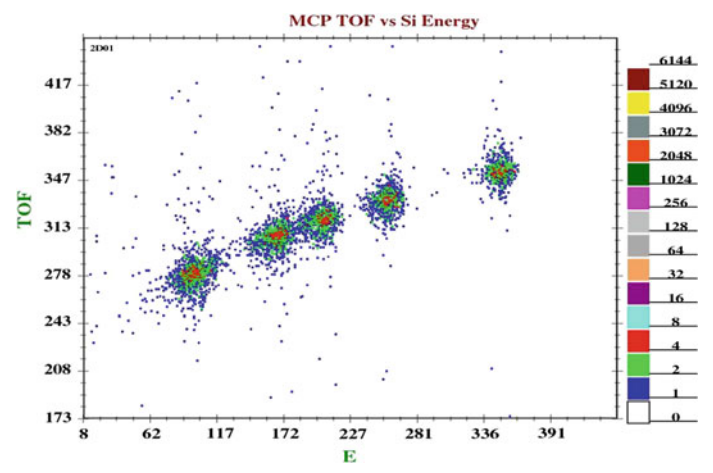


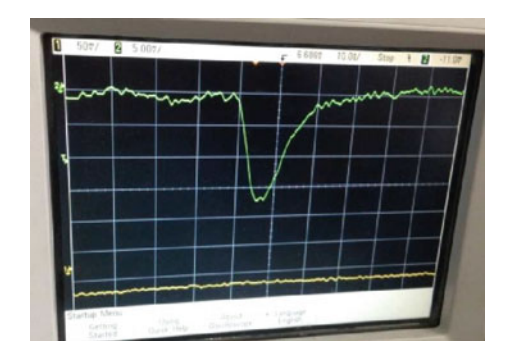
Fig. 24 TOF against energy for α 's from ²²⁹Th

the missing high-density multi-channel preamplifiers which can provide both fast timing and energy. Some developments and tests have been performed at GSI as well as IUAC. A custom-designed 16 channel FTA [26] has been developed. The 16 channels were assembled on an 8×5 cm² FR4 board (Fig. 25). A 34 pin (17 pairs) FRC socket is provided on the board compatible with DSSSD FRC pins. DSSSD is directly plugged into this socket thus eliminating cables between FTA and DSSSD. The timing outputs are driven by miniature coaxial cables (50 Ω) to a specially designed flange, having sealed PCB-based FRC feed through. Thereafter the signals are fed to Phillips 715 CFD followed by TDC. FTA extracts timing signal from the *p*-side of DSSSD. To extract energy information, the *n*-side signals are fed to Mesytec CSPA MPR-32 and shaping amplifier STM16 combination. The timing performance of the FTA with DSSSD (40 μ m) has been evaluated in GPSC at IUAC. TOF of light and

Fig. 25 Assembled FTA board



Fig. 26 α signal from DSSSD



heavy ions was measured with respect to a MCP detector. Rise time of 4 ns (Fig. 26) and a resolution of $\sim\!800$ ps FWHM (pixel gated) have been observed for 5.48 MeV α 's. An elastic scattering experiment was performed by bombarding a 197 Au target with 122 MeV 28 Si beam. The detector system was installed at 60°. An average pixel resolution of 200 ps FWHM was observed.

Acknowledgements We acknowledge the support of our group members P. Sugathan, N. Madhavan, T. Varughese, S. Nath, R. Kumar, K. S. Golda, J. Gehlot, N. Saneesh, M. Kumar, R. P. Singh, E. T. Subramaniam, S. Venkataramanan, R. Ahuja, A. Kothari, K. Singh, P. Barua and Jimson Zacharias. We also acknowledge the encouragement and support from our Drs. A. Roy, J. J. Das, S. K. Datta, D. Kanjilal, R. K. Bhowmik and G. K. Mehta. We thank the accelerator group for providing good quality beams for our experiments. We thank our collaborators Drs. B. R. Behera, S. K. Mandal, P. V. M. Rao, R. G. Thomas, B. K. Nayak, A. Saxena and Prof. H. J. Wollersheim. We thank and acknowledge our students Hardev Singh, S. Kalkal, R. Sandal, Varinderjit Singh, S. Appanababu, E. Prasad, G. Mohanto, Maninder Kaur, M. Saxena, Gurpreet Kaur, Ruchi Mahajan, K. Kapoor, M. Thakur, Priya Sharma, T. Banerjee and A. Yadav.

References

- 1. A. Jhingan, Pramana J. Phys. 85, 483 (2015)
- 2. N. Madhavan et al., Pramana J. Phys. 75, 317 (2010)
- 3. P. Sugathan et al., Pramana J. Phys. 83, 807 (2014)
- 4. http://www.iuac.res.in/
- 5. S. Beghini et al., Nucl. Instrum. Methods A **551**, 364 (2005)
- 6. A. Breskin et al., Nucl. Instrum. Methods A 221, 363 (1984)
- 7. A. Jhingan et al., Nucl. Instrum. Methods A **526**, 376 (2004)
- 8. A. Jhingan et al., Nucl. Instrum. Methods A **539**, 269 (2005)
- 9. J.J. Das et al., Nucl. Instrum. Methods B **241**, 953 (2005)
- 10. A. Jhingan et al., Rev. Sci. Instrum. **80**, 123502 (2009)
- 11. C. Yadav et al., Phys. Rev. C 86, 034606 (2012)
- 12. R. Dubey et al., Phys. Lett. B 752, 338 (2016)
- 13. A. Jhingan et al., Proc. DAE-BRNS Symp. Nucl. Phys. **60**, 936 (2015)
- 14. D.O. Kataria et al., Nucl. Instrum. Methods A 372, 311 (1996)
- 15. A.K. Sinha et al., Nucl. Instrum. Methods A 339, 543 (1994)
- 16. A. Jhingan et al., Nucl. Instrum. Methods A 745, 206 (2014)
- 17. S. Kalkal et al., Phys. Rev. C **85**, 034606 (2012)
- 18. A. Jhingan et al., Proc. DAE-BRNS Symp. Nucl. Phys. **59**, 830 (2014)
- 19. T. Banerjee et al., Phys. Rev. C 94, 044607 (2016)
- 20. G. Kaur et al., Phys. Rev. C 94, 034613 (2016)
- 21. A. Jhingan et al., Nucl. Instrum. Methods A **786**, 51 (2015)
- 22. A. Jhingan et al., Proc. DAE-BRNS Symp. Nucl. Phys. **61**, 966 (2016)
- 23. M. Saxena et al., Phys. Rev. C 90, 024316 (2014)
- 24. J. Vesic et al., Proc. DAE-BRNS Symp. Nucl. Phys. **61**, 958 (2016)
- 25. E.M. Kozulin et al., Exp. Tech. 51, 44 (2008)
- 26. A. Jhingan et al., Proc. DAE-BRNS Symp. Nucl. Phys. **61**, 964 (2016)

PET: A High Threshold Nuclear Track Detector (NTD) for Rare Event Search

Atanu Maulik

Abstract Search for rare events like strangelets or monopoles in cosmic rays or in particle accelerators is an active field of research. Nuclear Track Detectors (NTDs) are often the detectors of choice in such searches owing to their natural thresholds of registration which can suppress large parts or even the entirety of the background. A low-cost commercially available polymer in wide use as a packaging and bottling material, identified as Polyethylene Terephthalate (PET), was found to very effective as a NTD with detection threshold much higher than many other NTDs in wide use like CR-39, Lexan. Systematic studies were carried out to characterize and calibrate PET using ion beams from accelerators. In addition, pilot studies were carried out at various high-altitude locations where PET films were given open-air exposures. In this article, some of the results of those studies will be presented.

1 Introduction

Various phenomenological models [1] developed over the years have raised the possibility that Strange Quark Matter (SQM), containing roughly equal number of up, down, and strange quarks constitute the true ground state of quantum chromodynamics. Such studies [2, 3] have also hinted that even small nuggets of SQM, called strangelets, may also be stable. SQM, if they exist, is most likely to be found in the core of dense stellar objects like neutron stars, where matter density can exceed the nuclear matter density and the conversion of two-flavor to three-flavor quark matter can take place. Such stars containing SQM can form part of a binary system and as such can undergo mergers and collisions releasing SQM in their surroundings in the form of strangelets. Such strangelets will have a small positive charge (and hence anomalous Z/A ratio $\ll 1/2$ compared to ordinary nuclei) and can then be accelerated like other cosmic ray nuclei through the usual mechanisms like Fermi acceleration in supernova shocks. So one good place to look for such a new form of

A. Maulik (⊠)

Center for Astroparticle Physics and Space Science, Bose Institute, Kolkata 700 091. India

Koikata 700 091, India

e-mail: atanu.maulik@jcbose.ac.in

50 A. Maulik

matter is cosmic rays, and the search for strangelets in cosmic rays remains an active area of research [4].

Various authors have estimated the possible flux of such strangelets in the solar neighborhood [5–7]. Other competing models exist when it comes to the passage of strangelets through the earth's atmosphere. According to the model by Banerjee et al. [8, 9], an initially small strangelet will grow in size during their passage through the atmosphere by preferentially absorbing neutrons over protons (protons being Coulomb repelled) while interacting with nuclei of air molecules. Even the most conservative assumptions of this model predict a strangelet flux in excess of $\sim 10^{-12}$ cm⁻² s⁻¹ sr⁻¹ at mountain altitudes (~ 3000 m). Another propagation model by Wu et al. [10] also strongly hints at the presence of strangelets in cosmic rays at mountain altitudes or possibly even at sea level. In sharp contrast, the propagation model due to Wilk et al. [11, 12] conjectures that the mass of an initially large strangelet decreases rapidly through collisions with air molecules and eventually the strangelet evaporates into neutrons. Under this scenario, no significant flux of strangelets is expected at mountain altitudes. This fact offers an opportunity for subjecting the contrasting strangelet propagation models to experimental test through the deployment of large area detector arrays at high mountain altitudes, provided a suitable detector material is chosen which enables the efficient suppression of the low-Z background coming from cosmic ray secondaries, atmospheric radon alpha particles, etc.

Ever since Dirac introduced the concept of the magnetic monopole to explain the quantization of electric charges [13], the idea has intrigued the physics community. More recent research involving GUT and superstring theories also offer compelling theoretical arguments for the existence of monopoles [14, 15]. So search for monopoles in cosmic rays as well as particle accelerators also remains an area of active research [16, 17].

One of the most favored detector types when it comes to the search for rare particles like strangelets and monopoles is the Nuclear Track Detectors (NTDs). This is because NTDs offer huge advantages in the searches for rare, heavily ionizing, massive particles against a large low-Z background. In this article, a brief introduction to NTDs will be given. Also, the results of studies carried out on a particular brand of inexpensive, commercially available polymer, identified as Polyethylene Terephthalate (PET), to judge its suitability as NTD for rare event search, will be presented.

2 Nuclear Track Detectors (NTD)

Nuclear Track Detectors (NTDs) like CR-39, Makrofol, Lexan have been in use for decades for charged particle detection [18, 19]. NTDs are basically dielectric solids. When a charged particle passes through such material, they lose energy, with the energy loss dE/dx related to Z/β (where Z is the charge and $\beta = v/c$ the measure of the velocity of the impinging particle) as described by the Bethe equation [20].

For polymer materials like CR-39, Makrofol, Lexan, if the energy deposited by the impinging charged particle is above a certain threshold, which is different for different materials, then the polymer chains can break, leaving behind a permanent damage trail along the path of the passing particle. Those damaged regions naturally become chemically more reactive compared to the undamaged portions. On being treated with suitable chemical reagents (e.g., aqueous solution of NaOH), material along the damage trails are etched out at a faster rate, called the track etch rate (V_T) , compared to the rate of etching of the undamaged bulk material, referred to as the bulk etch rate (V_R) . Conical etch pits are formed as a result, and the dimensions of such etch cones for a given etching duration are a function of energy loss dE/dx. Figure 1 shows a typical etch cone as seen through an optical microscope. By studying the geometry of such etch cones resulting from known ions of known energies, the ratio of track and bulk etch rates (V_T/V_R) , called the charge response, can be determined and can be related to the corresponding dE/dx (as obtained using the standard Monte Carlo code SRIM [21]). This gives us the calibration curve for a particular NTD. Armed with the calibration curve, one can then try to identify any unknown ion from the corresponding etch pit. Also, the range (R) of the particle inside the material gives the measure of its energy.

It is the existence of natural thresholds of registration, which makes NTDs a detector of choice, when it comes to the search for rare, heavily ionizing, massive particles. Because the presence of a huge low-Z background is often the most significant challenge in such rare event search, the choice of a suitable material as a NTD has the potential to significantly reduce or even eliminate the entirety of the background. For example, CR-39 will not record tracks due to muons, pions, kaons, electrons, or positrons. Since these are the particles which constitute the most significant part of a cosmic ray shower, CR-39 can be an ideal choice of detector material for an experiment interested in only the heavy ion component present in cosmic rays.

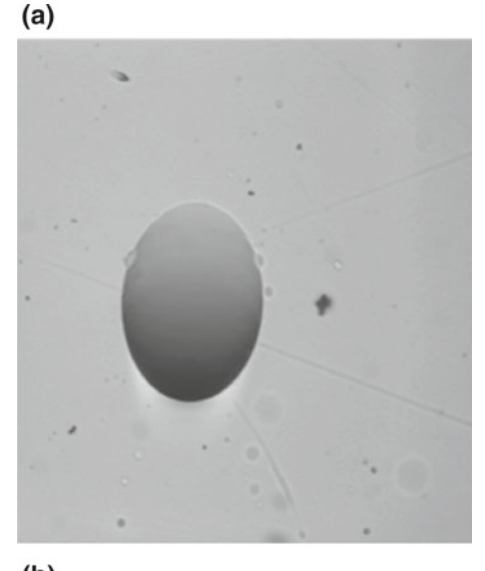
Also, since NTDs are passive detectors, i.e., they do not give real-time signals and hence do not require any electronic data acquisition system, they offer significant cost and logistical advantages when it comes to the deployment of large area arrays at remote locations. So for any experiment aiming for rare event search through the deployment of large area arrays at high mountain altitudes, NTDs offer an ideal cost-effective solution.

3 Signature of Strangelets and Monopoles in NTD

Phenomenological models predict that the strangelets will have small charges but arbitrarily large baryon numbers and hence highly skewed Z/A ratios compared to ordinary nuclei. So discrimination between any normal heavy ion track and a strangelet track can be done by determining the V_T/V_B ratios and hence the dE/dx values at various points along the track, as the rate of energy loss (dE/dx) will be different for normal cosmic ray heavy ions as compared to strangelets with much larger baryon numbers.

52 A. Maulik

Fig. 1 A typical etch cone seen with the microscope focussed on a the surface showing the etch pit opening and b focussed at a certain depth inside the plastic showing the conical profile of the etch pit. The sizes of the image frames are $67~\mu m \times 67~\mu m$



(b)

Monopoles, on the other hand, would be distinguishable by the fact that their ionization rate would remain roughly constant throughout their passage as opposed to ordinary nuclei for which dE/dx would increase as they slowdown in the plastic. So the dimensions of the etch pit openings for a monopole track will remain roughly constant throughout the NTD stack, whereas for ordinary heavy nuclei, the track dimensions increase as we approach the end of the track.

4 Polyethylene Terephthalate (PET) as NTD

Standard NTDs like CR-39, Makrofol have been in use for many years, and they have been used before in rare event search experiments [16, 17]. They have Z/β detection thresholds lying in the range 6–60. This is high enough to eliminate the background coming from lighter particles like muons, pions, electrons but not high enough to eliminate the background due to protons and alpha particles. This presents significant challenges in rare event search in cosmic rays at mountain altitudes as radon alphas are a significant background in such experiments. The usual search strategy in such experiments calls for the hard etching of the top layer of a NTD stack. This can cause the etch cones formed at both the top and bottom surfaces of the topmost NTD film, caused by the passage of a highly energetic through going particle, to merge and form a hole. Any such hole found in the top layer can then serve as an offline trigger, prompting the etching and scanning of subsequent layers. But the problem with such a strategy is that it constrains the parameter space that can be probed, as any exotic particle not having the energy to penetrate multiple layers will evade detection.

A particular brand of low-cost commercially available polymer, identified through chemical analysis and FTIR spectroscopy as Polyethylene Terephthalate (PET) with chemical formula $[(C_{10}H_8O_4)_n]$ (Fig. 2 shows the structure of PET monomer), widely used by the packaging industry, was investigated to test its suitability as a NTD.

Systematic investigations were carried out, wherein PET films of thickness 90 μm were irradiated with various heavy ion beams from particle accelerators at REXISOLDE, CERN; GSI, Darmstadt; IUAC, New Delhi; IBL, IOP, Bhubaneswar. The exposed PET samples were then etched in 6.25 N NaOH solution at a temperature of 55.0 \pm 0.5 °C, which was found to be the ideal etching condition for PET. The track measurements were then carried out with Leica DMR4000 optical microscopes interfaced with computers for image analysis, and the calibration curve for PET was obtained [22, 23]. The PET samples were recently irradiated with 3.77 MeV/n 35 Cl ions at IUAC, New Delhi. The PET films were cut into 5 cm \times 5 cm pieces, mounted on aluminum holders, and placed inside the GPSC for the purpose of this experiment as shown in Fig. 3.

The updated calibration curve incorporating the new data point due to 35 Cl is given in Fig. 4. The fitted line is given by $y = a + bx + cx^2$, where $a = -0.54 \pm 0.33$, $b = 0.28 \pm 0.01$, and $c = -(0.12 \pm 0.009) \times 10^{-2}$ where the parameter errors represent 95% confidence level.

Such studies have also shown [24] that PET has a charge resolution of ± 1 and an energy resolution of 10% in the energy regime (\sim few MeV/n) investigated. Most

Fig. 2 Structure of PET monomer

54 A. Maulik



Fig. 3 PET films mounted on aluminum holders and placed on two movable arms inside the general purpose scattering chamber

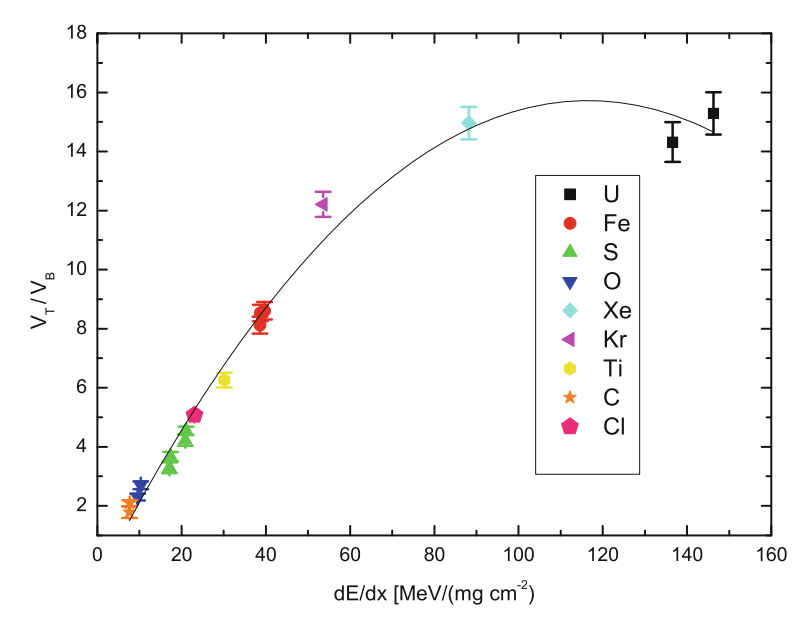


Fig. 4 Updated calibration curve for PET

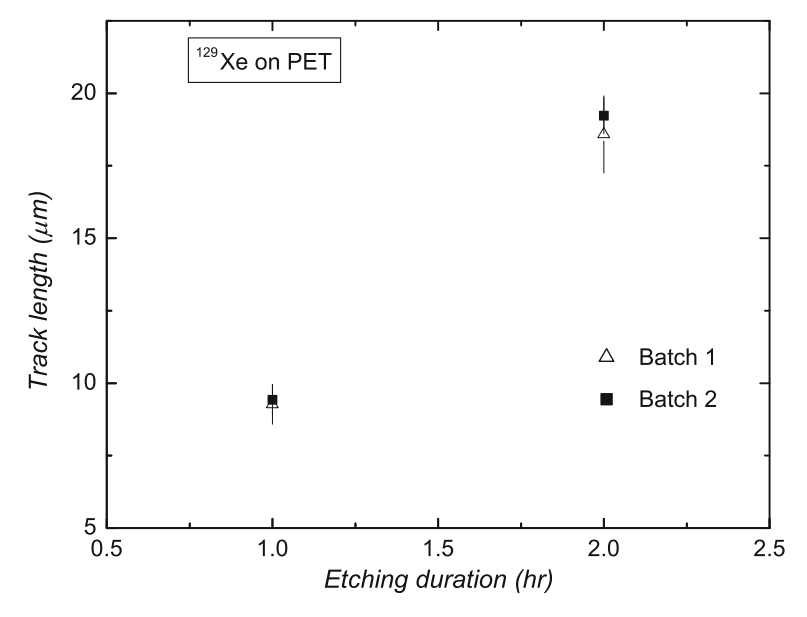


Fig. 5 Comparison of track length measurements for ^{129}Xe on PET from two different batches for two different etching durations

importantly, it was established [25] that PET has a much higher detection threshold $(Z/\beta \sim 140)$ compared to CR-39, Lexan, etc. So PET will not record tracks due to proton or alpha particles, and hence, PET used as NTD will be even better than CR-39 when it comes to background rejection.

Since PET films were commercially procured, it was essential to check whether the charge response of different batches of PET is remaining consistent. With that aim, the charge response of PET films procured 4 years apart was investigated. 2.82 MeV/n ¹²⁹Xe beams from REX-ISOLDE, CERN were utilized for this purpose. As shown in Figs. 5 and 6, the measured lengths and diameters of the etch pits on two different batches of PET films display a good overlap, showing the consistency of charge response.

Another significant advantage of PET is its low cost (by a factor of more than 1000) compared to CR-39. Cost considerations become particularly important when it comes to the deployment of large area arrays.

5 Pilot Studies at High Mountain Altitudes

Apart from experiments carried out to study the charge response of PET at various accelerator facilities, pilot studies were carried out where PET films, as well as CR-39 detectors, were given open air exposures at various high-altitude locations in

56 A. Maulik

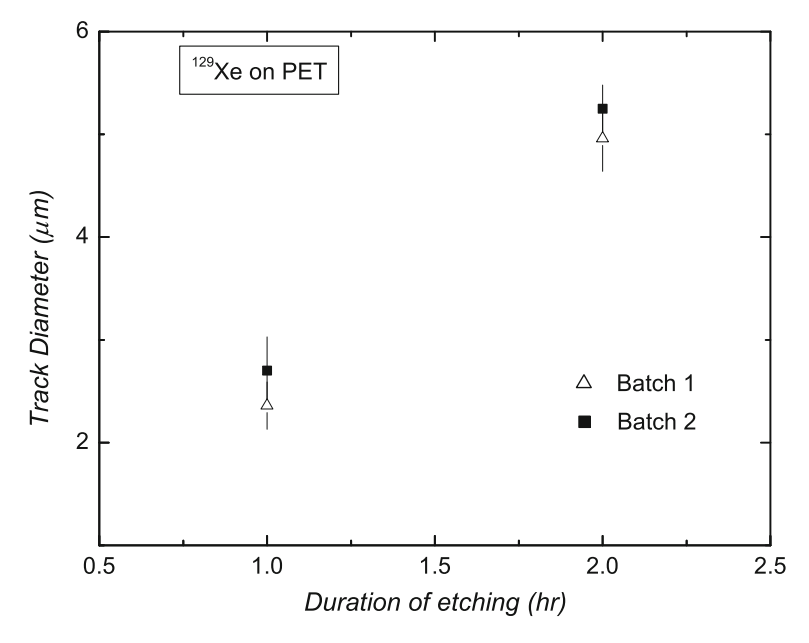


Fig. 6 Comparison of track diameter measurements for ^{129}Xe on PET from two different batches for two different etching durations

| 7D 11 4 | El 11 CD 00 1DEE 11 11 11 11 11 | |
|---------|--|----|
| Table I | Flux recorded on CR-39 and PET at three high-altitude location | ns |

| Place | Flux on CR-39 (cm ⁻² s ⁻¹ sr ⁻¹) | Flux on PET (cm ⁻² s ⁻¹ sr ⁻¹) |
|------------|---|--|
| Darjeeling | 6.0×10^{-4} | $<1.0 \times 10^{-11}$ |
| Ooty | 1.3×10^{-4} | $<1.0 \times 10^{-11}$ |
| Hanle | 4.6×10^{-4} | $<1.0 \times 10^{-11}$ |

India like Darjeeling (2200 m a.m.s.l), Ooty (2200 m a.m.s.l), and Hanle (4500 m a.m.s.l) for durations ranging from a few months to a few years. The main aim was to investigate the background recorded with the two types of detectors.

As shown in Table 1, the CR-39 is recording a large background coming from protons, radon alphas, neutron recoil tracks, etc. But no comparable track was found so far on PET films. This is in keeping with expectations, as PET detectors, with higher detection threshold compared to CR-39, do not record proton or alpha particle tracks and heavier ions are not expected to be present in any appreciable quantity in cosmic rays at these depths in the atmosphere. This clearly demonstrates the advantages of PET films over the more widely used CR-39 when it comes to rare event search in cosmic rays. The expectation is that the very high detection threshold of PET will suppress the entire low-Z background, so much so, that the observation of even a single track can indicate the presence of some unusual event.

An array of PET detectors covering an area of 100 sq.m. for a total exposure duration of one year will allow us to reach a sensitivity of $\sim 10^{-13}$ cm⁻² s⁻¹ sr⁻¹ and put to test competing models of strangelet propagation through the atmosphere. Since the flux of heavy ions from primary cosmic rays at mountain altitudes (~ 3000 m) is estimated to be $\sim 10^{-14}$ cm⁻² s⁻¹ sr⁻¹ [26], heavy ions are not expected to constitute a significant background for the purpose of strangelet search with PET detectors.

6 Conclusion

This research has shown that PET can be effectively used as a high threshold NTD, offering several advantages over the more widely used CR-39 when it comes to the search for rare events in cosmic rays at high mountain altitudes.

Acknowledgements The author would like to acknowledge the contributions of other group members, R. Bhattacharyya, S. Dey, Sanjay K. Ghosh, Sibaji Raha, and Debapriyo Syam. The work is funded by Intensification of Research in High Priority Areas Project (IRHPA) (IR/S2/PF-01/2011 dated 26.06.2012) of the Science and Engineering Research Council (SERC), DST, Government of India, New Delhi.

References

- 1. E. Witten, Phys. Rev. D 30, 272 (1984)
- 2. E. Farhi, R.L. Jaffe, Phys. Rev. D 30, 2379 (1984)
- 3. J. Madsen, Phys. Rev. D 50, 3328 (1994)
- 4. O. Adriani et al., Phys. Rev. Lett. 115, 111101 (2015)
- 5. J. Madsen, Phys. Rev. D 71, 014026 (2005)
- 6. S. Biswas, J.N. De, P.S. Joarder, S. Raha, D. Syam, Phys. Lett. B 715, 30 (2012)
- S. Biswas, A. Bhadra, J.N. De, P.S. Joarder, S. Raha, D. Syam, PoS ICRC2015 (2016) 504
- 8. S. Banerjee, S.K. Ghosh, A. Mazumdar, S. Raha, D. Syam, Astrophys. Space Sci. 274, 655 (2000)
- 9. S. Banerjee, S.K. Ghosh, S. Raha, D. Syam, Phys. Rev. Lett. 85, 1384 (2000)
- 10. F. Wu, R.-X. Xu, B.-Q. Ma, J. Phys. G: Nucl. Part. Phys. **34**, 597 (2007)
- 11. G. Wilk, Z. Wlodarczyk, J. Phys. G 22, L105 (1996)
- 12. G. Wilk, Z. Wlodarczyk, Heavy Ion Phys. 4, 395 (1996)
- 13. P.A.M. Dirac, Phys. Rev. **74**, 817 (1948)
- 14. G. Hooft, Nucl. Phys. B **79**, 276 (1974)
- 15. A. Rajantie, Contemp. Phys. **53**, 195 (2012)
- 16. S. Balestra et al., [SLIM Collaboration], Eur. Phys. J. C 55, 57 (2008)
- 17. B. Acharya et al., [MoEDAL Collaboration], Int. J. Mod. Phys. A 29, 1430050 (2014)
- R.L. Fleischer, P.B. Price, R.M. Walker, Nuclear Tracks in Solids (University of California Press, Berkeley, 1975)
- S.A. Durrani, R.K. Bull, Solid State Nuclear Track Detection Principles, Methods and Applications (Pergamon Press, Oxford, 1987)
- 20. G.F. Knoll, Radiation Detection and Measurement, 3rd edn. (Wiley, Hoboken, 2000)
- J.F. Ziegler, J.P. Biersack, The stopping and range of ions in matter (SRIM Computer Code), Version: 2003.26 (2003)

58 A. Maulik

 D. Bhowmik, S. Dey, A. Maulik, S. Raha, S. Saha, S.K. Saha, D. Syam, Nucl. Instr. Methods B 269, 197 (2011)

- S. Dey, D. Gupta, A. Maulik, S. Raha, S.K. Saha, D. Syam, J. Pakarinen, D. Voulot, F. Wenander, Astropart. Phys. 34, 805 (2011)
- 24. S. Dey, A. Maulik, S. Raha, S.K. Saha, D. Syam, Nucl. Instr. Methods B **336**, 163 (2014)
- 25. R. Bhattacharyya, S. Dey, S.K. Ghosh, A. Maulik, S. Raha, D. Syam, Nucl. Instr. Methods B 370, 63 (2016)
- 26. P.K.F. Grieder, Cosmic Rays at Earth (Elsevier Science, Amsterdam, 2001)

Detectors for Non-accelerator Particle Physics

B. Satyanarayana

Abstract In this paper, we will briefly review some of the prominent detectors that are most commonly deployed in the terrestrial non-accelerator particle physics experiments. Indigenous efforts for development of detectors for many of the past and current non-accelerator experiments as well as for home-grown mega science experiments of the future will be particularly highlighted. Other related research and development areas concerning electronics, data acquisition systems as well as other instrumentation of these detectors will also be mentioned.

1 Introduction

Non-accelerator experiments played a long and crucial roles in some of the major discoveries in and development of particle physics. These traditionally included cosmic ray physics, nucleon decay, neutrino physics, neutrino-less double-beta decay, dark matter and magnetic monopole experiments. Just a couple of earliest successful stories of detectors deployed in such non-accelerator experiments in India may be mentioned here. D.M. Bose's group built a large cloud chamber of 30 cm in diameter in 1941 which was triggered by a telescope. However, world's largest multi-plate cloud chamber was built and operated in Ooty (Udhagamandalam) in mid 50's along with an air shower array. It played crucial role in recording cores of cosmic ray showers as well as for studying high-energy nuclear interactions (Fig. 1a). First ever atmospheric neutrino event was recorded in mid 60's at Kolar Gold Fields (KGF) 2.3 km below ground. All the seven detectors had vertical walls of scintillators for triggering, neon flash tubes for tracking and absorber walls made up of lead, iron or magnetised iron (Fig. 1b).

Even though there is a large overlap of detectors used in the non-accelerator and accelerator physics experiments, gaseous detectors, liquid ionisation counters and scintillation and photo detectors are workhorses of the non-accelerator experiments.

B. Satyanarayana (⋈)

60 B. Satyanarayana



Fig. 1 High-energy hadron event in the Ooty cloud chamber (left), Neutrino detector at Kolar Gold Fields (right)

Some of the well-known examples of this kind are scintillators, photomultipliers, gas proportional counters, drift chambers, resistive plate chambers and so on. However, some of the non-accelerator physics experiments employ contrastingly different detection techniques or instrumentation methods compared to their counter parts. Massive water Cherenkov detectors (used in Super-Kamiokande and Ice Cube), ultra-cold solid-state detectors (used in CDMS) and magnetised iron calorimeter (proposed by ICAL) are some of the examples of this kind. While typically the accelerator physics experiments are built using more than half a dozen different types of detector layers, non-accelerator experiments are usually designed using a single type or at best a couple of types of detector elements. Even though many of the non-accelerator detector elements are fabricated using commonly available and inexpensive materials, there is also a demand for ultra-pure and exotic materials for building many of the modern non-accelerator 1detector elements as well.

2 Gas Proportional Chambers

During 70's, Indo-Japanese collaboration was studying multiple muon events at various underground locations at Kolar Gold Fields (KGF) using single wire gas proportional counters as active detector elements.

The proportional counters are made of hallow, 6-m-long iron pipes of wall thickness 2.3 mm and of 10 cm \times 10 cm square cross-section. Two end-plates each with a central hole are welded on the sides. A central anode wire of 100 μm thickness is held across with the help of hermetic glass to metal seals. A needle valve is welded onto one of the end plates for controlled gas filling. The counter is filled with P10 gas (90% Argon and 10% methane). Typically, 2900 V is applied to the anode. The proportional counters were found to offer layered efficiencies of about 90% for muons.

Later, they started operating the first dedicated nucleon decay experiment at about 2.3 km below ground in 1980. This tracking calorimeter was built using about 1600





 $\begin{tabular}{ll} Fig.~2 & Proportional counters~in~the~KGF~proton~decay~experiments~(left)~and~in~the~Grapes-3~experiment~in~Ooty \end{tabular}$

proportional counters—which were arranged in orthogonal layers, interleaved with about 140 tonnes of iron. This experiment was later complimented by another larger detector built with 400 tonne iron and about 4000 proportional counters at a depth of 2 km below ground [1] (Fig. 2a). Building of this ambitious experiment necessitated a large detector, instrumentation and electronics R&D programme and resulted for the first time, production of large number of proportional counters in the Indian industry as well as development of sophisticated online data acquisition system using fast electronics and microprocessors indigenously. Proportional counters of same design were also used for a magnetic monopole detector, which was also built and operated at the same depth. An on the surface experiment for studying extensive air showers was also built and operated around the same time at KGF. Muon stations of this experiment were also designed and built using gas proportional counters of the same type, making it one of the biggest deployment of these detectors in a town!

On closer of the KGF experiments, the proportional counters were shifted to GRAPES-3 experiment at Ooty and were used to build four muon detector stations as part of the scintillator detector-based large extensive air shower array. These detector stations track cosmic ray muons and measure their intensities at high cut-off rigidities along nine angular bins. Most of the proportional counters even 40 years after they were built are working very stably. Thanks to excellent operating conditions and calibration procedures employed by the collaboration, muon rates down to a fraction of a percentage were recorded by this experiment. The Grapes-3 experiment recently recorded a sudden burst of high-energy galactic cosmic rays that lasted for 2 hours. This event was correlated in time with a surge of 40 nT in the interplanetary magnetic field [2] (Fig. 2b).

3 Scintillation Detectors

Plastic scintillators traditionally are the most common detector components of radiation detectors. Planar shape of the detectors, ease of machining, ease of coupling to photo detectors by multiple methods, no running cost of the detectors make them the

B. Satyanarayana

popular choice by the nuclear and high energy physicists besides radiation monitoring device manufacturers. Indigenous development of the plastic scintillators based on polymers has been carried out for long time by BARC and other DAE establishments and were extensively used in many basic science experiments. They were also used for building radiation monitors for many applications, such as survey monitoring and contamination monitoring.

The 240 scintillation counters of average area of 250 cm \times 60 cm each covered the outside layer of proportional drift tubes of D0 detector on the Tevatron in the central region [3] (Fig. 3a). These scintillation detectors were jointly built at the Fermilab, USA, as well as at the Tata Institute of Fundamental Research (TIFR), Mumbai, using BC-404A plastic scintillators supplied by Bicron. Extensive fabrication, installation and commissioning activities of these detectors were taken up by TIFR. This scintillation muon veto detector was found to be very effective for rejecting cosmic ray background, accelerator muons which are out-of-time as well as backscatter particles in the collisions, while providing particle detection efficiency of better than 99%. In addition, an alternate design of the scintillation counters which has drastically minimised its machining, but satisfied its performance requirements for the D0 experiment was also worked out. This design was adapted for the subsequent production of these counters.

Stringent quality control of the produced scintillation detectors was ensured. Five cosmic ray telescopes, comprising of three scintillator paddles each are used for the test setup. Every finished detector was studied for its high voltage plateau characteristics, cosmic ray muon detection efficiencies, pulse height distributions and timing resolutions using this test setup.

The GRAPES-3 experiment which is being operated at Ooty at present deploys about 400 (each of 1 m²) plastic scintillator detectors to record the energy, direction and arrival time of cosmic ray showers [4] (Fig. 3b). This group has carried out extensive research and currently producing very high-quality fast plastic scintillators





Fig. 3 D0 muon scintillator detector (left), scintillator based timing detectors of Grapes-3 experiment (right)

with long attenuation length and high photon output which are comparable to the best commercially available scintillators.

4 Resistive Plate Chambers (RPCs)

The resistive plate chambers (RPCs) were first reported by Santonico and Cardarelli [5] in 1981. These planar, rugged and low-cost detectors are being extensively used in a number of high energy and astro-particle physics experiments. Due to their large signal amplitudes as well as good position and time resolutions, these versatile detectors find applications for charged particle detection, time of flight, tracking, digital calorimetry etc.

'Single gap' RPCs broadly operate on the same principle as that of classical Pestov's Planar Spark Chambers [6]. However, simplifications in construction and operation—such as gas flow at atmospheric pressure through the active volume, lower tolerances on mechanical components used for the gas gap and use of plastic and polymer materials instead of glass—were incorporated in case of RPC detectors. Together these merits made RPCs of potential interest in a different and wider range of applications in modern particle physics experiments.

Being planar in their construction, RPCs are intrinsically suitable for detectors where large coverage is requiring. They are easy to fabricate using commonly available materials, amenable for their large-scale production in industries and suitable to operate over long periods in normal environment. RPC detectors exhibit superior time resolution than that of classical wire chambers. This advantage is due to uniform field setup in case of RPCs as opposed to the 1/r field in case of wire chambers. The latter introduces large time fluctuations due to the drift motion of electrons.

Fast timing RPCs are made up of typically thin glass electrodes which define many narrow (0.1–0.3 mm) gas gaps. They offer time resolutions of the order of 50 ps, opening applications as low-cost high-granularity time-of-flight detectors. At the same time, excellent spatial resolution of better than 30 μm FWHM for X-rays in the digital readout mode has also been recently reported for these multi-gap RPCs (MRPCs). These novel detector architectures and developments have made possible new applications in medical imaging such as low-cost PET and reliable high-rate tracking of minimum ionising particles.

RPC detectors of various designs, making use of many inexpensive materials, built using a variety of construction techniques as well as operating modes are in use in many experiments which are currently in operation as well as being developed and prototyped for many future experiments. Due to the flexibility in their design and fabrication, RPC detectors are adaptable to a variety of detector applications and operating environments. Therefore, they are increasingly preferred by the experimentalists over the other competing choices for the accelerator as well as non-accelerator experiments, for trigger as well as timing applications.

Single- and double-gap RPCs operated in the streamer mode were deployed in many large-scale high energy physics experiments such as BaBaR at SLAC [7],

B. Satyanarayana

BELLE at KEK [8], ARGO at the Yang Ba Jing high altitude cosmic ray laboratory [9] (Fig. 4a), OPERA at LNGS [10], BESIII at IHEP [11]. RPCs operated in the avalanche mode are currently being used on a large scale for the muon trigger systems of the ATLAS [12] and CMS [13] experiments at CERN. One of the most successful large-scale (150 m² in area) implementation of fast timing RPCs is the time-of-flight barrel of ALICE [14] experiment also on the LHC at CERN.

The India-based Neutrino Observatory (INO) is deeply engaged in design and construction of a mega science experiment called magnetised iron calorimeter (ICAL) for studying many key open questions involving the elusive particles called neutrinos [15]. Due to excellent timing (better than 1 ns) and spatial (better than 1 cm) resolutions they provide, RPCs were chosen as the active detector elements for the readout system of the ICAL detector. ICAL will deploy 28,800 RPCs of 2 m \times 2 m in dimension. A large-scale detector R&D effort was undertaken to design, develop, characterise and produce the RPCs successfully. Generations of gas systems, including a closed-loop unit were built and developed. Now, a large number of 2 m \times 2 m RPCs are being produced in the glass industry [16].

A total of about 3.6 million ultra-high-speed detector signals need to be instrumented in this detector. The electronics comprising of indigenously developed custom ASICs and high-end FPGAs as well as programmable trigger and high-speed data acquisition systems are in the advanced stages of development, production and deployment.

A detector stack (Fig. 4b) comprising of 12 layers of 2 m \times 2 m RPCs was commissioned in the transit campus of IICHEP, Madurai. Main goal of this detector is to study stability and performance of large-scale RPCs produced in Indian industry. Several physics studies including angular distribution of incident cosmic ray muons are also being carried out using this stack.



Fig. 4 $6700 \, \text{m}^2$ RPC carpet array of ARGO-YBJ experiment (left), INO's $2 \, \text{m} \times 2 \, \text{m}$ RPC detector stack (right)

5 Summary and Conclusions

A brief review of some selected detectors which are commonly used in the non-accelerator experiments is given. Mention was also made about other related areas such as electronics, gas systems and other instrumentation development. While giving an historical perspective of the significant and often pioneering detector development activities in India dating back to several decades, current efforts to build state-of-art devices exclusively meant for deployment in the futuristic mega scale experiments are described. As stated earlier, there is a large overlap of detectors used in the non-accelerator and accelerator physics experiments. Therefore, both the communities are reaping the fruits of advances in others' research areas and developments. Dedicated efforts are underway both in India and abroad to research and develop novel detectors and hybrid detector configurations for equipping the futuristic large-scale detectors as well as very special purpose detectors.

References

- H. Adarkar et al., IJPAP 27, 679–690 (1989)
- 2. P.K. Mohanty et al., PRL 117, 171101 (2016)
- 3. B.S. Acharya et al., Nucl. Instr. Meth. A 401, 45–62 (1997)
- 4. P.K. Mohanty et al., Astroparticle Phy. 31, 24 (2009)
- 5. R. Santonico, R. Cardarelli, Nucl. Instr. Meth. A 187, 377 (1981)
- R. Santonico, R. Cardarelli, Nucl. Instr. Meth. A 18.
 Y. Pestov, Nucl. Instr. Meth. A 196, 45 (1982)
- 7. BaBar Collaboration, Nucl. Instr. Meth. A 479, 1 (2002)
- 8. M. Yamaga et al., Nucl. Instr. Meth. A **456**, 109 (2000)
- 9. YBJ-ARGO Collaboration, Nucl. Instr. Meth. A 588, 7 (2008)
- 10. OPERA Collaboration, Nucl. Instr. Meth. A 602, 631 (2009)
- 11. Yuguang Xie et al., Nucl. Instr. Meth. A **599**, 20 (2009)
- 12. ATLAS Collaboration, J. Instrum. S08003 (2008)
- 13. CMS Collaboration, J. Instrum. S08004 (2008)
- 14. A.N. Akindinov et al., Nucl. Instr. Meth. A 533, 74 (2004)
- 15. A. Kumar et al., Pramana—J. Phys. **88**, 79 (2017)
- 16. B. Satyanarayana, http://www.ino.tifr.res.in/ino/theses/satya_thesis.pdf

Device Physics Simulation of Gaseous Ionization Detectors

Supratik Mukhopadhyay

Abstract Gaseous ionization detectors depend on the ionization of the gaseous media due to the passage of ionizing radiation. The primary electrons/ions are transported and amplified through the application of suitable electromagnetic configuration and, finally, registered in the form of electronic signal. They are relatively inexpensive and have applications in wide-ranging fields related to fundamental studies and industry because of their excellent spatial, temporal and energy resolution leading to reliable particle identification. An array of complex physical and chemical processes occurring inside these devices determine their characteristics and demands close inspection before proper insight related to the device dynamics is obtained. Here, we will discuss recent advances in numerical simulation of the detailed device physics of gaseous ionization detectors. Discussions on the mathematical formulations, algorithms and simulation frameworks will be presented. Application of the simulation tools to investigate several physics issues of current interest will also be discussed.

1 Introduction

Gaseous ionization detectors are more than a century old now. They are very capable detectors that satisfy the stringent requirements of present-day experiments. In addition, they are flexible and relatively inexpensive. These factors have led to a large variety of applications in which gaseous detectors are, or are projected to be, deployed. These include fundamental areas such as high energy physics [1], nuclear physics [2], rare event detection [3], plasma physics [4] and technical applications such as medical imaging [5], cosmic ray muon tomography [6], nuclear reactor monitoring [7], fire detection [8] and many others.

S. Mukhopadhyay (⊠)

68 S. Mukhopadhyay

The century-long evolution have given rise to a large variety of gaseous detectors. Starting from the relatively naive wire counters of the early 1900s [9], developing the sophisticated crop of micro-pattern gaseous detectors (MPGD) [10] is a long way that has seen many significant intermediate breakthroughs, such as Geiger–Muller counter [11], multi-wire proportional chambers (MWPC) [12], resistive plate chambers (RPC) [13]. Because of the inherent complexity of the dynamics, numerical simulation has played a very crucial role in the advancement of the understanding of these devices. Here, we will discuss some of the typical approaches adopted to simulate gaseous ionization detectors, some case studies of current interest and areas demanding further investigations.

The processes occurring inside an ionization detector can be described as follows:

- 1. Primary ionization: Among several other possibilities, this can occur due to the passage of muon or X-ray through the gaseous medium, or can be generated by photo-ionization. Usually, the efficiency of primary ionization, their number and the location of the clusters are the information that are important for the rest of the dynamics.
- 2. Transport of electrons and ions, interactions, amplification, loss: The electrons and ions created through primary ionization are separated by the application of electric field. During their passage through the gaseous medium, they undergo longitudinal and transverse diffusion, get amplified by secondary ionization or lost by attachment. Other interactions such as elastic and inelastic collisions also keep on occurring depending on their relative probability. The electromagnetic field configuration and the medium through which the charged particles drift determine the dynamics of the device to a great extent.
- 3. Induction of signal on electrodes: The movement of charged particles in the gaseous medium induces current on the pick-up electrodes.

After the signal is induced on the electrodes, it is collected by the data acquisition system through a number of intermediaries that may include preamplifiers, amplifiers, digitizers, etc. Finally, it is analysed using suitable tools.

In order to numerically simulate the above sequence of events, different approaches are adopted. In the zeroth order, an electrical/electronic model is used to represent the detector [14]. For certain applications, a fluid model of the detector dynamics may be considered sufficient for simulating streamers [15], while for others, a more realistic particle model [16] becomes mandatory. Depending on the geometric complexity and the level of details necessary, an 1D, 1.5D, 2D or 3D model [16] of the detector geometry is numerically created. Similarly, depending on the goal, a simulation may need to be carried out till the generation and subsequent processing of signals [17], while in other cases, the simulation of the dynamics of the transport may be sufficient for understanding [18].

Considering the wide spectrum of possibilities, it is obvious that the present discussion will necessarily have to be a rather restricted one. Here, a relatively elaborate and flexible framework based on the Garfield program [19] will be described in some detail. Example applications based on the mentioned approach will be presented to illustrate its capabilities. Finally, present research activities related to this

framework will be mentioned. It should be mentioned here that there could be several other options of solving similar problems besides the one discussed here, and the user should make a judicial choice based on her/his requirements.

2 Background

As mentioned above, several processes need to be simulated in sequence in order to model the dynamics of a gaseous detector. They are (1) primary ionization, (2) transport, amplification, loss of electron and ions under the influence of electromagnetic field, (3) induction of signal/collection of charge on the electrodes, and (4) collection of signal by DAQ. The Garfield program, with appropriate interfaces to a large number of codes (HEED [20] for primary ionization, MAGBOLTZ [21] for transport properties, ANSYS [22], CST [23], COMSOL [24], Elmer [25], neBEM [26] for electric field calculation), acts as the simulation framework (see Fig. 1) necessary to follow the dynamics of the entire set of processes. In what follows, we will discuss this framework and its applications in some detail.

2.1 Simulation Framework

Garfield [27, 28] computes the drift of the charged particles through gaseous detectors, by implementing an elaborate Monte Carlo when requested. In the process, it also computes the signal induced on the electrodes. Garfield can set up a reasonably complex three-dimensional detector geometry from simple building blocks following

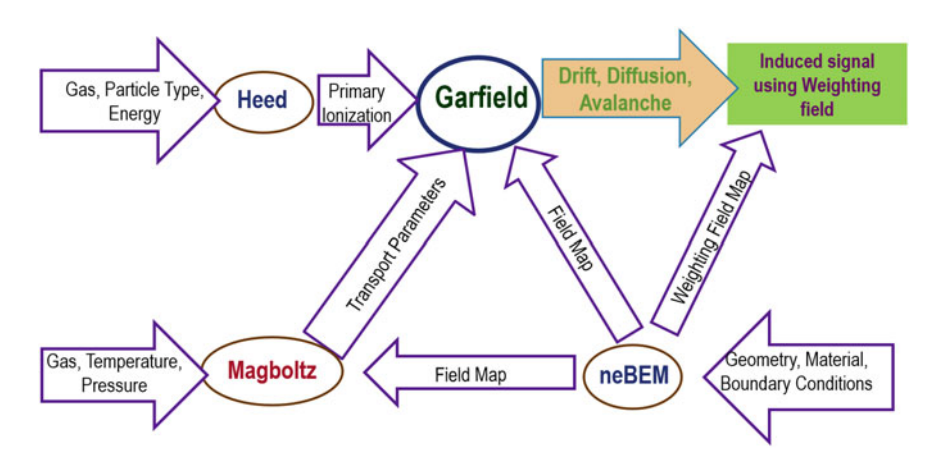


Fig. 1 The Garfield simulation framework. Garfield provides suitable interfaces to codes such as Heed, Magboltz and neBEM among others

70 S. Mukhopadhyay

the constructive solid geometry (CSG) approach. Finally, it has graphics capabilities for plotting information on-screen, or on paper. Garfield++ [29], the recent C++ version of the older FORTRAN code, has a more up-to-date treatment of electron transport. Moreover, its user interface is one that is derived from ROOT [30], which has a large user base. Although the Garfield++ toolkit has been used for detailed simulation of ionization detectors that use both gas and semi-conductors as sensitive medium, the main area of its application continues to be the MPGDs.

2.2 Computation of Primary Ionization

High Energy ElectroDynamics (HEED) is used to obtain the distribution of the individual ionizations along a particle track and their energies that will initiate the process of simulating the signal in a gas detector. Written by Smirnov [31] and based on Monte Carlo technique, it computes the energy loss of fast charged particles in gases, taking into account delta electrons and optionally multiple scattering of the incoming particle. The code is based on the photo-absorption ionization (PAI) model by Allison and Cobb [32] and also includes the modified version of PAI, called photo-absorption ionization and relaxation (PAIR) model which considers the cross sections of the individual shells. The program is able to compute the absorption of photons, as well as the primary ionization parameters, by simulating the atomic relaxation effects (by the emission of fluorescence photons and Auger electrons) and by tracking the emerging δ -electrons.

As a stand-alone example of using HEED, cluster statistics for a 3 GeV muon track in Argon–Isobutane (90:10) gas mixture at room temperature and pressure is presented in Fig. 2.

2.3 Computation of Transport Properties

The transport parameters of electrons drifting in the gases under the influence of electric and magnetic field are calculated by Magboltz, developed by Biagi [33]. The Boltzmann transport equation is numerically integrated to compute electron transport parameters. The drift velocity, the longitudinal and transverse diffusion coefficients and Townsend and attachment coefficients are computed by the program for various gases and their mixtures using Monte Carlo integration techniques. The Lorentz angle can also be computed by the code, if necessary due to the application of a magnetic field. Elastic and inelastic collisions, attachment, ionization and super-elastic collisions are among the interactions considered by the formulation. The collision angular distributions have also been introduced. The program contains electron cross sections for all relevant interactions with atoms and/or molecules for 60 gases, and the descriptions are being improved regularly [34].

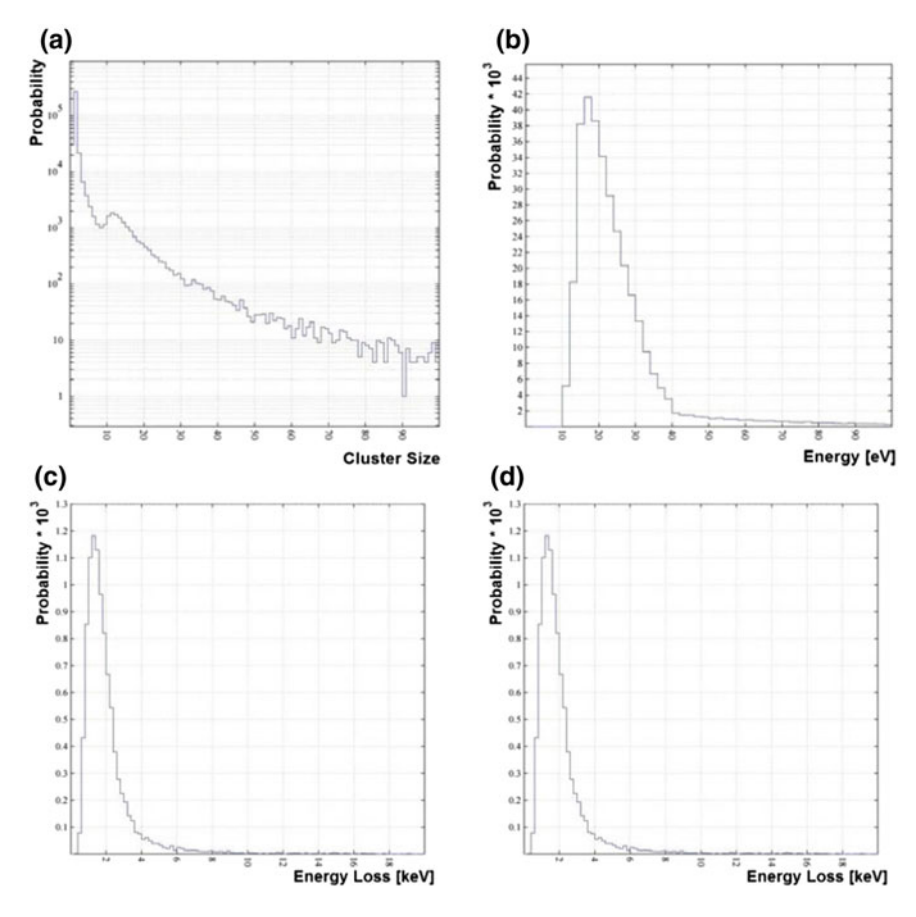


Fig. 2 For 3 GeV cosmic muon, in Argon–Isobutane (90:10) gas mixture a cluster size distribution, b energy per cluster, c energy loss per cm, d clusters per cm

Using a stand-alone version of the Magboltz code, the transport properties of Argon – CO_2 mixtures with three different mixing ratios (90:10, 80:20, 70:30 respectively) and Argon – CO_2 – CF_4 mixture (45:15:40 mixing ratio) have been studied. These gas mixtures are very commonly used in gaseous electron multipliers (GEMs) [35] that have drift and induction fields of around $2\,kV/cm$, whereas the amplification field inside the hole is $60\,kV/cm$. In Fig. 3, we present estimates using Magboltz covering the relevant range of electric field.

2.4 Computation of Electric Field

Most of the processes taking part in determining the device dynamics depend on the electromagnetic configuration of detector, one notable exception being the primary

72 S. Mukhopadhyay

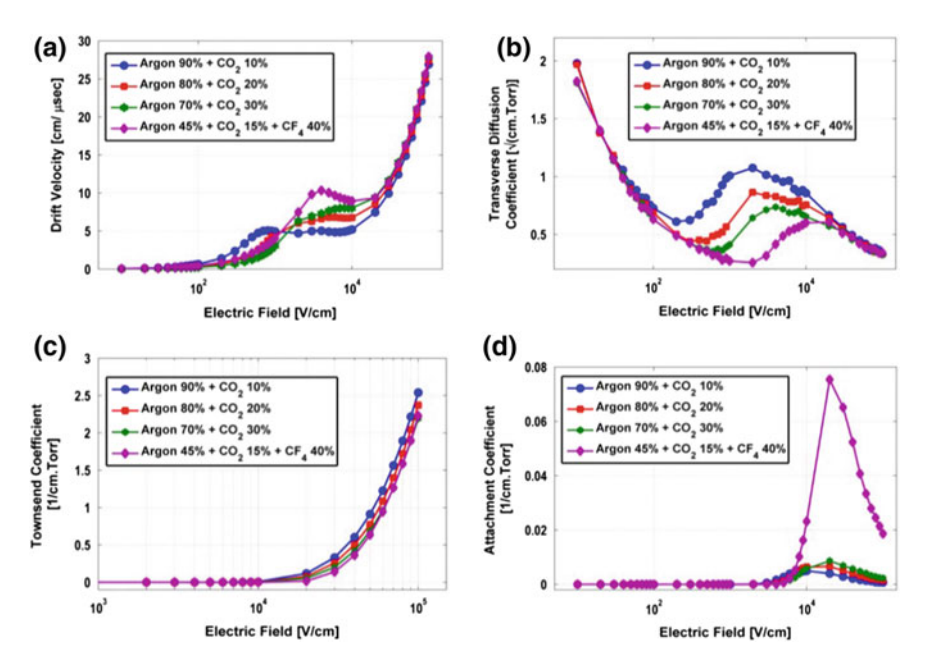


Fig. 3 Variation of a drift velocity, b transverse diffusion coefficient, c Townsend coefficient, d attachment coefficient

ionization. As a result, it is important to compute the electric field precisely and efficiently. While field for simple configurations can be computed by Garfield, it has to take the help of electrostatic field solvers for complex geometries. This is more so for arbitrary three-dimensional geometries, as encountered in MPGDs. The boundary element method (BEM) is a reasonably powerful technique in which the interfaces of a given geometry are endowed with distributions of singularities such as source or dipole of unknown strengths. The strengths of these singularities are obtained by satisfying boundary conditions of Dirichlet, Neumann or of the Robin type, the last one being a weighted combination of Dirichlet and Neumann boundary conditions. The nearly exact boundary element method (neBEM) [36, 37] was integrated to the Garfield simulation framework in 2009.

Wires are often an integrated component of gaseous ionization detectors, including MPGDs. They are correctly represented when they are modelled as a cylinder whose cross section is a polygon whose cross section matches that of the real wire. However, a close resemblance to the real wire usually leads to increase in computational effort. A thin wire model is the other extreme of the representation in which it is assumed that the real wire can be replaced by a line charge situated at the wire axis. The potential boundary condition is satisfied at the wire surface that imposes a cylindrical symmetry which leads to a compromise in 3D information, and thus, the thin wire approximation neglects the dipole moment. As a result, for a Micromegas detector [38], the cylindrical model is likely to be more accurate than the wire model

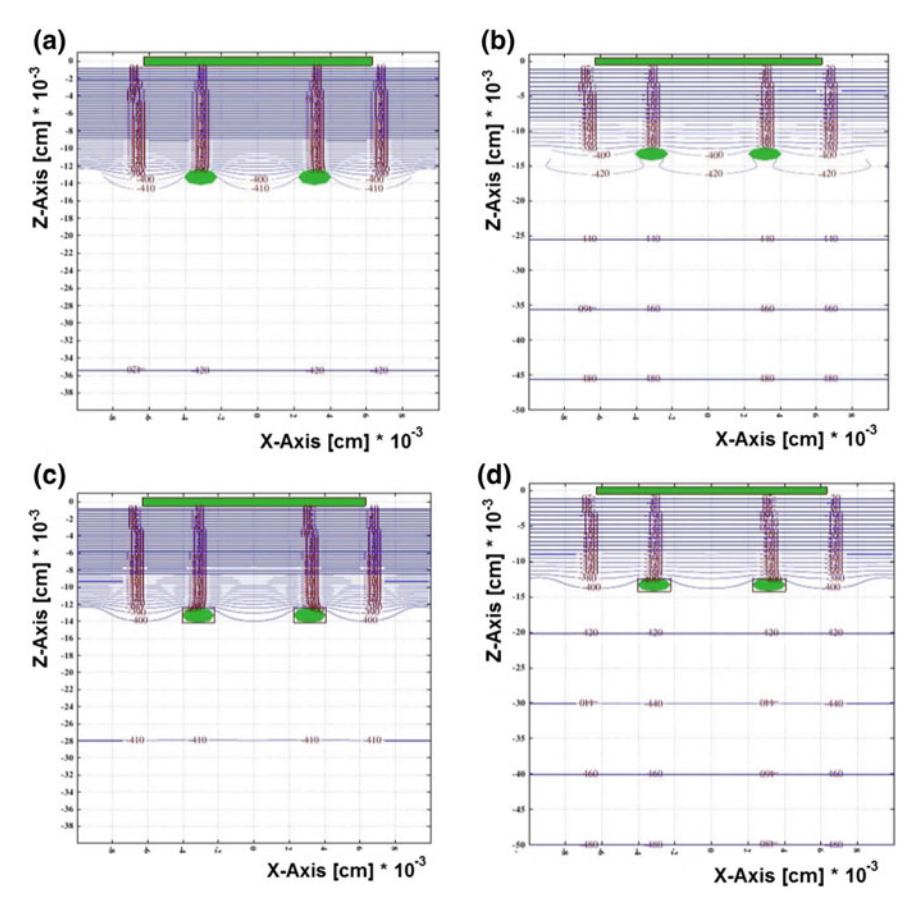


Fig. 4 The potential contours for wire element at a 200 V/cm, b 2000 V/cm and for cylindrical element at c 200 V/cm, d 2000 V/cm

since the drift and amplification fields for these detectors are different by orders of magnitude. In Fig. 4, we have presented the results of an investigation that looked into the consequences of using these two models. For these calculations, the anode plane has been kept at ground potential, whereas the mesh, $128\,\mu$ m away from the anode, has been given to a voltage of $-410\,\text{V}$. The drift cathode, placed at $1.2\,\text{cm}$ above the mesh plane, has been raised to a voltage of $-650\,\text{V}$ and $-2810\,\text{V}$ to create a drift field of $200\,\text{and}\,2000\,\text{V/cm}$, respectively, in the drift volume. As illustrated, the calculations using thin wire approximation leads to relatively inaccurate potential values (that in turn will further affect the electric field) which ultimately may degrade subsequent calculations.

74 S. Mukhopadhyay

2.5 Computation of Induced Signal

During the charge multiplication process, a large number of electron—ion pairs are created in the gas. The electrons and ions are separated by the field and move towards their respective electrodes. The motion of the electrons and ions in the gas induces charges on the electrodes. The current I that flows into one particular electrode under the influence of a charge q with velocity \mathbf{v} can be calculated using the equation [39, 40].

$$I = -q \frac{\mathbf{v} \times \mathbf{E_w}}{V} \tag{1}$$

This holds for an arbitrary potential V. Here $\mathbf{E_w}$ is the field created by raising this electrode to a potential V and grounding all other electrodes, in the absence of charge. To find this weighting potential as a function of position, one must solve the Laplace equation for the geometry of the detector, but with artificial boundary conditions. These are: (1) the voltage of the electrode on which the induced charge is being calculated is set to unity, and (2) voltages of all other electrodes are set to zero.

As a simple example for computing induced signal, a single wire proportional counter has been considered. The drift lines of electrons from a predefined track towards the anode wire and the resulting induced signal have been presented in Fig. 5. The electrons are found to drift towards the wire plane, whereas the ions (not shown in the figure) move towards the wall of the cylinder. The spikes in the induced signal are due to the electrons and the long tail is due to the slow movement of ions.

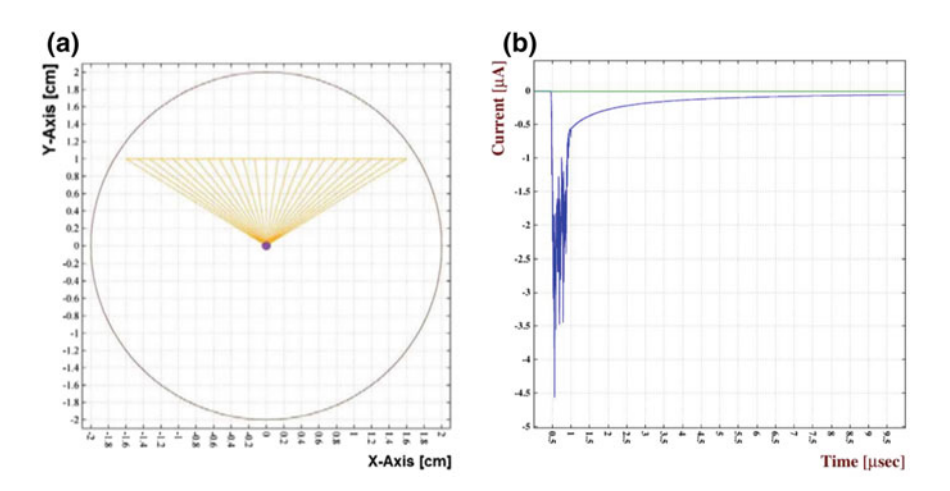


Fig. 5 The drift of a electrons and b induced signal

3 Case Studies

Based on the building blocks described above, it is now possible to investigate realistic problems involving MPGDs. In this section, the problem of estimating time resolution of gaseous detectors will be discussed in some detail to illustrate the capability of the simulation framework described here. The reason for choosing the problem, besides the current interest, is the fact that for estimating the time resolution of a detector, one needs to simulate the entire set of processes mentioned above. There are several factors that influence time resolution: (a) fluctuations in the primary ionization, (b) diffusion during transport, (c) gain fluctuation. In addition, signal processing methodologies also have an important contribution on this very important parameter.

3.1 Time Resolution of a Triple-GEM Detector

Cosmic muon (1–3 GeV) tracks in the drift volume at different inclinations have been used to create primary ionization. The drift time of the electrons which have hit the readout plane first has been recorded for every track, creating the time spectrum of the triple-GEM detector as shown in Fig. 6 for two different Argonbased gas mixture. The mean of this time spectrum gives the mean drift time of the first hit, and the r.m.s yields the temporal resolution. Due to higher drift velocity, the electrons in $Ar - CO_2 - CF_4$ mixture take less time to hit the readout plane. Also, the lower transverse diffusion coefficient in this mixture helps to obtain a better temporal resolution. It may be noted here that the numerical estimates (11 ns for Ar - CO₂ and 7 ns for Ar - CO₂ - CF₄) are quite close to experimentally measured values reported in the literature [41]. The variation of the first hit time and the corresponding temporal resolution with applied high voltage (being translated as current in the figures) for these two gas mixtures have also been plotted in Fig. 6. It is observed that an increase of the drift field, hole voltage and the induction field reduces the time taken by the electron to reach the readout plane, as well as improves the temporal resolution. It may be noted here that the effect of gain fluctuation and signal processing methodologies has been ignored in this study.

3.2 Time Resolution of MRPC

Advantages of dividing a continuous gas gap of an RPC into several smaller gas gaps, in relation to the time resolution of the detector, are well established now [42]. Next, we present a brief numerical study on the variation of time resolution on different experimental parameters. In Fig. 7, primary ionization due to the passage of a typical cosmic muon and the variation of time resolution due to the change

76 S. Mukhopadhyay

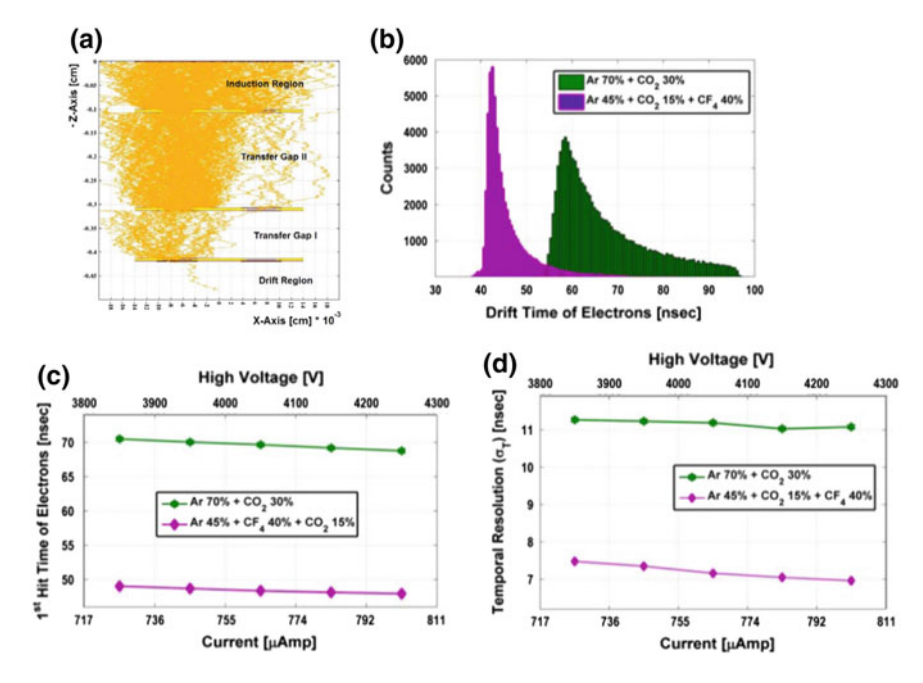
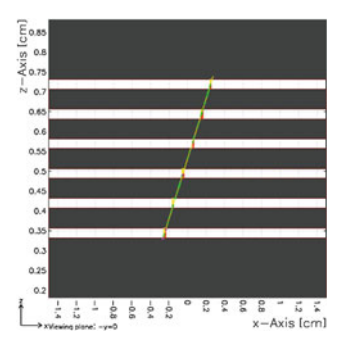


Fig. 6 For a triple-GEM detector $\bf a$ electron avalanche, $\bf b$ time spectrum, $\bf c$ the variation of first hit time of electrons, $\bf d$ temporal resolution with current and applied high voltage in different Argonbased gas mixture

Fig. 7 For an MRPC primary ionization due to the passage of a cosmic muon



in applied electric field across the gas gaps have been presented. Smaller gaps of MRPCs allow the application of larger electric field across each of the gas gaps. This sets up faster drift velocities and suppresses diffusion. In addition, since the total gas gap length remains unchanged in comparison to a single-gap RPC, the efficiency of primary ionization remains unchanged. Finally, the short distance over which the charge multiplication occurs ensure less gain fluctuation. Consequently, the time resolution of MRPCs improves significantly over single-gap RPCs.

4 Conclusion

A very brief overview of an existing simulation framework for simulating device physics of gaseous ionization detectors has been presented. The building blocks of the framework have been discussed and illustrated through simple stand-alone usages. Finally, the framework has been applied to investigate the time resolution of typical gaseous detectors. It has been found that the framework is a capable tool for carrying out similar studies of current interest.

Finally, there are several areas that demand development of new mathematical models and algorithms. Entirely new physics or chemistry may need to be included to solve some of these problems such as those related to charging up, space charge, discharges and ageing. These are some of the interesting and important areas that will need sustained experimental and numerical effort from the research community in future.

Acknowledgements This paper contains results from different studies carried out by my colleagues and students. I gratefully acknowledge their contribution.

References

- 1. http://www.lhc.web.cern.ch
- G.D. Alkhazov, M.N. Andronenko et al., Nuclear matter distributions in 6He and 8He from small angle p-He scattering in inverse kinematics at intermediate energy. Phys. Rev. Lett. 78, 2313–2316 (1997)
- 3. http://cast.web.cern.ch
- A. Wojenski, G. Kasprowicz et al., Multichannel reconfigurable measurement system for hot plasma diagnostics based on GEM-2D detector. Nucl. Instrum. Methods B 364, 49–53 (2015)
- M. Danielsson, P. Fonte et al., Novel gaseous detectors for medical imaging. Nucl. Instrum. Methods A 518, 406–410 (2004)
- K. Gnavo, L.V. Grasso III et al., Imaging of high-Z material for nuclear contraband detection with a minimal prototype of a muon tomography station based on GEM detectors. Nucl. Instrum. Methods A 652, 16–20 (2011)
- J. Pancin, S. Andriamonje et al., Piccolo Micromegas: first in-core measurements in a nuclear reactor. Nucl. Instrum. Methods A 592, 104–113 (2008)
- 8. G. Charpak, P. Benaben et al., Progress in the development of a S-RETGEM-based detector for an early forest fire warning system. J. Instr. 4, P12007 (2009)
- 9. E. Rutherford, H. Geiger, An electrical method of counting the number of α particles from radioactive substances. Proc. R. Soc. (London) Ser. A **81**, 141–161 (1908)
- A. Oed, Position-sensitive detector with microstrip anode for electron multiplication with gases. Nucl. Instrum. Meth. A 263, 351–359 (1988)
- H. Geiger, W. Muller, Elektronenzhlrohr zur Messung schwchster Aktivitten? (Electron counting tube for the measurement of the weakest radioactivities). Die Naturwissenschaften (The Sciences) 16, 617–618 (1928)
- 12. G. Charkpak, The use of multiwire proportional counters to select and localize charged particles. Nucl. Instrum. Meth. 62, 262–268 (1968)
- R. Santonico, R. Cardarelli, Development of resistive plate counters. Nucl. Instrum. Meth. 187, 377–380 (1981)

78 S. Mukhopadhyay

14. J. Galan, D. Attie et al., Characterization and simulation of resistive-MPGDs with resistive strip and layer topologies. Nucl. Instrum. Meth. A **732**, 229–232 (2013)

- 15. C. Li, J. Teunissen et al., A comparison of 3D particle, fluid and hybrid simulations for negative streamers. Plasma Sources Sci. Technol. **21**, 055019 (2012)
- C. Lippmann, W. Riegler, Space charge effects in resistive plate chambers. Nucl. Instrum. Meth. A 517, 55–76 (2004)
- P. Bhattacharya, S. Mukhopadhyay et al., The effect of spacers on the performance of Micromegas detectors: a numerical investigation. Nucl. Instrum. Meth. A 793, 41–48 (2015)
- P. Bhattacharya, S. Mukhopadhyay et al., A comparative numerical study on GEM, MHSP and MSGC. J. Instr. 7, P09007 (2012)
- 19. http://cern.ch/garfield
- 20. http://cern.ch/heed
- 21. http://cern.ch/magboltz
- 22. http://ansys.com
- 23. http://cst.com
- 24. http://comsol.com
- 25. http://csc.fi/we/elmer
- 26. http://cern.ch/nebem
- 27. R. Veenhof, Garfield, recent developments. Nucl. Instrum. Meth. A **419**, 726 (1998)
- R. Veenhof, Numerical methods in the simulation of gas-based detectors. Jour. Instrum. 4, P12017 (2009)
- 29. http://cern.ch/garfieldpp
- 30. http://root.cern.ch/
- 31. I.B. Smirnov, Modeling of ionization produced by fast charged particles in gases. Nucl. Instrum. Meth. A **554**, 474–493 (2005)
- 32. W.W.M. Allison, J.H. Cobb, Relativistic charged particle identification by energy loss. Ann. Rev. Nucl. Sci. **30**, 253 (1980)
- 33. S.F. Biagi, Monte Carlo simulation of electron drift and diffusion in counting gases under the influence of electric and magnetic field. Nucl. Instrum. Meth. A **421**, 234 (1999)
- 34. https://fr.lxcat.net/home
- F. Sauli, GEM: a new concept for electron amplification in gas detectors. Nucl. Instrum. Meth. A 386, 531 (1997)
- 36. S. Mukhopadhyay, N. Majumdar, Computation of 3D MEMS electrostatics using a nearly exact BEM solver. Eng. Anal. Boundary Elem. **30**, 687 (2006)
- 37. N. Majumdar, S. Mukhopadhyay, Simulation of three dimensional electrostatic field configuration in wire chambers: A novel approach. Nucl. Instrum. Meth. A **566**, 489 (2006)
- 38. Y. Giomataris, Ph Rebourgeard et al., MICROMEGAS: A High-Granularity Position-Sensitive Gaseous Detector for High Particle-Flux Environments. Nucl. Instrum. Meth. A **376**, 29–35 (1996)
- 39. W. Shockley, Currents to conductors induced by a moving point charge. J. Appl. Phys. **9**, 635 (1938)
- 40. S. Ramo, Currents induced by electron motion. Proc. IRE IEEE 27, 584 (1939)
- 41. G. Bencivenni, P. De Simone et al., Performance of a triple-GEM detector for high rate charged particle triggering. Nucl. Instrum. Meth. A **494**, 156–162 (2002)
- 42. A. Akindinov, F. Anselmo et al., The multigap resistive plate chamber as a time-of-flight detector. Nucl. Instrum. Methods A **456**, 16–22 (2000)

Part II Contributory Oral

Experimental Studies of Ion Backflow for a Bulk Micromegas Detector Using Various Argon-Based Gas Mixtures

Prasant Kumar Rout, Deb Sankar Bhattacharya, Purba Bhattacharya, Supratik Mukhopadhyay, Sudeb Bhattacharya, Nayana Majumdar, Sandip Sarkar, Paul Colas, David Attie, Serguei Ganjour and Aparajita Bhattacharya

Abstract The micropattern gaseous detectors (MPGD) are fast radiation detectors capable of operating in high-luminosity environment and offer high gain, good position and time resolutions. Avalanche-induced photons and ions lead to secondary effects that can limit the operation of gaseous ionization detectors. For example, ion backflow (IBF) makes a detector incapable in high-flux scenarios by distorting the electric field locally. In the present work, IBF has been measured using two drift meshes in the experimental set-up and several Ar-based gas mixtures, in particular, Argon + Isobutane (95:5), T2K gas composed of Argon + CF_4 + Isobutane (95:3:2) and Argon + CO_2 (80:20). We will present the effect of various experimental parameters on IBF and discuss optimization of the related experimental set-up.

1 Introduction

Classical gaseous ionization detectors, such as the MWPC, RPC, are found to be increasingly incapacitated in high-luminosity experiments. Due to the high event rate, it is not possible to evacuate the slowly drifting ions from the gas volume in time. While the number of primary ions is usually small and may often be ignored easily, the accumulation of secondary ions can be non-negligible, especially if the

P. K. Rout (⋈) · P. Bhattacharya · S. Mukhopadhyay · S. Bhattacharya

N. Majumdar · S. Sarkar

Saha Institute of Nuclear Physics, Kolkata 700064, India

e-mail: prasant.rout@saha.ac.in

D. S. Bhattacharya

Institute of Physics, Bhubaneswar 751005, India

e-mail: dsb.physics@gmail.com

P. Bhattacharya

Department of Particle Physics and AstroPhysics, Weizmann Institute of Science,

Herzl St. 234, 7610001 Rehovot, Israel

P. Colas · D. Attie · S. Ganjour

CEA, Saclay, Gif Sur Yvette 91191, France

A. Bhattacharya

Department of Physics, Jadavpur University, Jadavpur, Kolkata 700032, India

© Springer Nature Singapore Pte Ltd. 2018

S. Biswas et al. (eds.), *Advanced Detectors for Nuclear, High Energy and Astroparticle Physics*, Springer Proceedings in Physics 201, https://doi.org/10.1007/978-981-10-7665-7_7

P. K. Rout et al.

device amplification is large. Thus, ion backflow may lead to significant distortion of the local electric field, giving rise to complex and unreliable response from the detection system. Therefore, in many present experiments, it is crucial to limit the ion backflow and reduce the space charge effect to acceptable levels. The use of switching electrostatic ion gate is one of the common methods adopted to reduce ion backflow in many devices. Unfortunately, ion-gating turns out to be unsuitable for high-rate experiments.

Micropattern gaseous detectors are amplification devices that can provide good ion feedback suppression due to highly asymmetric electric fields in between the drift and the amplification regions. Micromegas is one of the successful MPGDs being used (or proposed to be used) for charged particle tracking in high-rate environments in many high energy physics experiments. For example, in the future linear collider experiment, it is proposed to build a high performance large TPC, using Micromegas as its readout [1].

In a bulk Micromegas detector [2], the drift region (low field, $\sim 200 \text{ V/cm}$) is separated from the amplification region (high field, ~50 kV/cm) by a very thin metal micromesh maintained in parallel to the drift and anode planes. The amplification gap between micromesh and the readout plate (anode) is very small, of the order of \sim 100 μ m. The drift gap between drift mesh and the micromesh is usually much larger than the amplification gap to ensure sufficient primary ionization. The micromesh and the anode plate are separated by means of dielectric pillars which holds the micromesh over the anode plate. Most of the electrons from primary ionization are created in the drift region since its volume is usually much larger than the amplification region. These primary electrons are transported from the drift region to the amplification region through the microholes of the micromesh. This transport occurs due to the field gradient between the drift and amplification regions that lead to a compression of field lines in the vicinity of microholes. This characteristic funnel-shaped field configuration is typically few microns wide in the amplification region. Thus, in the amplification region, the electrons tend to remain focused towards the hole axis and produce avalanches in the funnel. The avalanche spreads out of the funnel because of the transverse diffusion of the electrons. The avalanche creates as many number of positive ions as electrons. Being massive, these secondary positive ions produced by the avalanches are less influenced by diffusion and closely follow the drift lines. Almost all the positive ions are collected at the micromesh giving rise to mesh current. A small fraction of positive ions, however, escapes the micromesh and reaches the drift plane giving rise to drift current. Usually, the Micromegas detector is capable of stopping most of the secondary positive ions created in an avalanche.

Ion backflow fraction is defined as:

$$IBF = \frac{N_b}{N_t} \tag{1}$$

where, in an electron avalanche, the average number of positive ions created is denoted by N_t and the average number of backflowing ions, by N_b . It can be shown that [3], in the two-dimensional limit (neglecting longitudinal development) when

the transverse spread of the avalanche is small relative to the hole pitch

$$IBF \propto \frac{1}{FR} (\frac{p}{\sigma_t})^2 \tag{2}$$

where FR is the field ratio (amplification/drift), p denotes mesh hole pitch and σ_t incorporates the transverse diffusion of the electron and is estimated as $D_t \sqrt{z}$ where D_t is the electron's transverse diffusion coefficient and z is the traversed path. Thus, ion backflow fraction can be controlled by modifying the detector geometry, voltage configuration and gas parameters. The ion backflow fraction is very small in case of a micromegas but can still be significant for track distortion. Therefore, it is necessary to carry out extensive studies on ion backflow in Micromegas detectors, so that suitable design modifications of the Micromegas can be made and reconstruction algorithms can be improved.

2 Experimental Set-up

At SINP, the ion backflow of bulk Micromegas detectors has been measured by developing an experimental set-up [4]. The schematic diagram of the experimental set-up and photographs of the laboratory set-up are shown in Figs. 1 and 2, respectively. A typical bulk Micromegas detector consisting of stainless steel wires of diameter 18 μm , pitch 63 μm and amplification gap 128 μm has been placed inside a leak proof test-box. The primary electron—ion pairs in the detector volume have been generated using a low-energy (5.91 keV) X-ray source 55 Fe. In the test-box, the source can be moved to a desired location within the chamber without breaking the gas flow by using a Wilson seal.

Ion backflow measurements have been carried out for a bulk Micromegas detector in three Argon-based gas mixtures, namely Argon + CO₂ (80:20), Argon + Isobutane (95:5) and Argon + CF₄ + Isobutane (95:3:2). Two drift meshes have been used in this experiment in order to measure the IBF precisely for the ions coming from the amplification region. The presence of only one drift mesh allows the possibility of contribution of the ions coming from the drift and amplification regions, as well as the additional contribution of the ions generated in the region within the test-box above the drift mesh, i.e. region 2 and region 3 as shown in Fig. 1. A second mesh is added to the first drift mesh keeping a mutual distance of 1 cm in order to stop the primary ions generated in these two regions to get collected on the first drift mesh. Thus, the ions that are created in regions 2 and 3 are expected to be collected on the second drift mesh (second drift mesh in Fig. 1). As a result, only the ions created in the amplification region gives rise to the current collected from the first drift mesh (first drift mesh in Fig. 1). This current is a better representative of the ionic current arising from the avalanche in the amplification region and the primary ionization in the drift region.

The ratio of the currents from the drift plane and the micromesh, as measured experimentally, gives an estimate of the backflow fraction which is given by:

P. K. Rout et al.

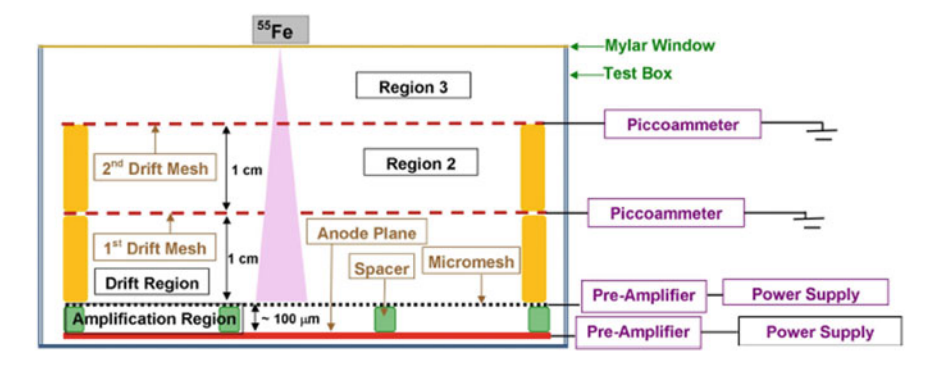


Fig. 1 Schematic of experimental set-up

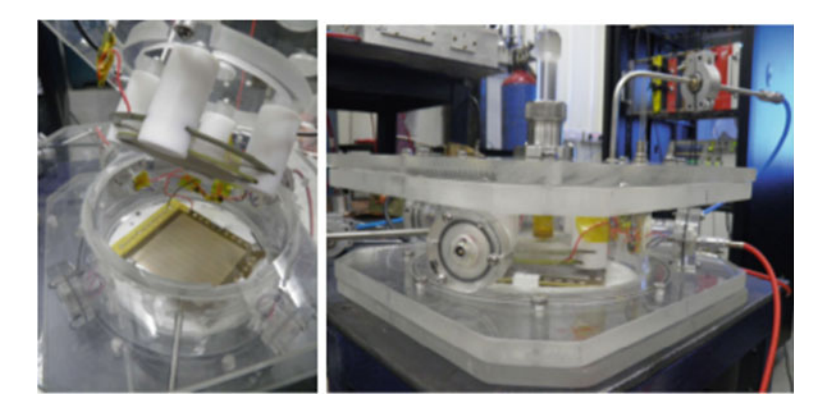


Fig. 2 Laboratory experimental set-up

$$IBF = (\frac{I_C}{I_M + I_C}) \tag{3}$$

where I_C is proportional to the number of ions collected on the drift mesh (current measured on the first drift mesh) and I_M is proportional to the number of ions collected on the micromesh (current measured in the micromesh). A pico-ammeter (CAEN model AH401D) has been used for the measurement of the currents. Since this pico-ammeter measures the current only from a grounded electrode, two different potential configurations have been used. For measuring anode current, anode plane has been connected to ground while the micromesh has a negative voltage, and the drift plane has been assigned a more negative voltage. For measuring current from the micromesh, the anode plane and the drift plane have been biased with more positive and more negative voltages with respect to the micromesh which is grounded. Similarly, drift current I_C has been measured by putting the drift plane at ground potential and the mesh to a positive voltage and the anode to a higher positive voltages.

3 Experimental Results

Electron transparency (the fraction of electrons passing through the micromesh holes from drift to amplification region) of a bulk Micromegas detector is estimated by varying drift field as shown in Fig. 3 for the three gas mixtures at room temperature and pressure. The figure shows that the electron transparency goes on increasing with the drift field becomes maximum at a certain drift field and then begins to decrease with the increase in drift field. The transparency is more than 90% in the drift field regions 50--400, 50--500 and $330\text{--}1100\,\text{V/cm}$ for Argon + Isobutane (95:5), Argon + CF₄ + Isobutane (95:3:2) and Argon + CO₂ (80:20) gas mixtures, respectively. After that, the transparency goes down with increase in the drift field in all these three gas mixtures.

The I_C and I_M have been measured by changing the electric field (E_z) in region -2 across first drift mesh and second drift mesh as shown in Fig. 1. IBF has been measured by varying drift field keeping the amplification field at a constant value. The results of I_C , I_M and hence IBF with FR have been shown respectively for three gas mixtures Argon + CO₂ (80:20), Argon + Isobutane (95:5) and Argon + CF₄ + Isobutane (95:3:2). Figures 4, 5 and 6 give the variation of I_C , I_M and IBF with FR estimated for Argon + Isobutane (95:5) gas mixture.

Similarly, Figs. 7, 8, 9, 10, 11, 12 represents the I_C , I_M and IBF with FR obtained for Argon + CF_4 + Isobutane (95:3:2) and Argon + CO_2 (80:20), respectively. The results of I_C with FR in the Figs. 4, 7 and 10 show that I_C increases for both positive and negative values of E_z . However, increase in I_C is more when E_z is positive. The results of I_M with FR in Figs. 5, 8 and 11 show that I_M also increases significantly, in comparison with its value when E_z is zero, significantly when E_z is positive. I_M also decreases when E_z is negative than when $E_z = 0$ in both Argon + Isobutane and

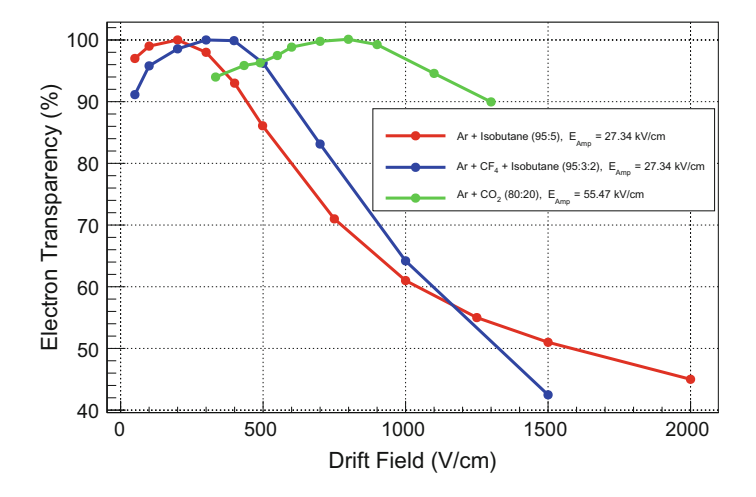


Fig. 3 Effect of drift field on electron transparency

P. K. Rout et al.

Fig. 4 Variation of I_C with FR

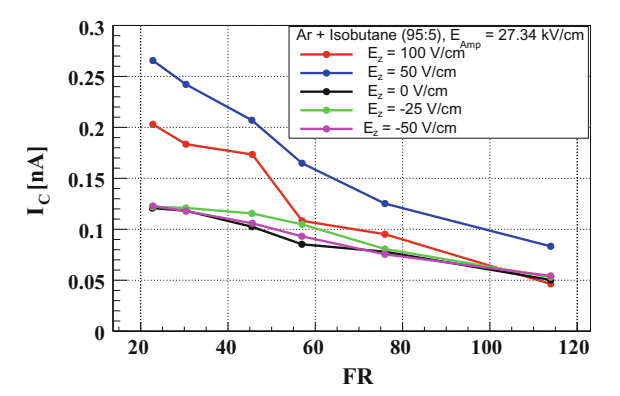


Fig. 5 Variation of I_M with FR

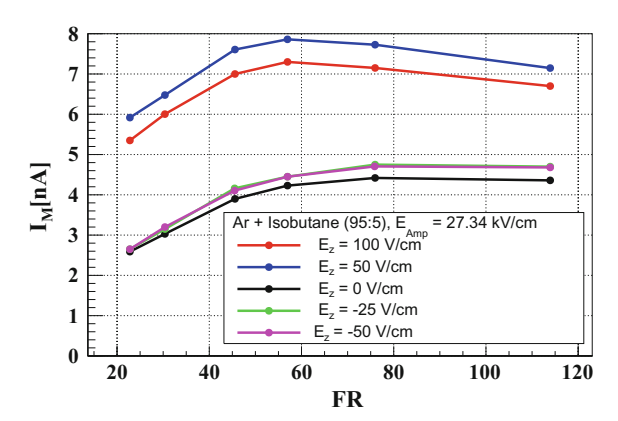


Fig. 6 Variation of IBF with FR

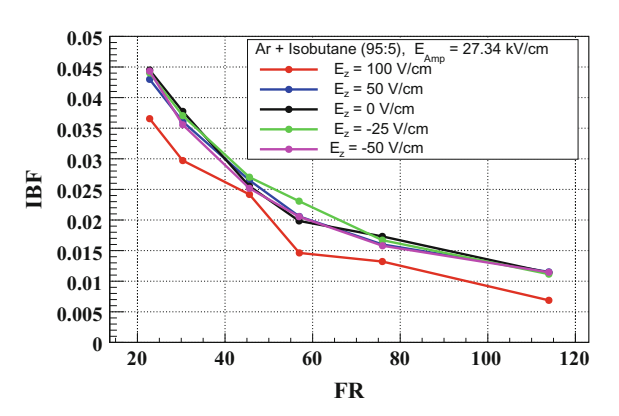


Fig. 7 Variation of I_C with ER

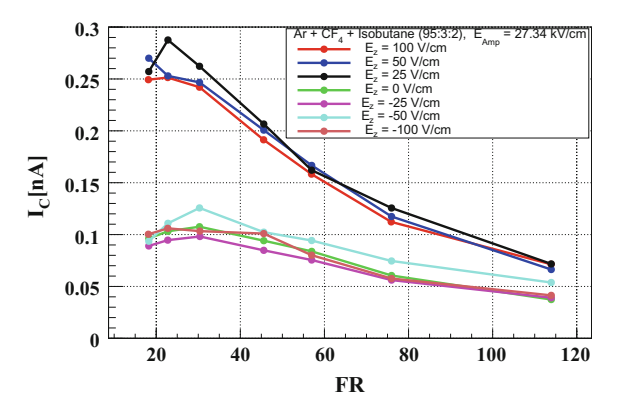


Fig. 8 Variation of I_M with FR

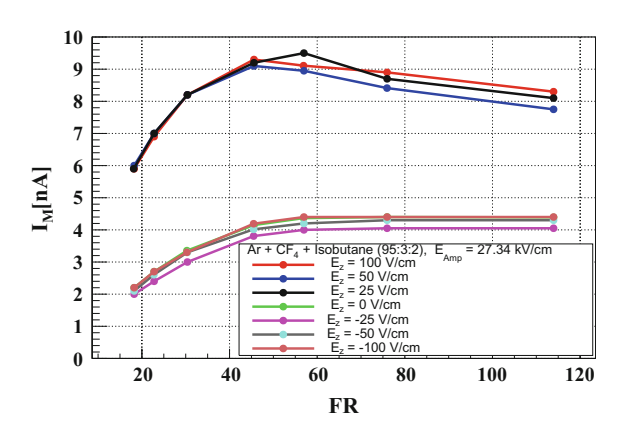
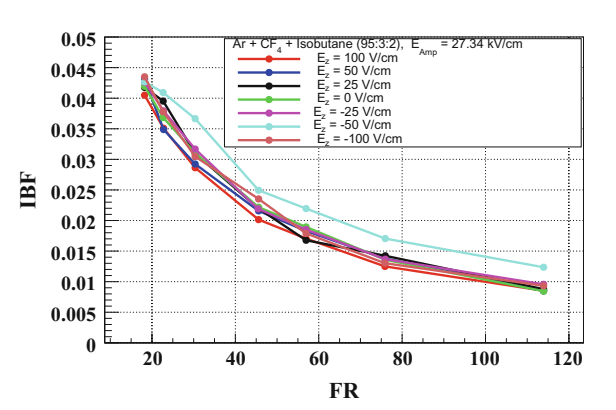


Fig. 9 Variation of IBF with FR



P. K. Rout et al.

Fig. 10 Variation of I_C with FR

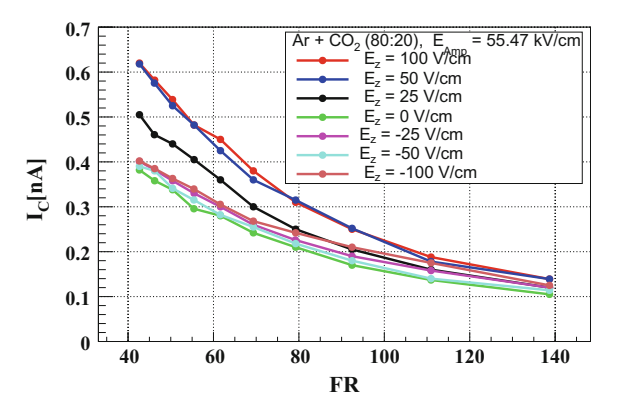


Fig. 11 Variation of I_M with FR

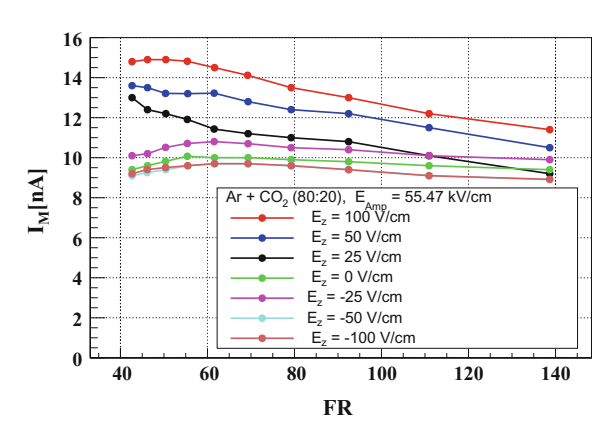
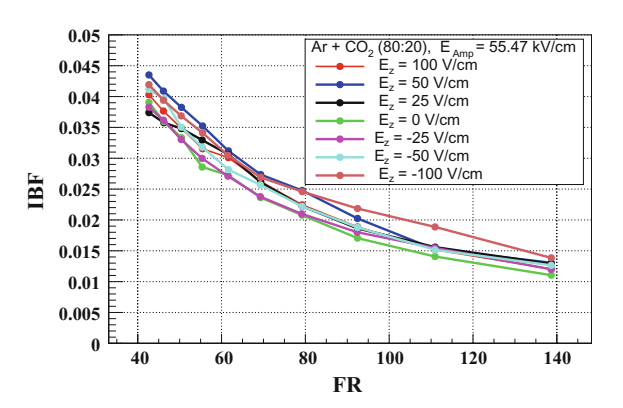
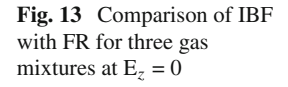
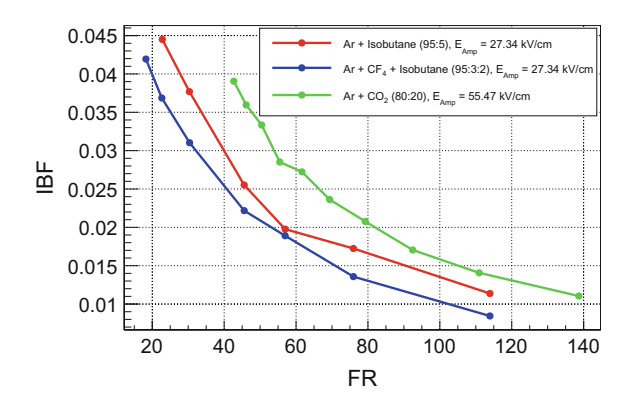


Fig. 12 Variation of IBF with FR







Argon + CF₄ + Isobutane gas mixtures as well. However, the trend is not same for Ar + CO₂ at $E_z = -25 \,\text{kV/cm}$. From the results of variation of IBF with FR, it is observed that IBF is more for $E_z = 0$ than those for E_z is positive and less than those for E_z is negative in case of the two gas mixtures, Argon + Isobutane and Argon + CF₄ + Isobutane as shown in Figs. 6 and 9, respectively. However, in case of Argon + CO₂ as shown in Fig. 12, IBF is less at $E_z = 0$ and increases for E_z as it becomes positive and negative.

At $E_z = 0$, the IBF for three gas mixtures has been compared with the range of field ratios as shown in Fig. 13. In the FR range 40–140, the IBF is higher in Argon + CO_2 gas mixture than the other two gas mixtures. The transparency is directly related to the performance of IBF. The electron transparency is good in the low-drift field regions for all the three gas mixtures, and it becomes bad in the high-drift field regions. The IBF decreases with increase in FR which falls in the lower drift field region and increases with decrease in FR which falls in the higher drift field region.

Ion backflow depends on geometrical parameters of the detector such as amplification gap and mesh hole pitch as well [3]. A bulk Micromegas detector with larger gap leads to less ion backflow than one with a smaller gap. This is because, to obtain the same order of gain, a lower amplification field is required in a detector with larger gap. Since transverse diffusion coefficient (σ_t) is larger for lower values of field, the backflow fraction is reduced as a consequence. Similarly, backflow fraction is higher for a detector with larger pitch due to the larger opening.

4 Conclusion

The present work involves the measurements of cathode and the mesh currents for three Argon-based gas compositions and estimation of corresponding ion backflow fraction of a $128 \,\mu\text{m}$ bulk Micromegas detector using experimental set-up comprising two drift meshes. The aim of this work has been to develop an experimental set-up

90 P. K. Rout et al.

for the measurement of ion backflow and optimization of different experimental parameters as well. We have measured the I_C , I_M and IBF for the bulk Micromegas detector by changing the electric field (E_z) . The optimization of IBF is non-trivial and needs to be investigated further.

Acknowledgements We thank Mr. Pradipta Kumar Das, Mr. Sridhar Tripathy, Mr. Abhik Jash and Prof. Satyajit Saha for their help and support. We also acknowledge Institutional help in terms of both necessary facilities and financial support.

References

- P. Colas, I. Giomataris, V. Lepeltier, Ion backflow in the Micromegas TPC for the future linear collider. Nucl. Instrum. Meth. A 535, 226 (2004)
- Purba Bhattacharya et al., Performance studies of bulk Micromegas of different design parameters. J. Instr. 9, C04037 (2014)
- 3. Purba Bhattacharya et al., Investigation of ion backflow in bulk micromegas detectors. J. Instr. **10**, P09017 (2015)
- Bhattacharya, D.S., et al., Experimental and numerical simulation of a TPC like set up for the measurement of ion backflow. Nucl. Instrum. Meth. https://doi.org/10.1016/j.nima.2017.04.031

Study of Characteristics of Quadruple GEM Detector with Different Gas Flow Rates

Sagarika Swain, P. K. Sahu, Deb Sankar Bhattacharya and S. Sahu

Abstract A systematic study is performed for a quadruple Gas Electron Multiplier (GEM) setup at High Energy Detector (HED) laboratory, IOP, by changing the gas flow rates. Gas flow rate can play a major role on the detector response for any gaseous detector operated in flow mode. In this study, we use a $10\,\mathrm{cm}\times10\,\mathrm{cm}$ double mask quadruple GEM detector prototype with Ar + CO₂ mixture in 70:30 ratio at different gas flow rates. For preliminary characteristics study, anode current and count rate are measured with voltage for the setup using Cs¹³⁷ source. The flow rates are recorded from a mass flow monitor built in house. The operating flow rate value for the detector setup is estimated from the results.

1 Introduction

In recent years, a significant development has occurred in the field of Micro-Pattern Gas Detector (MPGD), due to their potential applications in high energy particle and nuclear physics experiments [1]. Gas Electron Multiplier (GEM) detector draws a lot of attention worldwide because of its advanced features like high count rate measurements, excellent spatial resolution, gain stability, lower discharge probability, reduced ion feedback fraction, and flexibility in design and geometry [2–6].

The quadruple GEM detector used in these measurements consists of four GEM foils placed between a cathode (drift plane) and an anode (readout plane) electrodes. The gap between the cathode and the first GEM foil acts as drift region, where the primary ionization occurs by the incident radiation. The gap between the last GEM and the readout (anode) is induction region, where after avalanche, the charges are collected and induced a signal. The other gaps between the consecutive GEMs are the transfer gaps, where the fields transfer the secondary avalanched electrons to next level. Fields across all these gaps have proportional effect on gas gain and also on the

S. Swain (\boxtimes) · P. K. Sahu · D. S. Bhattacharya · S. Sahu Institute of Physics, HBNI P.O: Sainik School, Sachivalaya Marg, Bhubaneswar 751005, India e-mail: sswain@cern.ch; sagarika@iopb.res.in

92 S. Swain et al.

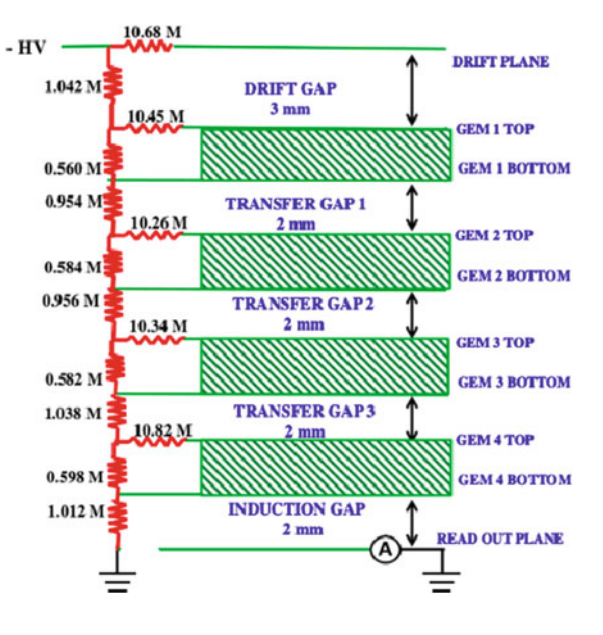
detector performance. But the typical gas gain value is highly dependent upon the parameters like temperature and pressure of the gas mixture [7–9]. In this paper, we have presented the study of the operation of a quadruple GEM prototype by varying the gas flow rates at room temperature. The effect of gas flow rate upon count rate measurement for Cs¹³⁷ source has also been investigated.

2 Detector Configuration

In this study, we have used a quadruple GEM setup, consists of four layers of $10\times10\,\text{cm}^2$ double mask GEM foils obtained from CERN. The drift gap, three transfer gaps, and the induction gap are made 3, 2, 2, 2, 2 mm, respectively. The drift plane is a 50 μ m kapton foil with a copper layer of 5 μ m on one side, which faces top of GEM1, the readout plane is a two-dimensional PCB with 120 readout pads each of area 9 mm \times 9 mm. All the readout pads are connected to a 128 pin connector. A sum-up board (provided by CERN) is used to add all the signals from all pads. The sum-up board has a female lemo output.

The whole setup along with the readout is placed on a copper plate and properly grounded. A voltage dividers circuit has been used externally for providing the potential to the drift plane and four GEM layers. The typical fields are in the order of 2–3.5 kV in transfer and induction gaps and 1.5–2.5 kV in drift gap. The potential difference across each GEM layer is 260–380 V. The setup with dividers circuit is given in Fig. 1.

Fig. 1 Schematic view of a quadruple GEM detector along with high voltage dividers scheme



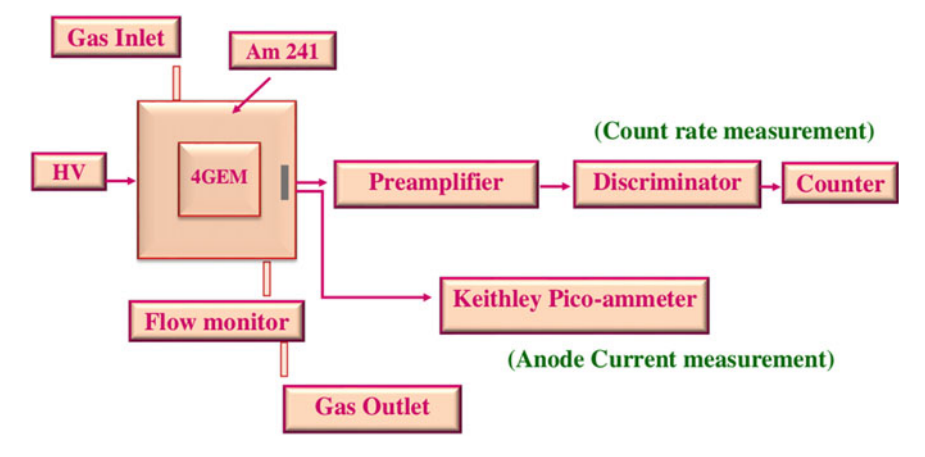


Fig. 2 Schematic diagram of experimental setup, used for count rate measurement and anode current measurements using $Ar + CO_2$ mixture in 70:30 ratio. Either count rate measurement or anode current measurement is done at a time

The chamber is continuously flowed with $Ar + CO_2$ gas mixture in 70:30 ratio throughout the experiment with a variation of flow rates from 40 to 160 SCCM (standard cubic centimeter per minute). The corresponding flow rates as well as the ambient parameters such as temperature, pressure, and relative humidity are recorded in a data logger [10]. A sum-up board with a female lemo output connector is used for extracting the signal, measuring total counts as well as anode current from the readout plane. The electronic signal is amplified through a charge sensitive preamplifier and recorded in a digital oscilloscope. A discriminator is used to reduce the electronic noise for a particular threshold voltage. The extracted signal is then fed to a scalar counter to measure count rates. For anode current, we have connected the detector output directly to a pico-ammeter via a lemo cable.

The count rate is observed with and without source by increasing applied voltage at a lowest flow rate, i.e., 40 SCCM. From now onward, the count rate means the difference of count rate with and without source, i.e., the count rate is for only source particles. To measure the count rate, the threshold to discriminator is set at 260 mV to cut maximum noise. For the count rate, a NIM scaler is used. For the same setting, the anode current is also measured. The same procedure is adopted, when we increase gradually the flow rates. For each flow rate settings, the detector is kept for sometime for a stable condition before taking any reading. The schematic diagram for total experimental setup is shown in Fig. 2.

3 Results

The detector has been operated with $Ar + CO_2$ gas in 70:30 ratio, with a different gas flow rates, e.g., 40–160 SCCM for a constant interval. At first keeping a voltage constant, the count rates are measured by varying the gas flow rate from 40 to

94 S. Swain et al.

160 SCCM. These measurements are repeated for several constant voltage settings from 4000 to 4600 V with an interval of 100 V. The variation of counts with applied voltages and flow rates are shown in Fig. 3. It clearly appears that the count is increasing with increasing gas flow rate and acquires a maximum at 120 SCCM for almost all the voltage settings. Same kind of behavior for triple GEM detector is reported in [11].

It is observed from Fig. 3 for all voltage settings, the count rate is maximum at a gas flow rate 120 SCCM. Hence, the variation of count rate as a function of voltage at a gas flow rate 120 SCCM is plotted in Fig. 4. It clearly shows that the count rate increases with increasing applied voltage and, after a certain voltage, it shows a saturating behavior. In this measurement, a plateau is obtained at 4300 V onward. Since this measurement is carried out with a source that can emit a constant rate of particles, it can be said that the full efficiency of the detector obtained is above 4300 V.

Fig. 3 Count rates for quadruple GEM prototype as a function of gas flow rates for different voltage settings

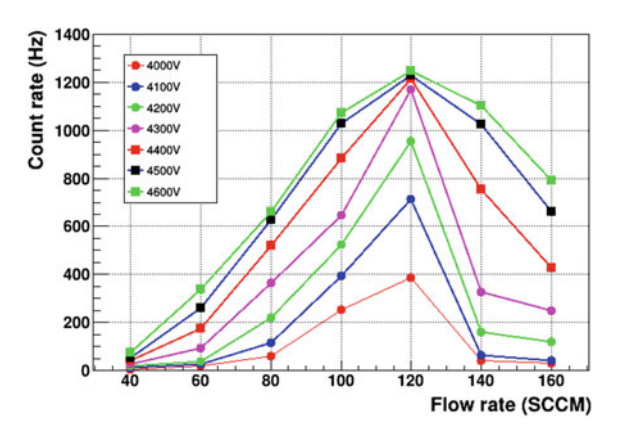


Fig. 4 Count rates for quadruple GEM prototype as a function of high voltages at gas flow rate 120 SCCM

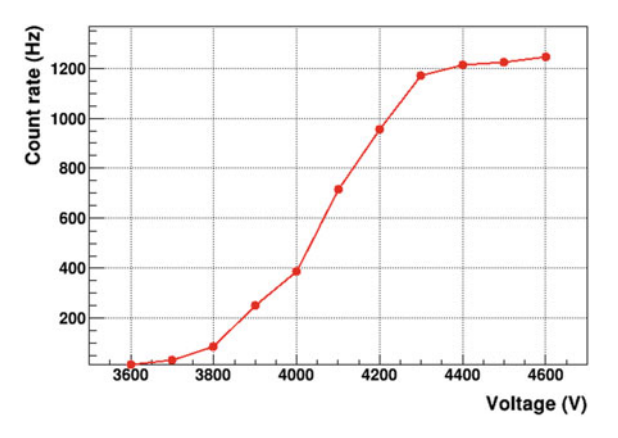
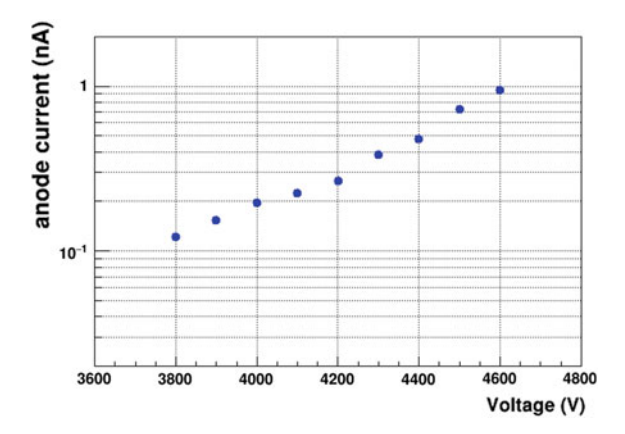


Fig. 5 Anode current as a function of applied voltage for Cs¹³⁷ for the quadruple GEM detector at a gas flow rate of 120 SCCM



Another important measurement in this study is the anode current measurement. The anode current from the detector readout is measured for Cs^{137} radioactive source with increasing voltage. Keeping the gas flow rate at 120 SCCM, the anode current is measured with and without the source at different voltage settings. For a particular voltage setting, the difference of currents with and without source gives the anode current for the source. The variation of anode current for the source as a function of applied voltage is shown in Fig. 5. We observe an exponential increasing of current with the increasing voltage.

4 Summary and Outlooks

The basic characterization has been carried out for a quadruple GEM detector prototype with conventional NIM electronics. All the measurements have been done using Cs^{137} source with premixed $Ar+CO_2$ gas in 70:30 ratio. Main emphasis is given to the performance of a GEM detector at different gas flow rates. Gas flow rate is varied from 40–160 SCCM at an interval of 20 SCCM, and the count rate is measured. The result shows that count rate increases with gas flow rate, reaches a maximum at a flow rate of 120 SCCM, and again decreases. At a gas flow rate of 120 SCCM, the anode current is measured varying the applied voltage to the divider. An exponential increase of anode current with voltage guarantees the proper operation of a detector. It also shows that gain is also increasing with voltage exponentially.

The measurement reported here has been performed with Cs^{137} source. Since the number of primary electrons for Cs^{137} source in $Ar+CO_2$ gas mixture is not known, the absolute gain cannot be calculated. The same measurement will be carried out in near future with a strong Fe^{55} X-ray source, where the number of primary electrons in $Ar+CO_2$ gas mixture is known. We would also like to repeat the measurement of gas flow rate dependency with smaller interval of flow rate.

96 S. Swain et al.

Acknowledgements The authors are thankful to Prof. Sudhakar Panda, Director, IOP, Bhubaneswar for his support in this work. This work is also partially supported by the ALICE-India fund of DAE-DST, Government of India. Authors would also like to thank Dr. Saikat Biswas for the fruitful suggestion and discussion.

References

- 1. L. Shekhtman, Micro-pattern gaseous detectors. Nucl. Instr. Meth. A 494, 128–141 (2002)
- F. Sauli, GEM: a new concept for electron amplification in gas detectors. Nucl. Instr. Meth. A 386, 531–534 (1997)
- 3. S. Bachmann et al., Development and applications of the gas electron multiplier. Nucl. Instr. Meth. A 471, 115–119 (2001)
- F. Sauli, The gas electron multiplier (GEM): operating principles and applications. Nucl. Instr. Meth. A 805, 2–24 (2016)
- A. Bressan et al., High rate behavior and discharge limits in micro-pattern detectors. Nucl. Instr. Meth. A 424, 321–342 (1999)
- A. Bressan et al., Two-dimensional readout in GEM detectors. Nucl. Instr. Meth. A 425, 254 (1999)
- A. Bondar et al., High pressure operation of the triple-GEM detector in pure Ne, Ar and Xe. Nucl. Instr. Meth. A 481, 200–203 (2002)
- 8. S. Biswas et al., Study of the characteristics of GEM detectors for the future FAIR experiment CBM. Nucl. Nucl. Instr. Meth. A **718**, 403–405 (2013)
- 9. R.P. Adak et al., JINST 11, T10001 (2016). https://doi.org/10.1088/1748-0221/11/10/T10001
- Sahu,S. et al.: Design and fabrication of data logger to measure the ambient parameters in gas detector R&D, 2017 JINST 12 C05006, https://doi.org/10.1088/1748-0221/12/05/C05006
- R.N. Patra et al., Characterisations of GEM detector prototype. Nucl. Nucl. Instr. Meth. A 824, 501–503 (2016)

Comparison of Si, Ge, and Diamond Sensors for Using It in HEP Experiments

Shyam Kumar, Raghava Varma, K. Das Gupta, Pradeep Sarin and S. K. Deb

Abstract Silicon detectors are widely used in high energy physics experiments for high precision tracking and reconstruction of primary and secondary vertices with good resolution. These detectors are close to the interaction points so they suffer very high fluence of particles and can be infected with radiation damage which can reduce the signal-to-noise ratio which is a very important quantity in any experiment. In this paper, we compare some of the important quantities such as the energy loss and the charge created by minimum ionizing particle (MIP), noise levels, multiple scattering, and radiation damage of Si, Ge, and Diamond and investigate which one will more suited for future collider experiments, where the luminosity and energy of the collision will be very high. We also show the results of diamond film grown by us in the laboratory and also the testing of various diamond films.

1 Simulation for Energy Loss and Charge Created by MIP

The simulation for energy deposited and charge created by MIP in 300 μ m thick Si, Ge, and Diamond have been done in the PANDARoot framework using GEANT3 [1]. The distribution of energy loss is Landau with a long tail which shows the creation of delta electrons. The mean and most probable value (MPV) of energy deposited in Si, Ge, and Diamond sensors of 300 μ m thickness are shown in Fig. 1. The energy deposited is larger in case of Ge ($\rho = 5.3 \, \text{g/cm}^3$) and Diamond ($\rho = 3.51 \, \text{g/cm}^3$) than Si ($\rho = 2.33 \, \text{g/cm}^3$) because of them having larger density. The distribution of the charge collected is shown in Fig. 1. The charge created is responsible for the signal formation.

S. Kumar (⊠) · R. Varma · K. Das Gupta · P. Sarin Department of Physics, IIT Bombay, Powai, Mumbai 400076, India e-mail: shyam055119@gmail.com

S. K. Deb

CRNTS, IIT Bombay, Powai, Mumbai 400076, India e-mail: sudip.deb@iitb.ac.in

[©] Springer Nature Singapore Pte Ltd. 2018
S. Biswas et al. (eds.), Advanced Detectors for Nuclear, High Energy

98 S. Kumar et al.

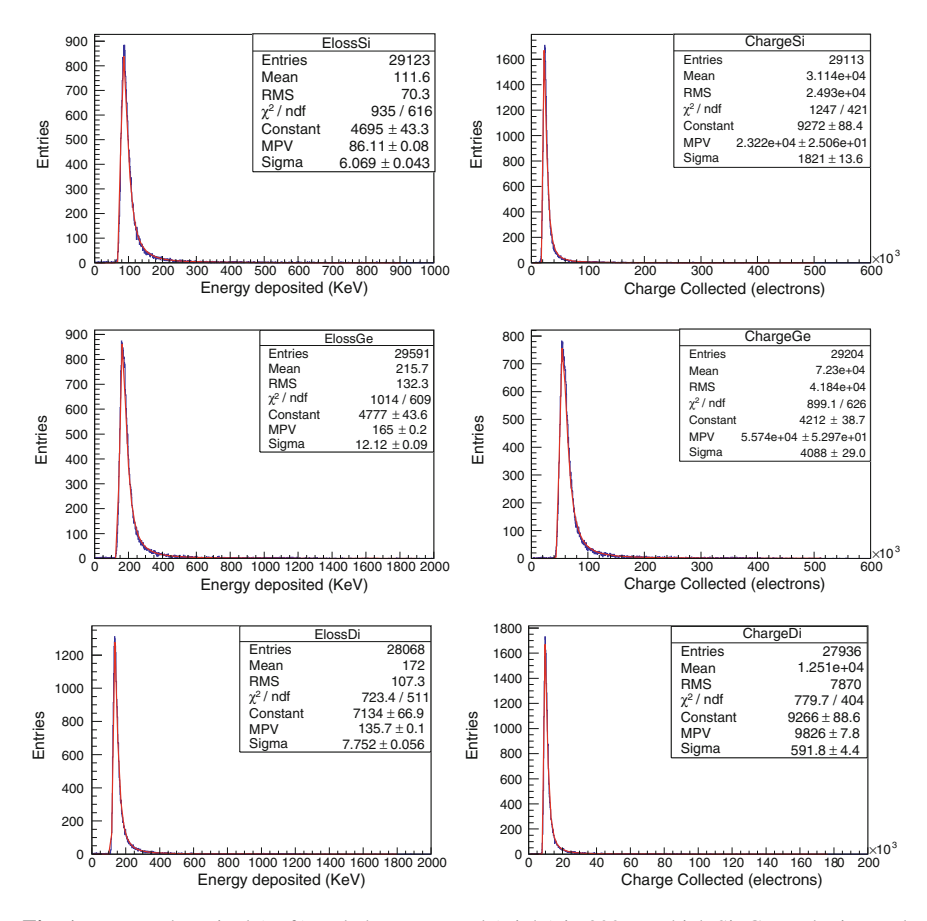


Fig. 1 Energy deposited (Left) and charge created (Right) in $300\,\mu m$ thick Si, Ge, and Diamond sensors

Table 1 Signal and intrinsic noise levels for $5.0 \times 5.0 \times 0.3$ mm³ Si, Ge, and Diamond sensors

| Material | MPV signal (e) | ρ (Ωm) | $\mu_e(\frac{\mathrm{cm}^2}{Vs})$ | $\mu_h(\frac{\text{cm}^2}{Vs})$ | Noise (e) |
|-----------|----------------|------------------|-----------------------------------|---------------------------------|----------------------|
| Silicon | 23,220 | 640 | 1450 | 505 | 3.8×10^{8} |
| Germanium | 55,740 | 0.46 | 3900 | 1800 | 1.5×10^{11} |
| Diamond | 9826 | 10 ¹² | 1800 | 1600 | 0.14 |

| Material | MPV signal (e) | Voltage (V) | Current | ρ (Ωm) | Noise (e) | Signal/noise |
|----------|----------------|-------------|---------|----------------------|-----------|--------------|
| Silicon | 23,220 | 300 | 1 μΑ | 2.5×10^{7} | 9591 | 2.421 |
| Silicon | 23,220 | 300 | 1 nA | 2.5×10^{10} | 10 | 2322 |

Table 2 Reverse biased Silicon sensor of dimension $5.0 \times 5.0 \times 0.3 \,\mathrm{mm}^3$

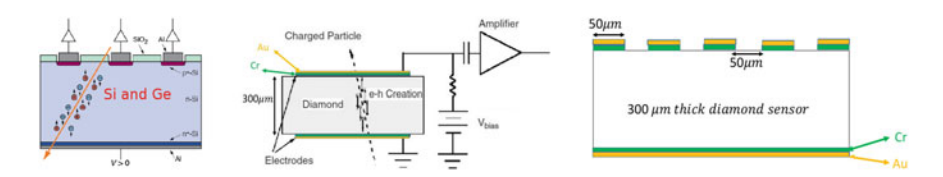


Fig. 2 Si and Ge detector concept (Left), diamond pad detector (Middle) and single-sided strip detector of diamond (Right)

2 Concept of Detector

The concept of detector depends on the intrinsic noise levels of the sensors. If we have $5.0 \times 5.0 \times 0.3$ mm³ Si, Ge, and Diamond sensors, then the intrinsic noise level can be calculated by using the formula $\sigma = q(n_e\mu_e + n_h\mu_h)$, for intrinsic material $n_e = n_h = n_i$. The charge created depends on the thickness of material is responsible for the signal as shown in Fig. 1. The signal created by MIP can only be increased by increasing the thickness of the material. The intrinsic signal-to-noise ratio for Si $(\approx 10^{-4})$, Ge $(\approx 10^{-6})$ are very small but for diamond this is of the order of $\approx 10^5$ (Table 1). The intrinsic diamond has very high signal-to-noise ratio so intrinsic diamond can be used as detector material just by depositing ohmic contact, while intrinsic Si and Ge cannot be used as detector, so we have to somehow decrease the noise levels (or equivalently increase the resistivity), the only way of doing this is the doping (making p-n junction) in the material. The doping in silicon reduces the intrinsic carriers drastically and equivalently enhances signal-to-noise ratio Table 2. We have used some rough numbers for the leakage current to get an idea about signal-to-noise ratio. For Si and Ge, if we want to use as sensors in these collider experiments, we need to make p-n junction, while intrinsic diamond can be used as detector applications just by depositing ohmic contact on it (Fig. 2).

3 Estimation of Signal-to-Noise Ratio

The noise is characterized in terms of equivalent noise charge (ENC). There are several sources of noise, shot noise due to leakage current (ENC_{I_L}), thermal noise due to parallel resistance (ENC_{R_p}), series thermal noise due to metal strip resistance (ENC_{R_p}) and preamplifier noise which depends on amplifier design parameters and

100 S. Kumar et al.

also on the detector capacitance ($ENC_C = a + b C_d(pF)$). The overall noise is characterized by ENC in terms of electrons (e) which can be calculated from the individual sources of noise [2].

$$ENC(e) = \sqrt{ENC_{I_L}^2 + ENC_{R_p}^2 + ENC_{R_s}^2 + ENC_C^2}$$
 (1)

The various noise contribution can be calculated by the expression given below:

$$ENC_{I_L} \approx 107 \sqrt{I_L(nA) t_p(\mu s)}$$
 (2)

$$ENC_{R_p} \approx 44.5 \sqrt{\frac{T(K) t_p(\mu s)}{R_p(M\Omega)}}$$
 (3)

$$ENC_{R_s} \approx 0.025 C_d(pF) \sqrt{\frac{T(K) R_s(\Omega)}{t_p(\mu s)}}$$
 (4)

To minimize the various noise contribution, the criteria below can be used.

- To minimize ENC_{R_s} and ENC_C , there should be small load capacitance $C_d = C_{strip}$ (depends on strip dimension)
- To minimize ENC_{I_t} , leakage current should be small
- To minimize ENC_{R_p} , there should be a high parallel resistance
- To minimize ENC_{R_s} , there should be a small series resistance.

For that are short-lived particles (lifetime of the order of is $10^{-13}-10^{-11}$ s), impact parameter of track will range from 30–3000 m ($c\tau$). To measure this small value, we should have good resolution in impact parameter measurement, which depends on position resolution of detectors. There are various algorithms used for position reconstruction inside sensors, digital algorithm, digital head-tail algorithm, analog head-tail algorithm and charge center of gravity method (COG) linear and nonlinear algorithms, etc. Different algorithms are used in different angles of the incident tracks and give the better results. If we use binary algorithm for position reconstruction inside sensors, the position resolution is given by $pitch/\sqrt{12}$ (for single strip cluster) and $pitch/2\sqrt{12}$ (for two strip cluster). If we use above-mentioned suitable analoge algorithm, we can get the best position resolution ($\propto pitch/(Signal/ENC)$) by using a material with large Signal/ENC (Table 3) [4].

| ENC silicon (DELPHI microvertex) [2] | ENC Diamond (Estimation) |
|--|--|
| $t_p = 1.8 \mu\text{s}, I_L = 0.3 \text{nA}, R_p = 36 \text{M}\Omega,$ $R_s = 25 \Omega, C_d = 9 \text{pF (strip)}, a = 340, b = 20$ and $T = 20 ^{\circ}\text{C}$ | $t_p = 5.0 \text{ ns}, I_L = 1.0 \text{ pA}, R_p = 36 \text{ M}\Omega,$ $R_s = 25 \Omega, C_d = 2 \text{ pF}, a = 135, b = 13 \text{ and}$ $T = 20 ^{\circ}\text{C}$ |
| $ENC_{I_L} = 78 e$ | $ENC_{I_L} = 0.24 e$ |
| $ENC_{R_p} = 170 e$ | $ENC_{R_p} = 9 e$ |
| $ENC_{R_s} = 14 e$ | $ENC_{R_s} = 61 e$ |
| $ENC_C = 520 e$ (preamplifier) | ENC_{C} =161 e (VIKING preamplifier) [3] |
| ENC = 553 e | ENC = 172 e |
| Signal/ENC = 23220/553 = 41.9 | Signal/ENC = 9826/172 = 57.1 |

Table 3 Estimation of Signal/ENC for 300 μm thick Si and Diamond by using MIP

4 Testing of Diamond Films in Department of Physics IIT Bombay

4.1 Film Grown in Laboratory

The diamond is grown in the laboratory by using MPCVD process in Department of Physics IIT Bombay. We have grown diamond film in the laboratory up to thickness 1 mm. The growth of diamond film is done on HPHT (100) diamond substrate. The substrate is cleaned with isopropyl alcohol (IPA) for 15 min in ultrasonic bath thrice, then it is baked in hydrogen environment for 15 min. The growth parameters used were $CH_4 = 5$ sccm, $H_2 = 250$ sccm, substrate temperature = 916–938 °C, pressure = 90–91 torr, power input= 0.7 kW, power reflected = 0 kW, and time = 198 hours. The diamond is cut off from the substrate by laser cutting and then polished in Surat (India). The film grown in the laboratory shows good XRD and also Raman spectra as shown in Fig. 3. The film is cleaned and then oxygen plasma treatment is done on the surface, then we have deposited the Chromium (Cr- 20 nm) and Gold (Au- 100 nm) by thermal evaporation on the surface to make ohmic contact on both sides. The I-V characteristic shows straight line up to 250 V. From Fig. 4, one can conclude that the film has a large nitrogen content as it looks yellow. We also tried to get the signal by the transient current technique (TCT) measurement but large nitrogen present in the device traps all the charges and no signal is seen. We are still trying to improve the quality of film to get the signal.

4.2 Film Grown in Commercial System

We tried to compare our results with another film grown in commercial system to improve the quality of film grown by us. The film has nitrogen content of the order S. Kumar et al.

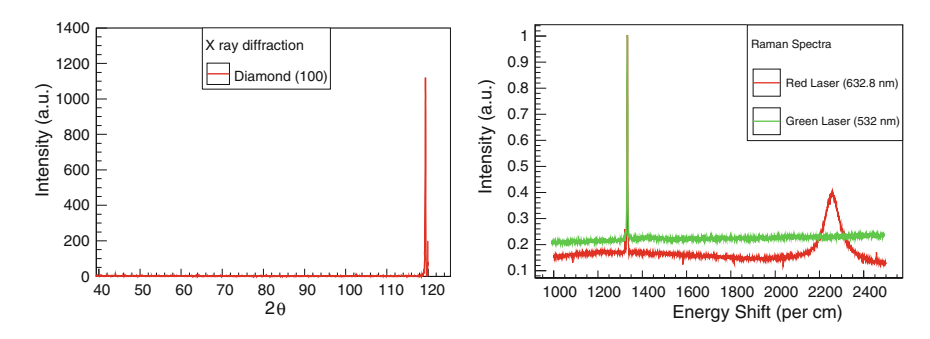


Fig. 3 XRD of the diamond film grown in laboratory shows Di (100) peak at 119.443° (Left) and Raman spectra also shows the sharp peak of diamond at 1332.3 cm⁻¹ (Right)

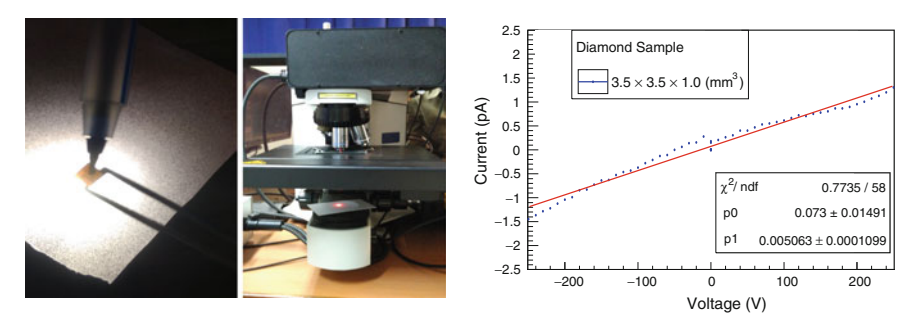


Fig. 4 Cutted and Polished diamond snap (Left), Raman spectroscopy of diamond (Middle), and I–V characteristic of diamond (Right)

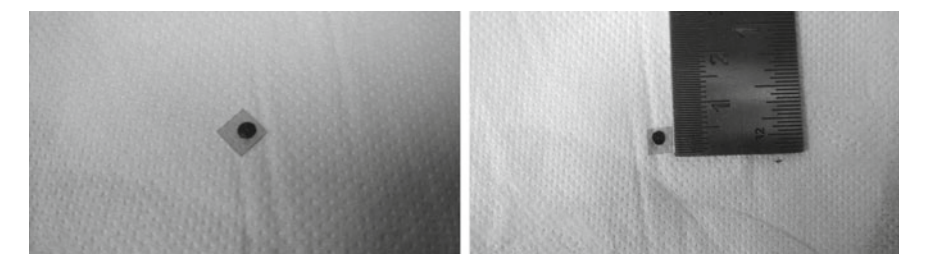


Fig. 5 Snaps of ohmic contact on diamond film grown in Surat (Left) and size of the diamond (Right)

of parts per million (ppm). Figure 5 shows the Raman spectra of film. The film is cleaned and then ohmic contact is made as mentioned above. The I–V characteristic is a straight line and shows very less current (\approx pA) as shown in Fig. 6. In this film also we tried to get the signal in transient current technique (TCT) measurement but large nitrogen traps all the charges and no signal is seen. We are still trying to improve the quality of film to get the signal.

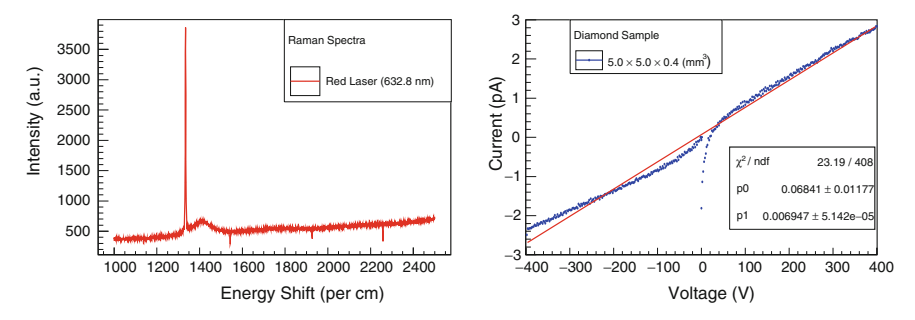


Fig. 6 Raman spectra also shows the sharp peak of diamond at 1332.3 cm⁻¹ (Left) and I–V characteristic of diamond (Right)

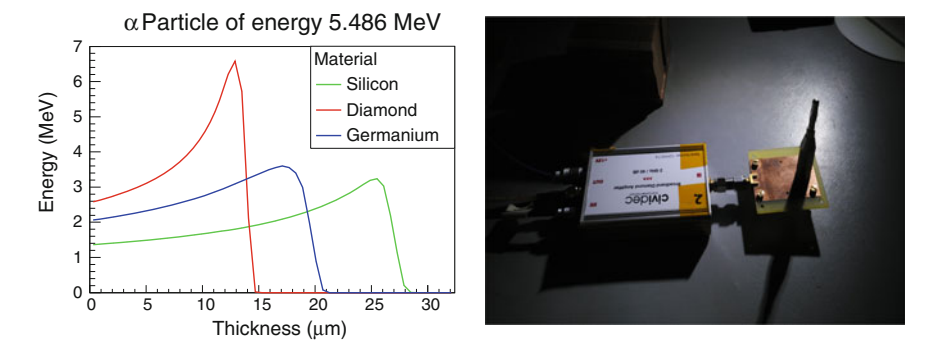


Fig. 7 FLUKA simulation for the range of α in Si, Ge, and Diamond (Left) and Cividec amplifier (CERN) setup used for TCT measurement (Right)

4.3 Film from IIa Technologies

Another diamond film of size $(3.5 \times 3.5 \times 0.4 \, \text{mm}^3)$ was purchased from IIa Technologies, Singapore. It is electronic grade and has very low nitrogen content of parts per billion (ppb) level. The diamond film is cleaned by standard process, then ohmic contact is made on it. The film has very low leakage current (\approx pA) and also low capacitance (\approx pF). TCT measurement can be used to calculate the mobilities and also charge collection efficiencies [5]. We have used alpha particle of energy 5.486 MeV from Am 241 source. Figure 7 shows the energy deposited profile in Si, Ge, and Diamond by using FLUKA simulation [6]. The charge collection efficiencies come out to be 70% at 400 V [7].

104 S. Kumar et al.

5 Conclusion

Another advantage of using diamond ($X_0 = 12.14 \, \mathrm{cm}$) as sensor in collider experiments is that it suffers from much lower multiple scatterings than Si ($X_0 = 9.37 \, \mathrm{cm}$) and Ge ($X_0 = 2.3 \, \mathrm{cm}$). Diamond because of its larger atomic displacement energy is much more radiation hard than Si or Ge [8]. Further more, because of the large mobility diamond has fast timing and hence can be used as time of flight detector and can also be used as trackers for getting good position resolution [7]. The only problem with diamond is presently we can only have high-quality single crystal diamond (charge collection efficiency = 100%) in small size and the cost is very high. We are working to grow the high-quality diamond in the laboratory (Figs. 8 and 9).

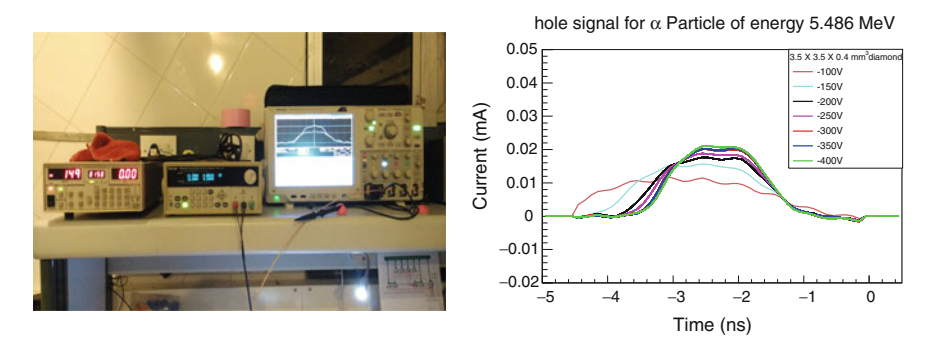


Fig. 8 Signal measurement on Digital Sampling Oscilloscope (DSO) (Left) and hole current at different voltages

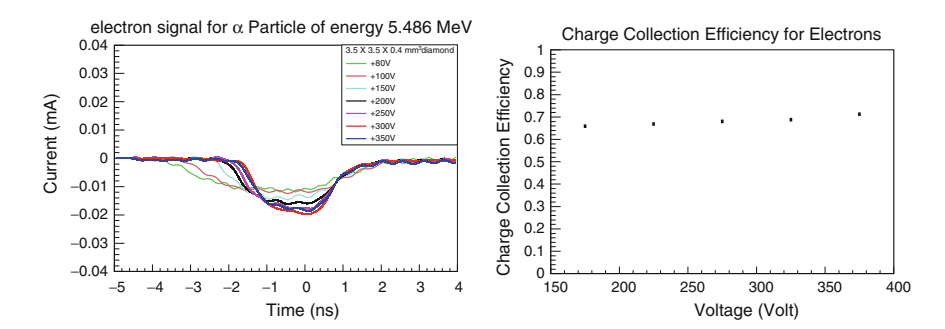


Fig. 9 Electron current at different voltages (Left) and Charge collection efficiency for electrons (Right)

References

- 1. PANDA Collaboration, Technical Design Report for the \bar{P} ANDA Micro Vertex Detector, Nov 2011
- 2. F. Hartmann, Evolution of Silicon Sensor Technology in Particle Physics (Springer, Heidelberg, 2009), pp. 26–29
- 3. F. Borchelt et al., First measurements with a diamond microstrip detector. Nucl. Instrum. Methods Phys. Res. A **354**, 318–327 (1995)
- R. Turchetta, Spatial resolution of silicon microstrip detectors. Nucl. Instrum. Methods Phys. Res. A 335, 44–58, North-Holland (1993)
- 5. H. Pernegger et al., Charge-carrier properties in synthetic single-crystal diamond measured with the transient-current technique. J. Appl. Phys. 97, 073704 (2005)
- A. Ferrari, P.R. Sala, A. Fasso, J. Ranft, FLUKA: a multi-particle transport code. CERN-2005-10. INFN/TC₀5/11, SLAC-R-773 (2005)
- S. Kumar et al., Comparison of silicon, germanium and diamond sensors for using it in HEP detector applications. Advanced Detectors for Nuclear, High Energy and Astroparticle Physics (Bose Institute, Kolkata, 2017)
- 8. S. Kumar, Comparative study of radiation damage in Si, Ge and diamond used as detector. In *Proceeding of DAE Symposium on Nuclear Physics*, vol. 61 (2016)

An Efficient Approach to Manage DMA Descriptors and Evaluate PCIe-Based DMA Performance for ALICE Common Readout Unit (CRU)

S. Mukherjee, F. Costa, R. Paul, A. Chakrabarti, S. A. Khan, J. Mitra and T. Nayak

Abstract This paper presents the status of performance evaluation of Peripheral Component Interconnect (PCIe)-based Direct Memory Access (DMA) engine for A Large Ion Collider Experiment-Common Readout Unit (ALICE-CRU) upgrade program using advanced Intel Arria 10 FPGA. The CRU will mainly read out most of the upgraded sub-detectors data and transport the same through the PCIe-DMA engine to server. DMA engine moves data using descriptor. DMA controller pushes those descriptors toward DMA engine. The main goal of this paper is to explain the way DMA engine is to be controlled by DMA controller such that max DMA performance can be achieved. The DMA performance has been evaluated on various server grade machines using Intel Arria 10 FPGA kit (https://www.altera.com/ products/boards and kits/dev-kits/altera/kit-a10-gx-fpga.html, [1]). The result is around 95% of theoretical DMA engine bandwidth.

S. Mukherjee (⋈)

Centre for Astroparticle Physics and Space Science, Bose Institute,

Kolkata 700091, India

e-mail: sanjoy.mukherjee@cern.ch, sanjoym@jcbose.ac.in

F. Costa · T. Nayak

Organisation Europeenne Pour la Recherche Nucleaire, Geneva, Switzerland

e-mail: filippo.costa@cern.ch

T. Navak

e-mail: tapan.nayak@cern.ch

R. Paul · A. Chakrabarti

University of Calcutta, Kolkata 700098, India

e-mail: rourab.paul@cern.ch

A. Chakrabarti

e-mail: amlan.charkrabarti@cern.ch

S. A. Khan · J. Mitra

Variable Energy Cyclotron Centre, HBNI, Kolkata 700064, India

e-mail: shuaib.ahmad.khan@cern.ch

J. Mitra

e-mail: jubin.mitra@cern.ch

© Springer Nature Singapore Pte Ltd. 2018

S. Biswas et al. (eds.), Advanced Detectors for Nuclear, High Energy and Astroparticle Physics, Springer Proceedings in Physics 201, https://doi.org/10.1007/978-981-10-7665-7_10

S. Mukherjee et al.

1 Introduction

ALICE is the detector system at Large Hardon Collider, Organisation Europeenne Pour la Recherche Nucleaire, (LHC, CERN) dedicated particularly to study the properties of Quark Gluon Plasma (QGP). The detector system of ALICE will undergo a major upgrade during the upcoming Long Shutdown 2 (LS2) which is at present foreseen to start in July 2018. Most of detector sub-systems will upgrade their detector hardware and associated electronics to support higher collision rate and luminosity aimed at precision measurements of the OGP.

A new readout card, CRU [2], has been developed, and it will be used by all the upgraded detector systems to read out detector data. The card will receive detector data in either triggered or continuous readout mode with a new detector data link called Giga Bit Transceiver (GBT) [3]. The detector data might be processed inside CRU, and then, the CRU will store the data in the memory of the server through two PCIe [4] Gen.3 x8 performing DMA.

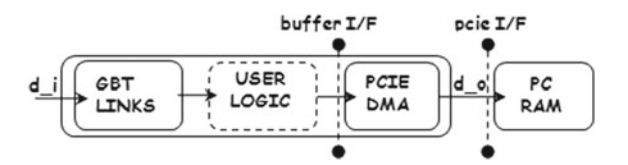
In this paper, we introduce the motivation behind the evaluation of DMA engine implemented in FPGA and then briefly describe design based on DMA engine. The paper explains the details of implementation and the interfacing between firmware and software during evaluation. It also shows the results obtained during the test concerning data throughput and PCIe usage.

2 Motivation Behind Evaluation

The main task of CRU is to transport the data received over GBT with or without processing to the memory of readout server. The total input data throughput will be very high as CRU will receive detector data over several GBT links @4.8 Gbps maximum. As an example, in case of Time Projection Chamber (TPC), the incoming user data bandwidth will be around 90 Gbps. The CRU is equipped with an Intel Arria 10 FPGA that provides two PCIe endpoints Gen.3 x8 to provide raw bandwidth of 128 Gbps. DMA will be used to move the data over PCIe. Fig. 1 shows preliminary data flow model of CRU. The first motivation behind DMA evaluation is to find out maximum bandwidth that can be achieved.

The second motivation is related to buffer interface shown in Fig. 1. It has been implemented to manage CRU data flow. The time required to read out the data from card using DMA is larger than to write the same into card; this is due to PCIe protocol

Fig. 1 CRU data flow model



overhead, and unless the old data has not been moved out completely, we could not push new data. This creates dead time between two memory writes. For this reason, a First In FIRST Out (FIFO) is used as buffer to keep the data received during dead time. The dead time can vary from its mean value due to unavailability of PCIe. It is therefore very important to collect statistical values of the PCIe unavailability time to tune the buffer size.

3 Evaluation Goals

To measure the throughput of DMA engine, an internal data generator has been developed to push the data in card memory at maximum rate and DMA controller logic has to be operated in such a way that data could be read out as fast as possible. This will give us the maximum rate at which DMA can move data over PCIe.

Once we achieved maximum DMA performance, the next goal is to measure mean dead time due to inherent latency of firmware logic and variation of dead time over long period due to PCIe unavailability. The FIFO size based on those values will be optimum as those values are collected during peak time of DMA performance.

The ultimate goal is to check the consistency of the data in system memory. The tests will validate the readout data with input data, sequence of the data received, number of received data, behavior of the system under stress, and so on.

The above goals had been achieved in two stages of evaluation. In Sect. 4, the design under evaluation will be explained and also the requirements of CRU to be fulfilled by the design. Then, in Sect. 5, we will explain about the changes made in the design to meet the requirements.

4 PCIe-DMA Design Overview

Among various designs available with Altera, we have selected design [5], shown in Fig. 2a as it provides memory mapped (MM) DMA engine to reduce some of the complexities associated with the PCIe protocol. The salient features of the PCIe-DMA core are as follows. It includes read DMA (RD DMA), write DMA (WR DMA) engines, and separate DMA controller. It does not require address translation as it supports 64-bit MM interface. In addition, the IP core handles Transaction Layer Protocol (TLP) encoding and decoding.

4.1 Design Blocks

The design has three main blocks related to DMA: Avalon MMDMA-TLP Bridge attached with PCIe Hard IP (HIP), DMA/descriptor controller, and on-chip memory.

S. Mukherjee et al.

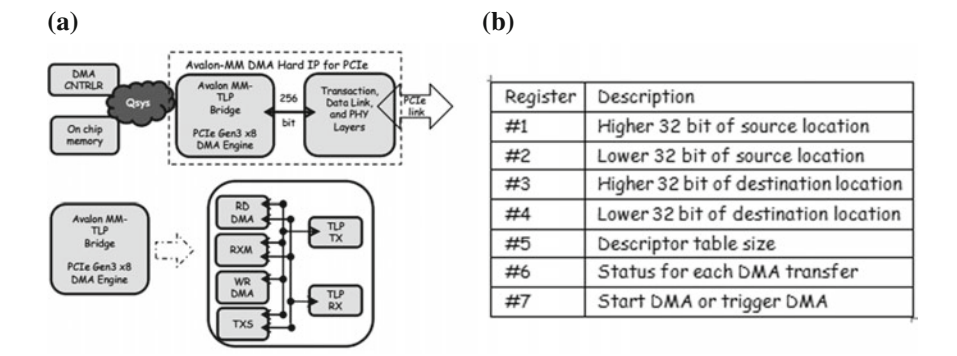


Fig. 2 a Blocks of PCIe design. b Descriptor controller registers

The internal blocks of Avalon MMDMA-TLP bridge are also shown in Fig. 2a. The modules will be explained briefly, and then, working principle of DMA will be discussed.

4.2 Avalon MMDMA-TLP Bridge

This IP core includes highly efficient RD DMA and WR DMA modules. In addition, it includes two main control modules, namely TXS and RXM, which will be explained later in this section.

The RD DMA module is optimized for moving large blocks of data from the PCIe address domain to the Avalon-MM address domain using burst data transfers. The Read Data Mover sends memory read TLPs upstream. After the completion is received, it writes the received data to the on-chip memory.

The WR DMA module is optimized for moving large blocks of data from the Avalon-MM address domain to the PCIe address domain using burst data transfers. The Write Data Mover reads data from on-chip memory and sends it upstream using memory write TLPs. Both the read DMA and write DMA modules use a 256-bit Avalon-MM datapath width.

The TX Slave module propagates 32-bit Avalon-MM reads and writes upstream. External Avalon-MM masters, including the DMA control master, can access PCI Express memory space using the TX Slave. The DMA uses this path to update the DMA status.

The RX Master module propagates single dword read and write TLPs from the Root Port to the Avalon-MM domain via a 32-bit Avalon-MM master port. Software used this master port to write and read Avalon-MM domain registers.

4.3 Descriptor Controller

The descriptor controller module manages the DMA read and writes operations. Inside the controller, there is a FIFO which is used to store the descriptors to be executed. Registers related to descriptor controller are shown in Fig. 2b.

4.4 On-Chip Memory

This IP core stores the user data. This memory has a 256-bit data width, and size is 32 kB.

4.5 Working Principle

The working principle of DMA engine is based on descriptor table. The host software programs the internal registers of the Descriptor Controller with the location and size of the descriptor table residing in the PCIe memory space through the RXM. Based on this information, the descriptor controller directs the read DMA to copy the entire table and store it in the internal FIFO. Then, the controller fetches the table entries and directs the write DMA to transfer the data from the Avalon-MM domain to the PCIe domains. It also sends DMA status upstream via the TXS slave port.

4.6 Requirements

Now, we brief the requirements of CRU which can be considered as challenges in the evaluation process. The loopback data flow of the design restricts us to push the external data. Although the descriptor controller supports a maximum transfer size of 1 MB, but the on-chip memory in this design is smaller. Consequently, this design cannot handle the maximum transfer size. The large data movement with limited card memory was one of the major challenges of evaluation process. The DMA throughput depends on the management of handshaking signal used between software and firmware. So, handshaking signals could be optimized to improve DMA performance. We managed to find out the solutions to these challenges during evaluation process.

S. Mukherjee et al.

5 PCIe-DMA Design Evaluation

In this section, we will describe the PCIe-DMA design data flow model and changes done on the same to meet CRU requirements. The non-pipelined memory write and memory read by DMA will be discussed in Sect. 5.2. The management of descriptors to read out memory by DMA in order to achieve pipelined data flow will be explained in Sect. 5.3. Then, we will discuss the interlinking that has been made between memory write and read to keep the pipeline and the effect of that on DMA performance as well as dead time. The data flow model with FIFO and further optimization of dead time will be discussed in Sects. 5.5 and 5.6, respectively.

5.1 Data Flow Model

We found that read DMA module reads data from system memory and writes into card memory and write DMA module reads back the same data from card and writes into system memory. So, it is basically loopback data flow model. In CRU, the data is to be moved from card to system side; i.e., DMA movement is unidirectional. The necessary changes have been done to break the loop and make data flow model shown in Fig. 3a. The internal data generator discussed in Sect. 3 is used to push data, and DMA engine is used to read out the same from memory.

As per the design, three kinds of memory are to be implemented in system side for DMA-based data transfer. They are descriptor memory to store the descriptors (locations and size of transfer), status memory to store the status received when one DMA transfer gets executed, and data memory to store the data.

Mainly, three handshaking signals have been shared between firmware and software to establish communication. They are as follows. The firmware sends ready signal to software once the memory has been completely written. The software triggers DMA to read out on-chip memory as soon as it receives ready signal. Once the software will receive status, i.e., DMA transfer is finished, it sends one feedback signal to firmware to fill the on-chip memory again.

5.2 Non-pipelined Memory Write and DMA Read

In non-pipelined model, entire on-chip memory has been filled up and then read out by DMA. The memory is overwritten only when it has been read out completely. So, memory write and read are going on sequentially. This is the readout scheme in non-pipelined way. This repetitive memory write and memory read by DMA has been achieved by means of status memory polling in PCIe memory space.

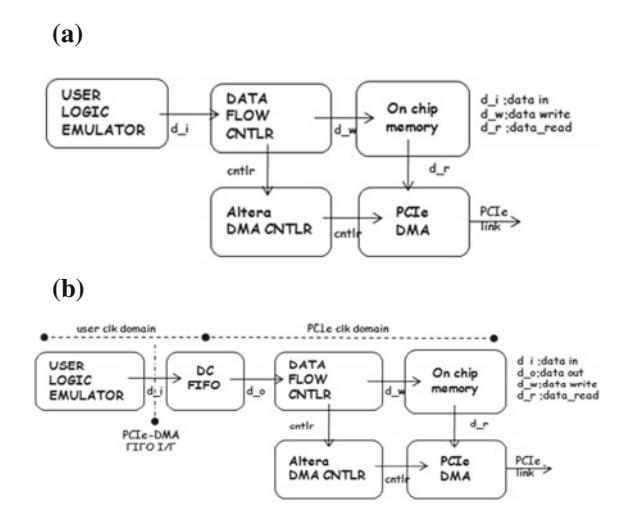


Fig. 3 a PCIe data flow model (without FIFO). b PCIe data flow model (with FIFO)

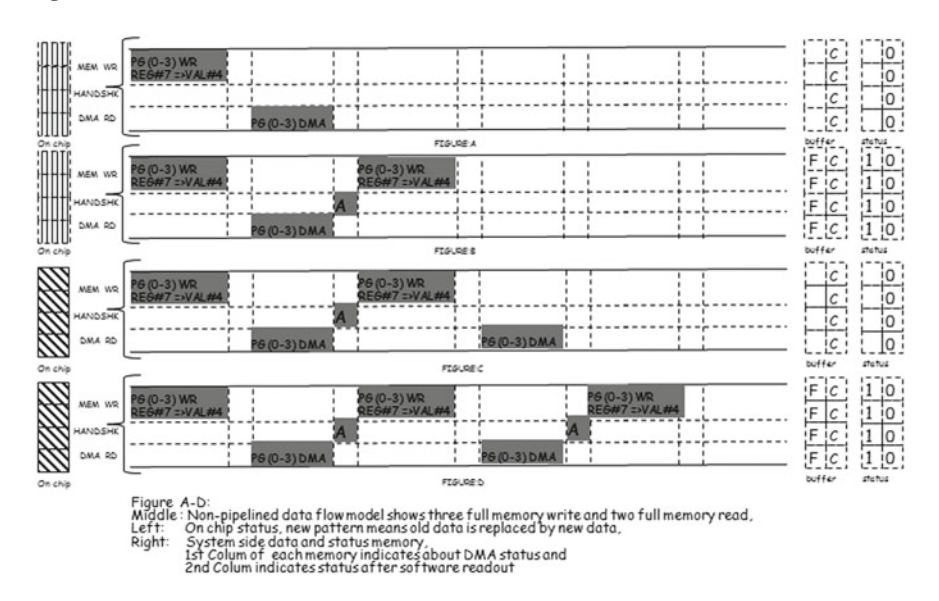


Fig. 4 Non-pipelined data flow model

The main drawback of this model is that it creates gap between two memory writes and two memory reads. The gap between two memory reads makes DMA performance low, and the gap between two memory writes creates large dead time. The non-pipelined data flow diagram is shown in Fig. 4.

S. Mukherjee et al.

5.3 Pipelined Memory Write and DMA Read

In pipelined data flow model, instead of sequential memory write and read, it has been done in parallel. This kind of readout scheme reduces dead time and makes the performance better. The page-wise memory write and read is the main motivation of this readout scheme.

The DMA transfer size is 8 kB in pipelined data flow model, and the term page is used to define 8 kB memory in card as well as system side. The term buffer is used to define 32 kB memory on system side having four pages unless otherwise specified.

At very beginning, once all pages are filled (F) up completely, software receives ready signal from firmware and triggers DMA to read out four pages. As soon as software received first status, i.e., when first page was read out successfully, software cleaned (C) and reallocated the same 8 kB buffer and sends feedback signal to firmware. Based on that, firmware filled the same page with new data as the old data had already been moved. The same logic is used for each status. So, when software received status for all four pages, firmware filled up 75% of on-chip memory with new data and rest 25% was going on.

In this way, page wise memory read and write are going on simultaneously. These are pipelined memory read and write. The pipelined data flow diagram is shown in Fig. 5.

5.4 Interdependent Memory Write and Read

The next challenge was to keep this pipelined data flow. The idea behind continuous pipelined data flow was to find out a way to interlink memory read and write in such a way that one process will trigger the other. Pipelined memory write would be continuous if we received status in continuous fashion. We will receive status only when software could trigger DMA. Software could use page ready signal, generated during page-wise memory write to trigger the DMA. Then, at the end of first 32 kB pipelined memory read, DMA transfer will be still going on as from firmware point of view, there are still some DMA transfer to be done. In this way, memory read and memory write will trigger one another by means of status and page ready signal, respectively. This interlinking between two processes makes pipelined data flow.

5.5 Dead Time and Descriptor Table Size

Each 32kB pipelined DMA transfer could reuse the same descriptor table as both source and destination memory are same and free. There is one register #5 (see Fig. 2b) in descriptor controller module to set the size of descriptor table. Based on that, descriptor controller does modulo operation on DMA programming register #7

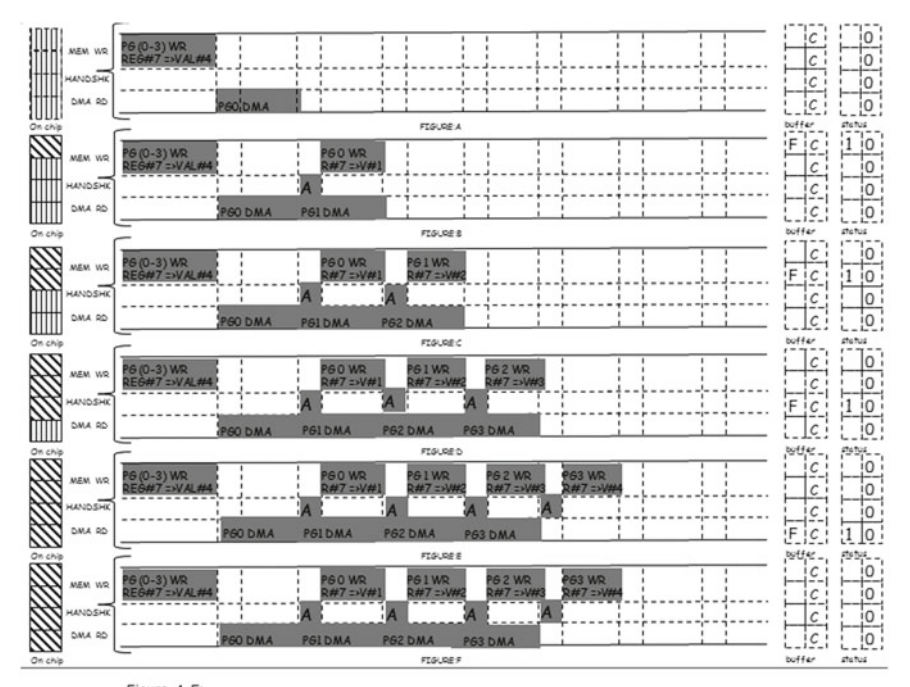


Figure A-F:
Middle: Pipelined data flow model shows four page wise memory write and four page wise DMA,
back to initial state of ter four page movement

Left:
On chip status, new pattern means old data is replaced by new data,
System side data and status memory,
1st Colum of each memory indicates about DMA status and
2nd Colum indicates status after software readout

Fig. 5 Pipelined data flow model

(see Fig. 2b). Due to modulo operation, the value of register #7 always loops within four and thus same descriptor table can be reused.

There is one drawback of using limited buffer. The tight buffer model could increase dead time. This is due to delayed feedback signal received from software if it would take much time to clean 8kB buffer and reallocate the same. Large size of buffer could minimize this issue. In this way, the dead time could be reduced further as software has large number of free 8kB pages in system memory. We allocated 1MB buffer in system memory as design support descriptor table size up to one twenty-eight. Now, the dead time is mainly due to inherent firmware and software latency plus PCIe unavailability.

S. Mukherjee et al.

5.6 Data Consistency with FIFO

In this subsection, the internal data generator that emulates the CRU user logic and writing data into on-chip memory through FIFO will be discussed. The optimization of one of the handshaking signals will be discussed very briefly after that.

Dual Clock (DC) FIFO has been instantiated to implement PCIe-DMA buffer interface. The user logic emulator shown in Fig. 3b has data generator logic. This module pushes data into FIFO interface in its clock domain, and data flow controller reads the FIFO in PCIe clock domain and writes the data into on-chip memory. Data will be pushed into FIFO when on-chip memory could not be written and until FIFO does not assert almost full. Data generation is stopped and resumed as soon as almost full flag goes up and down respectively. In this way, we can reproduce exact input data pattern at output. Figure 3b shows the PCIe-DMA data flow model including FIFO.

During optimization, we removed handshaking signal used by the software to trigger the DMA. The same signal has been used internally by the firmware to program DMA controller register #7 and trigger DMA. This gives us a little bit improvement in DMA performance.

6 Theoretical DMA Performance

The theoretical DMA performance is explained in this section. The DMA engine exchanges memory write TLP packets with PCI HIP to move the data. The TLP packet is shown in Fig. 6. The TLP packet has different kinds of headers like start, sequence ID, TLP header, and data payload field. The header of TLP ranges from 5 to 7 DWs, i.e., from 160 to 224 bits maximum, and the existing design supports maximum 256 bytes as payload in TLP packet.

As the TLP bridge interface between DMA engine and PCIe HIP is 256 bits, it requires nine clock cycles to move one single TLP packet. Out of nine clock cycles, eight clock cycles are used to write the payload and one clock cycle is used for header. So, the transmission efficiency is 8/9. Now, the effective link bandwidth of Gen.3 x8 is around 63 Gbps instead of 64 Gbps due to 128/130 b encoding. So, the theoretical maximum data throughput for eight lanes is = (8/9) *63 Gbps = 55.44 Gbps.

Fig. 6 TLP packet

| 1 Byte | 2 Bytes | 3-4 DW | 0-1024 DW | 1 DW | 1 DW | 1 Byte |
|--------|----------------|---------------|--------------|------|------|--------|
| Start | Sequence ID | TLP Header | Data Payload | ECRC | LCRC | End |

7 Result and Analysis

In this section, we will discuss the performance achieved at each stage of evaluation and compare the result obtained in hardware with theoretical value. The tests about data consistency will be explained also in this section.

We gained in terms of performance at each stage. In non-pipelined DMA transfer, we achieved around 39 Gbps. We gained 12 Gbps more in pipelined transfer with respect to non-pipelined transfer and again improved 2 Gbps through optimization of handshaking signal. We gained 2 Gbps further by optimization in software. So, the maximum throughput achieved in hardware is around 55 Gbps. So, we reached almost at peak in hardware.

The dead time a.k.a. idle time including PCIe unavailability was around $4 \mu s$ at peak performance. The DMA performance in hardware in different iteration and idle time variation are shown in Fig. 7a, b, respectively.

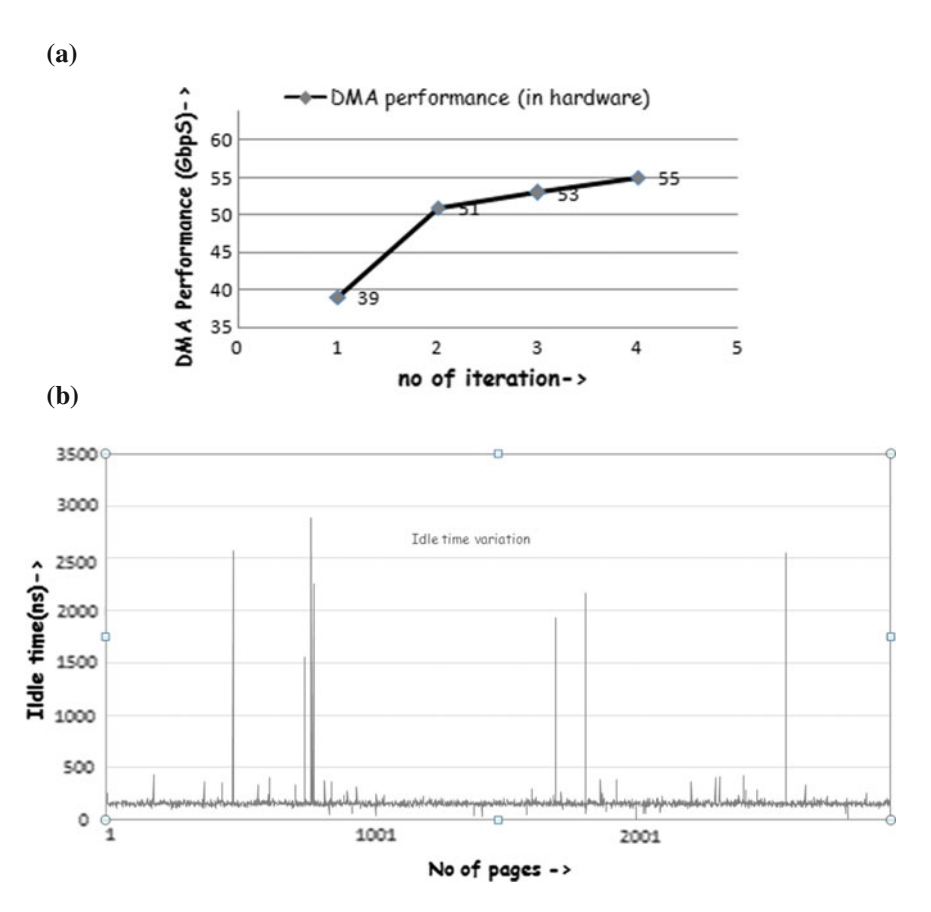


Fig. 7 a DMA performance (in hardware). b Idle time variation

S. Mukherjee et al.

The design was under lot of stress during data consistency test. We paused randomly the input data generation and emulate empty state of FIFO. We also randomly paused to create back pressure from system side and emulate full state of FIFO. We switched randomly between pause and resume state. There were no errors when the design was under stress.

8 Summary and Outlook

This development-related PCI DMA module is in current firmware release. We are 8 Gbps ahead of our requirement. The main drawback of this design is high CPU utilization, and our future aim is to reduce it as much as possible.

References

- 1. https://www.altera.com/products/boards_and_kits/dev-kits/altera/kit-a10-gx-fpga.html
- 2. https://twiki.cern.ch/twiki/bin/viewauth/ALICE/CRU
- 3. P. Moreira, A. Marchioro, K. Kloukinas, The GBT: a proposed architecture for multi-Gb/s data transmission in high energy physics. In *Topical Workshop on Electronics for Particle Physics*, Prague, Czech Republic, 37 Sept 2007, p. 332 [CERN-2007-007.332]
- 4. https://www.alterawiki.com/wiki/Category:PCI_Express
- 5. https://www.altera.com/en_US/pdfs/literature/an/an690.pdf

Sensitivity of ICAL to TeV Gamma Rays at INO

Nitali Dash and Reetanjali Moharana

Abstract We report the sensitivity of Iron CALorimeter (ICAL) detector to the detection of TeV gamma rays from various astrophysical sources at India-based Neutrino Observatory (INO). The ICAL detector is proposed to be of 51 kton with an average magnetic field of $\sim 1.3\,\mathrm{T}$. The electromagnetic showers generated by high-energy gamma rays at the atmosphere will produce down-going muons through either muon pair production or pion decay. The gamma rays can be traced by detecting these muons using ICAL. Most of the space- and underground-based experiments have detected them directly and indirectly, but the advantage of using ICAL for their detection is to measure the μ^+ to μ^- ratio, which is 1 in case of pair production, at very high energy ($\geq 50~\mathrm{GeV}$). Here, we have shown its detection ability for the appropriate astrophysical 2FHL sources listed in "The Second Catalog of Hard Fermi-LAT Sources," where the signal-to-noise ratio is suppressed by factor of 5σ for ICAL running period of five years for spectral index of ≤ 0.45 .

1 Introduction

Astrophysical sources like pulsars, supernova, blazars, and transient astrophysical objects are expected to produce high-energy γ -rays, neutrinos, and cosmic rays. Recent observation of high-energy starting events (HESE) detected by IceCube [1, 2] has given hint for the presence of TeV–PeV hadronic astrophysical machines in the space. TeV γ -rays are expected to be the counterpart of high-energy neutrino events.

N. Dash (⊠)

Centre of Excellence in Theoretical and Mathematical Sciences, Siksha 'O' Anusandhan University, Bhubaneswar 751030, India e-mail: nitali.dash@gmail.com

R. Moharana

The Racha Institute of Physics, 91904 Jerusalem, Israel e-mail: moharana.reetanjali@mail.huji.ac.il

120 N. Dash and R. Moharana

The space-based experiments detect γ -rays with up to energy 300 GeV, directly by Large Area Telescope (LAT) detector of Fermi Gamma-ray Space Telescope (GLAST). Higher energy (50 GeV to ~10 TeV) γ -rays have been detected by Earth-based Cherenkov observatories indirectly, by detecting the secondaries produced while traveling through the Earth atmosphere. Ground-based gamma-ray detectors like VERITAS, H.E.S.S-I and II, Milagro are some of the ongoing observers for GeV, TeV γ -rays, adding to the list, recently HAWC [3] has also started its observation. Upcoming Cherenkov Telescope Array (CTA) [4] is expected to explore the TeV sky with larger sensitivity. The observed highest energy γ -ray sources are listed in the catalog TeVCAT [5] detected with energy more than 50 GeV by ground-based detectors. The other high-energy γ -ray catalog is named as The Second Catalog of Hard *Fermi*-LAT Sources (2FHL) listing both galactic and extragalactic sources within energy range 50 GeV–2 TeV [6].

The electromagnetic (EM) shower produced by high-energy γ -ray in the atmosphere contains very high-energy muons [7] which survive to reach underground detectors and may have less background due to the rock cover. The 51 kton magnetized Iron CALorimeter detector (ICAL) [8] is proposed to be placed in a cavern at India-based Neutrino Observatory (INO) under a rock cover of \sim 1 km from all around. The detector parameters are mainly optimized for the atmospheric neutrinos (ν_{μ}) , in particular the mass hierarchy [9] of neutrinos, octant sensitivity [10]. Irrespective of that due to its adorable characteristic, it can also be used for new physics studies. Such as searching for sub-relativistic Dirac magnetic monopole [11], to observe or set limits on the lifetime of dark matter by considering their number in the ICAL cavern [12], annihilation or decay products of the dark matter by looking at the center of the solar system, neutrino nonstandard interaction [13], CPT violation [14], and ultrahigh-energy muons [15].

In this chapter, we demonstrate the detectability of γ -rays from galactic sources listed in 2FHL catalog⁵ by ICAL assuming ICAL will be exploring Southern sky more efficiently. Due to magnetized iron plates ICAL will be able to identify the charge ratio of muons giving more stringent limit to background muons.

2 Muon Rates from γ -ray-Induced Showers

The EM-showers of high-energy γ -rays contain particles that increase at each step of the shower with decreased average energy. But the high-energy secondary muons of the EM-shower can reach the underground detectors. The γ -ray spectrum at a depth t

¹https://www-glast.stanford.edu/.

²http://veritas.sao.arizona.edu/about-veritas-mainmenu-81.

³https://www.mpi-hd.mpg.de/hfm/HESS/.

⁴http://scipp.ucsc.edu/milagro/papers/.

⁵http://www.asdc.asi.it/fermi2fhl/.

with energy E_{γ} , having probability of electron–positron pair production per radiation length (σ_0) , along with scale length for the shower growth (λ_1) and dissipation (λ_2) in the atmosphere is,

$$\gamma(E_{\gamma},t) = \gamma_0 \frac{(\sigma_0 + \lambda_1)(\sigma_0 + \lambda_2)}{\lambda_2 - \lambda_1} \left[\frac{e^{\lambda_1 t}}{\sigma_0 + \lambda_1} - \frac{e^{\lambda_2 t}}{\sigma_0 + \lambda_2} \right]. \tag{1}$$

where the initial spectrum follows power law, $\gamma_0 = AE_{\gamma}^{-(b+1)}$, having spectral index b and normalization constant A.

The dominant secondary muon production channels from these γ -rays interacting with atmospheric nucleus N [7] are photo-production ($\gamma + N \to N' + \pi^{\pm}$) and direct muon pair production ($\gamma + N \to N' + \mu^+ + \mu^-$), respectively. At high energy nearly at TeV, photo-production become suppressed by direct muon pair production channel, a detail analysis is reviewed in [16]. As above photo-production threshold the muon energy is proportional to the primary γ -ray energy, detecting muons will indirectly give the evidence on γ -ray. Again the generated muon direction is along the primary photon direction, and their direction can be inferred in few degree accuracy.

Using standard two-body decay kinematics, assuming muon energy loss but not decaying, the muon flux at the surface of the Earth due to pion decay is,

$$\frac{dN_{\mu}}{dE_{\mu}} = \int_{0}^{t_{max}} dt B_{\mu\pi} \int_{E_{\mu}}^{E_{\mu}/r} \frac{dE^{'}}{(1-r)E^{'}} \frac{\pi(E^{'},t)}{d_{\pi}(t)}.$$
 (2)

where

$$\pi(E,t) = \gamma_0 \frac{Z_{\gamma\pi}}{\lambda_{\gamma A}} \frac{(\sigma_0 + \lambda_1)(\sigma_0 + \lambda_2)}{\lambda_2 - \lambda_1}$$

$$\mathbf{Min} \left(\left[\frac{1}{\sigma_0 + \lambda_1} \sum_{j=1}^{100} \frac{\lambda_1^{j-1} t^j}{(j-1)!(\delta+j)} - \frac{1}{\sigma_0 + \lambda_2} \sum_{j=1}^{100} \frac{\lambda_2^{j-1} t^j}{(j-1)!(\delta+j)} \right], \left[\frac{e^{\lambda_1 t} - e^{t/\Lambda_{\pi}}}{(\sigma_0 + \lambda_1)(\lambda_1 + \frac{1}{\Lambda_{\pi}})} - \frac{e^{\lambda_2 t} - e^{t/\Lambda_{\pi}}}{(\sigma_0 + \lambda_2)(\lambda_2 + \frac{1}{\Lambda_{\pi}})} \right] \right).$$
(3)

The differential pion spectrum in high- and low-energy regions is given in detail in [17]. The flux of muons from direct muon pair production is given by [18]

$$\frac{dN_{\mu}}{dE_{\mu}} = 2 \lambda_{rad} \frac{N_A}{A} \gamma_0 \int_0^1 dx \, x^b \frac{d\sigma}{dx} (x, \frac{E_{\mu}}{x}) \int_0^{t_{max}} dt \, \gamma_2(t, b), \tag{4}$$

where

$$\frac{d\sigma(x, E_{\mu}/x)}{dx} = 4\alpha Z^2 \left(r_0 \frac{m_e}{m_{\mu}} \right)^2 \left[1 - \frac{4}{3} x (1-x) \right] \left[\phi_{el}(\delta) + \frac{1}{Z} \phi_{In}(\delta) \right]. \quad (5)$$

The parameters are well defined in [16].

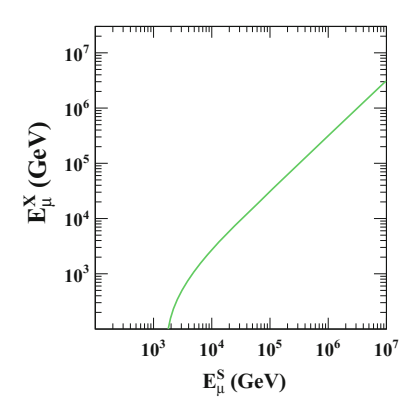
3 Energy Loss of High-Energy Muons in Rock

Muon loses energy via bremsstrahlung, pair production, and hadroproduction in addition to ionization at very high energies, while passing through matter. The energy loss rate for muon following [19] is

$$\frac{dE}{dX} = -\alpha - \frac{E}{\xi}. (6)$$

where α is due to ionization and ξ^{-1} is the contribution from bremsstrahlung, pair production, and hadroproduction. Using (6), the minimum energy required for a muon at the surface to reach slant depth X is $E_{min} = \varepsilon \left(e^{X/\xi} - 1 \right)$. The critical energy of muon in the rock is $\varepsilon \sim 500$ GeV and $\xi \sim 2.5 \times 10^5$ gm/cm². So, the minimum energy of muon should be > 1 TeV, considering density of rock as ~ 2.89 gm/cm³ [11] for a height of ~ 1 km in case of INO site. But for directional inclination up to 60°, the minimum energy varies from 1 to 4.5 TeV. For vertical muon, the comparison of energy at the Earth surface and at the ICAL detector is shown in Fig. 1.

Fig. 1 Muon energy at the Earth surface compared to energy due to radiation loss after a depth of 1 km of rock cover for an inclination of 0°



4 Detection of TeV γ -ray Using ICAL

In this section, we have studied the high-energy γ -ray detection sensitivity of 2FHL galactic sources by ICAL detector. Here, we have assumed, the sources produce γ -rays with same spectral index and fluence as seen by Fermi-LAT at least till 300 TeV.

ICAL is a rectangular-shaped detector carrying three modules, each of 17 kton and dimensions of $16 \times 16 \times 15 \, \text{m}^3$. The module consists of passive target like iron plates and active detector such as resistive plate chambers (RPCs) which are interleaved in between. The iron plates are magnetized with an average magnetic field of 1.3 T. The energy resolution of muons [20] in the energy range 1–20 GeV using ICAL detector is 9–14% for zenith angle <70° with direction resolution better than a degree for each bin. For muon energy above 4 GeV, the relative charge identification (CID) efficiency is around 98% for each direction bin.

The possible backgrounds for high-energy γ -ray-generated muons are the muons produced from cosmic ray interacting with atmosphere. For a rock cover of approximately 3.8 km water equivalent at INO site the cosmic ray muons flux [21] reduced to million fold around 10^{-4} m⁻² sr⁻¹ s⁻¹. So this can be removed by looking events from a fixed direction, where the number is large compared to the cosmic ray muons. The background of muons generated by the decay of pions and kaons produced in interactions of primary cosmic rays in the atmosphere is calculated using the modified Gaisser's formula [22].

The distributions in Fig. 2 show the muon flux from the 2FHL galactic sources with both photo-production and muon pair production processes as well as from the cosmic rays using (2) and (4). The band region in the energy range from 1 to $10\,\text{TeV}$ is the detection region for ICAL at INO. In Fig. 2, the γ -ray sources are with spectral index of 0.3, 0.5, 0.7, and 0.9. With increase in spectral index, the crossover region between photo-production and muon pair production shifted toward the higher energy. So sources with small value of spectral index are discussion of interest, as we are interested for muons from pair production (detail in Sect. 4.2). In further calculation as mentioned in Sect. 4.1, we have limited to sources with spectral index of 0.6 where the intersection point is $1\,\text{TeV}$.

4.1 Expected Signal-to-Noise Ratio

In order to suppress the background/noise (N) over signal (S), we have calculated the signal-to-noise ratio. Because the background is limited to a circle in the sky of angle $\delta\theta$ around the direction of the point sources. Here, $\delta\theta$ is the angular resolution of the detector. The number of cosmic ray muons [23] at zenith angle θ with intensity $I_{\mu}(\theta)$ for duration T and detection area A is given by,

$$N = I_{\mu}(\theta) \times A \times T \times \delta \theta^{2}. \tag{7}$$

124

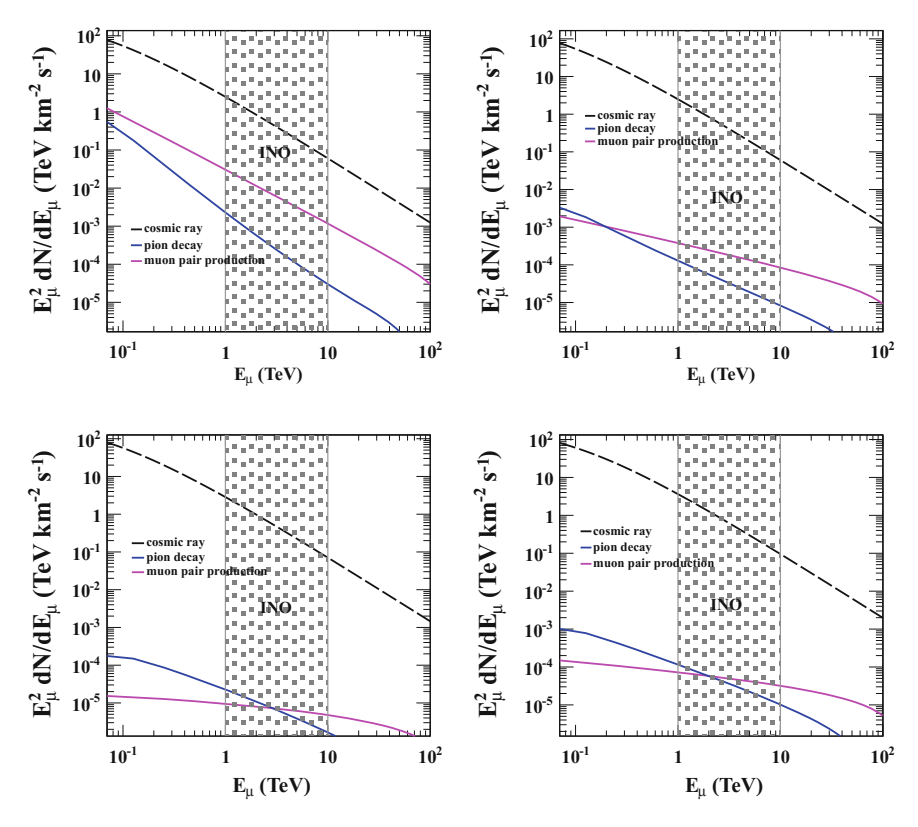


Fig. 2 Spectrum of muons from cosmic ray (black dashed line), direct muon pair production (magenta line), and pion decay (blue line) for 2FHL sources J0048.0 + 5449, J2321.1 + 5910, J0310.4 - 5019, and J0138.2 + 5811 (in clockwise direction from top left) with γ -ray spectral index of 0.3, 0.5, 0.7, and 0.9. The shadowed band shows the probable energy band of INO, which we interpreted as 1 \sim 10 TeV

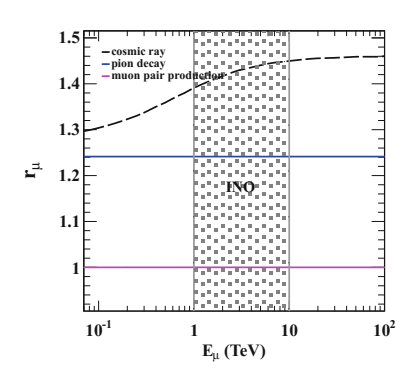
The signal-to-square root of noise ratio then scales as

$$\frac{S}{\sqrt{N}} = \frac{\sqrt{A}}{\delta \theta}.$$
 (8)

Equation (8) shows that the sensitivity increases for large area and better angular resolution. All the characteristics of γ -ray sources like spectral index and photon energy fluxes are noted down in Table 1 using Fermi catalog [6]. The muon energy threshold for ICAL detector at INO is 1 TeV. It has a transverse area of 768 m² and an intrinsic angular resolution of about 1°. In Table 1, we present the number of muons at 1 TeV energy from sources with different spectral indices (0.15–0.45) for a duration of 10 s. The result (column V of Table 1) shows with respect to cosmic ray muons using the above specified parameters like detector area, direction resolution, and duration.

| Table 1 Illustration of 2 FFLL sources of noise ratios for μ energy of 1 TeV | nt zFHL sources with dinergy of 1 TeV | merent spectral indices | s, pnoton energy nux n | n tne energy range ot 3 | OGEV to 2 lev and in | Lable 1 integration of ZFRL Sources with different spectral indices, photon energy flux in the energy range of 50 GeV to 2 TeV and the signal-to-square foot of moise ratios for μ energy of 1 TeV |
|---|---------------------------------------|---|--------------------------|-------------------------|------------------------------|--|
| Source 2FHL | Spectral index, b | Energy flux (TeV km $^{-2}$ S $^{-1}$) | Signal | S | $(\mu^+) \frac{S}{\sqrt{N}}$ | $(\mu^-) \frac{S}{\sqrt{N}}$ |
| J0537.4 - 6908 | 0.15 | 0.126078 | 504.493 | 3647.42 | 9.46361×10^{6} | 1.11975×10^{7} |
| J1703.4 - 4145 | 0.24 | 0.180379 | 0.060046 | 0.434125 | 1126.38 | 1332.75 |
| J1745.1 - 3035 | 0.25 | 0.167896 | 0.0552138 | 0.399188 | 1035.74 | 1225.5 |
| J0048.0 + 5449 | 0.30 | 0.047685 | 0.000234282 | 0.00169383 | 4.39481 | 5.20001 |
| J0316.6 + 4120 | 0.34 | 0.083012 | 0.000388381 | 0.00280794 | 7.2855 | 8.62032 |
| J0319.7 + 1849 | 0.45 | 0.075522 | 2.52345×10^{-5} | 0.000182442 | 0.473365 | 0.560093 |

Fig. 3 Ratio (r_{μ}) between the flux of μ^+ to μ^- versus energy of muon (E_{μ}) from photon shower with any index and any influence, in case of both pion decay (blue line) and muon pair production (magenta line), and cosmic ray muons (black dashed line)



4.2 Muon Charge Ratio

As Iron CALorimeter is a magnetized detector, we have further compared the charge ratio of muons for each source with respect to cosmic ray muons. For the cosmic-ray-generated muons at the sea level both the pion and kaon contribute to their flux and so on their charge ratio [24]. Figure 3 shows the charge ratio for cosmic ray muons and muons from γ -ray-induced shower as a function of muon energy. The charge ratio for cosmic ray muons increases with increase in energy resulting in higher μ^+ than μ^- at high energies. But in case of high-energy γ -rays, the muon charge ratios due to photo-production and muon pair production are 1.24 and 1 as shown in Fig. 3. In case of photo-production, the ratio comes only from the pion decay. The ratio is constant throughout the energy as it is independent of energy and similarly for muon pair production which produces equal number of μ^+ and μ^- .

From [20], it is very clear that the charge of muon with energy 4–20 GeV can be identified by 98% for incident direction up to 70°. The extension of energy of muon will reduce the CID efficiency due to their more or less straight path in the magnetic field. So if the CID efficiency is around 80–90% for 50 GeV muon using ICAL, then it can also identify the charge of muons from γ -rays. In the last two columns of the Table 1, we have noted down their ratio for running period of five years with respect to cosmic ray muons separately for μ^+ and μ^- .

5 Summary

We have investigated the sensitivity of magnetized Iron CALorimeter detector for the detection of high-energy muons from few observed galactic γ -ray sources from "The Second Catalog of Hard Fermi-LAT Sources." The analysis shows that within five-year run time of ICAL, it might be able to detect to γ -ray fluxes from γ -ray source with lower value of spectral index within energy range of 1 to 10 TeV. Because these sources have larger muon flux than the muons from cosmic rays. However, the detailed analysis of the sensitivity of γ -ray detection needs further simulation.

References

- M.G. Aartsen et al., Observation of high-energy astrophysical neutrinos in three years of Ice-Cube data. Phys. Rev. Lett. 113, 101101 (2014)
- M.G. Aartsen, et al., The IceCube neutrino observatory—Contributions to ICRC 2015 Part II: atmospheric and astrophysical diffuse neutrino searches of all flavors. In *Proceedings of 34th International Cosmic Ray Conference (ICRC 2015)*, The Hague, The Netherlands, 30 July–6 Aug 2015
- A.U.E. Abeysekara, On the sensitivity of the HAWC observatory to gamma-ray bursts. Astropart. Phys. 35, 641–650 (2012)
- 4. A. Abchiche, et al., in Contributions of the Cherenkov Telescope Array (CTA) to the 6th International Symposium on High-Energy Gamma-Ray Astronomy (Gamma 2016) (2016)
- S.P. Walely 1, D. Horan, TeVCat: an online catalog for very high energy gamma-ray astronomy. In *Proceedings of 30th International Cosmic Ray Conference (ICRC 2008)*, vol. 3 (2008), pp. 1341–1344
- M. Ackermann et al., 2FHL: the second catalog of hard Fermi-LAT sources. Astrophys. J. Suppl. 222(1), 5 (2016)
- 7. M. Drees, F. Halzen, K. Hikasa, Muons in γ showers. Phys. Rev. D 39, 1310 (1989)
- 8. A. Kumar et al., Invited review: physics potential of the ICAL detector at the India-based neutrino observatory (INO). Pramana **88**(5), 79 (2017)
- A. Ghosh, T. Thakore, S. Choubey, Determining the neutrino mass hierarchy with INO, T2K. NOvA and reactor experiments. JHEP 04, 009 (2013)
- T. Thakore, A. Ghosh, S. Choubey, A. Dighe, The reach of INO for atmospheric neutrino oscillation parameters. JHEP 05, 058 (2013)
- N. Dash, V.M. Datar, G. Majumder, Sensitivity of the INO-ICAL detector to magnetic monopoles. Astropart. Phys. 70, 33–38 (2015)
- 12. N. Dash, V.M. Datar, G. Majumder, Sensitivity for detection of decay of dark matter particle using ICAL at INO. Pramana **86**(4), 927–937 (2016)
- 13. S. Choubey, A. Ghosh, T. Ohlsson, D. Tiwari, Neutrino physics with non-standard interactions at INO. JHEP 12, 126 (2015)
- 14. A. Chatterjee, R. Gandhi, J. Singh, Probing Lorentz and CPT violation in a magnetized iron detector using atmospheric neutrinos. JHEP **06**, 045 (2014)
- S. Panda, S.I. Sinegovsky, High-energy atmospheric muon flux expected at India-based neutrino observatory. Int. J. Mod. Phys. A 23, 2933–2942 (2008)
- T.L. Astraatmadja, On the detection of TeV gamma-rays from GRB with km-cube neutrino telescopes—I. Muon event rate from single GRBs. Mon. Not. Roy. Astron. Soc. 418, 1774– 1786 (2011)
- F. Halzen, A. Kappes, A.O. Murchadha, Gamma-ray astronomy with muons: sensitivity of IceCube to PeVatrons in the Southern sky. Phys. Rev. D 80, 083009 (2009)
- 18. H. Bethe, W. Heitler, On the stopping of fast particles and on the creation of positive electrons. Proc. Roy. Soc. Lond. A **146**, 83–112 (1934)
- 19. T.K. Gaisser, R. Engel, E. Resconi, *Cosmic Rays and Particle Physics* (Cambridge University Press, Cambridge) (1990)
- A. Chatterjee, K.K. Meghna, K. Rawat, T. Thakore, V. Bhatnagar, R. Gandhi, D. Indumathi, N.K. Mondal, N. Sinha, A simulations study of the muon response of the iron calorimeter detector at the India-based neutrino observatory. JINST 9, P07001 (2014)
- 21. C. Arpesella, A review of running underground experiments. Nucl. Instrum. Meth. A 277, 1–10 (1989)
- 22. M. Guan, J. Cao, C. Yang, Y. Sun, K.B. Luk, Muon simulation at the Daya Bay site. In *Lawrence Berkeley National Laboratory Paper LBNL-4262E* (2006)
- 23. N. Gupta, P. Bhattacharjee, Detecting TeV gamma-rays from gamma-ray bursts by ground based muon detectors. arXiv:astro-ph/0108311
- P.A. Schreiner, J. Reichenbacher, M.C. Goodman, Interpretation of the underground muon charge ratio. Astropart. Phys. 32, 61–71 (2009)

Qualification of Eco-Friendly Gas Mixture for Avalanche Mode Operation of RPC

Jaydeep Datta, Abhik Jash, Nayana Majumdar and Supratik Mukhopadhyay

Abstract The gas mixture to be used in the RPCs of INO-ICAL experiment is a mixture of R-134a, isobutane and SF₆. Owing to huge Global Warming Potential of this mixture (GWP 1403), this needs to be substituted with an eco-friendly gas mixture without compromising the performance of ICAL. In this work, we propose to study the qualification of a mixture of argon and CO_2 for avalanche mode operation of RPC, which has a very low GWP (<1). To estimate the streamer probability of the new gas mixture at different operating voltages, the electronic charge produced in RPC signal has been simulated using two numerical methods.

1 Introduction

India-based Neutrino Observatory (INO) [1] is an underground scientific facility to study different properties of atmospheric neutrinos. The major component of this facility is a 50 kton Iron Calorimeter (ICAL), a sampling calorimeter, which comprises of nearly 30,000 Resistive Plate Chambers (RPCs) arranged in 151 layers interspersed with iron plates. The present gas mixture of RPCs comprises of R-134a, a kind of Freon, isobutane and sulphur hexafluoride (SF₆) with a volumetric percentage of 95.5, 4.3 and 0.2, respectively. Although the performance of the RPCs with the said gas mixture has been found to meet the requirement of the ICAL satisfactorily, it is advisable to reduce its use due to its high Global Warming Potential (GWP 1403). According to Kyoto Protocol [2], use of any gas or gas mixture having GWP more than 150 should be discontinued. This constraint has motivated us to explore the use of an eco-friendly gas mixture to operate the RPCs, replacing the existing one without

J. Datta (☒) · A. Jash · N. Majumdar · S. Mukhopadhyay SINP, Block - AF, Sector - 1, Bidhannagar, Kolkata 700064, West Bengal, India e-mail: jaydeep.datta@saha.ac.in

J. Datta · A. Jash HBNI, Training School Complex, Anushaktinagar, Mumbai 400094, India

[©] Springer Nature Singapore Pte Ltd. 2018 S. Biswas et al. (eds.), *Advanced Detectors for Nuclear, High Energy and Astroparticle Physics*, Springer Proceedings in Physics 201, https://doi.org/10.1007/978-981-10-7665-7_12

compromising the objectives of the INO-ICAL experiment. In order to achieve this, the new gas mixture should be suitable for running the RPCs in avalanche mode with reasonably high efficiency and good position and timing resolutions. Several attempts have been made in this direction to use another version of Freon (HFO-1234 ze) [3] as an alternative of the existing R-134a which has GWP 1430. Being the major component in the gas mixture, it contributes heavily in terms of the GWP. However, this replacement version has exhibited high streamer probability apart from being costly [4, 5]. In the present work, we have attempted to explore the qualification of a mixture of argon and CO₂ (GWP < 1) for operating the RPCs in avalanche mode. A numerical simulation work has been carried out to estimate the streamer probability in the proposed gas mixture for a given operating regime. The charge amplification in the RPC for the given gas has been simulated in two different ways. One is a Monte Carlo (MC) calculation using particle-in-cell (PIC) method [6] and carried out with software MATLAB (V. R2014b) [7], while the other one is a simulation based on a hydrodynamic model done on the platform of commercially available software, COMSOLTM Multiphysics (V. 5.2a) [8].

In the next Sect. 2, both of the simulation methods have been described briefly, while their results have been discussed in Sect. 3. In Sect. 4 final remarks about the work have been made.

2 Simulation Methods

RPC is a gaseous chamber used as charged particle/radiation detector on the basis of ionization of gaseous molecules in the interaction of the incident particle/radiation with the gas medium. The ions and electrons thus generated move and accelerate under the action of the applied electric field across the medium. The electrons in particular produce further ionization through collision with the gaseous molecules leading to an amplification of electronic charge. Depending on the amount of multiplication, the avalanche and streamer mode of the RPC is distinguished. Here, the two methods used to simulate the avalanche and streamer in the given gas mixture for an applied electric field have been described briefly. The MC code takes into account the collision of electrons with background particles and calculates the number of electrons and ions. In the COMSOLTM code, the electron and ions are treated as fluid and the Boltzmann equation for the ions and electrons is solved to find their transport properties.

2.1 PIC-MC Method

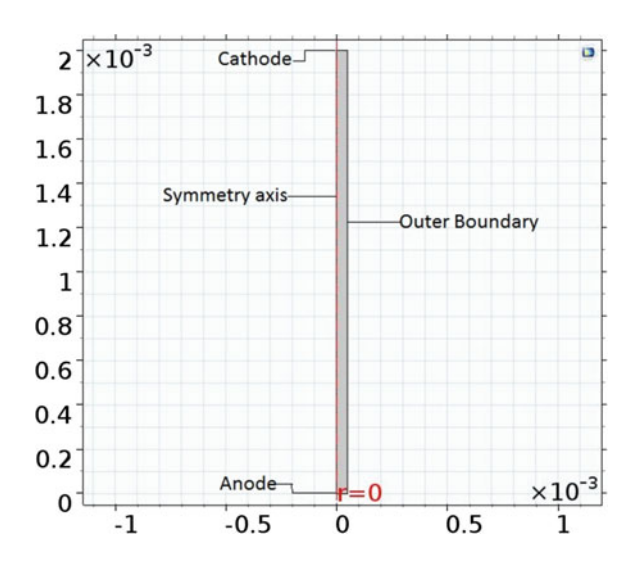
For simulation of avalanche formulation and avalanche to streamer transition, it is necessary to take into account the kinetics of both the electrons and ions. Their collisions with the background particles, such as the gas molecules, along with their

motion in the resultant electric field due to the applied electric field and the space charge should be taken into account. There are some empirical formula to define the avalanche to streamer transition, but for precise calculation of avalanche to streamer transition, one must use the parameters which are derivable from the system, such as sudden change in average energy of electrons or number of electrons. METHES [10] is a MATLAB-based code which solves the particle motion using PIC method. To calculate the collisions of the electrons and ions with the gas molecules, the cross sections are imported from LXCat database [9]. To determine the collision type, the null collision technique is used. For each electron, a random number is chosen and compared with the cross sections corresponding to that electron's energy. If the random number is the smallest, the first interaction occurs; if it is the largest one then no collision occurs. For any other case the interaction corresponding to the cross section which is nearest and larger than the random number, that one occurs. The following inputs are required for the code, like the names of the gas components and their proportions in the mixture, the number of initial electrons, their position, momentum and velocity, the electric field (in Townsend unit) along with the temperature and pressure. It assumes a cubic volume of 1 m dimension and the number of grid in each direction is to be given.

The calculation starts with a free flight for each of the initial electrons. It calculates the force on the electrons and ions after finding out the electric field from the given temperature, pressure and the reduced field value. The velocity of the electron is determined thereafter and then the energy from the velocity depending on whether the electron is relativistic or not. Once the energy information is obtained, using the cross-sectional database, it finds out the type of collision to happen for that electron using the null collision technique. Due to the limitation of the available computational resource, the computation speed gets reduced as the number of the electron and ion reaches to the order of 10⁶. So there is an option to conserve the number of probe electrons by setting up a pre-fixed value. Once the number of electrons reaches the value, for the next collision, if it is ionizing collision, an electron is randomly chosen from the bulk and discarded from the probe electron group. For attachment collision, an electron from the rest of the probe electrons is chosen and is used for calculation [10, 11]. So once the collision type is determined, new electrons and ions are generated. The mean drift velocity and the diffusion rate are calculated along with the position and energy distribution. The 3D Poisson equation is solved in the Jacobi relaxation method to find out the field. Then the electron and ion density in each grid of the test volume is found out. Using this density, the total number of electrons and ion is obtained. As the change in electron and ion number is not much, the field calculated in the previous step is given as the input for the next step, which leads to a fast convergence. Once the new electric field is calculated, then each step is repeated for each electron. Detailed discussion can be found in the [10].

J. Datta et al.

Fig. 1 RPC geometry



2.2 Hydrodynamic Model Method

A hydrodynamic model has been developed to simulate the streamer in the GEM detector based on COMSOLTM Multiphysics software [12]. The same has been modified for simulating the streamer in case of RPC in this work. A 2D geometry has been considered for the calculation. As shown in Fig. 1, an axis-symmetric plane perpendicular to the cathode and anode of the RPC has been considered.

As the streamer inside a 2 mm gas gap does not get broader than $100~\mu m$ [13], the width of the plane is taken same and the height is 2 mm. The region of interest has been considered far away from both the button spacers and edge spacers, and the electrodes are assumed perfectly plain so that the electric field remains uniform and normal to the electrodes. To calculate the electric field and potential, the electrostatic module has been used. To take into account the space charge effect, the charge density has been considered as a function of the instantaneous electron and ion density. The equations used for the electric field calculation are:

$$\nabla \cdot \mathbf{D} = \rho \tag{1}$$

$$\mathbf{E} = -\nabla \cdot V \tag{2}$$

where **D** is the electric displacement vector, **E** is the electric field, V is the potential, and ρ is the instantaneous charge density. To estimate the electronic motion, the Boltzmann equation has been solved.

$$\frac{\partial ne}{\partial t} + \nabla(-D_e \nabla ne + \mathbf{u}_{ne}) = R_{ne}$$
(3)

$$R_{ne} = S_e + S_{nh} \tag{4}$$

Here ne is the instantaneous electron density, D_e is the diffusion coefficient for electron in the gas, \mathbf{u}_{ne} denotes the drift velocity of the electrons, and R_{ne} is the reaction part of the Boltzmann equation. In R_{ne} , the contribution of the electron interaction (S_e) and photo-ionization (S_{ph}) has been taken into account. For calculating the motion of the electrons, both the drift motion (\mathbf{u}_{ne}) and the motion due to diffusion have been considered. The diffusion rate (D_e) and drift velocity have been given as functions of electric field, calculated using MAGBOLTZ (V.11.2) [14]. Similarly for the ions also, the Boltzmann equation has been solved.

$$\frac{\partial ni}{\partial t} + \nabla(-D_i \nabla ni) = R_{ni} \tag{5}$$

$$R_{ni} = S_e + S_{nh} \tag{6}$$

Here ni is the instantaneous ion density, D_i is the diffusion coefficient for ion in the gas, R_{ni} is the reaction part of the Boltzmann equation. As the drift velocity of ions is much less than the electrons, it has not been taken into account. Also no inflow or outflow of the ions has been considered. For interaction, again electronic interaction and the photo-ionization have been considered. The boundary conditions used are:

- 1. Initial voltages at cathode and anode have been -5000 and 5000 V, respectively.
- 2. The inward flux of electrons has been from the cathode of the RPC.
- 3. It has been assumed that the created electrons could flow out of the geometry. So a outflow has been given to the anode side surface and also at outer boundary (see Fig. 1).
- 4. No outflow or inflow has been considered for ions.
- 5. It has been assumed that due to the interactions of the photons, the cathode might release some electrons which have been taken into account.
- 6. No charge has been considered on any boundary.

For the photons created in the gas gap, a quantum efficiency of the gas has been assumed. To estimate the field due to the photons, the Helmholtz equation has been solved.

$$\nabla(-c\nabla\cdot\Psi) + a\cdot\Psi = f\tag{7}$$

where Ψ is the photon field, c is the diffusion coefficient, a is the absorption coefficient, and f is the source term. It may be noted here that MAGBOLTZ provides only the flux data not the bulk data. However, it has been seen that for a RPC of 2 mm gas gap, the flux data and bulk data do not differ much [15].

3 Results

The freely available METHES code has been used to carry out a test run for pure SF₆. The electric field has been fixed at 700 Td. The following plot in Fig. 2 has shown the change in number of electron as a function of time in case of SF₆.

J. Datta et al.

Fig. 2 Number of electrons with time in the gas gap for SF_6

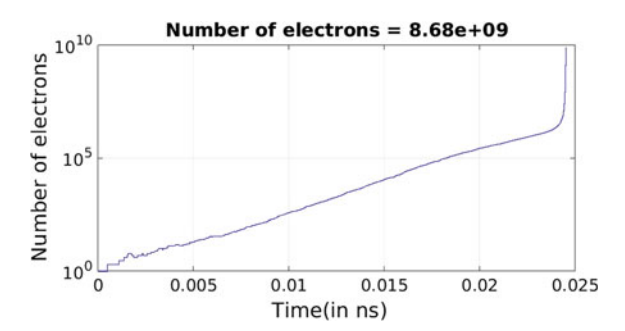
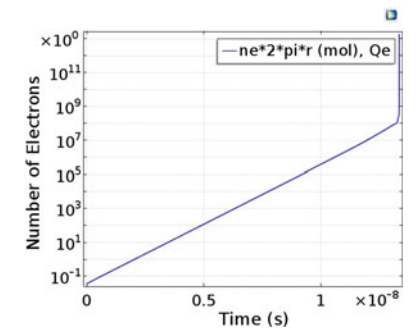


Fig. 3 Number of electrons versus time for present gas mixture



The sudden increase in the number denotes the initiation of streamer. The data for SF_6 cross sections have been taken from [16].

However, the code does not take into account the primary ionization which has been incorporated by us doing the necessary modifications. This has caused a slowing down of the code. As it does the calculation for each and every electron and ion generated in each step, the speed slows down a lot when number reaches to the order of 10^6 . In the case of a gas mixture, it further slows down as it has to calculate with which gas molecule the collision occurs.

We have used the COMSOLTM model to simulate the electron production in the RPC with the present gas mixture. The drift velocity, diffusion coefficient and the effective Townsend coefficient for the given gas mixture have been calculated using MAGBOLTZ and have been provided as the input to the model. The generation of electrons has been displayed in Fig. 3 as a function of time which has indicated a development of a streamer at around 13 ns after the primary ionization took place. The evolution of the electric field and voltage inside the gap are shown in Figs. 4a, b and 5a, b respectively.

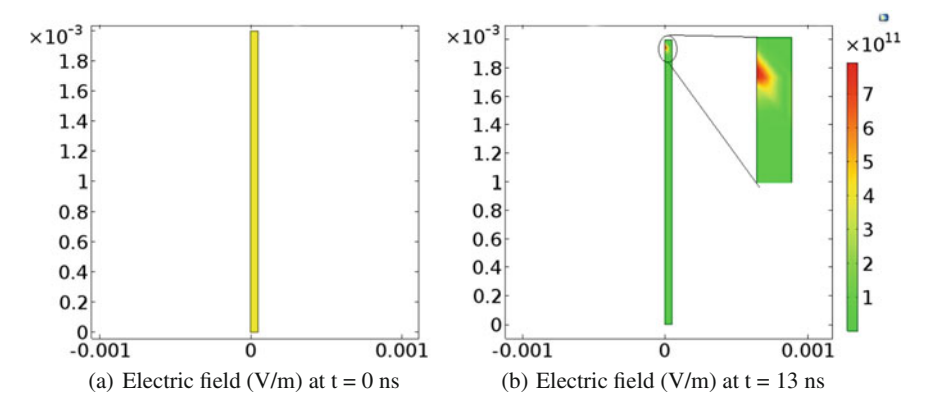


Fig. 4 Change of electric field from hydrodynamic model

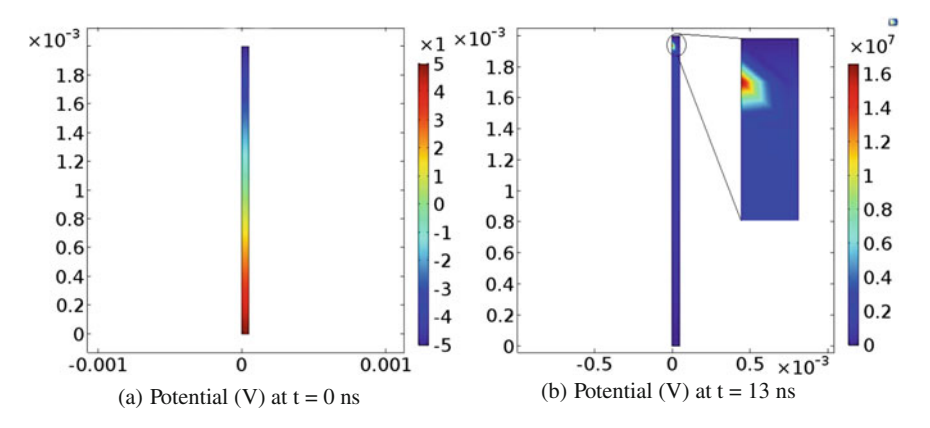


Fig. 5 Change of voltage from hydrodynamic model

4 Conclusion

The LXCat database does not have the cross-sectional data for R-134a and isobutane, so it is not possible to compare the simulation result with available experimental result for the present gas mixture's streamer probability. Work is being done in that direction. The breakdown for SF₆ occurs when the number of electrons reaches to 10^6 , which is two order of magnitude less than the Raether limit. The COMSOLTM model is showing that the breakdown occurs when the number of electrons reaches 2.5×10^8 and after 13 ns of the primary ionization for the present gas mixture. Though the number of electrons matches Raether limit, the time when the streamer started is larger than typical RPC signal arrival time (5–7 ns). It is justified because here the simulation started with only 20 electrons and they were near the cathode. More realistic primary ionization may produce more realistic data.

Acknowledgements We are grateful to the members of ANP division of SINP and INO collaboration for their help and valuable suggestions.

References

- A. Kumar, A.M. Vinod Kumar, A. Jash, et al., Pramana. J. Phys. 88, 79 (2017). https://doi.org/ 10.1007/s12043-017-1373-4
- 2. United nations framework convention on climate change. In *Kyoto Protocol to the United Nations Framework Convention on Climate Change: Annex B*, 8 Oct 2011
- G. Aielli, B. Liberti, et al., Further gas mixtures with low environment impact. JINST 11, C09012 (2016)
- A. Longhin, A. Paoloni, et al., Gas mixture studies for streamer operated resistive plate chambers. JINST 11, C06001 (2016)
- 5. B. Liberti, et al., New RPC gas mixtures for large area apparatuses. JINST 9, C11003 (2014)
- C.M. Franck, M. Rabie, A study of the avalanche-to-streamer transition in arbitrary gases by particle simulation. J. Phys. D Appl. Phys. 49, 175202 (2016)
- 7. MATLAB, https://www.mathworks.com/
- 8. COMSOL Multiphysics, https://www.comsol.co.in/
- 9. LXCat Database, https://fr.lxcat.net/data/set_type.php
- 10. C.M. Franck, M. Rabie, METHES: a Monte Carlo collision code for the simulation of electron transport in low temperature plasmas. Comput. Phys. Commun. **203**, 268–277 (2016)
- Z.L.J. Petrovic, S. Dujko, R.D. White, R.E. Robson, Benchmark calculations of nonconservative charged particle swarms in DC electric and magnetic fields crossed at arbitrary angles. Phys. Rev. E 81, 046403 (2010)
- P. Fonte, Modelling of avalanches and streamers by finite elements with COMSOL: step-bystep guide. Technical Report, Notes for the RD51 Simulation School, CERN, 19–21 Jan 2011
- J. Capeillre, et al., The finite volume method solution of the radiative transfer equation for photon transport in non-thermal gas discharges: application to the calculation of photoionization in streamer discharges. J. Phys. D Appl. Phys. 41, 234018 (2008)
- 14. S. Biagi, http://magboltz.web.cern.ch/magboltz/
- R.D White, D. Bonjakovi, Z.L.J. Petrovic, S. Dujko, Boltzmann equation and Monte Carlo studies of electron transport in resistive plate chambers. J. Phys. D Appl. Phys. 47, 435203 (2014)
- 16. Phelps Database, https://fr.lxcat.net/data/set_type.php. 11 June 2015

Analysis of Ultra-High-Energy Muons at INO-ICAL Using Pair-Meter Technique

Jaydip Singh, Srishti Nagu and Jyotsna Singh

Abstract The proposed ICAL detector at India-based Neutrino Observatory (INO) is a large-sized underground magnetized iron detector. ICAL is designed to reconstruct muon momentum using magnetic spectrometers as detectors. Muon energy measurements using magnets fail for high-energy muons (TeV range), since the angular deflection of the muon in the magnetic field is negligible and the muon tracks become nearly straight. A new technique for measuring the energy of muons in the TeV range used by the CCFR[1] neutrino detector is known as the pair-meter technique. This technique estimates muon energy by measuring the energy deposited by the muon in several layers of an iron calorimeter through e⁺ and e⁻ pair production. In this work, we have performed Geant4-based preliminary analysis for iron plates and have demonstrated the feasibility of detection of very high-energy muons (1–1000 TeV) at the underground ICAL detector operating as a pair-meter. This wide range of energy spectrum will not only be helpful for studying the cosmic rays in the Knee region but also aid in understanding the atmospheric neutrino flux for the running and upcoming ultra-high-energy atmospheric neutrino experiments.

1 Introduction

Iron CALorimeter (ICAL) at INO is a 52 ktons detector [2] proposed to be built at Theni district of Tamil Nadu in Southern India. It is essentially designed to study the flavor oscillations of atmospheric neutrinos. The main goal of the ICAL detector is to precisely measure the neutrino oscillation parameters and determine the neutrino mass hierarchy [2]. At a depth of around 1.2 km, the INO-ICAL detector will be the biggest magnetized detector to measure cosmic ray muon flux with the capability to

J. Singh $(\boxtimes) \cdot S.$ Nagu \cdot J. Singh

Department of Physics, Lucknow University, Lucknow 226007, India e-mail: jaydip.singh@gmail.com

S. Nagu

e-mail: srishtinagu19@gmail.com

J. Singh

e-mail: jyo2210@yahoo.com

© Springer Nature Singapore Pte Ltd. 2018

S. Biswas et al. (eds.), *Advanced Detectors for Nuclear, High Energy and Astroparticle Physics*, Springer Proceedings in Physics 201, https://doi.org/10.1007/978-981-10-7665-7_13

J. Singh et al.

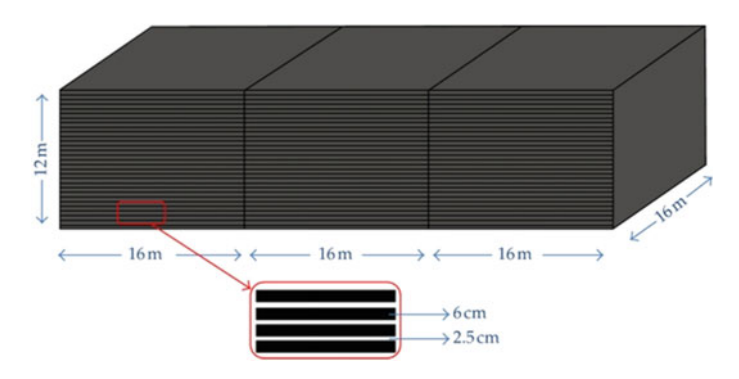


Fig. 1 Schematic view of three modules proposed iron calorimeter detector for INO

distinguish μ + from μ -. The existing direct and indirect methods of muon spectrometry at accelerator-based and in cosmic ray (magnetic spectrometers, transition radiation detectors) experiments involve certain technical problems and limitations in the energy region $\geq 10^{13}$ eV. These disadvantages vanquish in this alternate method where the muon energy is estimated by measuring the energy of secondary cascades formed by muons losing their energy in thick layers of matter, mainly due to the process of direct production of e⁺ and e⁻ pairs. Using this technique, we can estimate energy of very high-energy muons (1–1000 TeV) in our large mass underground INO-ICAL detector operating as a pair-meter. The primary cosmic rays which are approximately in 50 TeV–50 PeV energy range correspond to this energy range [3] (Fig. 1).

This work presents a simulation based on the latest version of Geant4 INO-ICAL code, developed by the INO-collaboration for momentum reconstruction of muons in GeV energy range using INO-ICAL magnet. We have developed a separate Geant4 code for counting the muon bursts in iron plates for ultra-high-energy muon analysis using pair-meter techniques. Details of the components and dimensions are discussed in [2].

2 Momentum Reconstruction Analysis with ICAL Magnet

In this section, we have discussed the simulation for momentum reconstruction of muons in magnetic field. Details of the detector simulation for muons with energy of few 10's of GeV with older version of INO-ICAL code are already published in the [4]. For simulating the response of high-energy (100's of GeV) muons in the ICAL detector, 10,000 muons were propagated uniformly from a vertex randomly located inside a $8 \, \text{m} \times 8 \, \text{m} \times 10 \, \text{m}$ volume. This is the central region of the central module where the magnetic field is uniform of 1.5T. In our analysis, we have considered only those events whose z-coordinate of the input vertex lies within

 $z_{in} \leq 400\,\mathrm{cm}$ which comprises the vertex to the central region. The input momentum and zenith angle are kept fixed in each case while the azimuthal angle is uniformly averaged over the entire range $-\pi \leq \phi \leq \pi$. In each case, we have studied the number of reconstructed tracks, the direction resolution, including up/down discrimination, and the zenith angle resolution. In this work, we have followed the same approach as in [4] for muon response analysis up to energies 500 GeV inside the detector [5]. Momentum reconstruction efficiency in the energy range of 1–400 GeV is shown in Fig. 2, and this energy range at the detector corresponds to the surface muon lying in the energy range $1600-2000\,\mathrm{GeV}$ from the top of the surface. Muon will lose around $1600\,\mathrm{GeV}$ in the rock overburden [5] to reach at the detector from the top surface. Energetic muons from other directions will also hit the detector since the rock cover in other direction of detector is very huge, so we have not discussed it here.

The momentum reconstruction efficiency (ε_{rec}) is defined as the ratio of the number of reconstructed events, n_{rec} , to the total number of generated events, N_{total} . We have

$$\varepsilon_{rec} = \frac{n_{rec}}{N_{total}},$$
 with error, $\delta \varepsilon_{rec} = \sqrt{(\varepsilon_{rec}(1 - \varepsilon_{rec})/N_{total})}$.

Figure 2 shows the muon momentum reconstruction efficiency as a function of input momentum for different $\cos\theta$ bins; here, left and right panels demonstrate detector response for low and high energy (in 100's of GeV) muon momentum, respectively. One can see that the momentum reconstruction efficiency depends on the incident particle momentum, the angle of propagation, and the strength of the magnetic field. As the input momentum increases, the reconstruction efficiency increases for all angles because with increase in energy, the particle crosses more

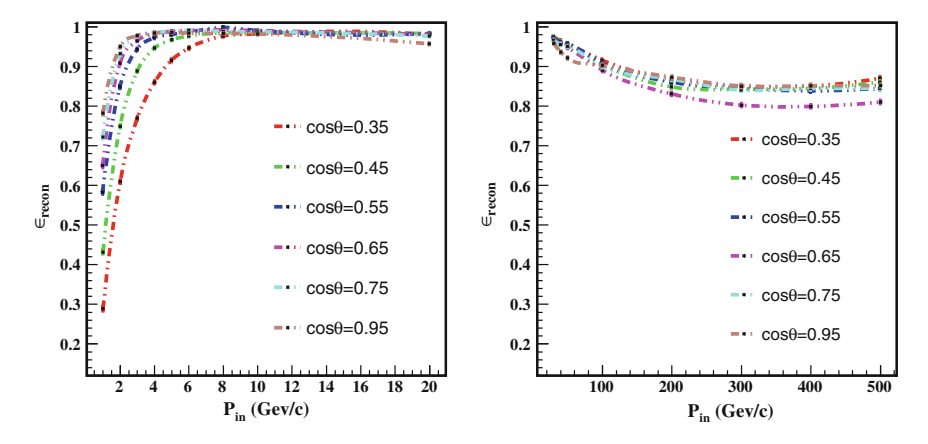


Fig. 2 The relative charge identification efficiency as a function of the input momentum for different $\cos\theta$ values at low and high-energy

number of layers producing more hits in the detector. But at sufficient high energies, the reconstruction efficiency starts decreasing, since the muons travel nearly straight without being deflected in the magnetic field of the detector. Track reconstruction is done using Kalman Filter techniques [4], tracks for few energies are plotted in Fig. 3, which shows the deflected and undeflected muon tracks depending on the energy of muons in a fixed magnetic field (1.5T).

Pair Meter Techniques:

6.8 5 GeV/c -1 GeV/c ຂດດດ Z Position (m) Position (m) 6.2 5.4 0.5 1.5 2.5 X Position (m) X Position (m) 10 GeV/c 20 GeV/c Z Position (m) Position (m) 2.5 X Position (m) X Position (m) 50 GeV/c — 100 GeV/c Z Position (m) X Position (m) X Position (m) 200 GeV/c 300 GeV/c Z Position (m) Position (m)

Fig. 3 Fixed energy muons track stored in X-Z plane of the detector going in the downward direction

X Position (m)

X Position (m)

- High-energy muons produce secondary cascades mainly due to electron pair production process.
- 2. It is one of the most important processes for muon interaction at TeV energies; pair creation cross section exceeds those of other muon interaction processes in a wide region of energy transfer:
 - $100 \, \text{MeV} \le E_0 \le 0.1 \, \text{E}\mu$, E_0 is threshold energy.
- 3. Average energy loss for pair production increases linearly with the increase in the muon energy, and in the TeV region, this process contributes more than 50% of the total energy loss rate.
- 4. Pair meter method for energy reconstruction of high-energy muons has been used by the NuTeV/CCFR collaboration [1].

Average No. of Burst Calculation [3]:

The e⁺ and e⁻ pair production cross section by a muon of energy E_{μ} with energy transfer above a threshold E_0 increases as $\ln^2(2m_e E_{\mu}/m_{\mu}E_0)$ where m_{μ} is the mass of muon and m_e is the mass of the electron. Defining $v = E_0/E_{\mu}$, above $v^{-1} = 10$, this cross section dominates over other processes by which the muon loses its energy when it passes through dense matter, generating observable cascades.

- The pair production cross section depends upon E_{μ}/E_0 which allows one to estimate the energy of muon by counting the number of interaction cascades M in the detector with energies above a threshold E_0 .
- Differential cross section for pair production is estimated in [3] and that expression is given by:

$$v\frac{d\sigma}{dv} \simeq \frac{14\alpha}{9\pi t_0} ln \left(\frac{km_e E_\mu}{E_0 m_\mu}\right) \tag{1}$$

- where $\alpha = 1/137$, k $\simeq 1.8$ and t₀ is the radiation length (r.l.) of the material, for iron t₀ = 13.75 gm/cm².
- The average number of interaction cascades M above a threshold E₀ is given by:

$$M(E_0, E_u) = Tt_0\sigma(E_0, E_u)$$
 (2)

$$E_{\mu} = (E_0 m_{\mu} / k m_e) \exp(\sqrt{9\pi M / 7\alpha T - A})$$
(3)

– where T is target thickness and $\sigma(E_0,E_\mu)$ is the integrated cross section (in unit of cm²/gm) and A \simeq 1.4.,

$$\sigma(E_0, E_\mu) \simeq \frac{7\alpha}{9\pi t_0} \left(ln^2 \left(\frac{km_e E_\mu}{E_0 m_\mu} \right) + A \right) \tag{4}$$

J. Singh et al.

3 Counting the Burst Using Pair Meter

A muon traversing vertically from the top will cover $151 \times 5.6 \simeq 845\,\mathrm{cm}$ in iron plates; this is equivalent to a path length of $\simeq 480\,\mathrm{r.l.}$ The number of cascade produced by high-energy muon for a path length of 450 r.l. can be calculated using (2). The number of cascades produced as a function of muon energy is shown in Fig. 4.

3.1 Penetration Depth of Electron in the Iron Plates

Estimation of muons burst energy in iron plates will be evaluated by e^+ and e^- energy, for that electron produced in iron plates must come out of the iron plates and hit the detector active element resistive plate chamber(RPC). The energy loss of electron in iron is given by: $E=E_0\ e^{-x/x_0}$, where x is distance traveled in the iron plate and x_0 is the radiation length. Electron of sufficient energy will come out of the iron plates and hit the RPC. Figure 5 shows electron energy and their range in iron plates.

Fig. 4 Average number of bursts above a threshold E_0 versus muon energy for E_0 = 1.0, 10.0 and 100.00 GeV, with T fixed to 450 r.l

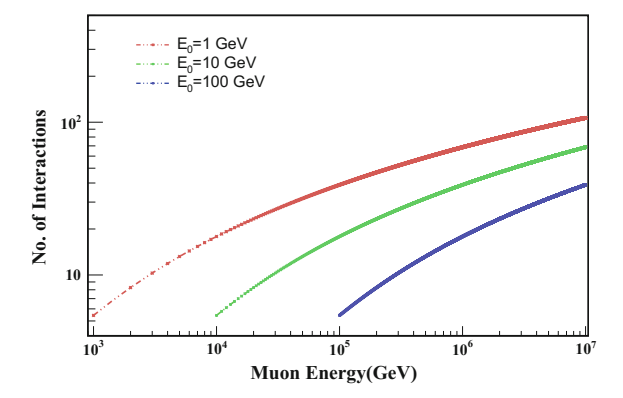
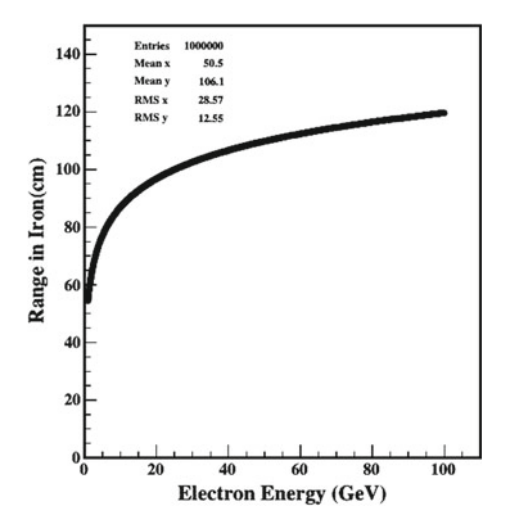


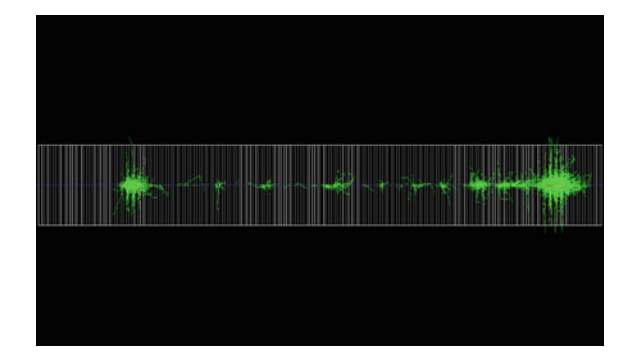
Fig. 5 Energy of the electron and the corresponding penetrating range in the iron plates



3.1.1 10 TeV Muon Burst in the Iron Plates

A Geant4-based code is developed for simulating the muons burst in iron plates; here, horizontal axis is the z-axis of INO-ICAL detector, in which 152 layers of iron plates of width 5.6 cm are placed vertically, interleaved with 4.0 cm for placing the RPC. Muons are propagated using Geant4 particle generator class, and generated bursts in the iron plates are counted; a 10 TeV muon burst is shown in Fig. 6.

Fig. 6 Cascade generation in the iron chamber, blue line (muon)represents z-axis of the detector, and green line represents the electron-positron cascade in the x-y plane



J. Singh et al.

3.2 Operating ICAL Using Pair Meter Technique

See Fig. 7.

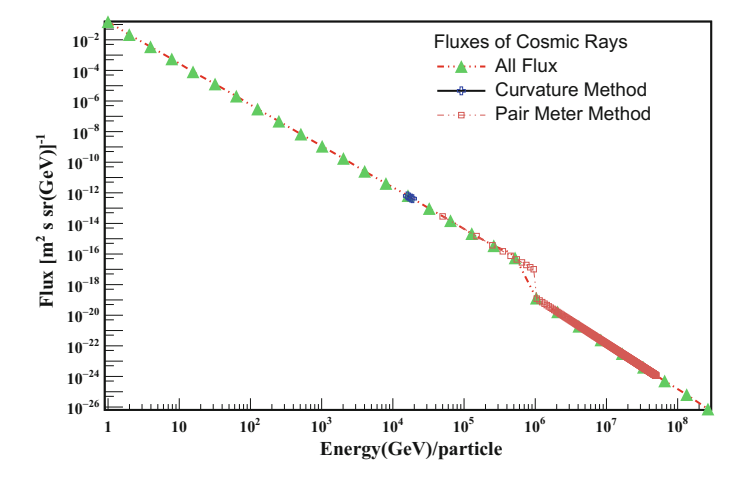


Fig. 7 Primary cosmic ray flux ($\phi \simeq KE^{-\alpha}$, where $\alpha \simeq 2.7$ and for KNEE (3 PeV) $\alpha: 2.7 \to 3$) versus energy of primary particle, and limited range for ICAL to cover the spectrum using magnetic field and pair meter technique

4 Results and Discussion

In Sect. 2, we have discussed the limitation of magnetized ICAL detector to be used as a magnetic spectrometer, which limits the efficiency of the detector to discriminate between $\mu+$ and $\mu-$ at higher energies and reconstruct momentum. Variation in efficiency of muon momentum reconstruction as a function of input momentum is shown in the Fig. 2, which shows clear fall in efficiency for energetic muons; we can also see the muon track in Fig. 3, which is undeflected for energetic muons. Finally, we conclude that with ICAL detector, we can do analysis for muons in the energy range of 1–400 GeV. This corresponds to surface muons in the energy range of 1600– 2000 GeV, because muons lose around 1600 GeV energy in the rock overburden to reach at the detector from the top of the INO-ICAL surface. ICAL can not be used as a magnetic spectrometer for highly energetic cosmic ray muons. For energetic (TeV) muons, pair-meter technique [6] can be used for momentum reconstruction as discussed in Sect. 3 [3]. This technique is tested by a few detectors, since INO-ICAL will be large in dimensions so it will be a perfect machine to test the capability of this technique. We have developed a separate Geant4 code for counting the bursts in the iron plates and also a technique to measure the energy of the bursts with the produced

electrons pairs in to the iron plates. In Fig. 6, we can see the burst of muons in iron plate, some of the bursts are bigger and some are smaller as discussed in Sect. 3. The variation of these burst number is shown in Fig. 4, which is a function of the muon energy.

4.1 Summary and Conclusions

- The pair-meter technique can competently measure muon energy in the energy range of 1–1000 TeV at INO-ICAL detector operating as pair-meter.
- One can probe very high-energy muon fluxes and primary cosmic rays in the Knee region which will aid in accurate background muon and neutrino flux measurement in the forthcoming detectors designed for ultra-high-energy neutrino experiments.
- Our Geant4 analyses for central module of INO-ICAL detector is successfully performed, and variation in the cascade number of varying energy is also observed in the iron plates. Highly energetic bursts will be bigger in size, and lesser energetic bursts will be smaller in size, in the X-Y plane of the iron plate.

Acknowledgements This work is partially supported by Department of Physics, Lucknow University, Department of Atomic Energy, Harish-Chandra Research Institute, Allahabad and INO collaboration. Financially, it is supported by government of India, DST project no-SR/MF/PS02/2013, Department of Physics, Lucknow University. We thank Prof. Raj Gandhi for useful discussion and providing hospitality to work in HRI, Dr. Jyotsna Singh for her support and guidance in completing this work from Lucknow University.

References

- A.P. Chikkatur, L. Bugel et al., Test of a calorimetric technique for measuring the energy of cosmic ray muon in TeV energy range. Z. Phys. C 74, 279289 (1997)
- S. Ahamed , M.S. Atahar et al., Physics Potential of the ICAL detector at the Indian Based Neutrino Observatory, (INO Collab) arXiv:1505.07380
- 3. R. Gandhi, Sukanta Panda J. Ref.: JCAP **0607**, 011 (2006)
- 4. A. Chatterjee et al., (INO Collab) JINST 9(2014) PO7001, July 2014
- 5. J. Singh, J. Singh et al., arXiv:1709.01064
- 6. R.P. Kokoulin, A.A. Petrukhin, Nucl. Instrum. Method Phys. Res. A263, 468–479 (1988)
- 7. D.E. Groom, N.V. Mokhov, S. Striganov, Muon stopping power and range
- 8. GEANT4 collaboration, S. Agostinelli et al., GEANT4: a simulation toolkit, Nucl. Instrum. Meth. A **506**, 250 (2003). http://geant4.cern.ch/

Characteristic Simulations of Stack of Four Gas Electron Multipliers (GEMs)

Mriganka M. Mondal, Sagarika Swain, P. K. Sahu and S. N. Nayak

Abstract Gas Electron Multiplier gained its importance in recent years due to high efficiency and high event rate handling capabilities with good time and position resolutions. Here, we made a simulation study on stacks of 4-GEM to characterize the properties like gas gain, effective gain, collection efficiency, ion backflow, energy and position resolution using Garfield++ and ANSYS field solver. A systematic analysis is done on induced signal shape for various detector field configurations, and a preferable zone of operation for the detector is being discussed.

1 Introduction

Gas Electron Multiplier (GEM) [1] developed in mid 90's is used extensively in current experiments for its various advantages over conventional detectors like wire chambers. The experiments like STAR [2], ALICE [3], and CBM [4] use GEM either as a tracking detectors and/or readout purposes for its high rate handling capabilities with relatively good position resolutions and with controlled ion backflow in the drift region. GEMs are radiation resistant and economic detectors with high detection efficiency. GEM has advantage to use in multiple layers of foils and leading to better control on gain, resolution, timing, and ion backflow. Simulations can give us a better understanding on transport for electrons and ions in various detector field configurations and therefore leading us to operate a detector in a more efficient way.

In this work, we first try to understand a 4-GEM detector which is fabricated in our laboratory for the purpose of study of its long-term stability and its response with various gas flow rate, as an additional feedback to ALICE 4-GEM [3] detector performance. Here, we try to figure out what should be the best field configuration for such a four GEM detector so that we get a reasonable energy resolution with preferred effective gains. To have a better time resolution, we carried out induced

M. M. Mondal (⋈) · S. Swain · P. K. Sahu Institute of Physics, HBNI, Bhubaneswar 751005, India e-mail: m.mriganka@gmail.com

S. Swain · S. N. Nayak

School of Physics, Sambalpur University, Jyoti Vihar, Burla, Sambalpur 768019, India

[©] Springer Nature Singapore Pte Ltd. 2018

148 M. M. Mondal et al.

signal shape analysis which has direct relation of collection time of electrons. This way, it is very important to understand the working philosophy and performance of the detector.

Detector hole alignment and GEM foils with different pitch size proved to be an important parameter for controlling ion flow in the drift region, and this is being used by ALICE for controlling ion backflow rate. The technique we have learned here is important to carry out simulations on resistive plate chambers (RPCs) and simulates its surface properties also.

2 Simulation Framework for GEM

The geometry of GEM is designed in such a way that it creates high electric field inside the holes enabling localized avalanches. Knowledge on creation and transport of avalanche electrons, its absorption is required to understand fully the detectors performance. The full simulations are done using Garfield++ package, which is a C++ version of the existing Garfield [5]. External field solver program, ANSYS [6] which uses finite element method for its solution is available at CERN, is used as an input for Garfield++.

X-rays from source like Fe⁵⁵ generate photoelectrons and Auger electrons, which in terms produce primary ionization in the drift region. HEED [7] program generates the distribution of the numbers and its energy distributions, which is very essential to carry out more realistic simulations. For all practical purposes, a single electron from such distribution in an event is sufficient to calculate the avalanche production, using Garfield++ and carry out all other calculations.

The motion of the primary and secondary electrons in the drift region is governed by the mechanisms of drift in the electric field and the random diffusion of the electrons and ions in the gas medium of the detector. Microscopic calculations of diffusion of primary and produced electrons are done using transport parameters, calculated with the Magboltz [8] program, which is interfaced into Garfield++.

Where GEM is used as tracking detector for charged particle detection like muons or pions, the track left primary ionization in the drift region, which is funneled into the GEM active region, i.e., the holes. The multiplication of the primary electrons by avalanches generate secondary electrons, which are eventually collected in the induction region. This is the simple working principle for a GEM. The effective gain for multiple layers of GEM detector can be interpreted as multiplies of the gains of all the layers. Successive layers of GEM sequentially multiplies the outputs of the avalanches from the previous GEM layers, and thus, relative high gains can be achieved with smaller applied voltage across a GEM. This reduces the spark probability and with high detection efficiency instead of using a single layer with a desired gain value. Moreover with more controlled parameters for multiple GEMs, one can obtain high energy resolution and controlled ion backflow in the drift region. This is a big advantage on use of GEM detector with multiple layers. The active GEM element used here is a thin $(50\,\mu\text{m})$ polyimide foil with a $(5\,\mu\text{m})$ copper coating on

both sides. Typically, their outer diameter is $70 \,\mu\text{m}$, the inner diameter is $50 \,\mu\text{m}$, and the hole pitch is $140 \,\mu\text{m}$. For ArC O_2 70/30% gas mixture, a penning factor p=0.57 is used. The drift gap, three transfer gaps, and the induction gap are taken to be 3, 2, 2, 2, and 2 mm, respectively, for the study. Single electron event by event with energy $0.5 \,\text{eV}$, placed at x = 0, y=0, and in the center of the drift region in z. The low energy of the starting electron ensures the probability to ionize further in the drift region to zero.

3 Detector Simulation and Results

The total number of electron-ion pairs produced or the gas gain are all determined by the applied voltages across each of the GEM layers. Voltages applied across GEM foils in principle fix the individual gains of each layer and the transport of the electrons is governed by the field configurations. So the effective gain, which is the total number of the electrons transported in induction region to the primary electrons all depend both on the gas gain and field configurations.

The field setup and the hole configuration influence the transparency factor of the detector, which are the number of electrons that are able to do the avalanche and collected in the readout without any loss. It is actually the product of collection and extraction efficiency. The other parameter is the electron collection efficiency, which is the ratio of electrons coming inside the GEM hole to the number of electrons just above it. The electron endpoints define the position, where an electron is being absorbed. The absorption may happen in Kapton and in copper layer by ions or in the anode plane. Figure 1 shows the z-positions, where electrons are being created in red and the absorption z-positions in green. A large fraction of the electrons gets absorbed in 5 μm copper layer of the GEM foil, where the voltage applied is positive compared to the other copper layer of the corresponding GEM foils before rest of the electrons being transferred below the GEM foil. The trend is same for all the four GEM foils.

3.1 Gas Gain and Effective Gain

The gas gain is the number of avalanche electron-ion pairs produced in the detector. The transport of electrons and ions depend on the geometry and field configuration of the detector and the number of electrons transported to the induction region define the gain or the effective gain of the detector. The effective gain for a single GEM foil can be expressed as (1) Primary electron detector efficiency, E_{pr} , (2) Multiplication coefficient in the hole, M_{hole} , (3) Secondary electron collection efficiency, E_{sc} , and (4) Induced charge factor \sim 2 for the signal created by the electron component, or greater if the ion component contributes to the signal (depends on the detector geometry and readout method) $M_{eff} = E_{pr} M_{hole} E_{sc} \times 2$ [9]. For multiple layers,

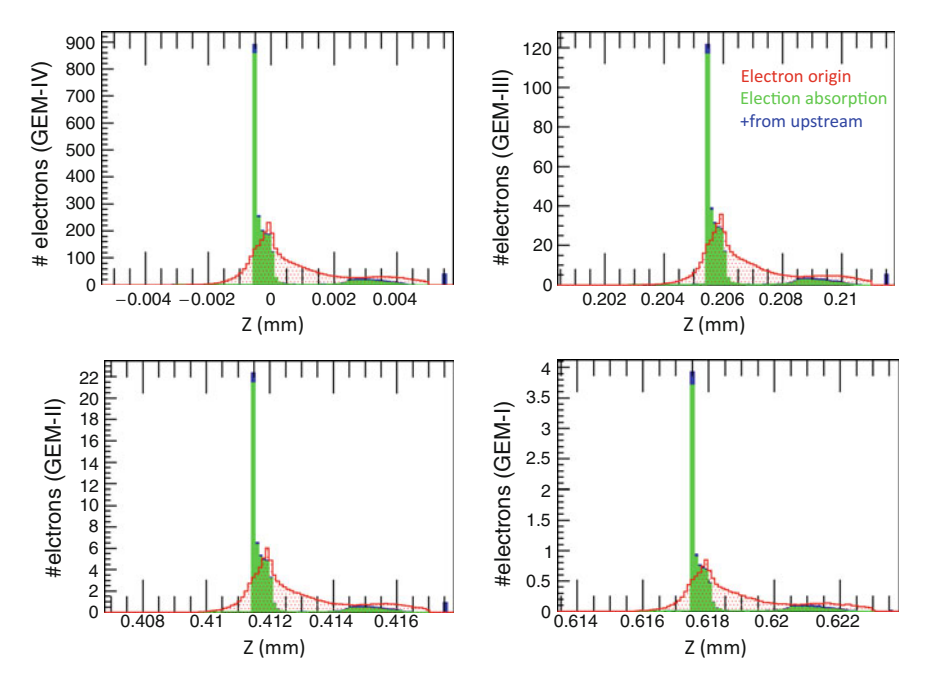


Fig. 1 The endpoints of electrons in different GEM layers with green and the z-position from where electron is produced is in red. The blue one is endpoints with the additional electrons coming from drift regions. The foil near to drift plane is marked as GEM-I and the consecutive layers are GEM-II, GEM-III, and GEM-IV where the GEM-IV is near to the induction plane

the secondary electrons collected to the next GEM foil and so on. Thus effective gain of each GEM layers convoluted with a loss factor of primary detector efficiencies time secondary electron collection efficiency for each layer. The effective gain for the detector can be calculated from simulations as the ratio of the number of electrons collected in the induction region to the number of electrons entering in the first GEM layer through the drift region. In Fig. 1, the left panel shows the intrinsic gain in blue markers and the effective gain is in red circular markers. The effective gain is not increasing after certain voltage, even though the intrinsic gain is increasing steadily. To investigate further, the effective gain for each GEM foil is shown in right panel of the figure. It seems that effective gains for the first two GEM layers do not show any drop within the voltage range shown but, the third GEM foil starts dipping after 4700 V, and the fourth GEM foil starts much earlier. The field configuration might not be suitable to transport the electrons in such a scenario. In Table 1, the voltage across GEM foils with the applied detector voltages are shown. With applied voltage 4400 V across the detector, where ΔV (GEM's) is within 336–359 V, we will tune the various fields in order to its effect on effective gain. The current drift, T_{12} , T_{23} , T_{34} (transfer) and induction fields are set as 2.08, 2.90, 2.87, 3.12, and 3.03 kV/cm, respectively. Here, T_{12} , T_{23} , and T_{34} are transfer files between the GEM layers in subscripts. This adjustment in the field for the setup would enable to transport most

| Voltages (V) | 3000 | 3500 | 4000 | 4200 | 4400 (gain~ 2k) | 4600 | 4800 | 5000 |
|----------------------|------|------|------|------|------------------------|------|------|------|
| ΔV (GEM-I) | 229 | 267 | 306 | 321 | 336 | 351 | 367 | 382 |
| ΔV (GEM-II) | 239 | 279 | 319 | 334 | 350 | 366 | 382 | 398 |
| ΔV (GEM-III) | 238 | 278 | 318 | 333 | 349 | 365 | 381 | 379 |
| ΔV (GEM-IV) | 245 | 286 | 327 | 343 | 359 | 376 | 392 | 408 |

Table 1 Voltages across various GEM foils with the applied voltages according to existing 4-GEM setup in our lab

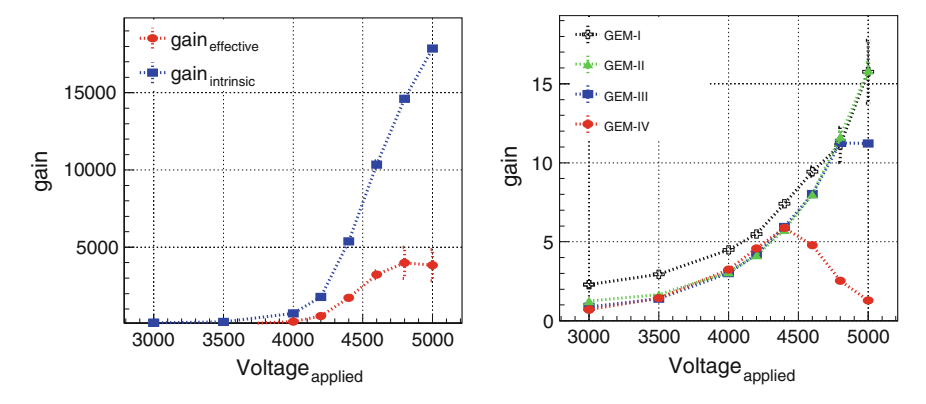


Fig. 2 The intrinsic or gas gain in left panel in blue and the effective gain in red with the voltages applied in x-axis. The effective gain for individual gem foils are in right panel

of the gas gain electrons in the induction zone and would raise effective gain. This would be discussed in the next sections (Fig. 2).

3.2 Field Configuration

With ΔV across the GEM foils being fixed to 229 (I), 239 (II), 238 (III), and 245 (IV) V and with the drift, T_{12} , T_{23} , and T_{34} (transfer) set to 2.08, 2.90, 2.87, and 3.12 kV/cm, respectively, the induction field is varied in between 0.5 and 9 kV/cm. Figure 3 in left shows the intrinsic and effective gains with the induction field. Though the intrinsic gain remains irrespective with the variation of induction field, the effective gains are increasing with the induction field. Figure 3 in right shows that the induction field influences collection efficiency for the fourth GEM layer, which in terms raise the effective gains. This clearly demonstrates that higher induction field pulling more electrons toward the anode plane and in general, the field should set at higher value. For the time being in the further studies, the induction field is set at $4.0 \,\mathrm{kV/cm}$.

Figure 4 shows the influence of the drift field on gain values and within the range of $0.2-1.5 \,\mathrm{kV/cm}$, and we do not see any significant effect in gain value shifting. We set the drift field to a value $0.4 \,\mathrm{kV/cm}$ for the next level of studies on variation of transfer field between GEM layers first and second, T_{12} . Figure 5 shows the gains

152 M. M. Mondal et al.

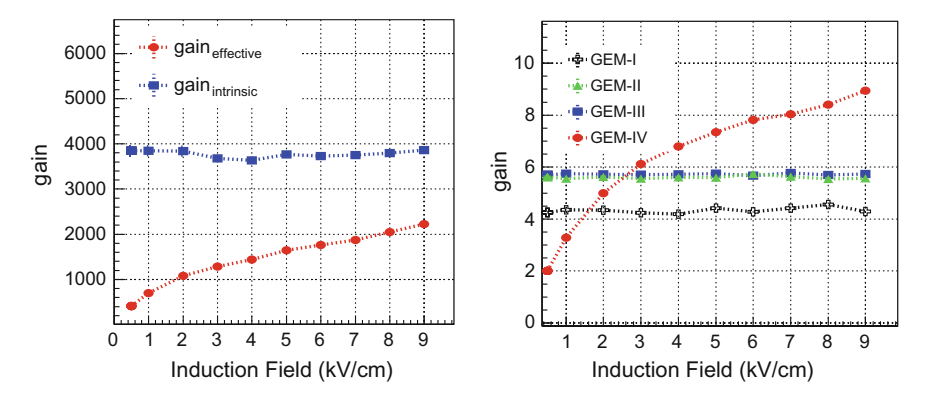


Fig. 3 Left: Intrinsic and effective gains with induction field. Right: Effective gains with induction field for each of the gem layers

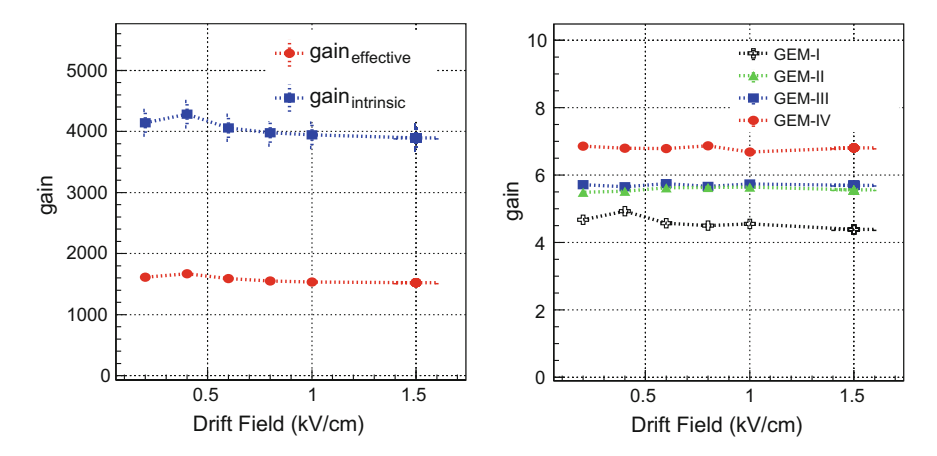


Fig. 4 Left: Intrinsic and effective gains with drift field. Right: Effective gains with drift field for each of the gem layers

with T_{12} in between 1.0 and 4.0 kV/cm, which shows an increase between 1 and 2 kV/cm and attaining a higher stable effective gain value \sim 1800 at higher T_{12} fields. Basically, whatever the changes in the effective gain is coming due to the change in transport properties variation for the GEM-I and which should be the case. In proper terminology, it can be said that the higher T_{12} field led to high collection efficiency for GEM-I.

Collection efficiency for each GEM foil is calculated for all the field settings, and it is found that for GEM-II, III, and IV, the value is just below 0.4 (\sim .038) and for the layer GEM-I it is \sim 1. Value for GEM-I seems to be reasonable, since we are leaving electrons at 0, 0 in x, y which is just above the hole centers, which leads to all of the initial electrons transported to the active areas of GEM foil. The variation is noticeable in Fig. 6 (left panel), where T_{12} field has an effect on GEM-II for higher

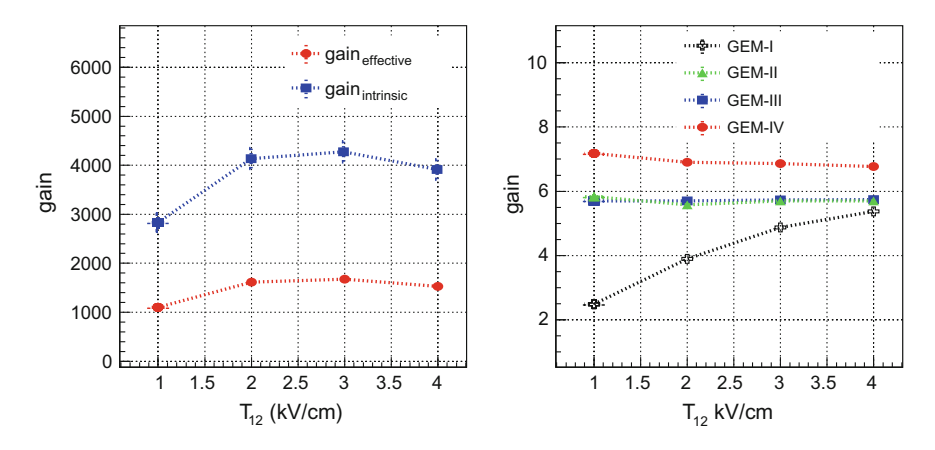


Fig. 5 Left: Intrinsic and effective gains with transfer field between GEM-I and GEM-II. Right: Effective gains for each of the gem layers

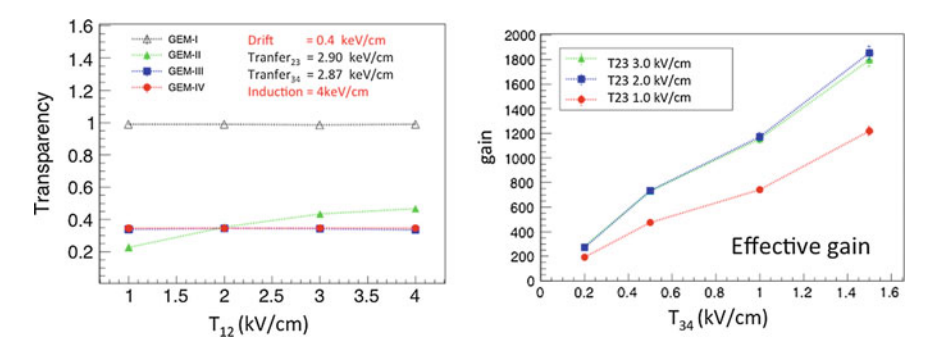
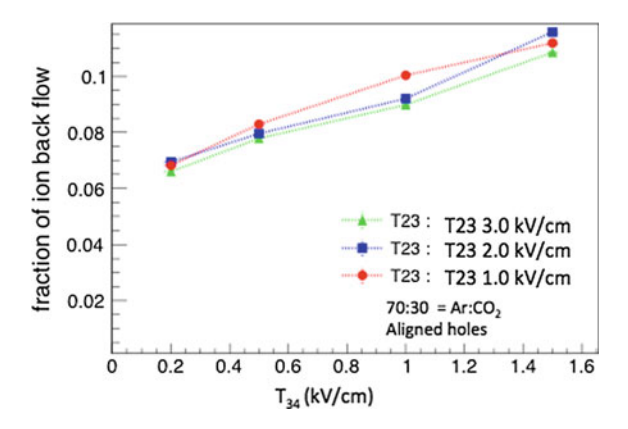


Fig. 6 Left: Collection efficiency for different gem foils with T_{12} . Right: Effective gain with T_{34} with $T_{23} = 1.0, 2.0, 3.0 \text{ kV/cm}$

collection efficiency at high T_{12} field. Therefore, we set T_{12} to 4.0 kV/cm and made a detailed scan over T_{23} and T_{34} fields. A study on effective gains with T_{34} is shown in Fig. 6 (right panel) where T_{23} is set to 1.0, 2.0, and 3.0 kV/cm. From the perspective of gains, we see that when the detector field T_{23} is set within 2.0–3.0 kV/cm, a higher value of T_{23} in between 1 and 1.5 kV/cm is required to operate the detector with an effective gain within 1200–1900. It is to be noted, if a factor 2 is multiplied to the gains according to [9], the effective gains would be in the range of 2400–3800. The other thing is quite important for readout purposes is to have the detector ion backflow values as minimum as possible. It has been found that ion backflow is 7% for $T_{34} = 0.2$ kV/cm and increasing to 11% for $T_{34} = 1.5$ kV/cm, and it is shown in Fig. 7. So, for maintaining low ion backflow, the detector should be operated at lower T_{34} field. In fact the ALICE collaboration has obtained much lower ion backflow rate but their geometry is quite different consisting of mixture of small and large pitch GEM foils with holes are being misaligned.

154 M. M. Mondal et al.

Fig. 7 Ion backflow with T_{34} for $T_{23} = 1.0$, 2.0, $3.0 \,\text{kV/cm}$

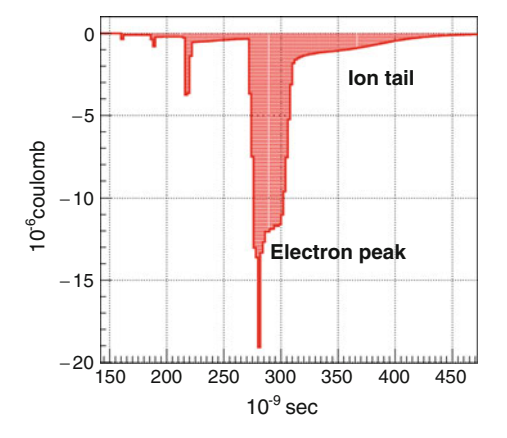


3.3 Induced Signals, Timing, and Spatial Resolutions

Electrons drift in the induction gap and the readout plate which has dimensions much larger than the hole get the effect of induced currents. ANSYS generates the weighted fields for the region and the velocity of the charge particles and the induction gap determines the induced signal width. T_{34} and T_{23} fields have also effects on signal timing and signal width due to their effect on drift velocity modifications. A typical induced signal shape is shown in Fig. 8, where the width is \sim 40 ns and it takes about 300–400 ns after a charged particle entering the detector to start develop the induced signals. There are three small spikes before main electron peak (in earlier times), which probably the effect from the rest three gem layers, where avalanches occur in different times.

The gain distributions from events by events give rise to a Gaussian peak and resolution found from the fits. The resolution for single electrons with T_{23} is shown in Fig. 9 (left). The resolution for a X-ray source like iron will be convoluted with the

Fig. 8 A typical signal shape for $T_{23} = 2.5 \,\mathrm{kV/cm}$ and $T_{34} = 1.5 \,\mathrm{kV/cm}$. There is a long tail for the induced signals from the slow-moving ions. signal width is $\sim 40 \,\mathrm{ns}$ and takes about 275 ns to start develop the electron peak which mostly the avalanches occurring in the GEM-IV



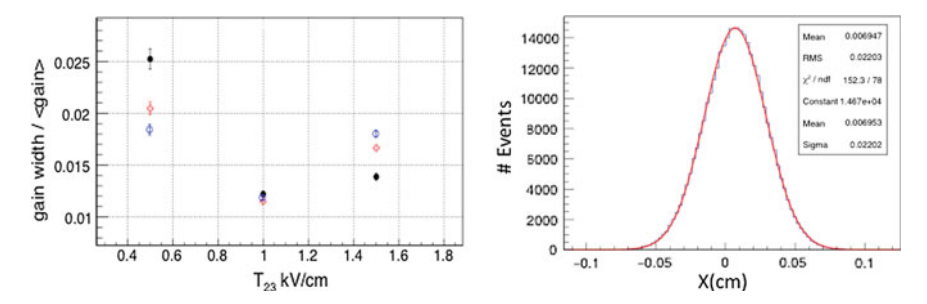


Fig. 9 Left: Single electron energy resolutions with T_{23} . $T_{34} = 1.0$ (black), 2.0 (red), 3.0 (blue) kV/cm. Right: Electron x endpoints at readout plate which gives spatial resolution scale

widths of the primary number of charge distributions in drift region. The x-position distributions of the electrons at anode are shown in Fig. 9 (right) which gives about $220 \mu m$ spatial signal spread.

4 Summary

We have performed a simulation study for 4-GEM of hexagonal structure to $140\,\mu m$ pitch. A typical configuration with GEMs voltages 229 (I), 239 (II), 238 (III), and 245 (IV) V and with drift field, induction field and T_{12} set 0.4, 4, and $4\,k$ V/cm, respectively, the detector can operate at $T_{23} = 3\,k$ V/cm and $T_{34} = 1.5\,k$ V/cm with a gain maximum of 3800. However, for low ion backflow, we need to set lower T_{34} compromising gains. For more detailed simulations, we may need to study with combination of large and small pitch to explore more on ion backflow rate. Induced signal shape study gives us about $40-50\,\mu m$ position resolution. For single electron, we have energy gain width in 1.5-2.0% range, which would increase when we include the extra width incorporated from primary ionization distributions for X-ray source like Fe⁵⁵. The position resolution found to be about $200\,\mu m$.

References

- 1. F. Sauli, Nucl. Instr. Meth. A 386, 531 (1991)
- 2. http://www.star.bnl.gov/
- Technical Design Report for the Upgrade of the ALICE Time Projection Chamber, ALICE-TDR-016, CERN-LHCC- 2013-020, 3 Mar 2014
- 4. http://www.fair-center.eu/for-users/experiments/cbm.html
- Veenhof, R.: GARFIELD, recent developments. Nucl. Instr. Meth. A419, 726730 (1998);
 Garfield++ simulation of tracking detectors, Available: https://cern.ch/garfieldpp
- 6. ANSYS Simulation Driven Product Development, Available: http://www.ansys.com/
- I.B. Smirnov, Modeling of ionization produced by fast charged particles in gases. Nucl. Instr. Meth. A 554, 474493 (2005)

M. M. Mondal et al.

8. S.F. Biagi, Monte Carlo simulation of electron drift and diffusion in counting gases under the influence of electric and magnetic fields. Nucl. Instr. Meth. A **421**, 234240 (1999)

9. O. Bouianov, M. Bouianov, R. Orava, P. Semenov, V. Tikhonov, Progress in GEM simulation. Nucl. Instr. Meth. A **450**, 277287 (2000)

Performance Study of Muon Detector with CBM Experiment at FAIR

Ekata Nandy and Subhasis Chattopadhyay

Abstract The Compressed Baryonic Matter (CBM) experiment at the Facility for Anti-Proton and Ion Research (FAIR) accelerator facility in Darmstadt, Germany, aims to explore the strongly interacting QCD matter at very high net baryon density and moderate temperature, by colliding heavy-ions in the beam energy range 4–40 AGeV. One of the main goals of CBM research program is to look for the signatures of deconfinement and chiral phase transition. Measurement of low mass vector mesons (LMVMs) via their di-muonic decay channel has been proposed to be a key observable in this context. The Muon Chamber (MUCH) at CBM, built with a novel technology of segmented absorber system, is a dedicated detector for muon identification and tracking. In this article, we discuss details of MUCH construction, its latest design and its overall performance in detection of di-muons from LMVMs.

1 Introduction

The Compressed Baryonic Matter experiment at the Facility for Anti-Proton and Ion Research is an extensive heavy ion research program, which aims to explore the QCD phase diagram at moderate temperature and high net baryon density of the order of 5–10 times of the normal nuclear density. It is believed, such high-density matter might exist in the core of the neutron stars. At such high net baryon densities, phase transition from the hadronic to partonic degrees of freedom has been predicted. Therefore, the CBM experimental program will offer a unique opportunity to study the QCD phase transition at baryon densities comparable to the core of the neutron stars.

The proposed CBM experimental program includes the search for deconfinement and chiral symmetry restoration in baryon rich QCD matter, search for critical end point and the study of equation of state of superdense baryonic matter.

E. Nandy (⋈) · S. Chattopadhyay

VECC, 1/AF, Bidhan Nagar, Kolkata 700064, India

e-mail: ekatanandy@gmail.com

S. Chattopadhyay e-mail: sub@vecc.gov.in

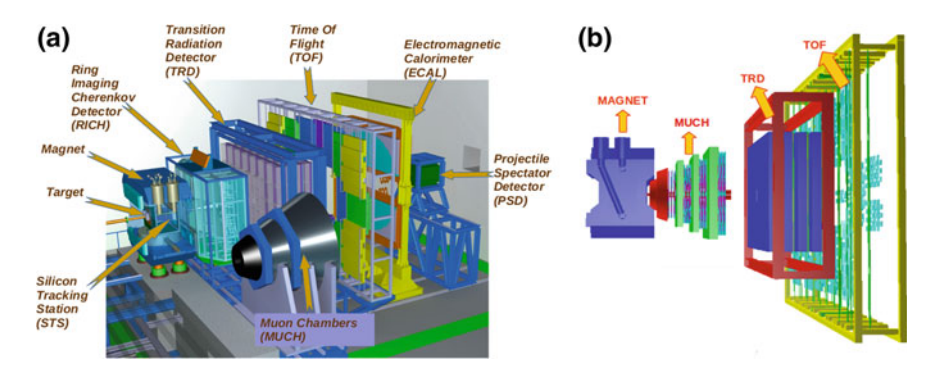


Fig. 1 $\,$ a General layout of CBM experimental setup. $\,$ b Simulation generated setup for detection of LMVMs

Thus the major challenge is to identify suitable probes which will be sensitive to such deconfinement phase transition and the restoration of chiral symmetry. One of the proposed signatures of the onset of chiral symmetry restoration is the in-medium modification of hadron properties like broadening and shifting of hadronic mass. In this context, short-lived low mass vector mesons could be a diagnostic probe, as they decay within the medium and can be detected from their di-muonic decay channels [1]. Since muons are not affected by strong interactions, when passing through high-density QCD matter, they carry almost undistorted information from the core of the collision zone. CBM experiment will perform the first exploratory and precise measurements of di-muon productions in the beam energy range 4–40 AGeV at a very high interaction rate of $\sim\!10$ MHz. In this article, we report the performance study of latest MUCH design and results on the feasibility of di-muon measurements in central Au+Au collision at 8 AGeV beam energy, using the CBM simulation framework which will be discussed in the subsequent sections.

2 CBM Experimental Setup

Figure 1a shows the general layout of CBM experimental setup. The proposed experimental arrangement for the detection of di-muon from LMVMs [2] is shown in Fig. 1b. It consists of the following components: Dipole Magnet, Silicon Tracking Station (STS), Muon Chamber (MUCH), Transition Radiation Detector (TRD), and Time of Flight (TOF) detector.

STS is placed inside the dipole magnet that provides magnetic field integral of 1 Tm. STS is a dedicated detector for tracking and momentum determination of charged particles. The MUCH detector is placed after STS, and it is responsible for muon identification. MUCH is immediately followed by TRD and TOF which find application in triggering and identification of hadrons at large momentum, respectively.

2.1 Muon Detector Setup

The muon detection system in CBM is known as Muon Chamber. It consists of segmented absorber layers and detector chambers. A triplet of detector layers known as stations are placed between absorbers for detection of low momentum muons, as well as to improve the precision of tracking parameters by joining many available hits at the detector layers. Absorbers are placed for hadron absorption and background suppression. Gas Electron Multiplier (GEM) is used as an active detector element that operates with Ar+CO₂ gas mixture in the ratio 70:30 by volume. The segmented absorber system, as used in MUCH, is a unique design that facilitates efficient detection of muons, particularly at low momenta. For the detection of LMVMs, a '4 station 4 absorber' configuration has been standardized and used in this simulation.

2.1.1 Latest MUCH Geometry

MUCH is a conical-shaped detector located at 125 cm downstream of the target and covers an angular region of 5.7°–25° on either side of the beam pipe. As mentioned above, the MUCH setup for LMVM detection has four hadron absorber layers, of thickness 60, 20, 20, and 30 cm, respectively. The first absorber has a biconical shape and is made of Carbon. The first absorber is again split into two parts, of thickness 24 and 36 cm, respectively. The first part of the first absorber is placed inside the magnet, and the other part is kept outside. Rest of the three absorbers are made of iron (Fe) and has a shape of a parallelepiped. There is shielding around the beam pipe in absorber region to reduce the background of secondary electrons produced in the beam pipe. Shielding in the region of first absorber is made of lead, and for others, it is made of Iron. Beampipe is made of aluminum. For muon setup magnetic shielding bars are removed to avoid overlap with MUCH absorber.

Triplets of GEM detectors, known as station, are installed between each consecutive absorbers. Gap between consecutive absorbers is 30 cm, and three detector layers are placed with a separation of 10 cm each. Detector layers are circular in structure. Each layer has several trapezoidal-shaped GEM modules placed in staggering manners with half of the modules in the front surface and half on the rear face of a support structure. Details of design specifications of absorbers and detectors of MUCH are shown in Fig. 2. A prototype of a real GEM module built at VECC is shown in Fig. 3.

3 Simulation Study

Simulation for the feasibility study of di-muon measurement is performed with the full CBM experimental setup for LMVMs detection that includes latest MUCH geometry, STS, MAGNET, TRD, TOF, beampipe, and shielding at 8 AGeV central Au+Au collisions.

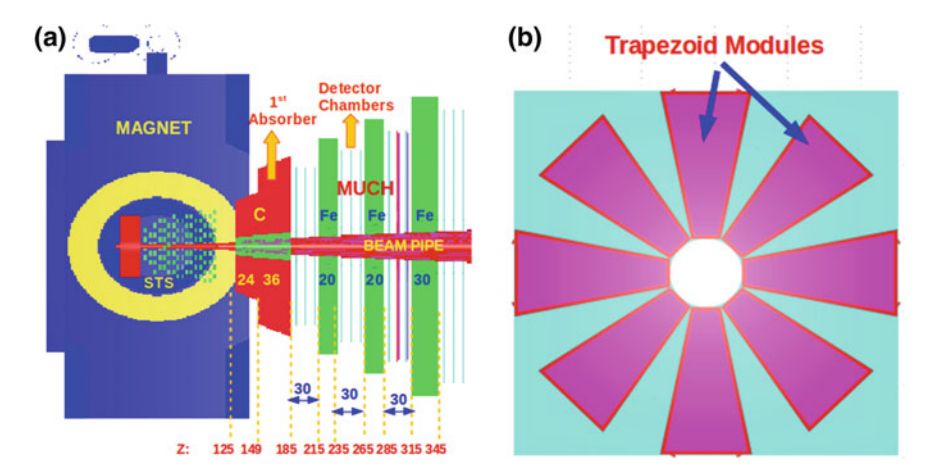


Fig. 2 a Latest design and specifications of absorbers and detectors of CBM-MUCH. b Arrangement of trapezoidal GEM modules in a detector layer

Fig. 3 Real prototype of GEM module designed at VECC



3.1 Tools Used

Full event simulation and reconstruction is done using the CBMROOT [3] framework. The contents of this simulation package are as follows: (a) GEANT3 [4] for geometry implementation and particle transport, (b) PLUTO [5] generator generates LMVMs and decay them into di-muons, and (c) UrQMD [6] for background particles.

3.2 Performance of GEM Detectors

Since CBM will operate at a very high interaction rate, detectors are required to be fast and capable of handling high flux rate. In Fig. 4a, we report the particle density,

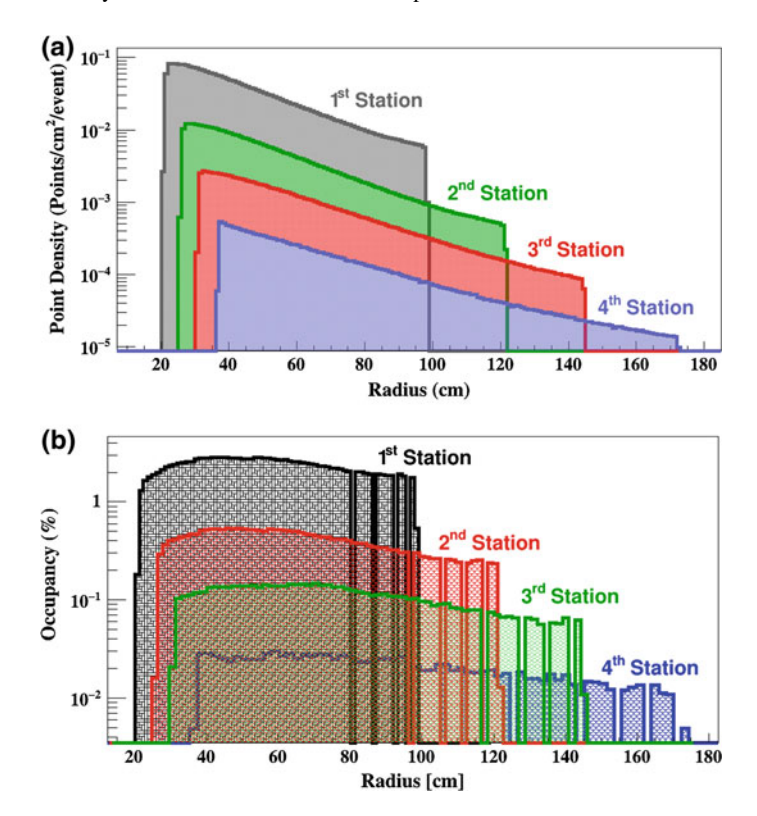


Fig. 4 a Radial distribution of particle density at different MUCH stations. b Radial distribution of occupancy at different MUCH stations. These results are obtained for central Au+Au collisions at 8 AGeV

i.e., number of particles impinging on the detector stations per unit area per event. It reaches up to a maximum value of \sim 0.08 particles/cm²/event at innermost radius of the first station for central Au+Au collisions at 8 AGeV. For 10 MHz interaction rate, detectors have to handle flux rate up to 0.8 MHz/cm². This is well within the limit of GEM detectors that could operate up to 1.4 MHz/cm².

Also shown in Fig. 4b radial occupancy distribution. Occupancy is defined as the ratio of fired pads to the total number of pads per event. Granularity of the detectors is optimized to keep the occupancy within the limit. Simulation shows detector occupancy reaches a maximum of $\sim 2-3\%$ at a forward angle of 5.7° and at a distance 20 cm from the beam pipe.

Shown in Fig. 5 momentum distribution of different particles at Monte Carlo level. Majority of the particles are pions and kaons.

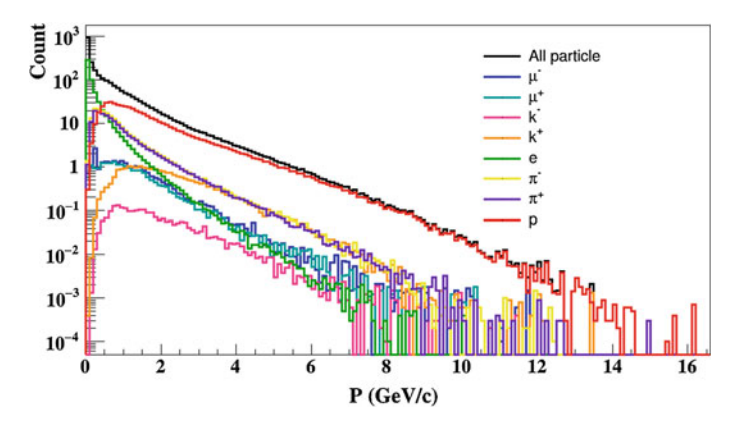


Fig. 5 Momentum distribution of different particles at input Monte Carlo level

3.3 Di-muon Detection Technique at CBM

3.3.1 Analysis Procedure

Identification of muon candidates involve track reconstruction in STS and extrapolation to MUCH. Track reconstruction in STS is done using cellular automaton method, then these tracks are propagated to MUCH detector layers through the absorbers as a straight line, as MUCH is placed outside the dipole magnet. Track propagation in MUCH is done using Kalman filter technique taking the MUCH hits in the vicinity of propagated track. Finally, few selection cuts are imposed to select true muons from a huge background. This will be discussed in next section. Here we have used embedded PLUTO + UrQMD events and transport them through CBM setup. Six di-muonic decay channels at 8 AGeV : $\rho^0 \rightarrow \mu^+\mu^-$, $\eta \rightarrow \mu^+\mu^-$, $\phi \rightarrow \mu^+\mu^-$, $\omega \rightarrow \mu^+\mu^-$,

3.3.2 Selection Cuts

From global reconstructed tracks, a set of selection cuts are applied at the analysis level to identify muons. For selection of a muon candidate, a global track should register at least 7 STS hits, 11 MUCH hits and the track should have $\chi^2_{Vertex} < 2.0$, $\chi^2_{STS} \le 2.0$, and $\chi^2_{MUCH} \le 1.3$. For rejection of high momentum punched through hadrons, a TOF mass cut is used. These cuts are optimized to reduce background

contributions from non-muonic tracks and muons from weak decays of pions and kaons and to obtain maximum efficiency and reasonable signal to background ratio. A summary of the cuts used in this analysis are as follows: Hits: STS hits ≥ 7 , MUCH hits ≥ 11 , on tracks: $\chi^2_{Vertex} \leq 2.0$, $\chi^2_{STS} \leq 2.0$, $\chi^2_{MUCH} \leq 1.3$, and TOF mass cut m² $< 0.05 \text{ GeV}^2/c^2$.

3.3.3 Results

Figure 6a shows the di-muon invariant mass spectra for signal cocktails (ρ^0 , η , ϕ , ω_D , ω , η_D) at the generator level as obtained from input PLUTO.

Also shown in Fig. 6b the reconstructed invariant mass distribution of hadronic cocktails (signal + combinatorial background). A plot of signal to background ratio as a function of invariant mass of di-muon pairs is shown in Fig. 7. This indicates, with the given experimental setup, some of the LMVM candidates can be identified well above the combinatorial background.

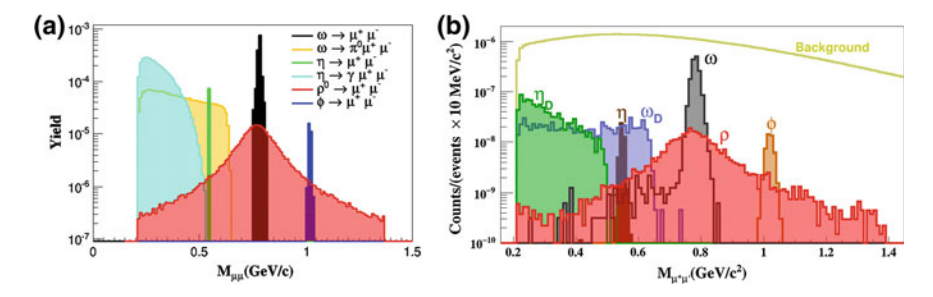
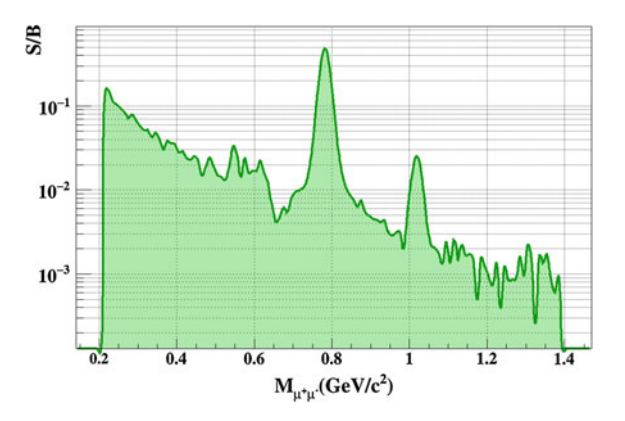


Fig. 6 a Invariant mass distribution of hadronic cocktails at the input PLUTO. b Invariant mass distribution of hadronic cocktails and combinatorial background at reconstruction level

Fig. 7 Signal to background ratio as a function of invariant mass distribution



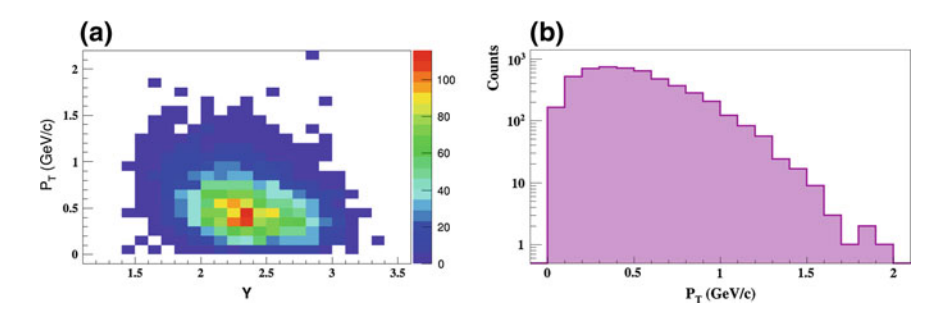


Fig. 8 a Y-p_T coverage of ρ . b p_T distribution of ω

Table 1 Table for efficiency and S/B for different LMVMs for latest geometry

| | $ ho^0$ | ω | φ | η | η_D | ω_D |
|----------------|---------|------|-------|-------|----------|------------|
| Efficiency (%) | 0.88 | 0.94 | 1.35 | 0.49 | 0.20 | 0.33 |
| S/B | 0.006 | 0.21 | 0.007 | 0.005 | 0.005 | 0.004 |

A plot for phase space coverage, rapidity versus transverse momentum (Y-P_T) of reconstructed ρ and transverse momentum spectra of the reconstructed ω is presented in Fig. 8a, b, respectively. It shows that rapidity is covered in the forward region.

Finally we have calculated the pair reconstruction efficiency and signal to background ratio of all cocktails and tabulated in Table 1.

4 Summary and Discussions

Relativistic heavy ion collisions are tools to explore the phase diagram of strongly interacting matter in the laboratory. At present QCD phase diagram is much less explored in the regime of high net baryon density. The CBM experiment at FAIR accelerator facility is aiming at the study of QCD phase diagram in this regime with bulk and rare probes. To enable the measurement of rare particles, CBM will operate at very high interaction rate (\sim 10 MHz). Di-muon measurements form an integral part of the physics program of CBM. They are believed to be penetrating probes carrying undistorted information of the dense collision zone. Till now there are no di-muon data in 4-40 AGeV, so CBM will make pioneering measurements in this energy region. A muon detector setup using novel concept of segmented hadron absorber has been designed. Detectors are now in developing stage. Research and development is ongoing, and design, shape, and sizes of the detectors are changing frequently as per physics and mechanical requirements. Its geometry has not frozen till date and we implement the latest designs in the simulation accordingly and check its effect. So realistic simulations via di-muon channel using optimized muon detector setup will establish the feasibility of such measurements.

References

- 1. H. van Hees, R. Rapp. arXiv:hep-ph/0604269v1
- 2. CBM MUCH Technical Design Report. http://repository.gsi.de/record/161297
- 3. http://www.gsi.de/fair/experiments/CBM
- 4. R. Brun et al., CERN-DD-EE-84-1
- 5. I. Froehlich et al., J. Phys. Conf. Ser. **219**, 032039 (2010)
- 6. S.A. Bass et al., Prog. Part. Nucl. Phys. 41, 255 (1998)
- 7. O. Linnyk et al., Nucl. Phys. A **786**, 183200 (2007)

Effect of Electric Field and Gas Mixture on RPC Time Resolution

Abhik Jash, Sridhar Tripathy, Navana Majumdar, Supratik Mukhopadhyay, Satyajit Saha and Subhasis Chattopadhyay

Abstract A large number of Resistive Plate Chamber will be used in the ICAL detector set-up in the proposed INO facility. The timing response from RPCs will govern the accuracy of ICAL in distinguishing the up-going muon tracks from the down-going ones by recording the time of passage of the muons through the RPCs. The timing performance of a bakelite RPC has been studied both experimentally and numerically to understand the effect of different operating conditions, like applied voltage and used gas mixture, on the timing properties. This can lead us to judge the suitability of bakelite RPC for application in ICAL set-up which is planned to be equipped with glass RPCs at present.

Introduction

The proposed iron calorimeter (ICAL) detector [6] at India-based Neutrino Observatory (INO) is designed to study several outstanding issues of neutrino oscillation physics including the fundamental issue of neutrino mass hierarchy. The ICAL setup consists of iron plates of thickness 5.6 cm, placed in 151 horizontal layers, with the Resistive Plate Chamber (RPC) [14] as the the active detector elements, interspersed between them. Measurement of energy, charge and direction of the muons, created in the interaction of atmospheric neutrinos with the iron mass, will facilitate to explore the earth matter effect which will be crucial to envisage the oscillation phenomenon. The precise tracking and timing measurements of the muons will be

A. Jash (⋈) · S. Tripathy · N. Majumdar · S. Mukhopadhyay · S. Saha Applied Nuclear Physics Division, Saha Institute of Nuclear Physics, Block AF, Sector 1, Bidhannagar, Kolkata 700064, India e-mail: abhik.jash@saha.ac.in

A. Jash

HBNI, Training School Complex, Anushakti Nagar, Mumbai 400094, India

S. Chattopadhyay

Experimental High Energy Physics Division, Variable Energy Cyclotron Centre, Block AF, Sector 1, Bidhannagar, Kolkata 700064, India

[©] Springer Nature Singapore Pte Ltd. 2018

168 A. Jash et al.

found out from the hit and timing information from each detector layer. To achieve the requisite precision of the observables, ICAL set-up requires muon detection with position resolution less than 1 cm and timing resolution better than 1 ns. The simple but robust design and inexpensive fabrication in addition to excellent position and timing resolutions pave the way of RPC to serve as the detection element in ICAL in a large number (of the order of 29,000). Although glass RPCs of dimension $2 \text{ m} \times 2 \text{ m}$ have been proposed to populate the ICAL set-up, a parallel R&D on bakelite RPCs also has been in progress to compare the choices in the context of fabrication, handling, performance, availability of materials, cost etc.

The timing information from RPC will be used to distinguish the up-going muon tracks from the down-going ones which will be necessary for determining the path length of the neutrinos, an important observable for studying neutrino oscillation. Hence, a thorough understanding of its working principle and the basis of its timing performance is necessary for optimizing its design and operation in the perspective of INO-ICAL experiment as well as predicting and analysing the experimental data. Apart from the experimental investigations, numerical simulation may be found as an useful tool in this regard which can emulate the RPC dynamics for the given physical parameters. The results can be compared to the measured performance of RPC to explore the dependence of the device performance on various physical parameters. The parameters of importance in governing the timing performance of RPC are the average signal arrival time and the time resolution, which in turn rely upon the electric field configuration of the device and the electron transport properties of the gas mixture used. In the present work, the timing performance of a bakelite RPC has been studied both experimentally and numerically with an emphasis on the dependence of the timing parameters specifically on the applied field and the gas mixture.

2 RPC: Design and Working Principle

RPC is a gas-filled chamber that works on the basis of gaseous ionization phenomenon caused by the passage of a charged particle/radiation through its gaseous volume. It utilizes a constant high electric field produced across its gas volume by applying a potential difference between two parallel plates made of very common, highly resistive ($\sim 10^{11}~\Omega$ cm) materials like glass or bakelite. The voltages are supplied to the resistive glass/bakelite plates via a conductive graphite coat applied on the outer surface of the plates. The signal generated due to the passage of charged particle/radiation is obtained from two pickup panels consisting of parallel strips, placed after the plates with an insulating layer in between. The pickup planes are arranged in an orthogonal manner to provide two-dimensional position information.

When a high energy charged particle passes through the RPC gas chamber, it ionizes the gas molecules. The electrons and ions created through primary ionization move towards anode and cathode, respectively, under the influence of the electric field. They may gain enough kinetic energy from the field to create further ionization

of the gas molecules through collisions. This process of charge multiplication may go on until the energy of the ions goes below the ionization potential of the gas. The movement of all the charges within gas volume induces a current on the pickup strip, capacitively coupled to the detector. The current induced by total charge q moving with an instantaneous velocity $\overrightarrow{v}(t)$ induces a current i(t), given by Shockley–Ramo theorem [10, 15], as shown in (1).

$$i(t) = q \overrightarrow{v}(t).\overrightarrow{W}(\overrightarrow{x}(t)) \tag{1}$$

 $\overrightarrow{W}(\overrightarrow{x},t)$ is the weighting field which is the electric field when the pickup strip is kept at unit potential while all other available conductors are grounded. The signal thus collected from the pickup strips is the characteristic response of RPC that depends on its geometry, electric field and the filling gas mixture for a given incident particle/radiation. The experimental work and the numerical simulation to study the RPC response and its timing response will be described in the next two sections.

3 Experimental Work

A few bakelite RPCs of dimension 30 cm × 30 cm with 2 mm gas gap have been fabricated using 3.2 mm thick bakelite plates of P-120 grade. A thin layer of silicone oil has been applied on the inner surfaces of the electrodes to ensure a smoothness of these surfaces in order to avoid undesirable effects like corona discharge or local perturbation of the electric field. A typical gas mixture of R-134A, isobutane and SF₆ has been used to operate the RPCs in avalanche mode. A few basic RPC characterization tests have been performed before the actual experiment. A pickup panel made of 11 copper strips of width 2.5 cm, laid side by side, with a pitch of 2.7 cm has been placed orthogonally on the top and bottom side of the RPC gas chamber to collect the RPC signal. The collected signal has been amplified ten times using a fast amplifier CAEN N979. A muon telescope set-up has been formed by using two paddle scintillators of dimension 93.5 cm \times 19.5 cm and 82.5 cm \times 19.5 cm, respectively, along with a finger scintillator of size $17 \, \text{cm} \times 4 \, \text{cm}$, coinciding with one pickup strip. The presence of threefold (3F) coincidence signal from all the three scintillators has been considered as to ensure the passage of a muon, and the presence of RPC strip signal within the 3F coincidence window has ensured the detection of the muon by RPC. The timing measurements have been done by using the 3F signal to START a TDC (model: PS 7186) module and the RPC signal to STOP it. Charge measurements have also been done in parallel using a QDC (model: PS 7166) to monitor the mode of operation (avalanche/streamer) of RPC. The schematic diagram of the electronic connections which has been used for these measurements is shown in Fig. 1.

A CAMAC-based data acquisition system, LAMPS [7], has been used to store the timing and charge data. The distribution of time difference between START and STOP of TDC has been fit with a Gaussian function, the mean of which has been

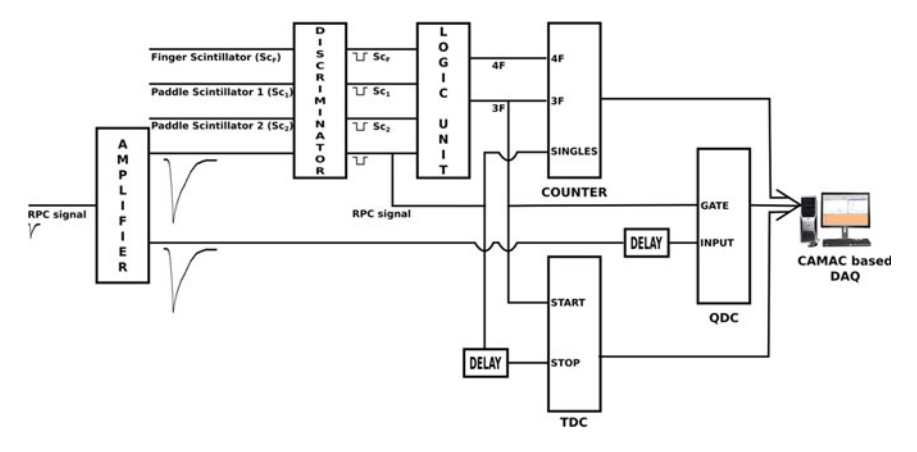


Fig. 1 Schematic diagram of the electronics set-up for time and charge measurement of RPC

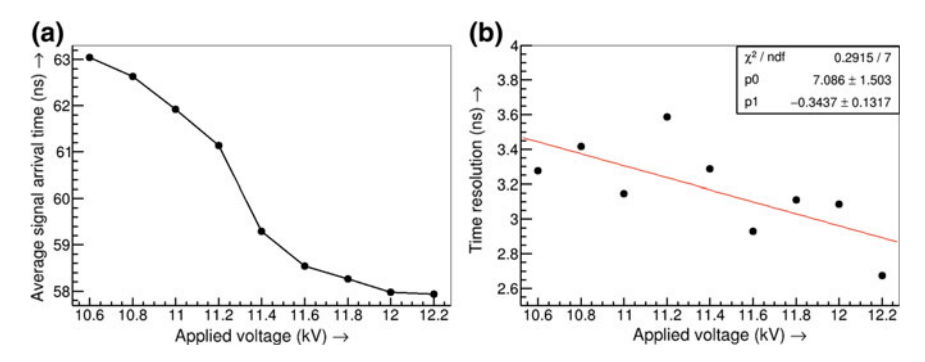


Fig. 2 Variation of **a** average signal arrival time and **b** time resolution of RPC and its linear fit with the applied voltage when operated with 95% R-134A + 4.9% isobutane + 0.1% SF₆

defined as the average signal arrival time and the standard deviation as the time resolution of the detector. The measurements have been repeated at different applied voltages, and the variation of both the timing parameters with the applied voltage is shown in Fig. 2.

It can be seen from Fig. 2a that the detector becomes faster at higher voltages which has been found earlier for a different gas mixture [3]. The data of time resolution have been fit with a linear function which is shown by a red line in Fig. 2b. An overall improvement of about 15% in the value of time resolution has been found with the increase in the applied voltage.

4 Numerical Calculation

A detailed numerical simulation has been carried out for computing the entire working procedure of RPC beginning from the primary ionization caused by the passage of muons through it, till the generation of signal on its readouts. The entire simulation of the RPC performance has been carried out by a simulation framework, Garfield [17]. It uses several solvers as its toolkits to perform several aspects of the dynamic process.

The detailed electrostatic field map of RPC may be calculated using two numerical methods, namely, finite element method (FEM) and boundary element method (BEM). The results from these two methods have already been produced and compared, and a good agreement between them has been found [4]. For the present case, only the BEM-based solver, neBEM [9] has been used to do the calculation, which serves as one of the toolkits to the Garfield framework. Primary ionization due to the passage of muons through the RPC gas chamber has been calculated using another toolkit, HEED [16]. For the present calculations, muons of energy randomly varying between 0.5 and 10 GeV have been passed through the detector in randomly varying directions restricting the range of incidence angle (θ) within 0°-10°. The transport parameters like Townsend coefficient (α), attachment coefficient (η), drift velocity (V_z) and diffusion coefficients (D_l, D_t) of electrons in the used gas mixtures of R-134A and isobutane with a small amount of SF₆ have been estimated at different values of electrostatic field using the third toolkit, Magboltz [2]. Finally, the movement of all the electrons and ions created in the gas mixture through the avalanche process has been tracked by the Garfield and the current induced on the pickup strip due to the movement of all those charges has been simulated at different instances of time using the data produced by the toolkits. The computed signal shapes have been analysed using Root data analysis framework [12] to find the timing properties of the detector.

A method of calculating the timing properties of the detector has been proposed earlier [5] where the time corresponding to crossing a certain percentage of signal amplitude has been defined as the signal arrival time. In the present work, instead the time corresponding to crossing a fixed value of current threshold has been used to define the arrival of signal. Following this procedure, a distribution of arrival times has been obtained for 2000 muon events. It has been fit with a Gaussian function whose mean and the standard deviation have been defined as the average signal arrival time and the intrinsic time resolution of the detector, respectively. An appropriate approach for this study would be to find out the signal in the presence of a dynamic electric field as the space charges created in the avalanche process tend to modify it [8]. Also, the time dependence of the electric field owing to the finite bulk resistivity of the RPC plate should be taken into account in order to carry out an extensive signal simulation. However, the present work involves calculations assuming a static electric field configuration where RPC is described as a multi-dielectric planar capacitor. It should be noted that no effect of electronic components has been taken into account.

A typical signal calculated using Garfield is shown in Fig. 3a along with the time corresponding to crossing of $-10\,\mathrm{nA}$ threshold. One of the experimentally obtained signal shapes in an oscilloscope is shown in Fig. 3b for comparison. Although the rising edges of the signal shapes are comparable, the long tail as found in the experiment is not present in the calculated signal. It should be noted here that the effect of bulk properties of the electrodes has not been considered in the present calculations which is expected to make the falling edge of the signal slower. Also the ions, having a larger mass and contributing to the slower falling edge, have been treated as moving with a constant velocity and not contributing to the growth of avalanche.

The average signal arrival time and intrinsic time resolution of the RPC, operated with 95% R-134A, 4.8% isobutane and 0.2% SF₆ have been calculated at different values of electrostatic field, and the variation of the two is shown in Fig.4. The detector becomes faster at higher field values, also its time resolution improves, which are at par with the available experimental results. The value of the average signal arrival time depends on the given threshold; however, the value of intrinsic time resolution seems to be independent of the set threshold.

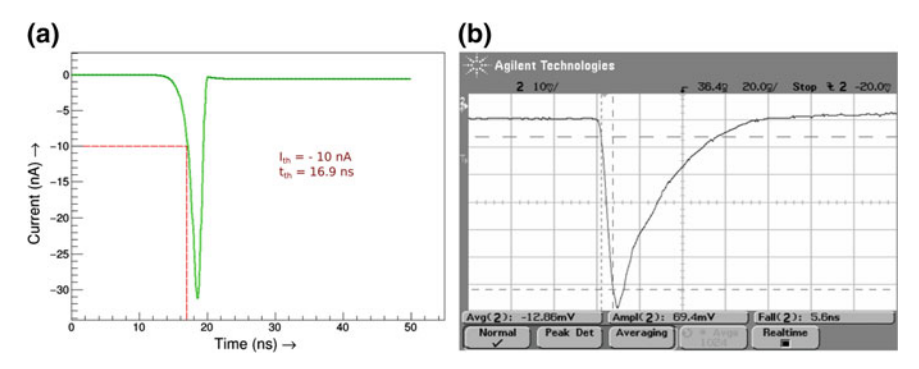


Fig. 3 a A typical signal shape calculated using Gafield; the time corresponding to the crossing of $-10\,\text{nA}$ threshold is also shown, **b** typical RPC signal seen on an oscilloscope

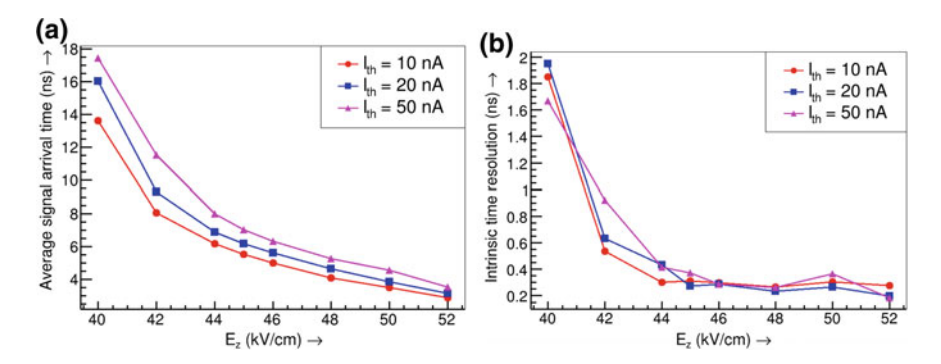


Fig. 4 Variation of $\bf a$ average signal arrival time and $\bf b$ time resolution of RPC with applied field, when operated with 95% R-134A + 4.8% isobutane + 0.2% SF₆

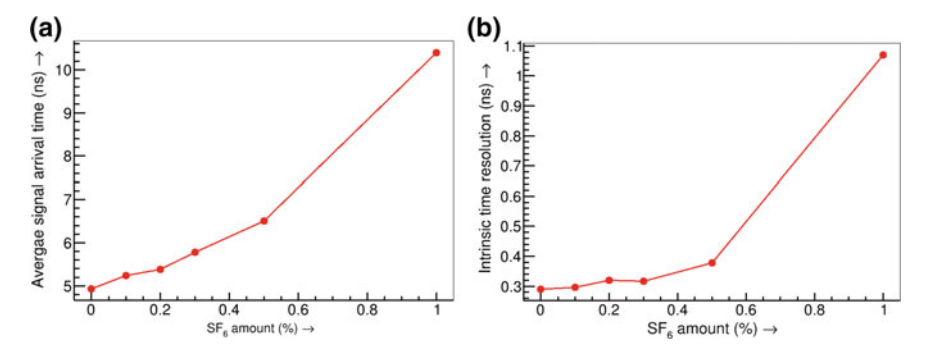


Fig. 5 Variation of **a** average signal arrival time and **b** time resolution of RPC with SF₆ amount (+5% isobutane + R-134A), present in the gas mixture for $E_z = 45 \text{ kV/cm}$ (threshold = 10 nA)

Next, the variation of the two timing parameters with the amount of SF_6 has been studied by repeating the calculations at the field value $45 \,\mathrm{kV/cm}$ with the gas mixture of 5% isobutane and different values of R-134A and SF_6 . The results are shown in Fig. 5. It can be seen that the timing performance of the detector deteriorates with the increase in SF_6 amount which has been observed earlier in experiments [1, 13]. The nature of the variation of time resolution with both of the electrostatic field and the percentage of SF_6 can be explained using analytic formulation [11] and has been described in detail in [5].

5 Conclusion

Both the experiment and the numerical calculations have shown that RPC becomes faster with the increase in applied voltage (or the field) and the time resolution improves. However, raising the field to a very high value will result in onset of streamer which may affect the RPC response adversely. Although a small amount of SF_6 is used to limit the streamer generation, the increase of SF_6 proportion in the gas mixture deteriorates the timing performance of the detector. So, to achieve the best timing performance in the avalanche mode operation with limited streamer contribution, RPC is required to be operated at an optimum voltage along with an optimum amount of SF_6 .

Acknowledgements The authors acknowledge the technical assistance received from Ganesh Das (VECC), Pradipta kr. Das (SINP), Chandranath Marick (SINP) during the experiment and the SINP workshop for many mechanical fabrications. We thank Dr. Saikat Biswas (Bose Institute), Prof. Sudeb Bhattacharya (SINP) and Rajesh Ganai (VECC) for their suggestions and helpful discussions at different stages of the work. The financial support extended to the author, A. J., from INO collaboration, is gratefully acknowledged.

References

- M. Bhuyan, V.M. Datar, S.D. Kalmani, S.M. Lahamge, S. Mohammed, N.K. Mondal, P. Nagaraj, A. Redij, D. Samuel, M.N. Saraf, B. Satyanarayana, R.R. Shinde, P. Verma, Development of 2 m × 2 m size glass RPCs for INO. Nucl. Instr. Meth. A 661, S64–S67 (2012)
- S.F. Biagi, Accurate solution of the Boltzmann transport equation. Nucl. Instr. Meth. A 273, 533–535 (1988)
- S. Biswas, S. Bhattacharya, S. Bose, S. Chattopadhyay, S. Saha, Y.P. Viyogi, Study of timing properties of single gap high-resistive bakelite RPC. Nucl. Instr. Meth. A 617, 138–140 (2010)
- A. Jash, N. Majumdar, S. Mukhopadhyay, S. Chattopadhyay, Numerical studies on electrostatic field configuration of Resistive Plate Chambers for the INO-ICAL experiment. J. Instrum. 10, P11009 (2015)
- A. Jash, N. Majumdar, S. Mukhopadhyay, S. Saha, S. Chattopadhyay, Numerical study on the effect of design parameters and spacers on RPC signal and timing properties. J. Instrum. 11, C09014 (2016)
- A. Kumar, A.M. Vinod Kumar, A. Jash et al., Physics Potential of the ICAL detector at the India-based Neutrino Observatory (INO). Pramana J. Phys. 88, 79 (2017)
- 7. LAMPS—Linux Advanced MultiParameter System. http://www.tifr.res.in/pell/lamps.html
- 8. C. Lippmann, W. Riegler, Space charge effects in resistive plate chambers. Nucl. Instrum. Meth. A 517, 54–76 (2004)
- 9. N. Majumdar, S. Mukhopadhyay, Simulation of 3D electrostatic configuration in gaseous detectors. J. Instrum. 2, P09006 (2007)
- 10. S. Ramo, Currents induced by electron motion. Proc. IRE 27(9), 584 (1939)
- W. Riegler, C. Lippmann, Detailed models for timing and efficiency in resistive plate chambers. Nucl. Instr. Meth. A 508, 14–18 (2003)
- 12. ROOT—Data Analysis Framework. https://root.cern.ch
- M. Salim, A. Jash, R. Hasan, B. Satyanarayana, N. Majumdar, S. Mukhopadhyay, Simulation of efficiency and time resolution of resistive plate chambers and comparison with experimental data. J. Instrum. 10, C04033 (2015)
- R. Santonico, R. Cardarelli, Development of resistive plate counters. Nucl. Instrum. Meth. A 187, 377 (1981)
- W. Shockley, Currents to conductors induced by a moving point charge. J. Appl. Phys. 9(10), 635 (1938)
- I.B. Smirnov, Modeling of ionization produced by fast charged particles in gases. Nucl. Instr. Meth. A 554, 474–493 (2005)
- 17. R. Veenhoff, GARFIELD, recent developments. Nucl. Instr. Meth. A 419, 726-730 (1998)

GEANT4 Simulation for Imaging of High-Z Materials Using Cosmic Ray Muons

Sridhar Tripathy, Abhik Jash, Nayana Majumdar, Supratik Mukhopadhyay, Sandip Sarkar and Satyajit Saha

Abstract High-energy muons generated from cosmic ray particle showers have been found to exhibit properties suitable for imaging the interior of large structures due to their high penetrating power. Based on absorption or scattering of the muons in the target object, a technique for producing three-dimensional image of the object, known as Muon Tomography, has been widely in practice for several decades for various applications in the fields of geology, industry, homeland security etc. In the present work, we attempt to produce numerically the shadows of different materials on detector planes placing it under muon shower using GEANT4 simulation framework. Cosmic ray muons of varying energy (10 MeV to 10 GeV) and of typical flux (1 muon/m²/s) have been emulated using Monte-Carlo technique from a plane placed above the material under inspection. A cubical box of different materials like Al, Fe, Pb, Ag has been placed symmetrically under the particle generation plane between two layers of detection plane. The hit positions on the detectors have been plotted to study the image pattern produced for different materials individually.

S. Tripathy (\boxtimes) · A. Jash · N. Majumdar · S. Mukhopadhyay · S. Sarkar · S. Saha Saha Institute of Nuclear Physics, 1/AF Bidhannagar, Kolkata 700064, India e-mail: sridhar.tripathy@saha.ac.in

A. Jash

e-mail: abhik.jash@saha.ac.in

N. Majumdar

e-mail: nayana.majumdar@saha.ac.in

S. Mukhopadhyay

e-mail: supratik.mukhopadhyay@saha.ac.in

e-mail: sandip.sarkar@saha.ac.in

S. Saha

e-mail: satyajit.saha@saha.ac.in

S. Tripathy · A. Jash

Homi Bhabha National Institute, Training School Complex, Anushaktinagar, Mumbai 400094, India

© Springer Nature Singapore Pte Ltd. 2018

S. Biswas et al. (eds.), Advanced Detectors for Nuclear, High Energy and Astroparticle Physics, Springer Proceedings in Physics 201, https://doi.org/10.1007/978-981-10-7665-7_17

1 Introduction

Muons are high-energy cosmic ray particles showering from the upper level of the atmosphere where they are generated as secondary product of the interaction between high-energy cosmic rays and atomic nuclei of particles in upper atmosphere.

$$\pi^+ \to \mu^+ + \nu_{\mu}$$

$$\pi^- \to \mu^- + \overline{\nu}_{\mu}$$
(1)

Cosmic ray muons are the most numerous charged particles at sea level. They are highly penetrating particles and are able to reach the ground and even below traveling a long distance through the atmosphere because they interact weakly with matter. The charged pions produced in this interaction actually decay into muons as shown above. The cascade of muons detected at sea level is directionally dependent on the zenith angle (θ) as $\cos^2\theta$.

The energy range of muons varies over a large range from 10 MeV to 10 GeV having peak around 1 GeV [1]. Muons as charged particles undergo electromagnetic interaction. They loose energy by ionizing atomic electrons and also doing Coulomb scattering off the atomic nuclei. In a material medium, an incoming muon faces millions of atomic nuclei and deflects multiple times from its path. This phenomenon is known as multiple Coulomb scattering. The distribution of scattering angles can be approximated to a Gaussian distribution [2] with mean at zero and standard deviation given by

$$\sigma = \frac{13.6}{\beta cp} \sqrt{\frac{L}{X_0}} (1 + 0.038 ln(\frac{L}{X_0}))$$

$$X_0 = \frac{716.4 \text{ g/cm}^2}{\rho} \frac{A}{Z(Z+1) ln(\frac{287}{\sqrt{\rho}})}$$
(2)

L is the length of the medium traversed, β is the ratio of speed of the muon to speed of light, p is the momentum of the muon, X_0 is the radiation length, Z is its atomic number, and ρ is the density. This deviation of the muon trajectory before and after its interaction with a medium owing to the multiple scattering inside can be observed by placing layers of detectors above and below. The scattering map based on the amount of scattering and its location can provide a basis of image pixel. Thus, layers of 2D scattering maps can be obtained which may be analyzed for producing 3D tomographic image of the object. It is also possible to distinguish different object materials studying the scattering maps as the scattering distribution is dependent on the material properties of the object $(Z, A, \rho, \text{etc.})$.

Imaging using cosmic ray muons is a noble idea to inspect suspicious shielded packages which may contain contraband materials. In conventional radiographic techniques, which are performed using X-rays and gamma rays, multiple sources of radiation are needed and they are potentially hazardous. On the contrary, muons are naturally available and do not cause any harmful radiation effect and hence a better choice for scanning purpose [3]. Successful application of muon detection for imaging purpose has been reported using position sensitive gas detectors, like Gas Electron Multipliers (GEM), drift chambers, Resistive Plate Chambers (RPCs) [4–6].

The RPCs are cost-effective, robust detectors which are much easier to build with commonly available materials. Moreover, they can have excellent position resolution (of the order of few hundreds of microns depending upon the choice of design parameters) and time resolution (few nanoseconds) [7] along with a high efficiency (more than 90% [7] in avalanche mode). A muon telescope has been planned to be set up using several RPC detectors and scintillators. As a precursor of the R&D work in this direction, a simulation work has been carried out to explore the muon imaging numerically which can lead to an optimized detector design. The computation has been done using high-energy simulation frame work GEANT4 [8]. The dimensions of the RPCs along with their physical location and the target object have been adapted in the current simulation model.

2 Simulation Framework

In the numerical simulation, two detectors on each side of the object have been considered. The detectors have been assumed to be fully efficient and their position resolution has not been considered in the calculation.

The muon energy has been varied from 10 MeV to 10 GeV. Both μ^- and μ^+ particles have been considered. The flux of cosmic ray muons at the present latitude following the EXPACS [1] has been taken. The plot of cosmic ray muon variation has been shown in Fig. 1.

The total simulation area has been filled with normal air. The world volume is $100\,\mathrm{cm} \times 100\,\mathrm{cm} \times 100\,\mathrm{cm}$, whereas each sensitive detector volume is $30\,\mathrm{cm} \times 30\,\mathrm{cm} \times 0.2\,\mathrm{cm}$. Cubes of different materials of side 5 cm have been considered as target objects. 60,000 muons have been made vertically incident from a plane considered above the setup, which is equivalent to an exposure of about more than an hour with the typical flux of the cosmic muons at the sea level.

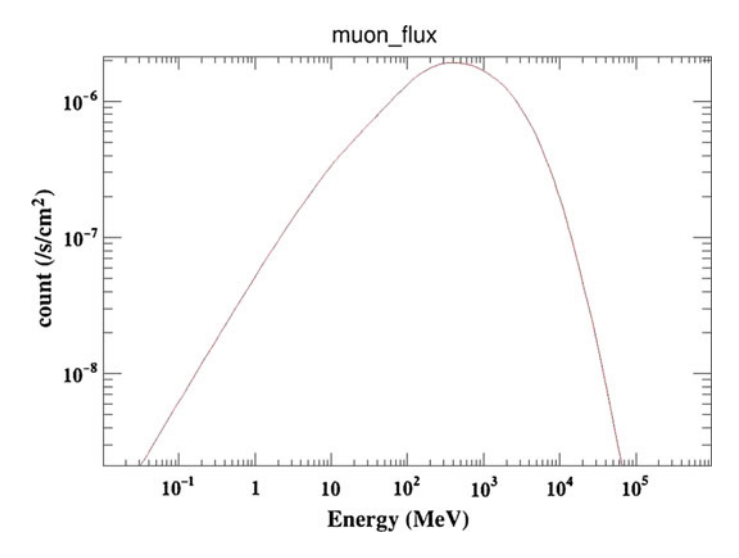


Fig. 1 Energy spectrum of the muons simulated

3 Results

The muon hits on different RPC planes as obtained for different objects have been used to generate the preliminary images.

For a Lead block of side 5 cm, the plot of the second detector plane which has been placed above the block has been shown in Fig. 2 and that of the third detector plane which is just below the block has been shown in Fig. 3. Comparing the plots in Figs. 2 and 3, one can see that there is no image seen on the pair of detectors which are kept above for obvious reasons, whereas there is clearly an image of block of same dimensions visible in the lower pair of detectors (Figs. 3 and 4).

To confirm and find the boundary of the material, a different structure has been tried to be imaged. A cylindrical cut of diameter 3 cm has been made through the block of Lead as shown in Fig. 5; and the simulation has been done for same number of events. The hit points in the detector-3 have been plotted and shown in Figs. 6 and 7.

In order to distinguish high-Z materials from low-Z materials, blocks of Lead (Z = 82), Silver (Z = 47), Aluminum (Z = 13) have been kept in the same plane between the detector planes. The hit points on the detector-3 below the material cubes have been shown in Figs. 8 and 9. It can be observed that the shadow of the Lead cube is clearly visible and that of Silver is not clear although distinguishable, whereas that of Aluminum is not at all visible.

Fig. 2 Hit points on detector-2

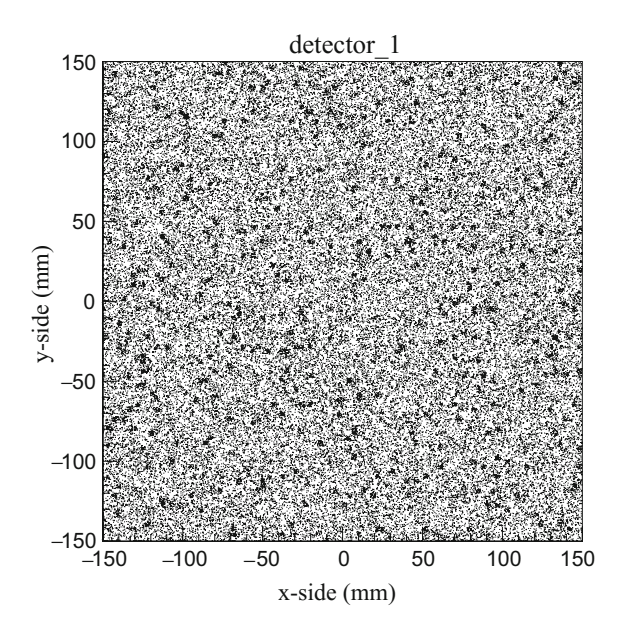


Fig. 3 Hit points on detector-3

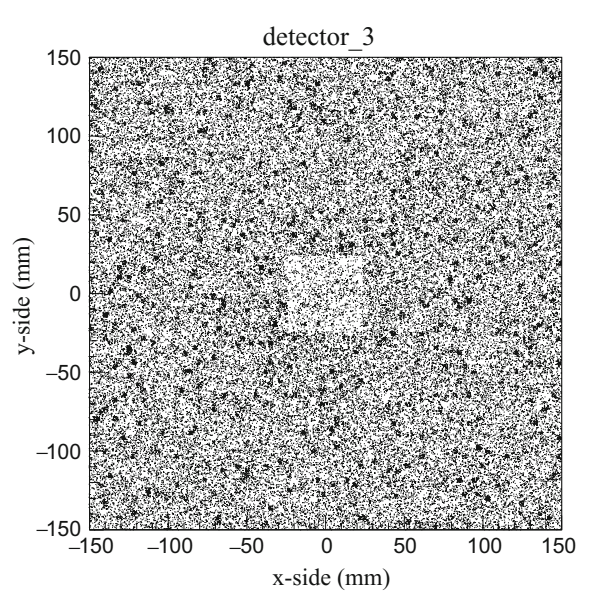


Fig. 4 Color image of hit points on detector-3

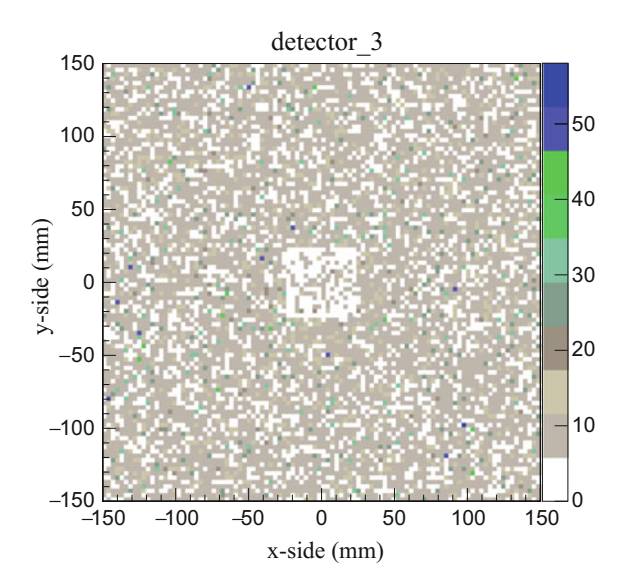


Fig. 5 Cylindrical cut of 3 cm diameter

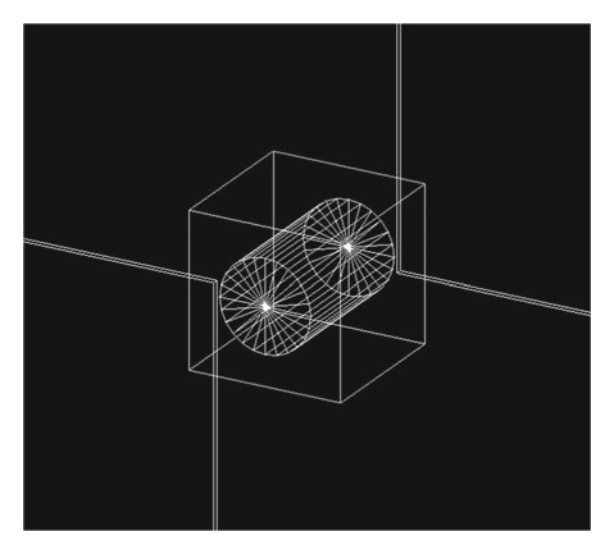


Fig. 6 Cube with cylindrical cut

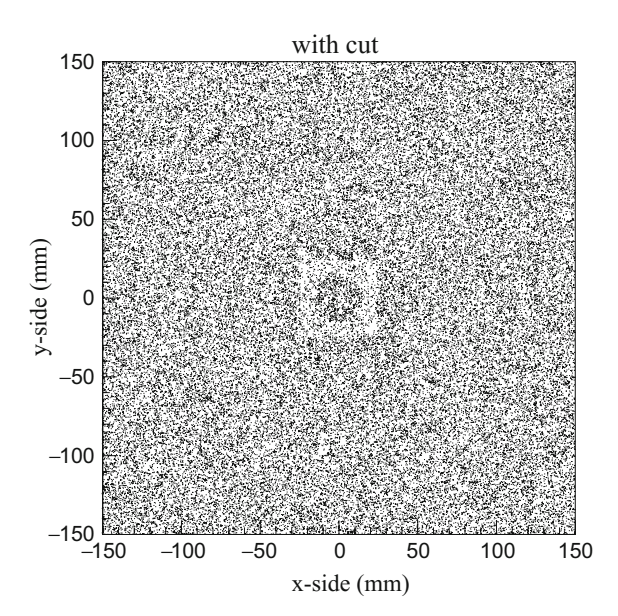


Fig. 7 Cube with cylindrical cut (in colour)

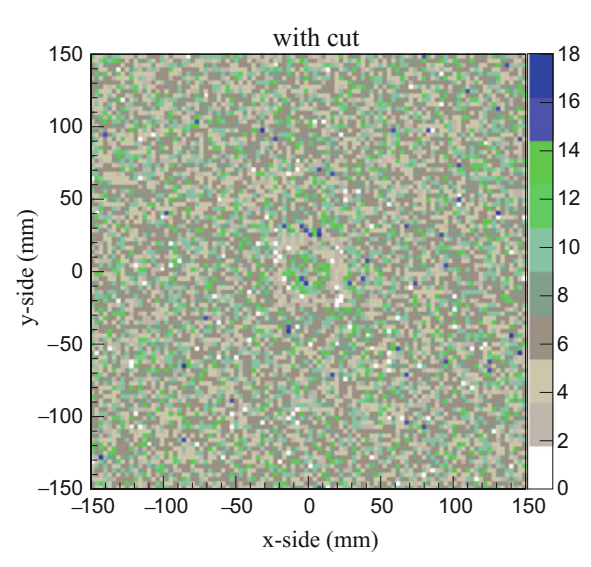


Fig. 8 Left bottom: Aluminum (not visible), center: Lead, right top: Silver

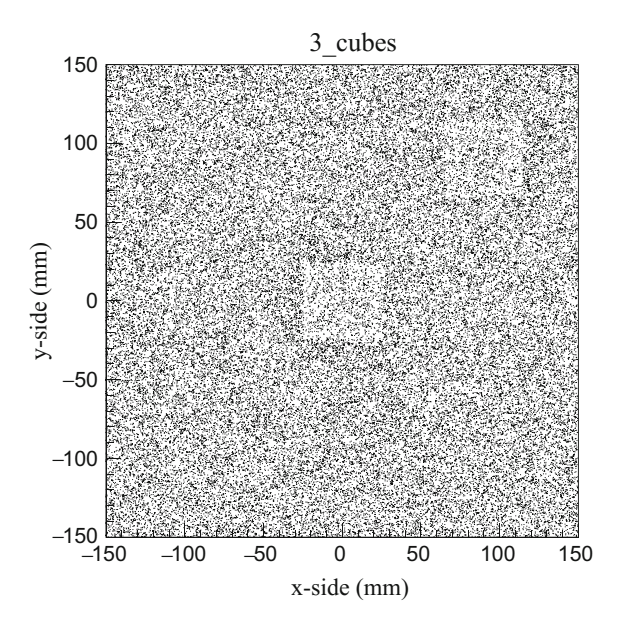
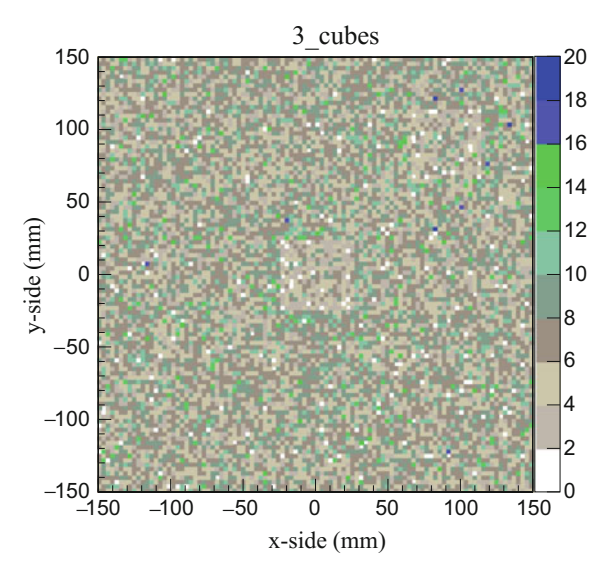


Fig. 9 Color plot of 3 cubes



4 Conclusion

The density and atomic number of the material decides the number of interactions the muons have in their path. May it be Coulomb scattering or ionization, for materials with higher atomic number and density like Lead, the number of interactions is high and in case of lighter materials like Aluminum it is low.

From this preliminary work, it can be seen that placing the detectors $30\,\mathrm{cm}$ away from each other and keeping the object of interest at $30\,\mathrm{cm}$ from top as well as bottom detector imaging lead is quite possible. The granularity of the images has been reduced and hence around $3\,\mathrm{mm}$ of position resolution is virtually achieved. Bakelite plate RPC detectors are reported to have spatial resolution of millimeter order; this can be achieved by reducing the width of the pick-up strip. However, the pick-up strip of the detector can be made narrow up to a limit. Another way to increase detection capability is to introduce asymmetry in the arrangement of detectors. If the separation between the material and the lower detectors increases, the δx required to distinguish the materials will be more.

Acknowledgements The authors thankfully acknowledge the technical help from Mr. Shaibal Saha, Mr. Chandranath Marick, Mr. Sudipta Barman, Mr. Pradipta Das of SINP and academic advices from Prof. Sudeb Bhattacharya. The author Sridhar Tripathy likes to thank the other members of the ANP division for their help. He also likes to thank INSPIRE Division, Department of Science and Technologies, Govt. of India for financial assistance.

References

- T. Sato et al., Development of PARMA: PHITS based analytical radiation model in the atmosphere. Radiat. Res. 170, 244–259 (2008)
- 2. H.A. Bethe et al., Phys. Rev. 89, 1256 (1953)
- 3. L. Cox et al., Detector requirements for a cosmic ray muon scattering tomography system, in *IEEE Nucelar Science Symposium Record* (2008)
- K. Borozdin et al., Cosmic-ray muon tomography and its application to the detection of high-Z materials. Nature 422, 277 (2003)
- K. Gnanvo et al., Imaging of high-Z material for nuclear contraband detection with a minimal prototype of a muon tomography station based on GEM detectors. Nucl. Instr. Meth. Phys. Res. A 652, 16–20 (2011)
- 6. C.L. Morris et al., Tomographic imaging with cosmic ray muons. Sci. Glob. Secur. **16**, 37–53 (2008)
- 7. J. Wing et al., Study of an avalanche-mode resistive plate chamber. J. Phys. G Nucl. Part. Phys. **8**, 548–554 (2013)
- S. Agostinelli et al., GEANT4 a simulation toolkit. Nucl. Instrum. Meth. Phys. Res. A 506, 250 (2003)

Part III Poster

Neutron Response of PARIS Phoswich Detector

Balaram Dey, C. Ghosh, S. Pal, V. Nanal, R. G. Pillay, K. V. Anoop and M. S. Pose

Abstract We have studied neutron response of the PARIS phoswich [LaBr₃(Ce)-NaI(Tl)] detector which is being developed for measuring the high-energy (E_{γ} = 5–30 MeV) γ rays emitted from the decay of highly collective states in atomic nuclei. The relative neutron detection efficiency of LaBr₃(Ce) and NaI(Tl) crystals of the phoswich detector have been measured using the time-of-flight (TOF) and pulse shape discrimination (PSD) technique in the energy range of E_n = 1–9 MeV and compared with the GEANT4-based simulations. It has been found that for E_n > 3 MeV, ~95 % of neutrons have the primary interaction in the LaBr₃(Ce) crystal, indicating that a clear n – γ separation can be achieved even at ~15 cm flight path.

1 Introduction

The measurement of high-energy γ -rays, emitted from the decay of highly collective states of atomic nuclei [1] as well as from nucleon-nucleon bremsstrahlung during the early stages of the target-projectile collision [2], is an excellent probe to study the atomic nuclei under the extreme conditions of temperature and angular momentum. Earlier, the study of high-energy γ -rays has been performed by many groups in the world and their studies are confined to regions near the valley of stability [3–5]. In the last few years, it is becoming possible to investigate the unexplored regions of the nuclear chart (especially on the neutron-rich side) with the availability of beams of short-lived nuclei, i.e., radioactive ion beams (RIBs).

A Photon Array for the Studies with Radioactive Ion and Stable beams (PARIS) is being developed in order to measure the high-energy γ -rays (E $_{\gamma}$ = 5–30 MeV) [6, 7]. The array consists of ~200 PARIS phoswich element. Each element is made up of 2" × 2" × 2" LaBr $_3$ (Ce) crystal optically coupled to a 2" × 2" × 6" NaI(Tl) crystal followed by a single Photomultiplier tube (PMT) for signal readout. Recently, two

B. Dey · C. Ghosh · V. Nanal (⋈) · R. G. Pillay · M. S. Pose

DNAP, Tata Institute of Fundamental Research, Mumbai 400005, India

e-mail: nanal@tifr.res.in

S. Pal · K. V. Anoop

Pelletron Linac Facility, Tata Institute of Fundamental Research, Mumbai 400005, India

[©] Springer Nature Singapore Pte Ltd. 2018

S. Biswas et al. (eds.), *Advanced Detectors for Nuclear, High Energy and Astroparticle Physics*, Springer Proceedings in Physics 201, https://doi.org/10.1007/978-981-10-7665-7_18

PARIS phoswich detector elements have been characterized over a wide range of γ -ray energies [8]. In the high-energy γ -ray measurement, the evaporated neutrons are the major sources of contamination, which can be rejected by time-of-flight (TOF) technique. On the other hand, the array should be placed as much close as possible to the target chamber due to low-intensity radioactive ion beam, in order to enhance the efficiency of the array which is important for low cross-sectional measurement. But, the rejection of neutron background becomes difficult if the detector array is placed very close to the target chamber. Therefore, the study of neutron response of the phoswich detector is very essential for the rejection of neutron contamination in the high γ -ray measurement as well as to optimize the distance between detector and center of the target chamber.

One of the major advantages of LaBr₃ in the PARIS design is the excellent timing characteristics, enabling $n - \gamma$ discrimination using TOF technique at close distances from target, which is essential for low-intensity RIB experiments [6, 7].

The $n-\gamma$ separation for smaller flight paths relies on the neutron interaction in LaBr₃(Ce) crystal of the PARIS phoswich detector. It is known that the neutrons of energy $E_n < 10$ MeV interact mainly through (n, γ) or $(n, n'\gamma)$ reactions, while $E_n > 10$ MeV more complicated reactions are involved producing charged hadrons [9]. The interaction probability is high in the LaBr₃ crystal of phoswich detector owing to its high density (5.08 gm/cm³). It is therefore important to measure the relative neutron detection efficiency in LaBr₃(Ce) and NaI(Tl) crystals of the PARIS phoswich detector.

In this work, we have measured the relative neutron detection efficiency of LaBr₃(Ce) and NaI(Tl) crystal of the phoswich detector as a function of neutron energy (1–9 MeV) and compared with the GEANT4-based simulation [10].

2 Experimental Details

The measurements were carried out at TIFR, Mumbai, using different neutron sources 252 Cf, 241 Am- 9 Be and 239 Pu- 13 C. A schematic diagram of experimental setup is shown in Fig. 1. A phoswich detector was placed at 50 cm distance from the source, and a BaF2 detector (hexagonal, 9 cm long and 6 cm face-to-face) was placed close to the source (<1 cm). The TOF technique was employed to measure the neutrons, for which the START and STOP triggers were taken from the BaF2 and the phoswich detector, respectively. A CAEN make VME-based digitizer V1751 (1 GHz, 1 Vpp, 10 bit) was used to acquire the data. Timing information was extracted using an algorithm implementing constant fraction discrimination with a delay of 6 ns and 20% fraction, incorporated in the online WAVEDUMP acquisition software [4, 11]. The TOF spectra for two different neutron sources are shown in the left panel of Fig. 2. A small peak to the left of the γ -prompt peak, corresponds to neutron events in BaF2 and γ events in the phoswich detector. This was confirmed by varying the neutron flight path. The time window used for chance correction is shown in the left

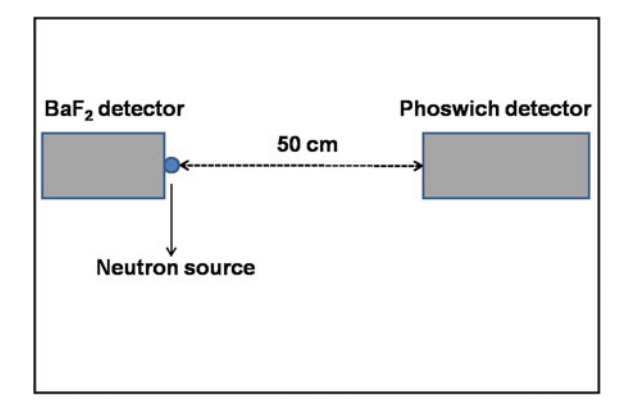


Fig. 1 A schematic diagram of experimental setup

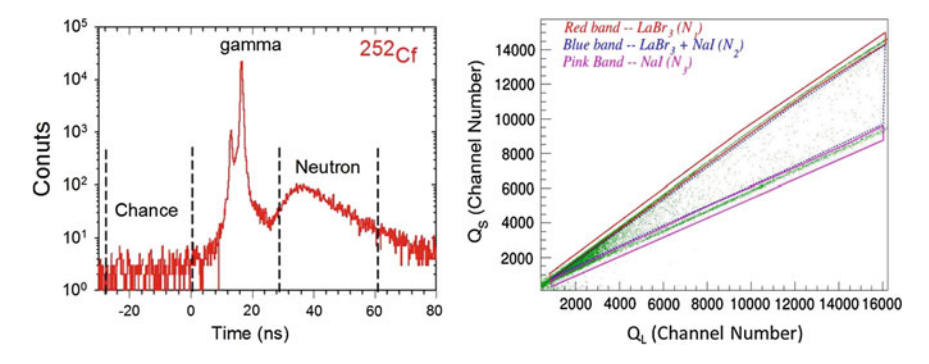


Fig. 2 Time-of-flight spectrum (left panel) and PSD spectrum (right panel) using ²⁵²Cf source

panel of Fig. 2. The data was also recorded without any neutron source to assess the background, which was found to be negligibly small.

Neutron energies are calculated from the neutron TOF using prompt γ -peak as a time reference. The identification of LaBr₃/NaI events was done by the pulse shape discrimination. The output pulse from PMT was integrated and recorded for different gate widths of 300 and 900 ns, to get the Q_S (corresponding to energy deposition in LaBr₃) and Q_L (corresponding to the energy deposition in NaI), respectively. The neutron TOF gated 2D spectrum of Q_L-Q_S is shown in the right panel of Fig. 2.

3 Relative Neutron Detection Efficiency

The observed neutron events in the phoswich detector are classified into three categories corresponding to energy deposition as shown in the right panel of Fig. 2: energy

190 B. Dey et al.

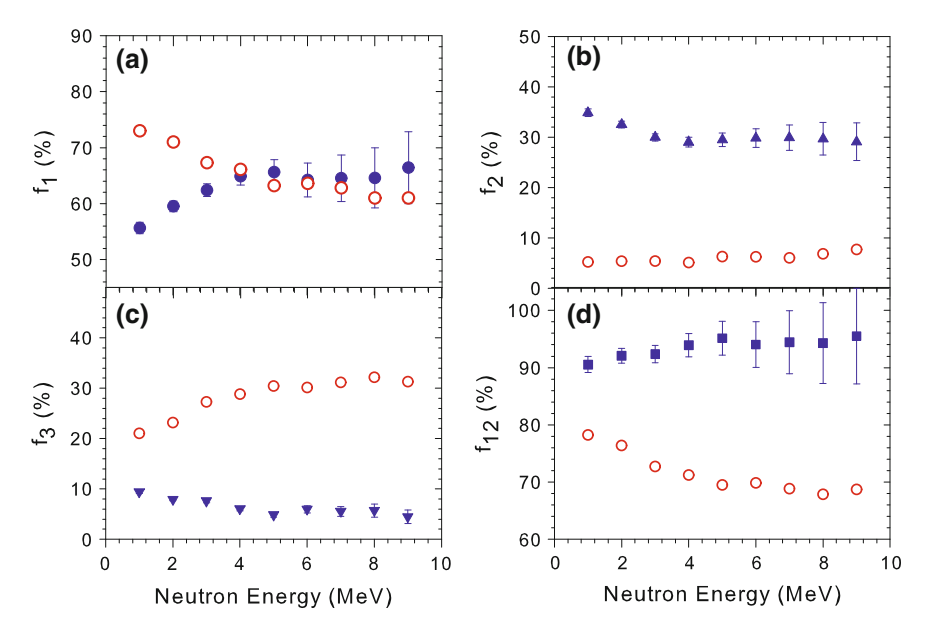


Fig. 3 Relative detection efficiency of neutrons in the phoswich detector (see text for details). Filled symbols represent the experimental data (252 Cf) and simulations are shown by open symbols

in only LaBr₃ (N₁), energy in both the LaBr₃ and NaI (N₂), and energy in only NaI (N₃). The relative neutron detection (f_i), defined ascomputed as a function of neutron N_i/N_{tot} (N_{tot} = N₁ + N₂ + N₃), is computed as a function of neutron energy for all three categories as shown in Fig. 3. In addition, $f_{12} = (N_1 + N_2)/N_{tot}$, corresponding to primary neutron interaction in LaBr₃, is also shown in Fig. 3d. The data for different neutron sources were found to be consistent within the error bars. The present results have been compared with the GEANT4 simulations as shown in Fig. 3 (Open symbols). The neutron data library ENDF/B-VI was used in the simulation code.

4 Results and Discussions

As can be seen in Fig. 3a, about 60–70 % of neutron energy deposition (N_1/N_{tot}) take place in only the LaBr₃ crystal of the phoswich detector. It is evident that the neutron interaction probability in LaBr₃ increases from 1 to 3 MeV and is nearly constant between 3 and 9 MeV. The simulations reproduce the observed trend at E > 4 MeV, but values are lower by about 10% than the data. However, the simulation result underpredicts the data for primary interaction in LaBr₃ (Fig. 3b), whereas it overpredicts the data for primary interaction in NaI (Fig. 3c), and hence mixed events are mismatched with the data (Fig. 3d). This discrepancy could be due to discrepancies in the neutron libraries used in the simulation, which was also reported

in [9]. Experimentally, it is clearly observed that $\sim 90-95\%$ of neutron events have the primary interaction in LaBr₃ crystal of the phoswich detector as can be seen from Fig. 3d. It should be mentioned that mixed events could also have contribution from primary interaction in NaI and subsequent back-scattering of neutron, γ , e^-/e^+ in the LaBr₃. This contribution was estimated from simulation and found to be $\sim 1-3\%$ of total events in the phoswich detector.

5 Summary and Conclusion

The response of a LaBr₃(Ce)-NaI(Tl) phoswich detector to low-energy neutrons (E_n < 10 MeV) has been measured using different neutron sources and compared with the GEANT4 based simulation. The present study has shown that ~90–95% of neutrons with E > 3 MeV have primary interaction in the LaBr₃ part of the PARIS phoswich detector. Thus, a clear n – γ separation can be achieved even at ~15 cm flight path for majority of events. For energies below 3 MeV, the flight time is sufficiently large at ~15 cm distance (T > 6 ns; enabling the n – γ separation) even in case of primary neutron interactions in NaI. Hence, overall neutron rejection with ~90% probability is feasible with flight paths of ~15 cm in the phoswich detector.

Acknowledgements We would like to thank Mr. K. V. Divekar for assistance with the setup. We would also like to thank the PARIS collaboration for their support.

References

- M.N. Harakeh, A. van der Woude, Giant Resonances, Fundamental High-Frequency Modes of Nuclear Excitation (Clarendon Press, Oxford, 2001)
- 2. H. Nifennecker, J.A. Pinston, Annu. Rev. Nucl. Part. Sci. 40, 113 (1990)
- 3. B. Dey et al., Phys. Lett. B **731**, 92–96 (2014)
- 4. C. Ghosh et al., Phys. Rev. C 94, 014318 (2016)
- 5. A. Bracco et al., Phys. Rev. Lett. 74, 3748 (1995)
- 6. paris.ifj.edu.pl
- 7. A. Maj et al., The PARIS project. Acta Phys. Pol. B **40**, 565 (2009)
- 8. C. Ghosh et al., JINST 11, P05023 (2016)
- 9. J.L. Tain et al., Nucl. Instr. and Meth. A **774**, 17–24 (2015)
- 10. S. Agostinelli et al., Nucl. Instr. and Meth. A **506**, 250 (2003)
- 11. K. V. Anoop et al., in *Proceedings of the DAE Symposium on Nuclear Physics*, vol. 59 (2014), p. 858

Simulation of Gamma Detection Using GEANT4

Abhishek Nag

Abstract NaI(Tl) scintillation detector is simulated, and the energy deposited by incoming gamma photons is obtained using GEANT4. Then the scintillation process is separately simulated statistically using R, which is a software environment for statistical computing, to produce scintillation photons and the corresponding electrons in PMT. We compared the obtained energy spectrum with the experimental data for Co⁶⁰ gamma source. The simulated result along with the comparison with experimental data is presented.

1 Introduction

The scintillation process remains one of the most useful methods for the detection and spectroscopy of a wide assortment of radiations [1] and thus provide a tool to measure the energy of the radiation and identification of radionuclides based on the energies of the gamma ray. Scintillation detectors have much greater efficiency for interactions with gamma rays and therefore widely used in different fields of science and technology. They are usually coupled with photomultiplier tubes (PMTs) which generate electrical signals in response to light incident upon their faces.

GEANT4 [2] is an object-oriented (OO) toolkit for the Monte Carlo simulation of the passage of particles through matter. R [3] is a programming language and software environment for statistical analysis, graphics representation and reporting. The aim of the project is to simulate gamma ray detection using GEANT4 and the scintillation process using R to obtain the multichannel analyzer (MCA) spectrum of Co^{60} .

194 A. Nag

2 Methodology

In GEANT4, the geometry, material and the sensitive region of the detector are designed. We first design the entire experimental situation/Hall which in GEANT4 terminology is referred to as world.

The scintillation material defined is NaI. A solid cylindrical detector of material NaI of radius 25.5 mm and length 51 mm is simulated as shown in Fig. 1a.

We also add a lead cylinder around the scintillator detector as we have in our laboratory. The MCA set-up in the laboratory is shown in Fig. 1b.

The type of the particle and its energy is set in PrimaryGeneratorAction command of ParticleGun class. The primary particle defined is a gamma of energy 1.173 and 1.33 MeV originating from a gun in all directions.

3 Results and Observations

A scintillation detector is built, and primary particles are generated. The GEANT4 gives the energy deposited by the gamma photons in the scintillation material.

The spectrum of energy deposited in the NaI crystal is shown in Fig. 2a, and a zoomed in spectrum at lower counts is shown in Fig. 2b.

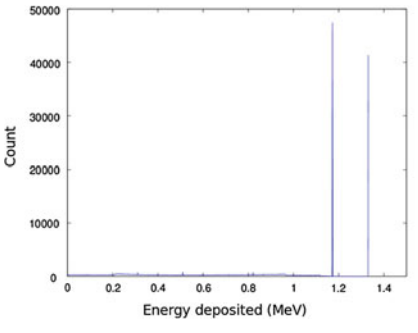


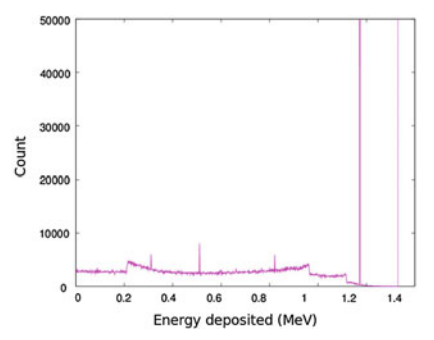
(a) Image of the detetcor as built in GEANT4



(b) MCA setup in laboratory

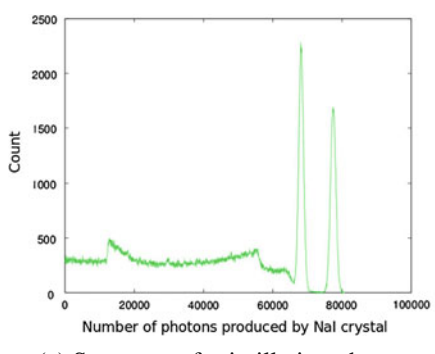
Fig. 1 Experimental setup

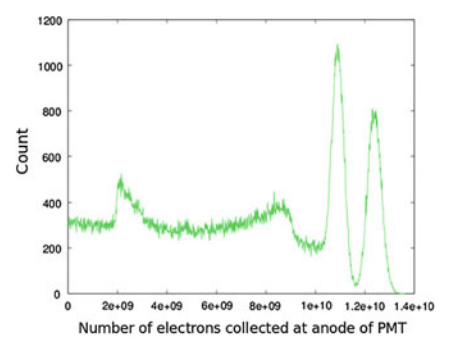




- (a) Spectrum of Energy deposited in NaI crystal. Most of the energy deposited is equal to the gamma photons
- (b) At lower counts the energy deposited in the Compton region can be seen

Fig. 2 Energy deposition simulation results from GEANT4





- (a) Spectrum of scintillation photons
- (b) Spectrum of PMT electrons

Fig. 3 Simulation results by R

The number of photons produced by the NaI scintillator due to the energy deposited is statistically generated using R such that each photon requires $17.2 \pm 0.4 \text{ eV}$ [4] as shown in Fig. 3a.

The photons when enter PMT produce electrons from the dynodes of PMT. Effect of PMT with five dynodes and a multiplication factor of 20 ± 0.3 for each dynodes is statistically generated corresponding to the energy and number of photons hitting the photocathode. The spectrum of the electrons, which are produced by PMT and give a pulse when deposited in the anode, is shown in Fig. 3b.

The calibrated spectrum of the Co⁶⁰ gamma source is shown in Fig. 4 (in green). The experimental data are compared with the simulated data to check how well they match. A normalized spectrum of both the data is shown in Fig. 4 so that the peak heights match.

196 A. Nag

Fig. 4 Comparison of MCA spectrum of Co⁶⁰ obtained from simulation and experiment. In blue is the experimental data and in green is the simulated data

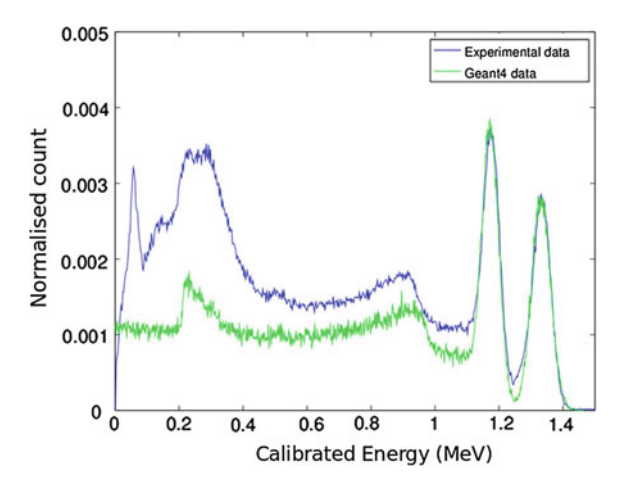
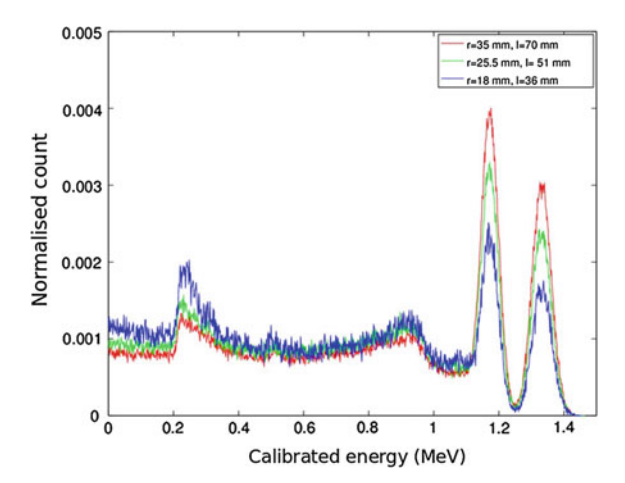


Fig. 5 Spectrum of Co⁶⁰ source with different size of NaI crystal. Increase in size increases the area under the photopeak and reduces the area under the Compton region



The spectrum for different size of the NaI crystal is compared to see the effect of size of NaI cylinder on the spectrum. The radius and the length of the detector are varied, and the spectrum of the normalized count is shown in Fig. 5.

4 Conclusion and Outlook

- 1. We see that the simulated data and the experimental data match quite well.
- 2. The spread in the photopeak region is mainly due to the spread in the number of photons produced in the NaI crystal.

- 3. When we increase the size of the scintillation detector, the counts in the Compton increase while that in the photopeak decrease.
- 4. The peaks which we have in the low-energy region of experimental data are due to backscattering from the lead cylinder covering the NaI crystal.
- 5. Further improvements
 - While taking the experimental data, the background data could be removed.
 - The lead cylindrical shield should have same dimensions as that in the experiment.
- 6. Thus GEANT4 is successful in producing data quite compatible with the experiment.

Acknowledgements I would like to thank my supervisor Dr. Ritesh K. Singh (IISER-K) for giving me this opportunity and idea to learn GEANT4 which would be very useful for my research career in High Energy Physics. I would also like to thank Prof. Satyaki Bhattacharya (SINP) and Prof. Subhasis Chattopadhyay (VECC) for their valuable guidance throughout my work.

References

- 1. G.F. Knoll, Radiation Detection and Measurement (1999), p. 219
- Geant4, a toolkit for the simulation of the passage of particles through matter http://geant4. web.cern.ch/geant4/
- 3. The R Project for Statistical Computing https://www.r-project.org/
- 4. M.M. Iyajima, S.S. Asaki, H.T. Awara, Number of scintillation photons produced in NaI(TI) and plastic scintillator by gamma-rays. IEEE Trans. Nucl. Sci. 40(4), 417–423 (1993)

Measurement of Angular Variation of Cosmic Ray Intensity with Plastic Scintillator Detector

S. Roy, R. P. Adak, R. Biswas, D. Nag, D. Paul, S. Rudra, S. Biswas and S. Das

Abstract A new and simple technique has been developed using plastic scintillator detectors for the study of angular variation of cosmic ray intensity near the sea level. A systematic study of the characteristics of the plastic scintillator paddle detector has been carried out. The yield uniformity of the detector has also been studied. The details of the measurement and the experimental result are presented in this article.

1 Introduction

The motivation of this work is to measure the cosmic ray flux at different zenith angles at the sea level (in Kolkata, India, during the beginning of 2017), using plastic

S. Roy (\boxtimes) · R. P. Adak · R. Biswas · D. Nag · S. Biswas · S. Das

Department of Physics and CAPSS, Bose Institute,

EN-80, Sector V, Kolkata 700091, India e-mail: shreyaroy2509@gmail.com

R. P. Adak

e-mail: ramaprasad.adak@gmail.com

R. Biswas

e-mail: biswas.rathijit@gmail.com

D. Nag

e-mail: dipanjannag19@gmail.com

S. Biswas

e-mail: saikat@jcbose.ac.in

S. Das

e-mail: supriya@jcbose.ac.in

D Pau

Ananda Mohan College, 102/1, Raja Rammohan Sarani, Kolkata 700 009, India

e-mail: dpaul0165@gmail.com

S. Rudra

Department of Applied Physics, University of Calcutta,

92, APC Road, Kolkata 700 009, India

e-mail: sr.phys@gmail.com

© Springer Nature Singapore Pte Ltd. 2018

S. Biswas et al. (eds.), *Advanced Detectors for Nuclear, High Energy and Astroparticle Physics*, Springer Proceedings in Physics 201, https://doi.org/10.1007/978-981-10-7665-7_20

scintillator detectors. Two scintillator detector modules using BC400 plastic have been fabricated and tested with cosmic ray muons and different radioactive sources. As a proof of principle, a preliminary study has been carried out using one paddle scintillator (named Sc-01) of dimension 20 cm × 20 cm and one finger scintillator (named Sc-02) of dimension 10 cm × 2 cm, each of thickness 1 cm, to measure the angular variation of cosmic ray flux [1–4]. The plastic scintillator material and the photomultiplier tube (PMT) are commercially procured. All other components such as Perspex light guide, coupler for light guide are fabricated in proper dimension at Bose Institute workshop. In this experiment, the conventional NIM electronics has been used. The data analysis has been carried out using ROOT software package [5].

In this article, the experimental set-up is described in Sect. 2, the measurement technique and results are shown in Sect. 3 and the summary is discussed in Sect. 4.

2 Experimental Set-up

In this study, the paddle scintillator has been kept fixed in position and the position of the finger detector has been changed. The detectors are placed in a specialised aluminium rack where both vertical (Y-axis) and horizontal (X-axis) movements are easily possible. The schematic of the experimental set-up is shown in Fig. 1. Bias voltage of $1650\,\mathrm{V}$ has been applied to both the detectors. The signals from the scintillator have been fed to a leading edge discriminator. Thresholds to the discriminator have been set at $-50\,\mathrm{mV}$. The discriminated NIM signals are put to a logic unit, and the coincidence count has been measured using a NIM scaler.

The X-axis is chosen to be parallel to the east—west direction. The number of coincidence signals has been counted for different angle of incidence of the cosmic

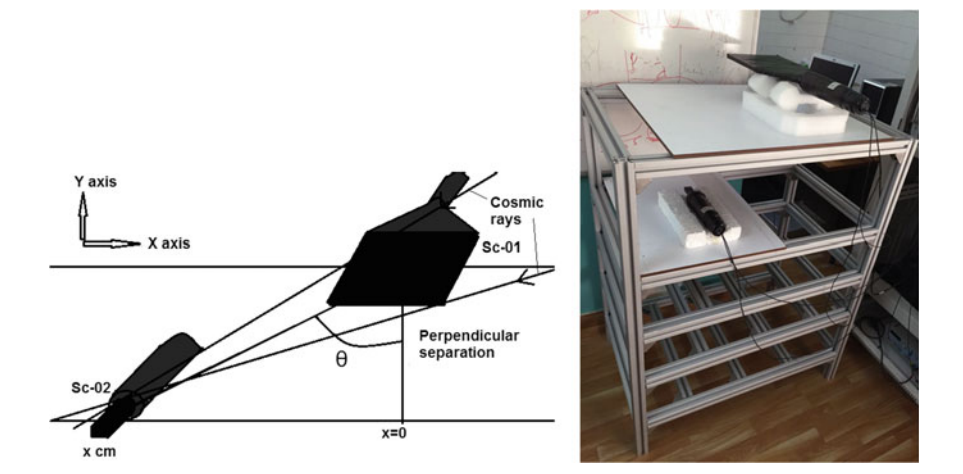


Fig. 1 Experimental set-up to study angular variation of cosmic ray flux

rays for a time duration of $60\,\mathrm{min}$. The Sc-02 is kept below the Sc-01 along vertical direction. Sc-02 is moved in horizontal plane, and coincidence counts have been measured at different positions of Sc-02 (along X-axis). Thus, the incident cosmic ray flux within the solid angle subtended by Sc-01 at Sc-02 for a particular angle of incidence is measured. This measurement is performed for different zenith angles. The expression for solid angle in steradian is calculated using a 2D integration program in ROOT. The coincidence count rate for different zenith angles of cosmic rays has been normalised by the solid angle. The same experiment has been repeated with different perpendicular separation between Sc-01 and Sc-02. The singles count for both the scintillators has also been measured in each set of readings to check the consistency of data. No remarkable variations in singles count have been observed. The cosmic ray shower rate, measured keeping two scintillators at the same horizontal plane with a separation of 3 m, has been found to be $\sim 10^{-5}$ per second per unit area and was subtracted from all data points.

3 Measurements and Results

In this study, the measured quantity is the coincidence count rate from the detectors. Initially, the scintillators are calibrated to get their operating voltages.

3.1 Calibration of the Photomultiplier Tube

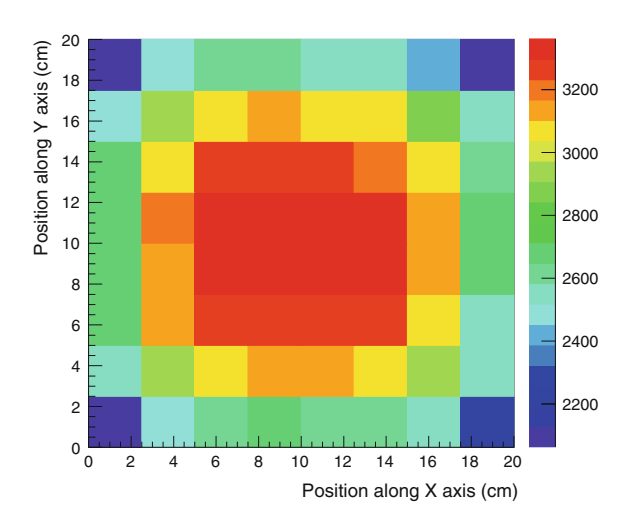
The PMTs have been calibrated by measuring the count rate of the scintillator paddle and the finger varying the applied voltages to the PMT from 1000 to 1850 V. The thresholds have been set at -50 mV. For each voltage settings, count rates have been measured using three different radioactive sources, e.g. $\mathrm{Cs^{137}}$, $\mathrm{Na^{22}}$ and $\mathrm{Co^{60}}$. The cosmic ray background count has also been taken for each settings, and it is subtracted from the count taken with source. It is observed that for each sources the count rate increases with voltage and reaches a plateau for voltage ~ 1600 V and onwards. So the bias voltage to both the detectors has been set to 1650 V for all the measurements.

3.2 Yield Uniformity of Paddle Scintillator

Yield uniformity has been checked using Co^{60} source. The active area of the scintillator Sc-01 has been divided into 64 imaginary grids each of area 2.5 cm \times 2.5 cm. The Co^{60} source has been placed at the centre of each grid, and count has been measured for a time duration of 60 s. The results are shown in Fig. 2. Though the yield is uniform in the central region, there is a variation of 12% in the entire scintillator.

202 S. Roy et al.

Fig. 2 Yield uniformity of paddle scintillator



3.3 Angular Variation of Cosmic Rays

To measure the angular variation of the cosmic ray flux, the detectors have been moved as described in Sect. 2. Firstly, the detector Sc-02 has been kept on the lower rack just below the Sc-01 scintillator. This position of Sc-02 has been marked as origin of the X-axis. Coincidence count rate of Sc-01 and Sc-02 has been measured for this arrangement. This reading corresponds to the cosmic rays that are vertically incident on our set-up. Sc-02 has been moved 5 cm along positive X-axis, and measurements have been repeated. This reading corresponds to the cosmic rays incident at a zenith angle given by $\theta = \tan^{-1}(5/y)$ in degrees, where y is the perpendicular separation of Sc-01 and Sc-02. Measurements have been repeated by moving Sc-02 in a step of 5 cm along X-axis. Thus, coincidence count rates for different zenith angle have been measured. The same process has been done by moving Sc-02 along negative X-axis. The average of the coincidence counts of both positive and negative X-axis has been taken. The solid angle $\Omega(\theta)$ subtended by Sc-01 at Sc-02 has also been calculated for each of such cosmic ray incidence angles, and the coincidence counts were normalised by $\Omega(\theta)$. Counts have been measured for a time duration of 60 min for each setting. The coincidence count rate per unit solid angle per unit area as a function of the zenith angle is shown in Fig. 3. It is seen from Fig. 3 that the cosmic ray intensity decreases from $\sim 7 \times 10^{-3}$ to 3×10^{-3} s⁻¹ cm⁻² sr⁻¹ corresponding to a zenith angle of 0° – 70° , respectively.

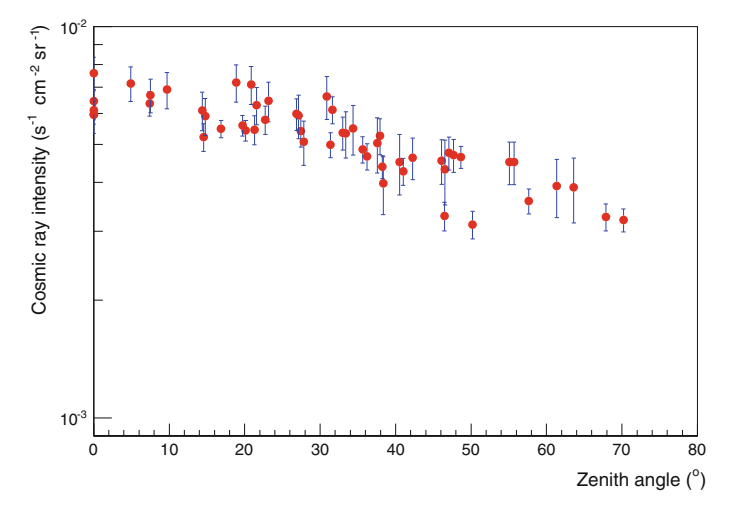


Fig. 3 Variation of cosmic ray intensity with the zenith angle

4 Summary and Outlook

One plastic scintillator paddle and one finger detector have been fabricated. The count rates are measured for both the detectors with cosmic rays, ${\rm Co^{60}}$, ${\rm Cs^{137}}$ and ${\rm Na^{22}}$ sources. The yield uniformity study of the paddle detector has been carried out. The angular variation of cosmic ray intensity is measured, in Kolkata, India, during the beginning of 2017, with the coincidence technique, and it is observed that the cosmic ray intensity decreases from $\sim 7 \times 10^{-3}$ to 3×10^{-3} s⁻¹ cm⁻² sr⁻¹ corresponding to an increasing zenith angle of 0° – 70° , respectively. This result is little bit different both in absolute magnitude and the angular variation as reported in [3]. Actually, the cosmic ray intensity at sea level is a quantity that varies with the geomagnetic latitude, altitude, solar activity and atmospheric conditions. When comparing cosmic ray flux at low energies (<20 GeV/c), it is important to know the year and location where the measurements are made.

The same measurement with scintillators of same dimension and taking coincidence with more than two scintillators are in future plan. The study of east—west asymmetry of cosmic muons will also be done.

Acknowledgements We would like to thank Prof. Sibaji Raha, Prof. Sanjay K. Ghosh, Dr. Rajarshi Ray and Dr. Sidharth K. Prasad for their valuable suggestion and discussions during the course of the study. We would also like to thank Mr. Aritra Mondal of Department of Physics, University of Calcutta, for his help in the study. We are thankful to Bose Institute workshop for all the mechanical work to build the light guide and coupler for light guide. Finally, we are thankful to GSI detector laboratory, Germany, for providing the optical glue, grease, etc., used to build the detector. R. P. Adak acknowledge the support UGC order no—20-12/2009 (ii) EU-IV. S. Biswas acknowledges the support of his Ramanujan Fellowship. This work is also partially supported by the research grant SR/MF/PS-01/2014-BI from Department of Science and Technology, Government of India.

S. Roy et al.

References

1. A.N. Dmitrieva et al., 29th International Cosmic Ray Conference Pune, vol. 6, 73–76, (2005). [arXiv:hep-ex/0611051v1]

- 2. Alexander Mishev, [arXiv: physics/0602120v.2]
- S. Cecchini., M. Spurio, Geosci. Instrum. Method. Data Syst. 1, 185–196, (2012). [arXiv:1208.1171v1]
- 4. M. Bektasoglu, H. Arslan, Pramana J. Phys. 5, 837–846 (2013)
- 5. ROOT, A Data Analysis Framework, CERN, website: http://www.root.cern.ch

Some Aspects of Characterization of GEM Detector

D. Nag, D. Paul, S. Roy, S. Biswas, S. Das, S. K. Ghosh, S. K. Prasad and S. Raha

Abstract Long-term stability test of Gas Electron Multiplier (GEM) detector has been carried out. We have studied the variation of the gain of a triple-GEM detector as a function of the relative humidity. The uniformity of gain over the entire surface of the detector has also been studied measuring the anode current. The details of the measurement process and the experimental results are presented.

D. Nag (\boxtimes) · S. Roy · S. Biswas · S. Das · S. K. Ghosh · S. K. Prasad · S. Raha Department of Physics and CAPSS, Bose Institute, EN-80, Sector V, Kolkata 700091, India e-mail: dipanjannag19@gmail.com

S. Roy

e-mail: shreyaroy2509@gmail.com

S. Biswas

e-mail: saikat@jcbose.ac.in

S. Das

e-mail: supriya@jcbose.ac.in

S. K. Ghosh

e-mail: sanjay@jcbose.ac.in

S. K. Prasad

e-mail: skp.alice@gmail.com

S. Raha

e-mail: sibaji.raha@jcbose.ac.in

D. Paul

Ananda Mohan College, 102/1, Raja Rammohan Sarani, Kolkata 700 009, India e-mail: dpaul0165@gmail.com

© Springer Nature Singapore Pte Ltd. 2018 S. Biswas et al. (eds.), *Advanced Detectors for Nuclear, High Energy and Astroparticle Physics*, Springer Proceedings in Physics 201, https://doi.org/10.1007/978-981-10-7665-7_21 D. Nag et al.

1 Introduction

The a large ion collider experiment (ALICE) [1] is a general purpose heavy ion detector system built at CERN, Geneva, that aims to study the Quark Gluon Plasma (QGP) phase of matter which is believed to have existed for a very small duration of time after the Big bang. The heart of ALICE detector system is the Time Projection Chamber (TPC), and the end-caps of the TPC are currently equipped with Multi-Wire Proportional Chambers (MWPC) read-out. Use of MWPC resulted in limited rate handling capabilities of the TPC (collision rate ~500 Hz for Pb–Pb collisions), thus for upcoming runs the MWPC's will be replaced by GEM chambers which will cope up the rate handling capability to the order of a collision rate of ~50 kHz (for Pb–Pb collisions).

As a part of the GEM detector R&D in our laboratory, we have tested a triple-GEM prototype for long-term gain stability [2]. In this particular article, dependence of normalized gain on relative humidity and the uniformity of gain over the total active area are presented.

2 The Gas Electron Multiplier

GEM foils are 50-µm-thick Kapton, sandwiched between two 5-µm-thick copper layers [3]. These copper foils serve the purpose of electrodes. Then, holes are etched into this configuration using photolithography technique.

The holes are generally conical or bi-conical in shape depending upon the mask used. In standard geometry, the GEM foils have an outer diameter of $70\,\mu m$ and a pitch of $140\,\mu m$. These holes are arranged in such a manner that they cover the maximum possible area, and the distance between neighbouring holes is the same. The geometry of a GEM foil is shown in Fig. 1(Left). When potential difference

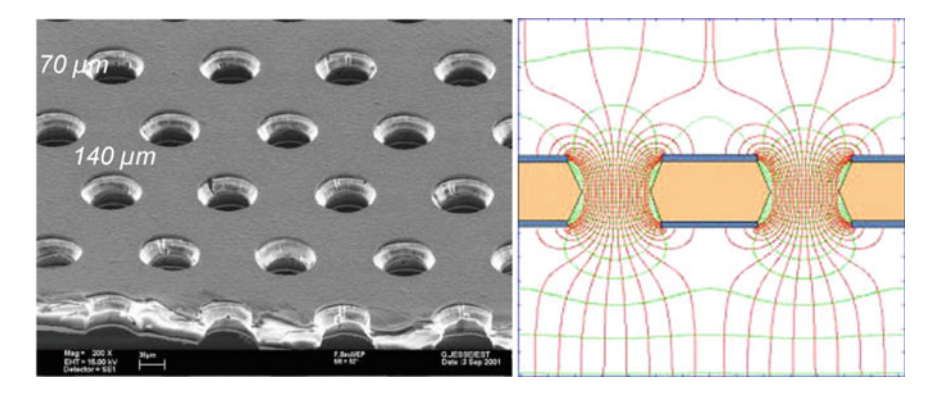


Fig. 1 Microscopic picture of GEM foil (left), electric field in the region of the holes of a GEM electrode (right), both pictures taken from [4]

 $(\sim 400\,\mathrm{V})$ is applied across the copper planes, the electric field inside the holes attains a value $(\sim 80\,\mathrm{kV/cm})$, which is strong enough to create avalanche multiplication. The electric field lines in the region of a hole are shown in Fig. 1 (Right). In order to achieve high gain at lower voltage and without leading to a discharge, several of such GEM foils could be stacked upon one another and connected in cascade mode.

In this particular study, a triple-GEM detector is used. The drift gap, 2-transfer gaps and the induction gap of the chamber are kept as 3, 2, 2, 2 mm, respectively. The detector has a XY printed board (256 X-tracks and 256 Y-tracks) in the base plate and that works as the readout plane. Four sum-up boards are used in this detector each having 128 connectors. Four sum-up boards are again summed and are directly connected by a short length Lemo cable to a 6485 Keithley pico-ammeter to measure the total anode current. The effective gain of the detector system is measured using the formula,

$$Gain(g) = \frac{i}{neR}$$

where

i = anode current

n = no of primary electron produced

e = electronic charge

R = Rate of the radioactive source.

The anode current is calculated using the formula, $i = i_{with source} - i_{background}$ as described in [2].

3 Gain Uniformity Test

The effective gain was measured keeping the Fe 55 source on a particular position of the detector and increasing the applied voltage. The effective gain as a function of the applied voltage is shown in Fig. 2. It is found from Fig. 2 that the effective gain increases with voltage exponentially. At an applied voltage of 4300 V, an effective gain of \sim 15,000 is achieved.

In ideal cases, the GEM foils are stretched uniformly and they are kept parallel to each other using spacers and frames. However, due to several mechanical limitations there might be some imperfections both in building the GEM foils (the layers not being uniform, defective hole geometries) and in the spacing between the foils. Thus, the gain of the foils can vary considerably over the active area of the detector. In order to measure that, we divided (virtually) the active area of the detector into several sectors. The source was kept on each sector, and the corresponding anode current was recorded at an applied voltage of $4300\,\mathrm{V}$. The active window of the detector is a square of $10\times10\,\mathrm{cm}^2$, thus allowing $9\times9=81$ squares on which the source was placed on and the corresponding gain was measured. After normalizing the gain with the highest value, the data is plotted. The distribution of normalized

D. Nag et al.

Fig. 2 The effective gain as a function of the applied voltage

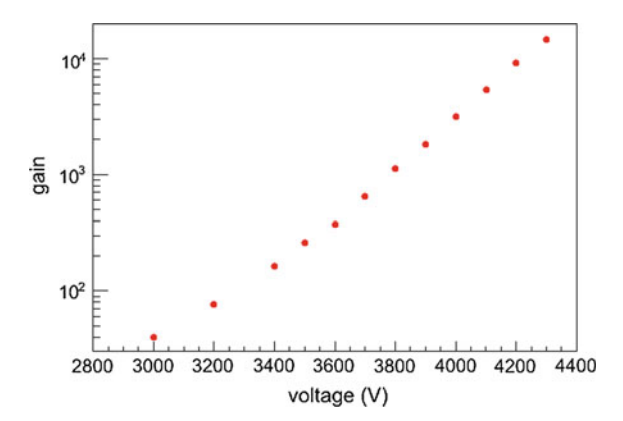
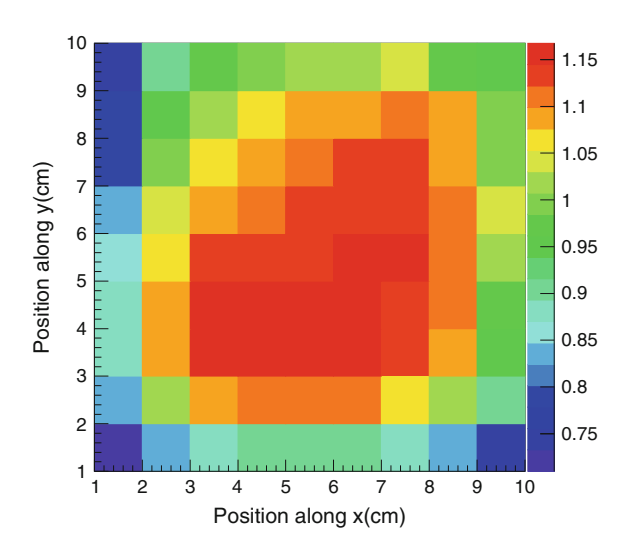


Fig. 3 The distribution of normalized gain on the active GEM area



gain on the active GEM area is shown in Fig. 3. Results show that there is a variation of gain \sim 11.7%.

4 Long-Term Stability Test

Since in a large experiment the detectors are exposed to high dose of radiation over a long duration of time, it is very important to check whether the gain of the detector remains constant over time. In order to test this, the detector was exposed to a Fe⁵⁵ source which emits X-Ray photons having a peak energy at 5.9 keV at an applied

voltage of 4300 V. The resulting anode current was measured with a Keithley pico-ammeter, and the gain was calculated [2].

The normalized gain can be calculated using the formula,

$$normalized\ gain = \frac{Calculated\ gain}{Theoretical\ gain}$$

where the theoretical gain was calculated using the formula

$$g = Ae^{B\frac{T}{p}}$$

where A, B are fit parameters obtained by plotting the value of gain with a variation of the absolute temperature (T in Kelvin) and atmospheric pressure (p in atmospheric pressure). To measure these ambient parameters, a data logger was built in house that is capable of measuring temperature, pressure and relative humidity [5]. The relative humidity is measured using a DHT11 module; however, it has limited resolution of 1%.

5 Dependence of Gain on Relative Humidity

While measuring the ambient parameters, the distribution of ambient relative humidity was also measured over time. An effort was made to find out any correlation between the gain and the ambient relative humidity. However, The temperature/pressure (T/p) corrected normalized gain was plotted against relative humidity and shown in Fig. 4. The data with temperature in the range of $21-23\,^{\circ}\text{C}$ and in three pressure region are shown in Fig. 4. The distribution of normalized gain for all the data points is shown in the inset of Fig. 4. There is no correlation found between these two, but there is a $\sim 6\%$ RMS variation from the mean value of 1.006 for the whole range of humidity values.

6 Summary and Outlook

Basic characterization of a triple-GEM detector has been carried out. Variation of gain over the active area of the detector has been checked, and the result shows a variation of $\sim 11.7\%$ over the area of 10×10 cm². Tests have been done to check the dependence of gain on ambient relative humidity, and the results show that gain does not show any correlation with relative humidity.

D. Nag et al.

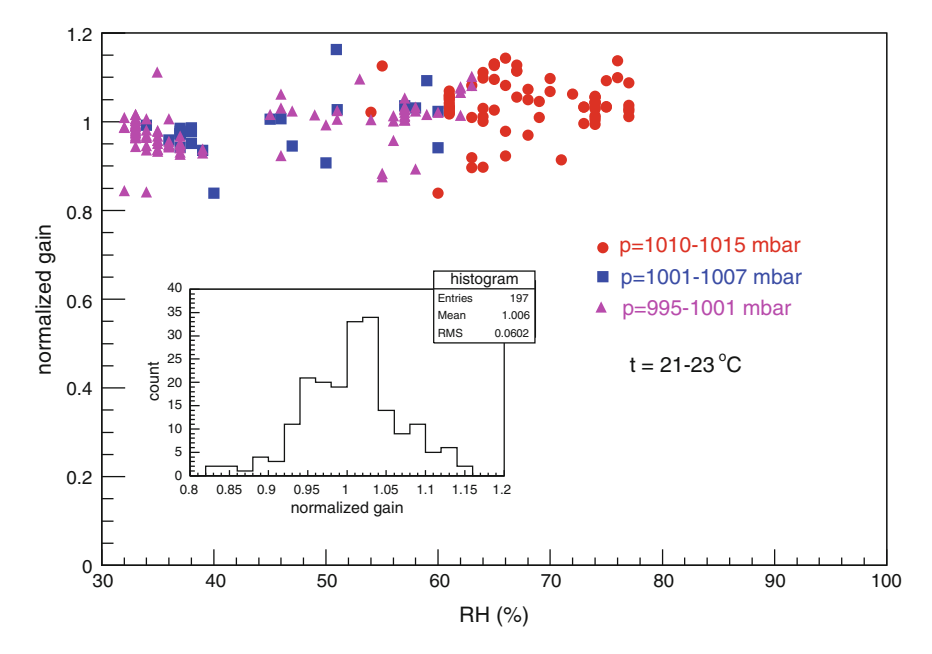


Fig. 4 The normalized gain as a function of relative humidity (inset). The distribution of normalized gain for all the data points

Acknowledgements We would like to thank Dr. Rajarshi Ray and Mr. Ramaprasad Adak for their valuable suggestion and discussions during the course of the study. We would also like to thank Mr. Aritra Mondal of Department of Physics, University of Calcutta, for his help in the study. This work is partially supported by the research grant SR/MF/PS-01/2014-BI from Department of Science and Technology, Government of India.

References

- Technical Design Report for the Upgrade of the ALICE Time Projection Chamber, ALICE-TDR-016, CERN-LHCC-2013-020, 3 Mar 2014
- R.P. Adak et al., JINST 11 T10001 (2016). https://doi.org/10.1088/1748-0221/11/10/T10001. [arXiv:1608.00562]
- 3. F. Sauli, Nucl. Instrum. Meth. A 386, 531 (1997)
- 4. Fabio Sauli, Nucl. Instrum. Meth. A 805, 2 (2016)
- 5. S. Sahu et al., Proceedings of the DAE Symposium on Nuclear Physics, vol. 59 (2014), p. 876

A TTL Fast Pulse Counter for Detector Signals

Sagarika Swain, S. Sahu, P. K. Sahu and S. Biswas

Abstract An ARM Cortex-M3-based fast TTL counter is developed in High Energy Detector(HED) laboratory at IOP. It can measure high-rate signals up to 84 MHz from any particle detector. The designed counter is presently operating with Low Voltage Transistor-Transistor Logic (LVTTL) signal having voltage range from 0 to 3.3 V, to count the pulses and display the corresponding data in an LCD panel. A programmable timer is included with the counter, which can be varied manually from 60 seconds to few hours. It can be operated in both manual and remote mode. In manual mode of operation, the required time interval for the count measurement can be set by the user externally. In the remote mode, a program is developed to start the counter on a LabVIEW platform. In this interface, it can also work for number of loops with different intervals. The detailed fabrication process and calibration result for this counter are presented here.

1 Introduction

A counter is an essential device for measuring pulses coming at a high rate in any nuclear and high energy physics experiments. The main objective to construct such a device is to overcome the deficiencies of many commercially available counters or scalars. The counter designed here is specially edge-triggered, so that it will not read multiple counts during any sudden jump of signals or during a spark. When there is a spark in the detector, a continuous discharge occurs, which gives a pulse of few hundreds of milliseconds. These extra counts are added to the counting unit as

S. Swain · S. Sahu (⊠) · P. K. Sahu Institute of Physics, HBNI, P.O: Sainik School, Sachivalaya Marg, Bhubaneswar 751005, India e-mail: ssahu@iopb.res.in

S. Biswas

Department of Physics, Centre for Astroparticle Physics and Space Science, Bose Institute, EN-80, Sector V, Kolkata 700091, India

long as the discharge continues inside the detector, where the commercial counters or state-sensitive counters take a spark as multiple counts. Our counter detects the pulses only during a rising edge transition, whatever may be the state value. It takes the transition as only one count rather than giving any false trigger. This counter has a 10-digit ($2^{32}-1=4294967295$) display in single unit. The programmable time interval can be set up to $68\,h$, with a minimum time resolution of 1 min. For detector like gas electron multiplier (GEM), the output pulse is very narrow and typically is in the order of $50-100\,n$ s width. To measure these pulses, we require a counter of lower bandwidth. Also to study long-term stability tests for GEMs, the counter should be capable of accumulating such high count rate for longer duration.

The development software and firmware of Arduino Due [1, 2] is an open source. The microcontroller board is designed with the Atmel SAM3X8E controller. The CPU used here is a single-core microcontroller with 32-bit processor. It has following components: digital input/output pins, ADC analog inputs, UARTs (hardware serial ports), a 84 MHz clock, digital-to-analog (DAC) output, eight 32-bit fast counters and controller lines for different serial bus (like I2C, SPI). The best performance can be achieved by using RISC processor.

The Arduino board has an inbuilt serial-to-USB converter, which we use as a interface to computer for remote operation. A conditioning circuit is designed to accept the TTL signals of 0–10 V DC unipolar pulse to interface the controller input limited to 3.3 V. This signal conditioning circuit is converted to 0–3.3 V.

2 Architecture of Counter Board

The counter board has the following major parts in the system: a custom-designed signal conditioning circuit, an open software/hardware Arduino DUE board and 4×16 LCD (specific software to control the counter unit) [1].

2.1 INPUT and OUTPUT Section

The signal conditioning circuit at the input is a high-frequency dual inverter to limit the amplitude of high state to $3.3\,\mathrm{V}$ to the controller. The transistors used here are RF transistors BF494 having gain bandwidth of $120\,\mathrm{MHz}$. For output, the 16×4 line LCD is interfaced with 4-bit data communication mode. The operating software is user-friendly to set the interval for event capture, providing standalone and remote mode. Also, it refreshes the counts in each second to indicate the cumulative value up to the interval from the starting point. The display unit with instantaneous and cumulative count value is displayed in Fig. 1a.

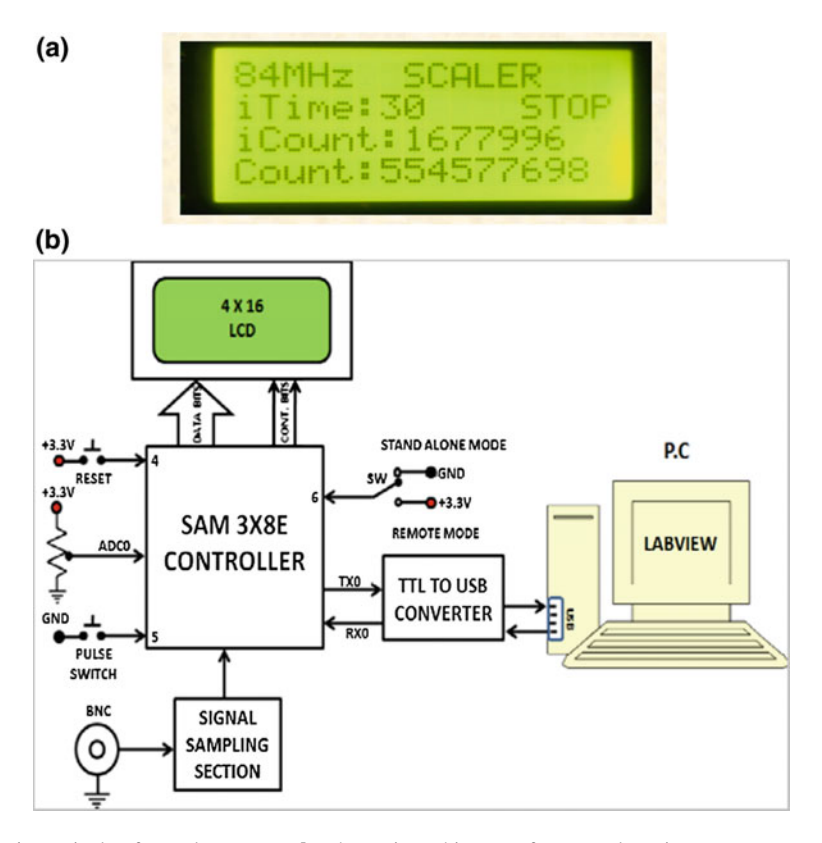


Fig. 1 a Display for scalar counter, b schematic architecture for control section

2.2 CONTROL Section

There is one push switch to reset the microcontroller. One pulse switch and one multi-turn 10 K potentiometer are connected to the ADC. The analog voltage which is adjusted in the potentiometer is fed to the 12-bit ADC, which in turn converted into time, to control the time interval of data capturing. The pulse switch is multi-functional and used as an acceptance of the user decision. The toggle switch is used as mode selection option for standalone and remote operation. The total setup for control section is shown in Fig. 1b.

2.3 CPU Section

The main components of Arduino DUE [1–3] are: a System-on-Chip (SoC), SAM3X8E and complex peripheral interfaces. The SAM3X8E is an ARM Cortex-M3 CPU core.

S. Swain et al.

The 16-channel multiplexed analog-to-digital converter, 9 Timer used as counter or pulse generator, different serial interfaces like I2C, SPI, one wire and RS232, two digital-to-analog converters with 12 bits resolution and multiple input—output pins are the main peripheral interfaces.

2.4 The Timer Counter Module

Three Timer module with three blocks generates digital signals in waveform mode and acts as 32-bit counter in capture mode. They can run as independent hardware without any direct control over CPU core due to their dynamic nature [2]. In our application, one timer counter is configured in capture mode to count the events as per the input availability and another one is configured in waveform mode to produce one second tick time to refresh the counter display.

There are three Timer module with three blocks each; any block can be used in waveform mode to generate digital signals and in capture mode as 32-bit counter. These timer blocks are very flexible and can run after the programming as independent hardware without the direct control of the CPU core. In our application, one timer counter is configured in capture mode to count the events as per the input availability and other one is configured in waveform mode to generate the one second tick time to refresh the counter display.

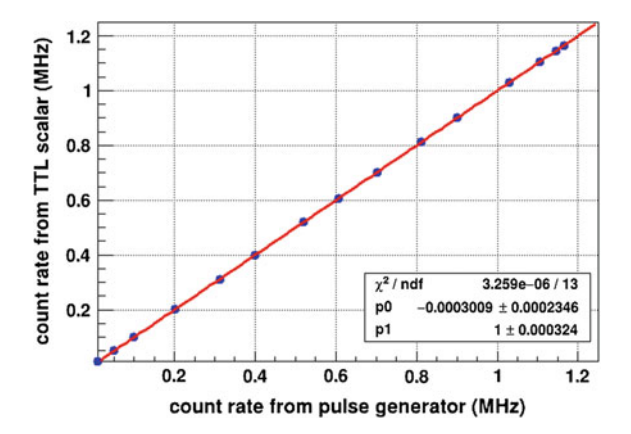
2.5 Serial Communication with PC Interface

There are four serial port communication channels available with the SAM3X8E controller, and Channel 0 of this is connected to a TTL to USB converter. It is interfaced to the computer, running with an application program developed on Lab-VIEW platform. This device is designed to communicate with a single baud rate of 115200 bits/s. The communication protocol of the Arduino Due is a 115200 baud rate serial port. The LabVIEW-based software developed and deployed in the PC, which runs to display the count and store the count in a file with time stamp. The LabVIEW-based software developed here with a nice graphical user interface.

3 Calibration

The TTL counter is calibrated by using a programmable pulse generator. The generator provides pulses with frequency which varies from 100 Hz to 1 MHz with constant amplitude. Since, the higher frequency limit can be adjusted up to a value of 1.16 MHz, we have done the counter calibration within this frequency range. Sinusoidal pulses with constant amplitude are directly fed to the counter input.

Fig. 2 Calibration curve for fast TTL counter. The curve is fitted with a straight line having p0 and p1 parameters with chisquare value



The frequency of the pulses are varied from 10 kHz to 1.16 MHz and simultaneously observed by an oscilloscope. With each frequency setting, the counts are recorded for a constant interval of time. Then they are plotted against the corresponding frequency and calibrated. The calibration plot is well fitted with a straight line and is shown in Fig. 2.

4 Summary

A fast TTL counter is built to measure the fast counting rates. It is an edge trigger-based counter and can be interfaced to LabVIEW platform. The counter has the following features: (a) based on edge trigger design, (b) 10-digit display unit, (c) the counter can accept TTL input, (d) it can accept the maximum count rate of 1.12 MHz, and (e) the maximum preset time can be set to 68 h. An inbuilt suitable NIM to TTL adopter can avoid the use of the NIM Bin Racks and make this scalar a standalone unit. Also, an Ethernet-based TCP/IP protocol can be employed to avoid using a lengthy USB cable. We are in a process to make one high-frequency function generator to calibrate this scaler up to 84 MHz. In future, we plan to implement multiple counter channels with individual counting and a dual timer unit for the system. This is used with GEM detector to measure such fast count rate [4].

Acknowledgements The authors are thankful to Prof. Sudhakar Panda, Director, IOP, Bhubaneswar, for his support in this work. This work is also partially supported by the ALICE-India fund of DAE-DST, Govt. of India. S. Biswas acknowledges the support of DST-SERB Ramanujan Fellowship (D.O. No. SR/S2/RJN-02/2012). We are also thankful to D. S. Bhattacharya for reading the manuscript and useful discussions.

S. Swain et al.

References

- 1. https://www.arduino.cc/en/main/boards
- V. Bocci et al., in The ArduSiPM a Compact Trasportable Software/Hardware Data Acquisition System for SiPM Detector. Nuclear Science Symposium and Medical Imaging Conference (NSS/MIC), 2014 IEEE, https://doi.org/10.1109/NSSMIC.2014.7431252
- 3. Atmel corporation data sheet; AT91 SAM3X8e
- R.P. Adak et al., Long-term stability test of a triple GEM detector. 2016 JINST 11 T1000; arXiv ePrint; 1608.00562

Implementation and Evaluation of Glue Logic for Various Configuration Schemes Based on I2C and HDLC Protocol for ALICE Common Readout Unit (CRU)

S. Mukherjee, F. Costa, R. Paul, A. Chakrabarti, S. A. Khan, J. Mitra and T. Nayak

Abstract This paper presents the preliminary results of various configuration schemes for onboard and off-board components using built-in Peripheral Component Interconnect (PCIe) interface of Intel Arria 10 FPGA. This is part of A Large Ion Collider Experiment-Common Readout Unit (ALICE-CRU) upgrade program that will configure CRU itself as well as associated on-detector ASICs of most of the sub-detectors prior data acquisition. In this paper, the different configuration schemes based on Inter-Integrated Circuit (I2C) and High-level Data Link Control (HDLC) protocol will be explained. The main motivation of this paper is to discuss the glue logics that have been developed during evaluation of those protocols. The result obtained during evaluation will also be presented.

S. Mukherjee (⋈)

Centre for Astroparticle Physics and Space Science, Bose Institute,

Kolkata 700091, India

 $e\hbox{-mail: } sanjoy.mukherjee@cern.ch, sanjoym@jcbose.ac.in$

F. Costa · T. Nayak

Organisation Europeenne Pour la Recherche Nucleaire, Geneva, Switzerland

e-mail: filippo.costa@cern.ch

R. Paul · A. Chakrabarti

University of Calcutta, Kolkata 700098, India

e-mail: rourab.paul@cern.ch

A. Chakrabarti

e-mail: amlan.charkrabarti@cern.ch

S. A. Khan · J. Mitra

Variable Energy Cyclotron Centre, HBNI, Kolkata 700064, India

e-mail: shuaib.ahmad.khan@cern.ch

J. Mitra

e-mail: jubin.mitra@cern.ch

© Springer Nature Singapore Pte Ltd. 2018

S. Biswas et al. (eds.), *Advanced Detectors for Nuclear, High Energy and Astroparticle Physics*, Springer Proceedings in Physics 201, https://doi.org/10.1007/978-981-10-7665-7_23

S. Mukherjee et al.

1 Introduction

ALICE is the detector system at CERN, LHC dedicated particularly to study the properties of Quark Gluon Plasma (QGP). The detector system of ALICE will undergo a major upgrade during the upcoming Long Shutdown 2 (LS2) which is at present foreseen to start in July 2018. Most of detector sub-systems will upgrade their detector hardware and associated electronics to support higher collision rate and luminosity aimed at precision measurements of the QGP.

The CRU [1] will be used by all the upgraded detector systems to read out detector data as well as for configuration of CRU itself and on-detector ASICs before readout. So, the CRU will have two kinds of slow control module related to configuration. In Run 3, the CRU will receive configuration data from readout server over PCIe interface. In this paper, we would like to discuss first the motivation behind the configuration and goals to be achieved. Then, in Sect. 4, the design based on configuration protocols will be described. The implementation details of glue logic will be explained in Sect. 5. The results obtained during configuration and aims in future release will be described in Sect. 6.

2 Motivation Behind Evaluation

There are many chips on CRU card that need to be configured first, before the card to be allocated. The chips are mainly related to optical modules through which CRU communicates with trigger and detector system and clock modules used to generate clock with very low jitter for CRU-GBT (Giga Bit Transceiver) [6] module and also sensor modules that will provide board and die temperature, power consumption of the card. The chips have I2C interface and can be configured and monitored from the FPGA.

The on-detector ASICs must be configured before data taking and the status of on-detector electronics should be monitored during data taking. This configuration and monitoring of on-detector electronics are possible through GBT-SCA (Slow Control Adapter) [4] chip. This chip will be on-detector electronics/Front End Electronic (FEE) board.

3 Evaluation Goals

The chips on CRU that are to be configured has I2C interface. The aim is to interact with each chip and write and read back chip registers over I2C bus. Once single read/write is done, the next step is to configure chips, i.e., read/write in proper sequence as per CRU requirements.

The GBT-SCA accepts only HDLC frame. The aim is to generate HDLC frame based on configuration data received over PCIe bus and send it to GBT-SCA for

the configuration of on-detector ASICs. The module inside CRU which controls on-detector ASICs is FEE slow control module.

4 Design Overview

In this section, we will describe briefly about designs related with I2C and HDLC protocol, respectively. The I2C core is from OPENCORE and the FEE slow control based on HDLC core is developed by the CERN ELECTRONIC group.

4.1 I2C-Based Design Related to CRU Slow Control

The I2C master [3] controller from open core is used to interact with chips. Each chip has its own address and set of registers. There is pre-defined way for each chip to write into or read back registers inside it. The I2C write and read operation is performed generally in the way following. The write operation is performed in three phases and read requires four phases. Figure 1a shows the sequence.

The open core I2C master has user logic based on wishbone bus interface and I2C core controller. The design supports user configurable SCL (Serial clock), and it includes scan features. It enables user to find out all slaves available in hardware. Figure 2 left and right shows the open core design user logic and core logic, respectively.

4.2 HDLC-Based Design Related to FEE Slow Control

The FEE slow control module from CERN electronic group based on HDLC core [2] formed HDLC frames from detector configuration data received over PCIe. The HDLC protocol defines only data link layer. We must add physical layer on top of it. GBT protocol is used as physical layer protocol. GBT protocol has specific 2-bit field called EC to include slow control data. The FEE-SC module fills the EC field of GBT frame 2 bit by 2 bit using entire HDLC frame, and thus, entire HDLC frame has been encapsulated inside GBT frame. The FEE-SC module would be acknowledged once SCA will receive the entire HDLC frame. Figure 1b shows HDLC as well as GBT frame format.

5 Design Evaluation Process

In this section, we describe the integration of the IP cores for I2C and HDLC protocol implemented in our project. These two blocks, i.e., I2C and HDLC are controlled in the final project using different BAR registers to send command and read back the

S. Mukherjee et al.

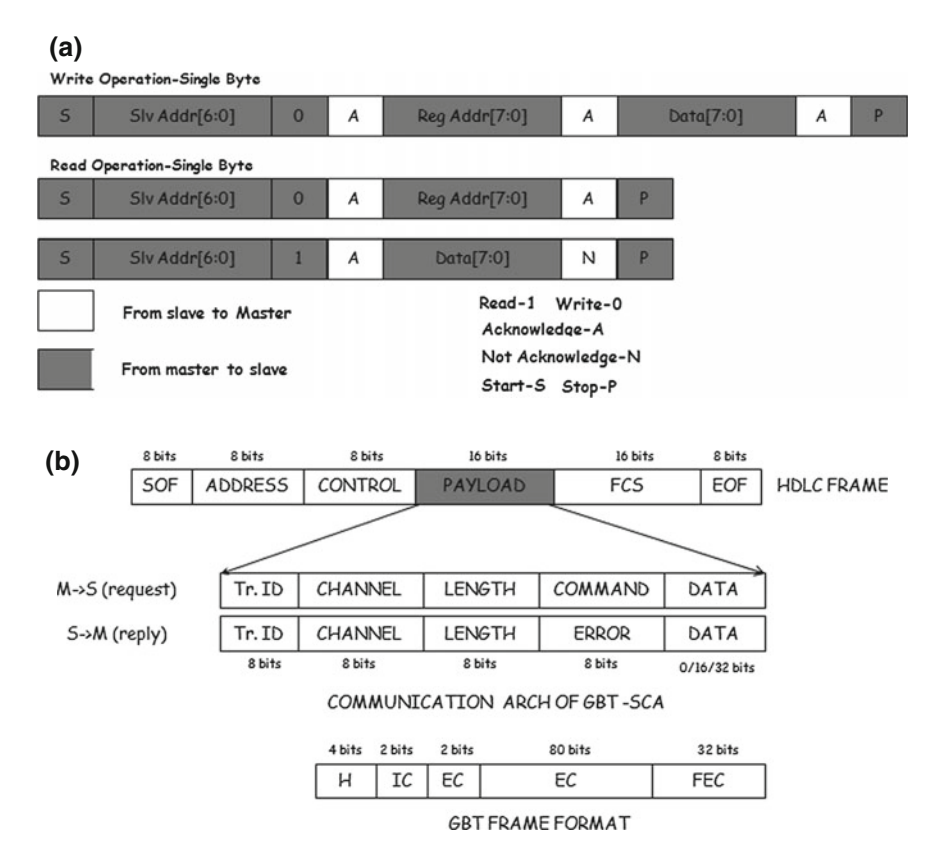


Fig. 1 a I2C write and read b HDLC and GBT frame format

reply. The necessary glue logic has been added to feed user data in each block in integrated framework. The brief details of glue logic for each block and the evaluation process are described in following subsection.

5.1 Integration of the I2C Core in the Project

The wishbone interface of open core described in Sect. 4 has been replaced by Avalon bus interface. The multiple control registers of open core design have been changed by three 32-bit registers which are used to pass control information to the I2C core controller and status read back. The data register shown in Fig. 2 middle has three 8-bit fields to hold I2C slave, register address and data to be written. The user logic handles single write and read operation by exchanging handshaking signals with the I2C core.

There are two kinds of address associated with each slave: I2C and chip address. The 8-bit chip address is defined as 7-bit I2C address plus read/write command bit

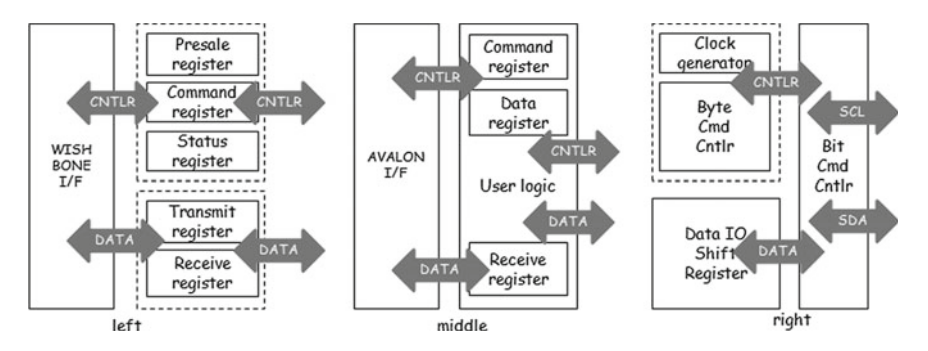


Fig. 2 User logic—left: open core, middle: modified, right: I2C core logic

as LSB. This is done internally inside user logic. Write and read back of registers are evaluated first and then, particular I2C chip is configured. Many chips have been configured successfully once I2C interface became stable.

5.2 Integration of the HDLC Core in the Project

The glue logic developed related to FEE-SC (slow control module) is to fed configuration data along with length, command, and channel number through proper interface into FEE-SC module such that the module will generate HDLC frames that will direct SCA chip to configure on-detector ASICs.

Figure 3a shows major blocks of generic FEE board. During evaluation, Versatile Link Demonstrator Board (VLDB) [5] used to test communication among GBT-SCA, GBTX chip [7], and FEE-SC module. We must configure GBTX chip first to interact with GBT-SCA chip.

The SCA is connected with GBTX chip via E-port. The slow control data will reach at GBT-SCA through GBTX chip. The SCA chip transports the same to FE ASIC using interfaces like GPIO, I2C. The choice of interface depends on configuration command. This information is embedded in HDLC frame.

One server was set up to push configuration data. The Intel Arria 10 card has been installed on that server. The bidirectional communication with SCA chip has been tested from server to VLDB board using CRU PCIe interface. The loopback flow is shown in Fig. 3b.

6 Summary and Outlook

The chips installed on the CRU have been successfully configured and monitored using I2C protocol. FEE board of detectors has been configured and monitored using

S. Mukherjee et al.

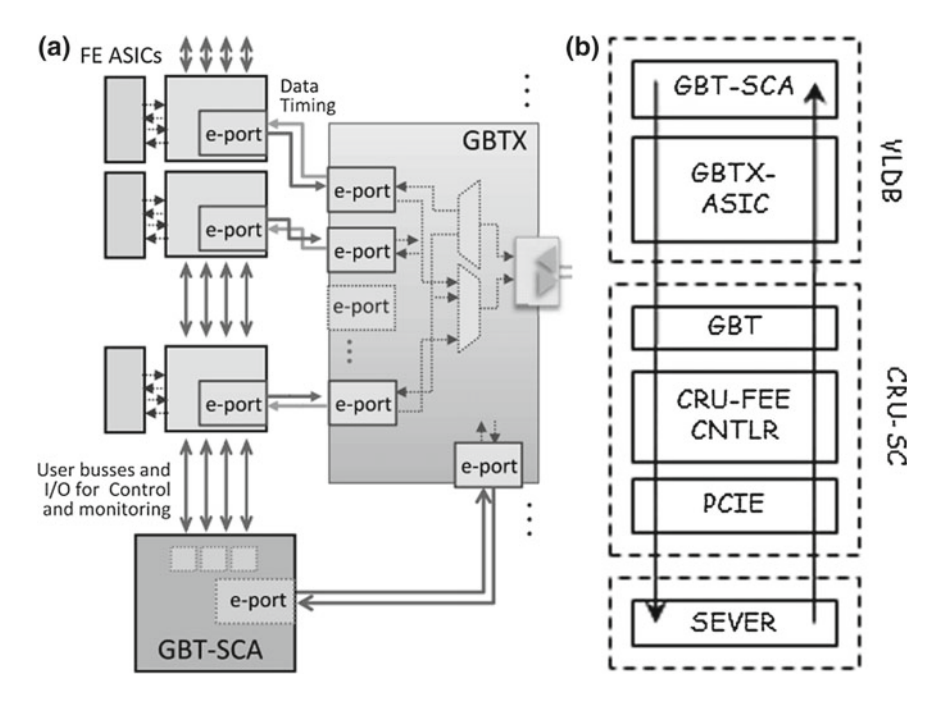


Fig. 3 a General architecture of FEE board b GBT-SCA loop back test

the GBT-SCA. The configuration of rest of chips and on-detector ASIC configuration with actual FEE board will be in future release.

References

- 1. https://twiki.cern.ch/twiki/bin/viewauth/ALICE/CRU
- 2. https://opencores.org/project,hdlc,systemspecandinteraces
- 3. https://opencores.org/project,i2c
- A. Caratellia, S. Bonacinia, K. Kloukinasa, A. Marchioroa, P. Moreiraa, R. De Oliveiraa, C. Paillarda, The GBT-SCA, a radiation tolerant ASIC for detector control and monitoring applications in HEP experiments, in *Topical Workshop on Electronics for Particle Physics*, Aix En Province, France, 22–26 Sept 2014
- R.M. Lesmaa, F. Alessioa, J. Barbosaa, S. Barona, C. Caplana, P. Leitaoa, C. Pecorarod, D. Porreta, K. Wylliea, The versatile link demo board (VLDB), in *Topical Workshop on Electronics for Particle Physics*, Karlsruhe, Germany, 26–30 Sept 2016
- P. Moreira, A. Marchioro, K. Kloukinas, The GBT: a proposed architecture for multi-Gb/s data transmission in high energy physics, in *Topical Workshop on Electronics for Particle Physics*, Prague, Czech Republic, 37 Sept 2007, p. 332 [CERN-2007-007.332]
- P. Moreira et al., The GBT-SerDes ASIC prototype, in *Proceedings of the Topical Work-shop on Electronics for Particle Physics, TWEPP2010*, Aachen, Germany, Sept 2010 [2010JINST5C11022]

A Simulation Model for Triple GEM Detector

Sagarika Swain, M. M. Mondal, P. K. Sahu and S. N. Nayak

Abstract A systematic model for simulating GEM detector is presented using Garfield++ package. ANSYS, a mechanical interface based on finite element analysis method is used to solve the electric field lines inside the detector. Garfield++, along with the implementation of two other softwares, Heed and Magboltz are used to simulate the ionization of gas molecule inside detector chamber and to investigate the electron transport property for a given electric field. The simulation is performed for a triple GEM prototype, having GEM foils of standard geometrical configuration. Preliminary calculations are done for extracting information like electron collection efficiency, extraction efficiency, and detector gain along with field distribution.

1 Introduction

A simulation study is performed for GEM operation with Garfield++ package [1]. This study requires the following procedures: setting the detector geometry, boundary conditions for field distribution, transport properties of used gas mixture, and initial particle distribution with energy for the analysis. Considering the detector geometry, we used a standard triple GEM prototype setup, assembled at IOP, High Energy Detector (HED) laboratory. It consists of three stacks of $10 \,\mathrm{cm} \times 10 \,\mathrm{cm}$ GEM foils placed in between a cathode (drift) and a readout plane, procured from CERN. The drift gap, two transfer gaps, and induction gap are kept as 3, 2, 2, and 2 mm, respectively. The GEM foils are of standard geometry consisting of 50 μ m kapton with 5 μ m copper electrodes on both sides. The foils are fabricated with array of equidistant holes (diameter is 70 μ m, and pitch is 140 μ m) [2]. This detector system

S. Swain (⋈) · M. M. Mondal · P. K. Sahu Institute of Physics, HBNI, P.O: Sainik School, Sachivalaya Marg, Bhubaneswar 751005, India e-mail: sagarika.swain@cern.ch

S. Swain · S. N. Nayak School of Physics, Sambalpur University, Jyoti Vihar, Burla, Sambalpur 768019, India is used as a reference model for setting up the background for simulation codes. Sample script files are executed in ANSYS framework for solving the field meshing and setting different boundary conditions [3]. ANSYS is also capable of delivering structural analysis for the graphical visualization of potentials. The produced three-dimensional field maps by ANSYS are loaded to main source code of Garfield++ for the further execution. Properties of the detector, such as its efficiency, gain, and field distribution, are explored with certain voltage distributions. Finally, the simulated results are compared with experimental measurements, which were carried out for triple GEM setup. All the measurements and simulations are done with Ar:CO₂ gas mixture in 70:30 ratio at standard room temperature and pressure.

2 Simulation Input

2.1 Garfield++

Garfield++ is a compact toolkit for the detailed simulation of two- or three-dimensional particle detectors. These detectors generally use gases or semiconductors as their interaction medium. The basic commands are written in C++ framework to fully utilize the object-oriented programming. It can also be executed in ROOT environment by interfacing with Garfroot. The main features involved in Garfield++ package are calculation of ionization phenomena due to the initial electron, propagation of avalanche electrons in different field mesh along with tracking endpoints of electrons and ions [4]. There are some interfacing features available with this package that can be used extensively to describe detector functioning in more complex environments.

Magboltz mainly deals with the phenomena of transport of electron in gas mixture. Measurements of electron drift velocity, different diffusion and attachment coefficients and gain variation with electric and magnetic fields are involved in this tool [5].

Heed is generally used for computing energy loss of fast charged particle in gases. It is also capable of measuring absorption of photons with ionization spectra. The number of cluster formation per cm along with cluster size distribution can also be investigated [6].

2.2 Geometry and Field Solver: ANSYS

The geometry formation and calculation of electric field for triple GEM setup are performed through ANSYS. It uses finite element analysis method to solve the field map by inserting appropriate boundary functions. For building GEM layers, first materials are defined by their corresponding permittivity and resistivity value with specific volume number. Different geometrical layouts including cone, cylinder, and

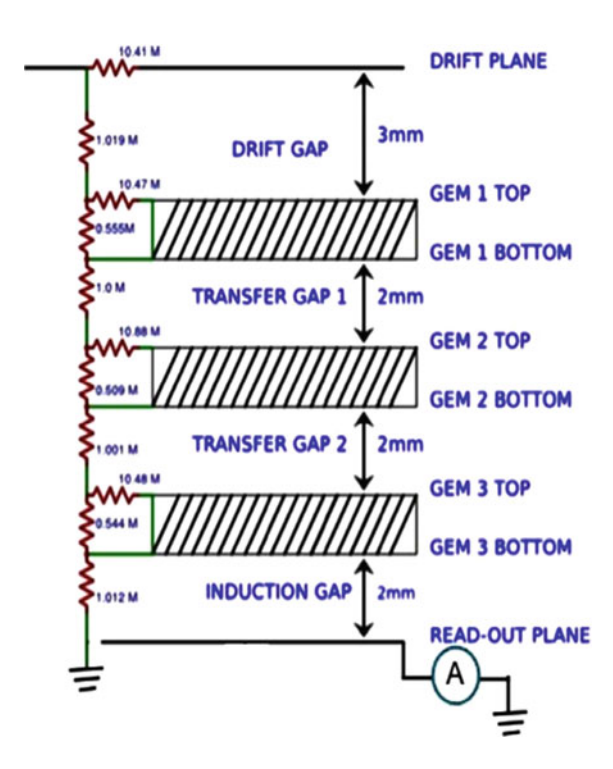
rectangle are incorporated to create the required shapes. Total volume is divided into bunch of interconnected nodes having simple tetrahedral patterns. So that, the field values can be assigned separately to individual points. After assigning different volume numbers and field values, all the structure are glued together. For geometry, we considered GEM foils of hexagonal configuration and the distance between two adjacent holes is $140~\mu m$. Corresponding diameters for inner and outer layers are $50~\text{and}~70~\mu m$, respectively.

Field meshing is started with setting material properties and specifying voltage boundary conditions to each node. As we want to keep the GEM voltage configuration similar to our experimental setup, voltages are calculated from the resistances values used in the voltage divider circuit in Fig. 1 and current measured from the pico ammeter.

For example, for a particular voltage $4400 \, \text{V}$, the obtained divider current is $785 \, \mu \, \text{A}$ and the corresponding voltages calculated from the resistances, 1.019, 0.55, 1.00, 0.509, 1.001, 0.544, and $1.012 \, \text{M}\Omega$, respectively, are 785, 436, 400, and $426 \, \text{V}$ in drift (= transfer1 = transfer2 = Induction), GEM1, GEM2, and GEM3, respectively.

For other voltage setups (3000–4600V), the calculated voltages are input to the ANSYS script. Finally, ANSYS produces four output text files, e.g., ELIST.lis, NLIST.lis, MPLIST.lis, and PRNSOL.lis that specify list of elements, list of nodes with their position in space, material property table, and estimated potentials at each of the nodes, respectively.

Fig. 1 Voltage divider circuit with specification of triple GEM detector



S. Swain et al.

2.3 Numerical Calculations

Output files are stored in an executable format in a specific directory, for interfacing with Garfield++ program. In the beginning, the gas mixture is assigned with all the transport parameters as a function of electric field by Magboltz interface. Here, we defined $Ar:CO_2$ gas in 70:30 ratio at room temperature and pressure as our working environment. As Magboltz interface does not contain any features for calculating transport properties for ions, the ion mobilities class is set manually. One more parameter that needs to set externally is the value of penning transfer. It is a process, where the excitation energy is used to ionize the gas molecule of admixture and increase the gas gain in a detector [7]. Probability of such transfer mechanism depends on both gas composition as well as pressure. For our gas composition, the penning transfer ratio is manually set to 0.57 as given in [8]. Here, the penning transfer rate is calculated by fitting the measured gas gain curve for argon mixture with 30% CO_2 at 1 atm pressure.

For initiating the avalanche process, a single electron with energy $0.5\,\text{eV}$ is placed 200 μm above the top of first GEM. Garfield++ is capable of tracking electrons and ions end points with energy and position information. Therefore, starting from a particular voltage setting, program is executed for the calculation of electrons and ions distribution along with corresponding efficiency and gain variations. Due to the requirements of more computation time, the program is run in batch mode in our local cluster with different required voltage configurations (3000–4600 V) as discussed in the previous section.

3 Simulation Results

A triple GEM setup is simulated with Garfield++ package for various voltages. The plot of produced electric field for first GEM layer is shown in Fig. 2. To study the charge transport phenomenon, following quantities are investigated.

- **Collection efficiency**: It is the fraction of total number of electrons entering GEM holes to the number of electrons generated just above foil.
- Extraction efficiency: It is the fraction of total number of electrons extracted from the GEM holes to the number of electrons generated inside it.
- Gain: It is the number of electrons that are collected at the readout after all the avalanche multiplication per incoming electron.

Initial measurements of collection efficiencies for different GEM layers are given in Fig. 3a. It is observed that for GEM1, it varies from 90% to 92 % and for other two layers, the values are 30–34% of the total electrons created above. Maximum number of electrons collected in GEM1 result due to the initial position of starting electrons, which is just above the hole. Variation in extraction efficiency as a function of voltage has also been calculated, as shown in Fig. 3b. The extraction efficiency is almost constant, and no significant variation is observed with function of total voltage. Gains

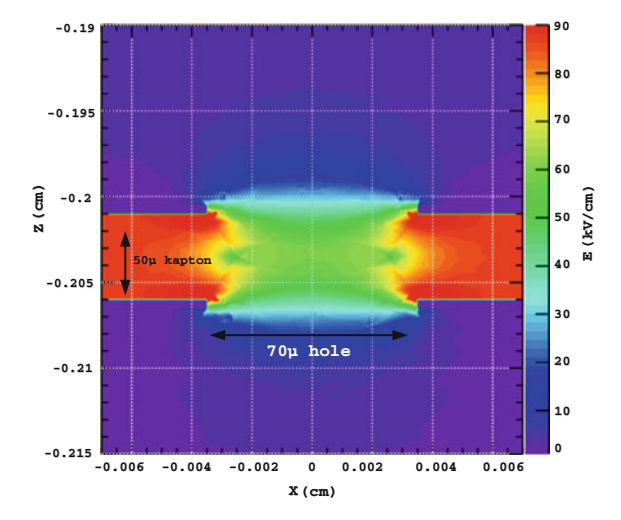


Fig. 2 The electric field distribution is plotted for first GEM layer at an applied voltage of 4400 V showing a variation in field strength up to 90 kV/cm. The axes (X and Z) are in cm. The lower region refers to the field distribution of drift gap and upper specifies the transfer gap 1

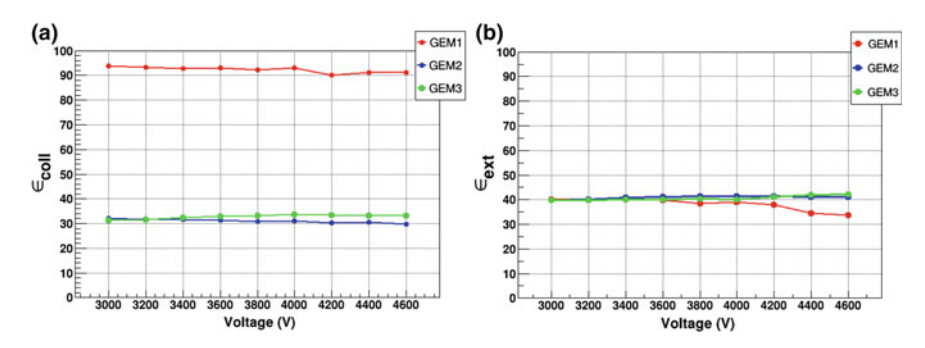


Fig. 3 Efficiency measurement for triple GEM setup: a Collection efficiency. b Extraction efficiency, as a function voltage for different GEM layers

for each GEM layers are observed and shown in Fig. 4a. An exponentially increasing trend of gain is found with voltage for GEM1 and GEM2. But for GEM3 after a certain limit (4000V), a sudden drop in gain value is noticed. This is due to the fact that with high gain value, more number of ions are accumulated near the last GEM (due to their low mobility), where the avalanche is maximum. Since this accumulation mainly leads to a space charge effect, the gain decreases thereafter. Finally, simulation results obtained for effective gain is compared with experimental measurements in Fig. 4b, that were done for Fe⁵⁵ source with triple GEM setup [9]. Recently, gain

S. Swain et al.

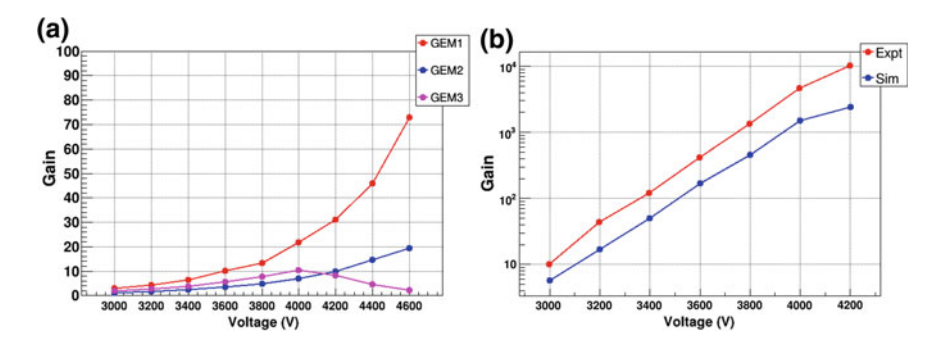


Fig. 4 a Individual gain for GEM layers. **b** Comparison between simulated gain and experimental gain: the experiment is performed for the triple GEM setup for Fe⁵⁵ iron source with Ar:CO₂ gas in 70:30 ratio

of similar order is measured experimentally [10] for triple GEM detector, same as our configuration. The difference between the simulated and experimental results is apparently visible. To minimize the difference between these results, we may tune the penning factor, which has a direct effect on gas gain.

4 Summary

We have performed a simulation study for triple GEM-based detector with Garfield++ package. ANSYS software is used for setting the detector geometry and field meshing with proper boundary conditions. Characteristics study for the detector with voltage variation is carried out. The simulation results with the existing lab configuration are presented here. The detector gain and efficiencies for each GEM layers are calculated with a variation of voltages. We have compared the effective gain obtained from simulation with experimental measurements done for Fe⁵⁵ source with Ar:CO₂ in 70:30 environment.

References

- 1. R. Veenhof, Garfield++ (2010–2012), http://garfieldpp.web.cern.ch/garfieldpp/
- F. Sauli, The gas electron multiplier (GEM): operating principles and applications. Nucl. Ins. Meth. A 805, 2–24 (2016)
- 3. Ansys Software. Maxwell, http://www.ansys.com/products/electronics/ansys-maxwell
- 4. R. Veenhof, GEM simulation methods development. Nucl. Ins. Meth. A 478, 452–459 (2002)
- 5. S. Biagi, Magboltz, http://consult.cern.ch/writeup/magboltz/
- 6. I. Smirnov, Garfield-9, http://consult.cern.ch/writeup/heed/, 1995-2012
- 7. O. Sahin, Penning transfer in argon-based gas mixtures. J. Instrum. 5, P05002 (2010)
- 8. O. Sahin et al., High-precision gas gain and energy transfer measurements in Ar- CO_2 mixtures. Nucl. Ins. Meth. A **768**, 104 (2014)

- R.P. Adak et al., Long-term stability test of a triple GEM detector. J. Instrum. 11, T10001 (2016)
- R.N. Patra et al., Measurement of basic characteristics and gain uniformity of a triple GEM detector. Nucl. Ins. Meth. A 862, 25–30 (2017)

Author Index

| A | J |
|---|--|
| Adak, R. P., 199 | Jash, Abhik, 129, 167, 175 |
| Anoop, K. V., 187 | Jhingan, Akhil, 29 |
| Attie, David, 81 | |
| | |
| | K |
| В | Khan, S. A., 107, 217 |
| Bhardwaj, Ashutosh, 3 | Kumar, Shyam, 97 |
| Bhattacharya, Aparajita, 81 | |
| Bhattacharya, Deb Sankar, 81, 91 | M |
| Bhattacharya, Purba, 81 | |
| Bhattacharya, Sudeb, 81 | Majumdar, Nayana, 81, 129, 167, 175 |
| Biswas, R., 199 | Maulik, Atanu, 49 |
| Biswas, S., 199, 205, 211 | Mitra, J., 107, 217 Moharana, Reetanjali, 119 |
| | Mondal, Mriganka M., 147, 223 |
| | Mukherjee, S., 107, 217 |
| C | Mukhopadhyay, Supratik, 67, 81, 129, 167, |
| Chakrabarti, A., 107, 217 | 175 |
| Chattopadhyay, Subhasis, 157, 167 | 173 |
| Colas, Paul, 81 | |
| Costa, F., 107, 217 | N |
| | Nag, Abhishek, 193 |
| | Nag, D., 199, 205 |
| D | Nagu, Srishti, 137 |
| Das Gupta, K., 97 | Nanal, V., 187 |
| Dash, Nitali, 119 | Nandy, Ekata, 157 |
| Das, S., 199, 205 | Nayak, S. N., 147, 223 |
| Datta, Jaydeep, 129 | Nayak, T., 107, 217 |
| Deb, S.K., 97 | • |
| Dey, Balaram, 187 | |
| | P |
| | Pal, S., 187 |
| G | Paul, D., 199, 205 |
| Ganjour, Serguei, 81 | Paul, R., 107, 217 |
| Ghosh, C., 187 | Pillay, R. G., 187 |
| Ghosh, S. K., 205 | Pose, M. S., 187 |
| Ghosh, Tilak Kumar, 15 | Prasad, S. K., 205 |
| © Springer Neture Singapore Pte I td 2018 | 221 |

© Springer Nature Singapore Pte Ltd. 2018

S. Biswas et al. (eds.), Advanced Detectors for Nuclear, High Energy and Astroparticle Physics, Springer Proceedings in Physics 201, https://doi.org/10.1007/978-981-10-7665-7

232 Author Index

| R Raha, S., 205 Rout, Prasant Kumar, 81 Roy, S., 199, 205 Rudra, S., 199 | Satyanarayana, B., 59 Singh, Jaydip, 137 Singh, Jyotsna, 137 Swain, Sagarika, 91, 147, 211, 223 |
|--|--|
| S Saha, Satyajit, 167, 175 Sahu, P. K., 91, 147, 211, 223 Sahu, S., 91, 211 | T Tripathy, Sridhar, 167, 175 |
| Sarin, Pradeep, 97 Sarkar, Sandip, 81, 175 | V Varma, Raghava, 97 |